A Retrofitting Framework for Pre-Northridge Steel Moment-Frame Buildings

Thesis by

Arnar Bjorn Bjornsson

In Partial Fulfillment of the Requirements

for the Degree of

Doctor of Philosophy

California Institute of Technology

Pasadena, California

2014

(Defended May 15 2014)

To Hildí

Acknowledgements

I am grateful to Caltech for the outstanding education that I have received and the generous financial support through the course of my stay here.

During my years at Caltech I have had the privilege of working with two advisors and learn two perspectives on science and research. Firstly, Dr. Swami Krishnan was my advisor for the first four years of my graduate studies and, not less importantly, during my SURF experience at Caltech before coming to campus as a graduate student. Secondly, Professor John Hall was my advisor in the homestretch of my graduate studies. I wish to extend my sincere gratitude for their influence on my academic development and career, and I hope that one day I will be able to pay it forward.

I would like to thank the members of my thesis committee, Professor Tom Heaton, Professor Jim Beck, and Dr. Robert Graves. Whenever I have turned to them for advice, I have found nothing but support and resourcefulness.

I wish to extend my gratitude to Professors Ragnar Sigbjornsson and Sigurdur M. Gardarsson, who inspired me to pursue a PhD degree in Civil Engineering. I would also like to acknowledge the continued support of Egill Thorsteins in all my endeavours.

I am thankful to Dr. Kristin Ingolfsdottir, Professor Jon Atli Benediktsson, and Dr. Kiyo Tomiyasu, who were key players in establishing a collaborative agreement in teaching and research between Caltech and the University of Iceland. Because of this agreement, I had the opportunity to participate in the SURF program at Caltech, which introduced me to research and higher education in the United States.

My thanks go to the MCE staff, Carolina Oseguera, Cheryl Greer, Chris Silva, Leslie Rico, Lynn Seymour, and Maria Koeper, for their hard work, which allows students focus on their studies.

Thanks to my fellow graduate students and friends that I have cherished during my stay in Southern California, a long way from my family and friends in Iceland. A special thanks to Francesco Restuccia, Anthony Massari, Grant Hollis, Ramses Mourhatch, and Chris Janover for their help in revising my thesis and prepairing for my thesis exam.

Above all, I am deeply thankful to my family. To my parents. Anything that I am and anything that I accomplish is because they gave me their unconditional love and support. To my brothers, who continue to break the waves for me and set the standards for me to live up to. To my parents-in-law for their continued encouragement through the course of my studies. To my wife Hildí and our daughter Emilía Ásta. All my work is dedicated to them. They bring me more happiness than anyone could ever wish for.

Abstract

In the 1994 M_w 6.7 Northridge and 1995 M_w 6.9 Kobe earthquakes, steel moment-frame buildings were exposed to an unexpected flaw. The commonly utilized welded unreinforced flange, bolted web connections were observed to experience brittle fractures in a number of buildings, even at low levels of seismic demand. A majority of these buildings have not been retrofitted and may be susceptible to structural collapse in a major earthquake.

This dissertation presents a case study of retrofitting a 20-story pre-Northridge steel moment-frame building. Twelve retrofit schemes are developed that present some range in degree of intervention. Three retrofitting techniques are considered: upgrading the brittle beam-to-column moment resisting connections, and implementing either conventional or buckling-restrained brace elements within the existing moment-frame bays. The retrofit schemes include some that are designed to the basic safety objective of ASCE-41 Seismic Rehabilitation of Existing Buildings.

Detailed finite element models of the base line building and the retrofit schemes are constructed. The models include considerations of brittle beam-to-column moment resisting connection fractures, column splice fractures, column baseplate fractures, accidental contributions from "simple" non-moment resisting beam-to-column connections to the lateral force-resisting system, and composite actions of beams with the overlying floor system. In addition, foundation interaction is included through nonlinear translational springs underneath basement columns.

To investigate the effectiveness of the retrofit schemes, the building models are analyzed under ground motions from three large magnitude simulated earthquakes that cause intense shaking in the greater Los Angeles metropolitan area, and under recorded ground motions from actual earthquakes. It is found that retrofit schemes that convert the existing moment-frames into braced-frames by implementing either conventional or buckling-restrained braces are effective in limiting structural damage and mitigating structural collapse. In the three simulated earthquakes, a 20% chance of simulated collapse is realized at PGV of around 0.6 m/s for the base line model, but at PGV of around 1.8 m/s for some of the retrofit schemes. However, conventional braces are observed to

deteriorate rapidly. Hence, if a braced-frame that employs conventional braces survives a large earthquake, it is questionable how much service the braces provide in potential aftershocks.

Contents

List of Figures

List of Tables

Chapter 1

Introduction

Steel moment-frames are rectilinear assemblages of beams and columns with the beams rigidly connected to the columns. The frames resist lateral loads primarily by developing bending and shear forces in the frame members. During strong ground motions the frames are expected to sustain multiple cycles of significant inelastic responses. Plastic deformations are intended to primarily be confined to plastic hinging of beams, but some yielding may occur in columns and in beam-to-column joints (panel zones). Through these plastic deformations, the frames dissipate the seismic energy to some extent. The integrity of the steel moment-frame is therefore dependent on the beam-to-column connections being capable of transfering the moments developed in the beams to the columns.

Steel moment-frames were first conceived as a means of building construction in the late 1800s with the Home Insurance Building in Chicago, a 10-story structure with a height of 42 m (138 ft) that is often credited as the first steel moment-frame building (and the first skyscraper) [37]. Soon after, engineers began to observe that steel moment-frames appeared to exhibit superior performance in earthquakes. For instance, 20 such buildings were subjected to and survived the 1906 M_w 7.8 San Francisco earthquake and the subsequent fires, while few other buildings in the central commercial district of San Francisco remained standing [37]. As a result of their apparently superior performance, steel moment-frames grew in popularity and became the preferred lateral-resisting structural system in seismically prone regions.

The early versions of steel moment-frame buildings were generally composed of built-up structural sections with nearly all beam-to-column connections detailed as moment resisting connections, and with masonry infill walls at their perimeter. These moment resisting connections consisted of stiffened or unstiffened structural angles, bolted or riveted to the beams and columns. Furthermore, the steel framing was typically completely encased in masonry, concrete, or a combination

of the two, to provide fire proofing. The composite actions of the steel framing with the masonry and/or concrete is likely to have contributed significantly to the earthquake resistance of these buildings [37, 19]. The more modern steel moment-frame buildings with lightweight fireproof coating sprayed on the structural steel elements do not have the benefit of this composite behavior.

Since then, steel moment-frame buildings have gone through several stages of development. The built-up sections were largely replaced by hot-rolled structural sections. The perimeter masonry infill walls receded after curtain wall systems became popular in the late 1940s and early 1950s. In the late 1950s, structural welding was introduced to the building industry. By the 1970s welded unreinforced flange, bolted web beam-to-column moment resisting connections had become the standard practice in the construction of steel moment-frames. The connections incorporated field-welded, complete joint penetration (CJP) groove welds to join beam flanges to columns, with shop-welded, field-bolted plates joining beam webs to columns. A schematic figure of this type of beam-to-column connection is presented in Figure 1.1. These connections would later become known as "pre-Northridge" moment connections. In the 1980s another important trend resulted from increasing cost of labour. Engineers had begun to economize their designs by using fewer bays of moment resisting framing that employed heavier structural sections, greatly diminishing the redundancy of steel moment-frame buildings [37, 19].

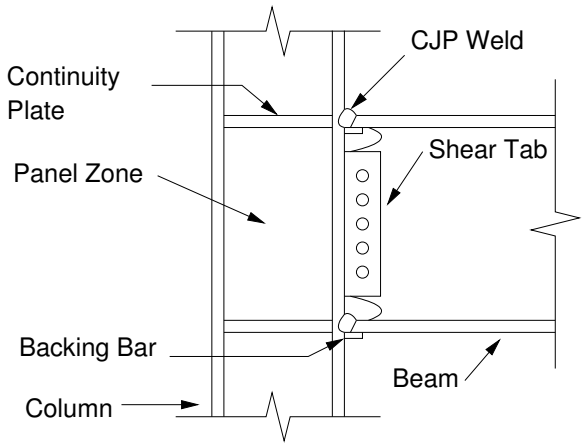

Figure 1.1: A schematic figure of welded unreinforced flange, bolted web beam-to-column moment resisting connection popularly used in the years 1970-1994. The connections would later become known as pre-Northridge moment connections.

In the 1994 M_w 6.7 Northridge earthquake, steel moment-frame buildings were exposed to an unexpected flaw. The commonly utilized welded unreinforced flange, bolted web connections were observed to experience brittle fractures in a number of buildings. The damaged buildings had

heights in the range of one story to 26 stories, and a range in age spanning from 30 years old to buildings that were under construction at the time of the earthquake. Also, the damaged buildings were spread over a large geographic area, including locations that experienced only moderate levels of seismic demands [20].

The fractures most commonly initiated at the CJP welds between beam bottom flange and the column flange. Once the fractures had initiated, they progressed along a number of different paths. In some instances, the fractures progressed completely through the CJP welds (Figure 1.2 (a)). In other instances, the fractures progressed into the column flange material behind the CJP welds. In these cases, a portion of the column flanges remained bonded to the beam bottom flange, and was ripped out from the column flange (Figure 1.2 (b)). A number of fractures were observed to have progressed completely through the column flange (Figure 1.2 (c)), and sometimes these fractures continued into the panel zones (Figure 1.2 (d)) [20].

Similar observations were made a year later in the 1995 M_w 6.9 Kobe earthquake. The confidence in steel moment-frames was shattered.

Following the startling discoveries in the Northridge earthquake, a federally funded partnership of the Structural Engineers Assoctiation of California (SEAOC), the Applied Technology Council (ATC), and the California Universities for Research in Earthquake Engineering (CUREe), known as the SAC Joint Venture, was charged with determining what contributed to the poor connection performance, in order to develop recommendations for retrofitting the flawed connections, and to develop recommendations for more robust construction techniqes for new moment-frame buildings. The research conducted through the SAC Joint Venture along with other independent studies concluded that the key contributers to the poor connection performance included [18]:

- The largest forces in the beam-to-column assembly generally occur near the column flanges where the beam is connected to the column. This is also the location where the beam cross-section is reduced to allow for connection details such as the weld access holes. As a result, concentrations of stresses are experienced in the reduced beam section.

- The beam bottom flange weld was generally made from an above position leading to a discontinuity of the weld at the location of the beam web, which often resulted in a poor quality weld at this location with slag inclusions, lack of fusion, and other defects that served as crack initiators.

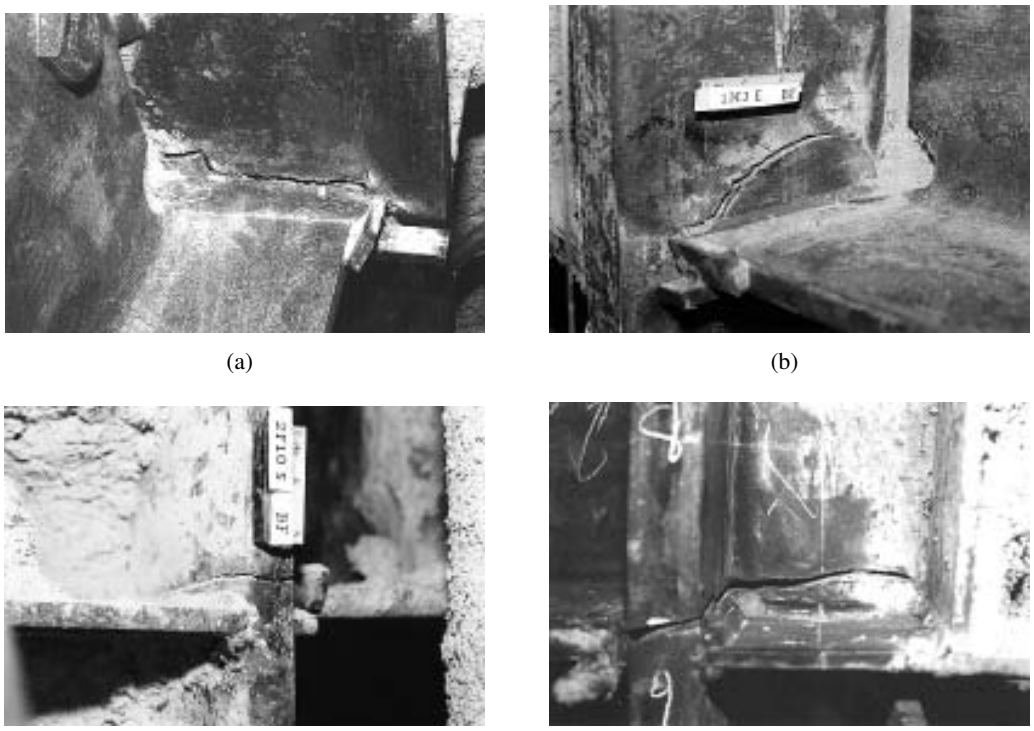

(a) (b)

(c) (d)

Figure 1.2: Example of connection fractures experienced in steel moment-frame buildings in the 1994 M_w 6.7 Northridge earthquake. The fractures commonly initiated in the beam bottom flange CJP welds. In some instances, the fracture progressed completely through the CJP welds (a). In other instances, the fractures progressed into the column flange material behind the CJP welds. In these cases, a portion of the column flanges remained bonded to the beam bottom flange, and was ripped out from the column flange (b). A number of fractures were observed to have progressed completely through the column flange (c) and sometimes these fractures continued into the panel zones (d) [20].

- The weld backing bar was generally left in place, which had several implications. It dissallowed visual inspections of the welds, and instead quality inspection of the welds relied on ultrasonic testing (UT). However, the presence of the backing bar made UT a very unreliable method for detecting weld defects. Finally, the backing bar and the column flange formed an initial crack in the weld, makin itf susceptible to brittle failure.

- In design, shear forces in the beams are assumed to be transferred to the columns primarily through the shear tab. In reality, the beam flanges carry a substantial portion of the beam shear forces, which leads to stress concentrations in the root of the beam flange welds.

- The geometry of the weld access holes often led to stress concentrations in the beam flanges near the toe of the access holes.

- Design practice in the years spanning from 1985 to 1994 encouraged connections with relatively weak panel zones. In connections with excessively weak panel zones, the plastic behavior of the beam-column assembly is dominated by shear deformations in the panel zone, and leads to increased stresses in the flanges of the connecting beam.

- In the mid 1960s the construction industry moved to welding techniques, and the use of welding consumables that produced welds with low toughness. The toughness of the weld was further compromised by excessive deposition rates commonly practiced by the welders.

- In earlier versions of steel moment-frame buildings nearly all beam-to-column connections were detailed to be capable to transfer moments from the beams to the columns. As cost of labor increased, engineers started to find it more economical to limit the number of moment resisting frames and instead used larger sections. Strain demands of moment-connections, however, are related to depth-to-span ratio of the members. Hence, as the member sizes increased, the connection strain demands also increased and made the connections more susceptible to brittle behavior.

- The steel properties delivered from the steel mills had considerably higher yield strengths than what was specified by the engineers. As a result, the toughness of the welding materials was undermatched.

To date there are several beam-to-column moment resisting connection configurations that are "pre-qualified" to be used for retrofitting pre-Northridge moment connections,f and for use in con-

struction of new steel moment-frame buildings. Since the Northridge earthquake, AISC 341 Seismic Provisions for Structural Steel Buildings have required special moment-frame connections to be demonstrated to reliably achieve 4% inter-story drift without excessive strength loss, when subjected to the cyclic loading protocol specified in AISC 341. Inter-story drift refers to relative displacments of two adjacent floors normalized by the height of the story defined by the two floors. The "pre-qualified" connection configurations have already been satisfactorily put through the extensive laboratory testings and can be readily used within the conditions set for each configuration, without further experiments.

Connection details that are "pre-qualified" to be used for retrofitting of pre-Northridge moment connections include [19]: welded bottom haunch moment connections, welded top and bottom haunch moment connections, and welded cover plated flange moment connections. Recently, Kaiser bolted bracket (KBB) moment connections have also been "pre-qualified" for the retrofitting of pre-Northridge moment connections. Connections details that are "pre-qualified" to be used in construction of new steel moment-frame buildings include [2]: reduced beam section (RBC) moment connections, bolted unstiffened and stiffened extended end-plated moment connections, bolted flange plate (BFP) moment connections, welded unreinforced flange-welded web (WUF-W) moment connections, and Kaiser bolted bracket (KBB) moment connections.

The cost of potential retrofitting schemes and their impact on the architecture are unknown, and owners of steel frame buildings have been reluctant to consider undertaking retrofit measures. Also, building owners have not been presented with financial incentives, such as tax discounts, to undertake retrofitting measures. Neither have the buildings been mandated to be retrofitted. As a result, many of these buildings have been left unaltered and may be susceptible to collapse in the event of a major earthquake. Although no steel moment-frame buildings collapsed in the Northridge earthquake, a majority of the seismic energy that was released in the Northridge earthquake was directed away from urbanized areas. Also, larger magnitude earthquakes are inticipated to strike the greater Los Angeles region [67, 68, 66]. Hence, the buildings have yet to be put to their ultimate test.

Several studies have shown that the pre-Northridge steel moment-frame buildings may be susceptible to collapse under strong ground motions. Hall et al. [32, 33, 34] and Heaton et al. [38] studied four fictional steel moment frame buildings, a six-story and another twenty-story steel moment-frame building designed to the 1994 Uniform Building Code (UBC), and equivalent "Japanese"

versions of the buildings designed to the more stringent building code that was enforced in Japan at the same time as the 1994 UBC. Furthermore, the study considered two versions of each building model. A version that included considerations of fracture susceptible connections to mimic the brittle behavior of the pre-Northridge beam-to-column connections, and a version with perfect connections. The pre-Northridge steel moment-frame buildings were simulated to collapse at a number of locations in a simulated M_w 7.0 earthquake on the Elysian Park blind-thrust fault directly beneath Los Angeles. The building models with perfect connections performed much better.

Olsen et al. [59] further investigated those four building models with a focus on quantifying the ground motion intensity parameters necessary to induce simulated "unrepairable" damage or simulated collapse. They concluded that a vector intensity measure of horizontal peak ground velocity (PGV) and peak ground displacement (PGD) best describes the potential of a ground motion time history to induce the two building performance levels. Furthermore, in PGD-PGV space they present curves that represent 10% chance of simulated "unrepairable" model damage or simulated collapse. The twenty-story UBC pre-Northridge steel moment-frame building model (with brittle connections) realized a 10% chance of simulated collapse at peak ground velocities of around 0.6 m/s. The Japanese version of that same building model realized a 10% chance of simulated collapse at peak ground velocities of around 0.75 m/s. The twenty-story building models with perfect connections and all four six-story building models proved to be much more resistant to simulated collapse.

Krishnan et al. studied the performance of two 18-story steel moment-frame buildings in an simualted M_w 7.9 earthquake on the San Andreas fault [45, 46, 47]. The two building models consisted of a model of an existing steel moment-frame building designed to the 1982 UBC, and a redesigned version of the existing building conforming to the more stringent 1997 UBC. The model fo the existing building included considerations of fractures of the beam-to-column moment resisting connections in a similar fashion as Hall et al. The building models were simulated to collapse at a number of locations in the Los Angeles metropolitan area, but the redesigned version of the existing model performed much better.

Muto and Krishnan studied the performance of three steel moment-frame building models in the M_w 7.8 ShakeOut scenario earthquake on the San Andreas fault [48, 57]. In fact, two of the building models were the same as those studied by Krishnan et al. [45, 46, 47]. The third building had an L-shaped footprint and was designed after the 1997 UBC. According to the UBC, the building is considered irregular and is therefore designed with 10% greater lateral foces than a regular building.

Two versions of each building model were assumed: a version with brittle connections, and a version with perfect connections. The building models were simulated to collapse at a number of locations in the greater Los Angeles metropolitan area, but the model of the existing building (with brittle connections) showed the poorest performance. Muto and Krishnan also presented fragility curves that showed the probability of the building models to be simulated to collapse given a horizontal peak ground velocity. The model of the existing building with brittle connections realized a 20% chance of simulated collapse at a horizontal peak ground velocity of around 0.75 m/s.

Krishnan and Muto further investigated the collapse behavior of the model of the existing building and the redesigned version of the building [49, 50]. They showed that in the event of simulated collapse, the building models form one out of only a few "preferred" collapse mechanisms confined in the lower half of the building models. Furthermore, through classical energy balance analyses they show that the "preferred" collapse mechanisms are characteristics of the building models and not the input ground motions. These findings raise interest in investigating what improvement in building performance can be achieved through retrofit schemes that focus on strengthening only the lower half of tall steel moment-frame buildings.

In order to reduce the collapse potential of pre-Northridge steel moment-frame buildings, retrofitting measures must be taken. These measures must realize a lower probability of collapse for the structures at a given intensity of ground shaking when compared to the existing versions. At the same time, they need to be economically feasible and, to the extent possible, must preserve the architechtural integrity and funcionality of the building.

Improved structural performance can be achieved in multiple ways. Some common rehabilitation techniques are summarized in FEMA 547 Techniques for the Seismic Rehabilitation of Existing Buildings [22]. The techniques described in FEMA 547 for steel moment-frames include upgrading the existing beam-to-column moment resisting connections, adding a concrete or masonry shear wall as a new lateral force-resisting system or in conjunction with the moment-frames, and converting the moment-frames to braced-frames by adding convetional or buckling-restrained brace elements to the existing moment-frames. Furthermore, FEMA 547 suggests that converting the moment-frames to braced frames can be one of the more economical retrofitting techniques available for steel moment-frames. Also, a retrofit scheme that consists solely of upgrading the existing beam-to-column moment resisting connections would clearly have the least impact on the architecture.

Other retrofitting techniques include a number of passive energy dissipation devices. Such devices that have most commonly been used for seismic protection of structures (in North America) include viscous fluid dampers, viscoelastic solid dampers, metalic dampers (e.g. buckling-restrained brace elements, added damping and stiffness (ADAS) dampers), and friction dampers [70]. The interested reader is directed to Symans et al. [70], which presents a summary of the current practice and recent developements in the application of passive energy dissipation systems for seismic protection of building structures.

In order to systematically develop a framework for retrofitting existing pre-Northridge steel moment-frame buildings, we start with a case study of a fictional 20-story building model, designed after the 1994 UBC. This is in fact the same building as was studied by Hall et al. [38, 32, 33, 34]. We develop twelve retrofit schemes with some progressively increasing degrees of intervention. The retrofit schemes considered in the present study consist of retrofitting the brittle beam-to-column moment resisting connections, or implementing either conventional or buckling-restrained braces. The retrofit schemes include some that are designed to the basic safety objective (BSO) of ASCE-41 Seismic Rehabilitation of Existing Buildings [4].

To investigate the effectiveness of the retrofit schemes, detailed finite element models of the base line building and the retrofit schemes are constructed in STEEL, a nonlinear structural analyses program for steel frames developed at Caltech (also referred to as FRAME-2D). The building models include considerations of brittle beam-to-column moment resisting connection fractures, column splice fractures, column baseplate fractures, accidental contributions from "simple" non-moment resisting beam-to-column connections to the lateral force-resisting system, and composite actions of beams with the overlying floor system. In addition, foundation interaction is included through nonlinear translational springs underneath basement columns. To address uncertainties associated with the modeling of the foundations, "soft" (and weak), "stiff" (and strong), as well as "expected" foundation spring stiffnesses and capacities are applied. Also, the modeling of both conventional and buckling-restrained brace elements is validated against experimental data.

Then, the building models are analyzed under ground motions from three large simulated earthquake scenarios in the greater Los Angeles metropolitan area, as well as under recorded ground motions from actual earthquakes that are applied in incremental dynamic analyses of the building models. The simulated improvement in building performance of the retrofit schemes over the base line models is then quantified, and the most successful retrofit schemes are identified.

Performing such analyses on several index buildings provides a clear picture of what degree of retrofitting is required to gain marginal reductions in collapse potential of this class of buildings.

A number of studies have been conducted on the effectiveness of different retrofit techniques applied to steel moment-frames (e.g. [51, 23, 11, 71, 31, 73]). Filiatrault et al. [23] investigated the effectiveness of implementing viscous dampers and friction dampers in a model of a fictional six-story pre-Northridge steel moment-frame building. The retrofit schemes consisted of implementing conventional brace elements in a chevron configuration in one out of three modeled moment-frame bays, with viscous or friction dampers connected to the lower ends of the brace elements. The building models included considerations of beam-to-column connections fractures. They concluded that both viscous and friction damping systems can significantly reduce the responses of the studied structure under near-field ground motions, but they cannot by themselves prevent fractures of beam-to-column connections and associated costly post-earthquake repairs. Also, in some cases the forces developed in the brace elements when applying viscous dampers would have caused substantial yielding in tension and buckling in compression, which would have severely limited the effectiveness of the viscous dampers, but neither was included in the modeling of the braces.

Uriz and Whittaker [73] studied the effictiveness of implementing fluid viscous dampers in a model of a fictional three-story pre-Northridge steel moment-frame building. The dampers were installed as diagonal elements in three out of three modeled steel moment-frame bays. The building models did not consider fractures of beam-to-column moment resisting connections. Similar to Filitrault et al., they concluded that fluid viscous dampers are effective in reducing displacements and deformations in steel moment-frames (under design level and maximum considered earthquake ground motions), but are unlikely to prevent beam-to-column connection fractures. They also reported elevated story shears forces and column axial forces in the retrofitted building model, compared to the base line model.

Sarno and Elnashai [11] investigated the applicability of implementing conventional and buckling-restrained brace elements in a model of a fictional nine-story steel moment-frame building that was intentionally designed with lateral stiffness insufficient to satisfy code drift limitations in zones with heigh seismicity. Two configurations of the brace elements were considered: an X-bracing configuration in two out of five moment-frame bays, and a “mega-brace” configuration. A “mega-brace” refers to a configuration of braces where the brace-line is extended over multiple stories and crosses several bays. They concluded that moment-resisting frames with insufficient lateral stiffness can

indeed be retrofitted with diagonal braces, either conventional or buckling-restrained. They also found that the "mega-brace" configuration resulted in better performance than the the X-bracing configurations.

Tafakori et al. [71] investigated eight variations of implementing friction dampers, mounted on conventional brace elements in a chevron configurations, to retrofit a fictional 15-story steel moment-frame building model that was intentionally designed with lateral stiffness insufficient to satisfy code drift limits. Through incremental dynamic analyses of detailed finite element models of the retrofit schemes and the base line model, the most optimal retrofit scheme was identified based on probabilistic seismic losses (including collapse-induced losses). They concluded that the use of damper-brace systems can be effectively applied in retrofitting steel moment-frames with insufficient lateral stiffness in the 15-story range. Also, the most optimal retrofit scheme employed dampers in every story with considerable concentrations of friction forces in the lower stories.

Some recent studies have focused on developing algorithms that optimize the topological location of added retrofit elements and their design parameters. For example, Apostolakis and Dargush [3] presented a formulation that applies a genetic algorithm and dynamic nonlinear building analyses to find an optimal retrofit design of implementing either buckling-restrained brace elements, friction dampers, or both, for two three-story steel moment-frame building models and another six-story, under four strong ground motion time histories. The optimization function considered transient and residual inter-story drift ratios, and floor accelerations. They found that friction dampers resulted in more optimal building performance for the two three-story building models, while buckling-restrained brace elemetns were found to be more optimal for the six-story model. Also, for the topological layout of the retrofit elements, it was found that "mega-brace" configurations were more optimal.

In the review of the literature, the author did not come across a study that investigated retrofitting of a pre-Northridge steel moment-frame building in the 20-story range. Also, the presented study incorporates a greater level of detail in the finite element modeling than is commonly observed in the literature. Another appealing feature of the present study is that the performance of the 20-story pre-Northridge steel moment-frame building model and the associated retrofit schemes are simulated regionally for three plausible earthquake scenarios in the greater Los Angles metropolitan area, and it is observed geographically how the spread of model damage and collapse can be reduced through the retrofit schemes. The body of work presented herein is meant to add to the rapidly growing body of knowledge on retrofitting steel moment-frame buildings and the design of new steel structures.

The remainder of the dissertation is structured as follows:

Chapter 2 - Description of Buildings: In this chapter the base line model of a fictional 20-story pre-Northridge steel moment-frame building is described, and the retrofit schemes considered in this study.

Chapter 3 - Modeling Considerations: In this chapter the details of the finite element modeling in STEEL are discussed, and efforts toward validating the modeling of conventional and buckling-restrained brace elements are presented.

Chapter 4 - Ground Motions: This chapter discusses the ground motions used to investigate the effectiveness of the retrofit schemes described in Chapter 2. The ground motions include ground motions from a simulated 1857-like M_w 7.9 San Andreas fault scenario earthquake, the simulated M_w 7.8 ShakeOut scenario earthquake on the San Anderas fault, a simulated M_w 7.2 earthquake scenario on the Puente Hills fault system directly underneath downtown Los Angeles, and a collection of recorded ground motions from actual earthquakes applied in incremental dynamic analyses of the building models.

Chapter 5 - Results: In this chapter, the simulated performances of the building models under the ground motions described in Chapter 4 are presented. The collapse mechanisms most frequently observed for the building models are described as well.

Chapter 6 - Summary, Conclusions, and Future Work: This chapter presents a brief summary of the research, a summary of key observations and conclusions, and some suggestions of future directions that the research can be expanded to.

Chapter 2

Descriptions of Buildings

2.1 Base Line Model

The base line model considered in this study is a fictional twenty-story "pre-Northridge" steel moment-frame building developed by Hall [33]. The height of the building (above ground) is 77.9 m (255′-6″) with a typical story height of 3.8 m (12′-6″) and a taller first story at 5.5 m (18′-0″). The building has a single basement story of same height as the first story. An isometric view of the building is shown in Figure 2.1, and typical floor plan showing the arrangement of moment-frame bays is presented in Figure 2.2.

The building was design to conform to the 1994 Uniform Building Code. Dead loads are assumed as 3.83 kPa (80 psf) for the roof, 4.55 kPa (95 psf) for the floors, and 1.68 kPa (35 psf) for the cladding. The floor live loads are taken as 2.39 kPa (50 psf). The self weight of the steel frames is considered to be included in the dead loads above. Since the earthquake response of the narrow dimension of the building is of most interest, designs were carried out in this direction only. Similarly, analysis included herein is only of the narrow dimension. Details of the design are given in [33]. An elevation view of frames A and B is shown in Figure 2.3. Frames A and E are identical, and similarly frames B, C, and D are identical to each other. Panel zones of columns are reinforced with doubler plates as needed such that the panel zone yield moment is equal to 0.8 times the sum of the plastic moments of the connecting beams. A 61 cm (24 in) concrete wall is assumed continuous along the perimeter of the building at the basement story. A concrete slab on a metal deck is assumed with the ribs of the steel deck oriented perpendicular to the frames of interest. The material properties for beams and columns are given as:

E	199.9 GPa (29000 ksi)
E_{sh}	4.0 GPa (580 ksi)
σ_y	289.6 MPa (42 ksi)
σ_u	344.7 MPa (50 ksi)
ε_{sh}	0.012
ε_{rup}	0.308
τ_y	165.5 MPa (24.0 ksi)
G	80.0 GPa (11600 ksi)

Where E is the Young's modulus, E_{sh} is the initial strain hardening modulus, σ_y is the yield stress, σ_u is the ultimate stress, ε_{sh} is the strain at onset of strain hardening, ε_{rup} is the strain at rupture, τ_y is the shear yield stress, and G is the shear modulus.

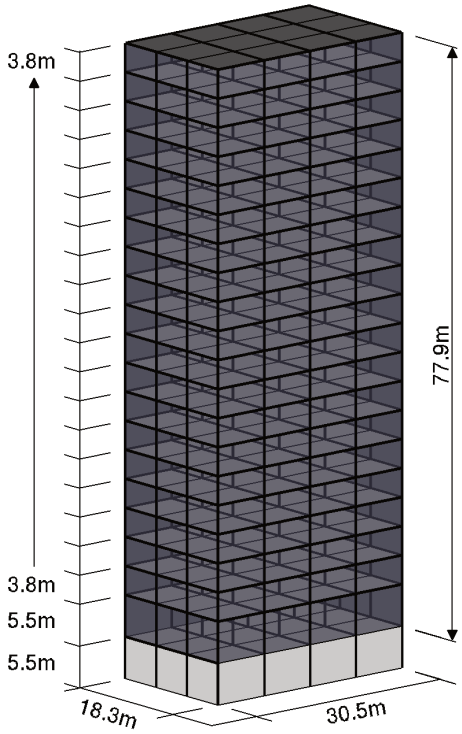

Figure 2.1: Isometric view of the building under study.

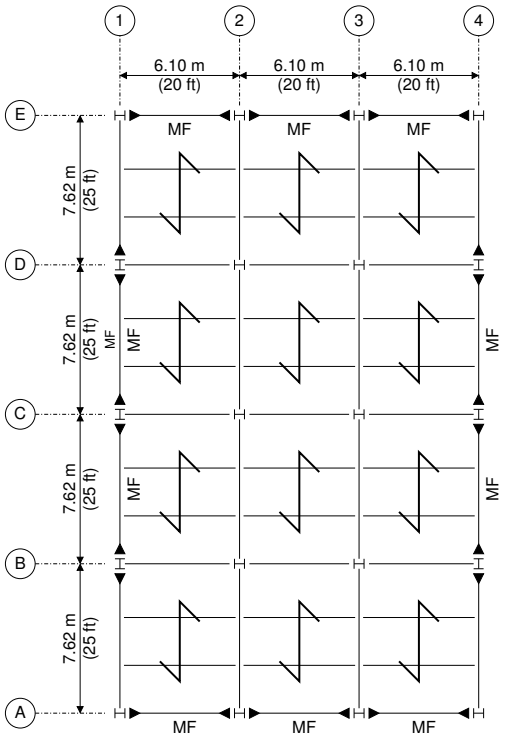

Figure 2.2: Typical floor plan of the building under study. Moment-resisting beam-to-column connections are indicated by solid black triangles.

Computer analyses are carried out in a planar-frame analysis program developed at Caltech called STEEL. The capabilities and features of the program are discussed in Chapter 3. The computer models take advantage of symmetry and only half-building models are employed, i.e., only

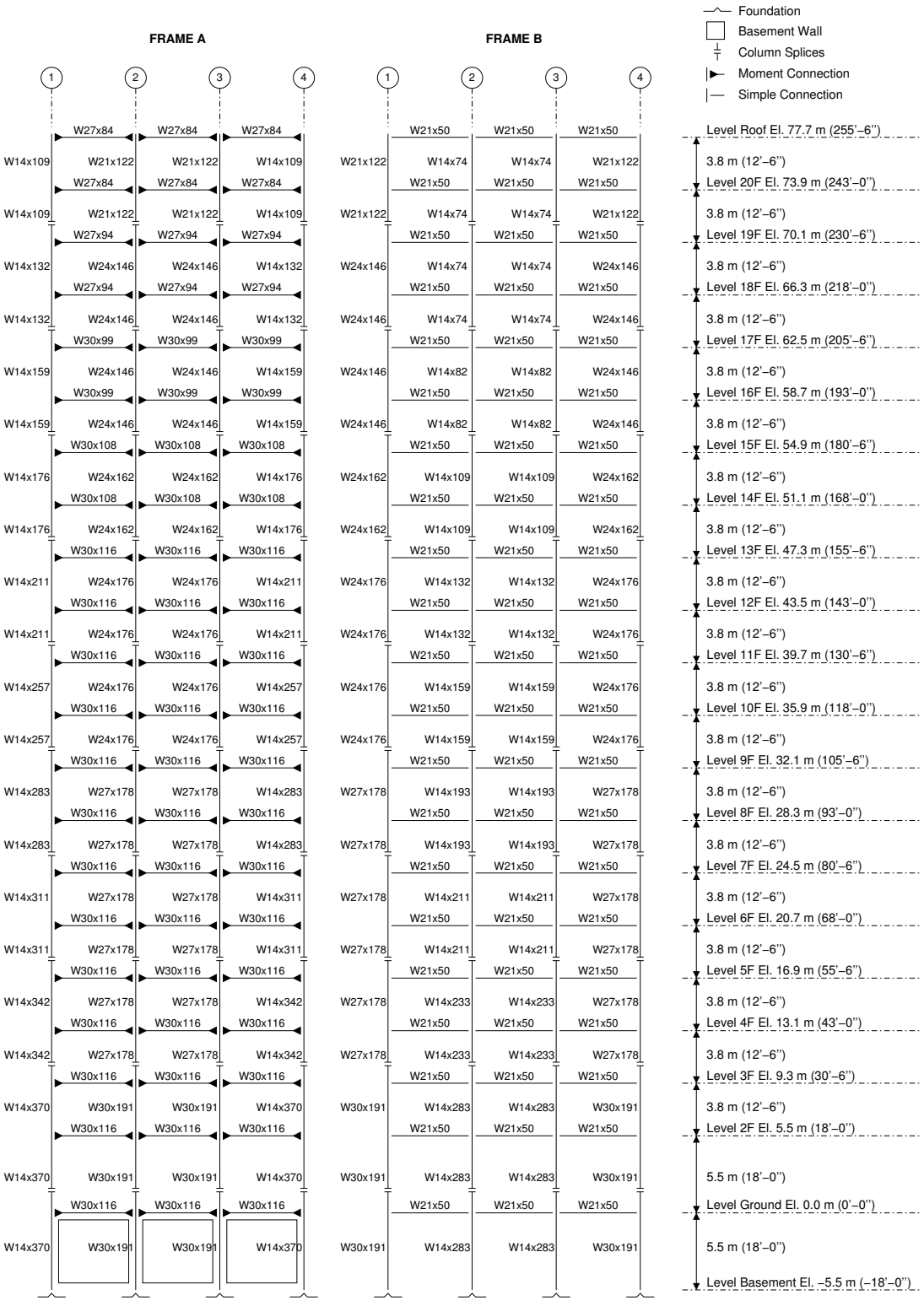

Figure 2.3: Elevation view of frames A and B of the building under study.

frames A, B, and half frame C are modeled. Since frames B and C are identical, they are lumped into a single frame by increasing the width of beams, columns, panel zones, slabs, and foundations by a factor of 1.5. Gravity loads are computed using the full dead load and 30% of the floor live load. Gravity loads are applied directly on the columns, and girders are not loaded within their spans. The seismic mass is assumed to be the same as the gravity loads for the vertical degrees of freedom, while only 20% of live load is assumed to contribute to the seismic mass of the horizontal degrees of freedom.

Composite action of beam elements with the overlying floor system is included. The effective area of the floor slab along the perimeter frame A is taken as 1160 cm^2 (179.8 in^2) and as 3136 cm^2 (486.0 in^2) along the lumped frames B and C. The distance from the beam top flanges to the centroid of the slabs is taken as 7.6 cm (3 in). Since the ribs of the steel deck are oriented perpendicular to the modeled frames, contribution from the steel deck is assumed negligible. Elastic modulus of the concrete slab is taken as E_C=20.7 GPa (3000 ksi), the compressive strength as σ_{YC}=27.6 MPa (4 ksi), and the tensile strength as σ_{FC}=σ_{YC}/10. The same modulus is taken for the basement walls. The effects of the basement walls perpendicular to the modeled frames are included, as well as the effects of the walls in the plane of frame A.

Effects of residual stresses are included and described in Section 3.1. "Accidental" contributions of simple connections to the lateral force-resisting system are also included through methods described in Section 3.2. Fracture susceptibility of pre-Northridge beam-to-column connections, column base plate connections, and column splices is treated in a probabilistic fashion, and is described in Section 3.2.

Foundation interaction is included through nonlinear translational springs underneath basement columns. The downward yield strengths of the foundation springs are computed as three times the foundation reaction forces under gravity loads (dead loads plus 30% of the floor live loads). The same yield strength is assumed for the horizontal springs and half of the downward yield strength is assumed in the upward direction. The spring stiffnesses are obtained from assumed yield displacements of 25.4 mm (1 in) in the downward and horizontal directions and 12.7 mm (0.5 in) in the upward direction. The springs are assumed perfectly-plastic beyond yielding. To address uncertainties associated with the modeling of foundation interaction, three foundation models are applied. The "expected" foundation model, as described above, and "soft" and "stiff" realizations of the foundations obtained by dividing the spring yield strengths and stiffnesses by a factor of two, and multiplying the spring yield strengths and stiffnesses by two, respectively. The "expected"

foundation spring stiffnesses are presented in Table 2.1.

Table 2.1: The "expected" foundation spring stiffnesses (kN/cm).

	Line 1	Line 2	Line 3	Line 4
Frame A	4616.2	3296.9	3296.9	4616.2
Lumped frames B and C	5385.0	8561.1	8561.1	5385.0

Viscous damping consists of a small amount (0.5%) of stiffness-proportional damping at the fundamental mode plus a larger amount of nonlinear (elastic-perfectly plastic) inter-story damping. The strengths of the inter-story dampers are taken to be equal to the story shears produced by the seismic design forces scaled to 1% of the seismic-design weight. The seismic design weight of the base line model, W_{BLM}, is based only on the dead loads above ground and is given as 31,315.5 kN (7040 kips). The seismic design forces are presented in [33]. As an example, this gives a total damper strength of 313.2 kN tons (70.4 kips) for the first story. The story shear velocity at yield is set to 10 cm/sec (3.9 in/sec). The elastic undamped first-mode periods for the "soft", "expected", and "stiff" realizations of the foundation interactions are 3.63 sec, 3.31 sec, and 3.13 sec, respectively.

2.2 Retrofit Schemes

Improved structural performance can be achieved in multiple ways. Some common rehabilitation techniques are summarized in FEMA 547 Techniques for the Seismic Rehabilitation of Existing Buildings [22]. The techniques described in FEMA 547 for steel moment-frames include upgrading the existing beam-to-column moment resisting connections, adding a concrete or masonry shear wall as a new lateral force-resisting system or in conjunction with the moment-frames, and converting the moment-frames to braced-frames by adding either conventional or buckling-restrained brace elements to the existing moment-frames. Furthermore, FEMA 547 suggests that converting the moment-frames to braced frames can be one of the more economical retrofitting techniques available for steel moment-frames. Also, a retrofit scheme that consists solely of upgrading the existing beam-to-column moment resisting connections would clearly have the least impact on the architecture.

Other retrofitting techniques include a number of passive energy dissipation devices. Such devices that have most commonly been used for seismic protection of structures (in North America) include viscous fluid dampers, viscoelastic solid dampers, metallic dampers (e.g. buckling-restrained

brace elements, added damping and stiffness (ADAS) dampers), and friction dampers [70]. The interested reader is directed to Symans et al. [70], which presents a summary of the current practice and recent developments in the application of passive energy dissipation systems for seismic protection of building structures.

In the present study, three retrofitting techniques are considered: upgrading the brittle beam-to-column moment resisting connections, and implementing either conventional or buckling-restrained brace elements within the existing moment-frame bays.

Conventional braces refer to brace elements made of structural steel sections that buckle laterally if loaded in compression beyond their critical buckling strength. The lateral buckling mechanism leads to concentration of strains and often local buckling of the cross-section at mid-span of the element. The local buckling of the cross-section further localizes strains, which leads to severing of the cross-section and rapid deterioration of the element [15, 16]. Buckling-restrained braces have been developed to avoid the pitfalls associated with lateral buckling of conventional braces. They are generally composed of a structural steel section that has a reduced cross-sectional area over a central portion of the element. The central portion is restrained from lateral and local buckling by an external mechanism, and is detailed such that the central yielding core can deform and yield longitudinally independently from the external mechanism.

Adding brace elements to the structural system renders it being much stiffer, thus generally shifting the dynamic character of the structure to a more energetic regime of earthquake ground motions, which results in greater forces. Hence, in addition to installing brace element, columns (and foundations) may need to be strengthened as well. In this study, strengthening of columns is assumed to be achieved by welding cover plates between opposite flanges, or as shown in Figures 2.12, 2.13, and 2.14.

Because comprehensive retrofit schemes can be very expensive, it raises the interest in investigating what improvement in performance can be achieved through partial retrofit schemes. Hence, we developed twelve retrofit schemes with some progressively increasing degrees of intervention. Six retrofit schemes are obtained from upgrading the brittle beam-to-column moment resisting connections in one of the moment-frame bays, in two of the moment-frame bays, or in all three bays, over half the height of the building or over the full height (RMF retrofit schemes). Another two retrofit schemes consist of two variations of implementing conventional brace elements in a reversed-V (or chevron) arrangement over the full height of the building (retrofit schemes RBR-1 and RBR-2). A third retrofit scheme is a “partial” retrofit scheme that consists of employing conven-

tional brace elements in the lower half of the building (retrofit scheme RBR-3). Three more retrofit schemes are obtained by replacing the conventional brace elements with buckling-restrained ones (retrofit schemes RBRB-1, RBRB-2, and RBRB-3). A schematic overview of the retrofit schemes considered in this study is shown in Figure 2.4. The first mode natural periods are presented in the figure as well.

The upgrade of the moment-frame connections is achieved computationally by removing the probabilistic fiber fracture susceptibility discussed in Section 3.2. That is, beams are assumed to be capable of forming stable fully plasticized hinges near column faces. In the braced retrofit schemes, the moment-frame connections are assumed to have the same brittle, pre-Northridge properties. In reality, some strengthening of the connections can be expected through the addition of the gusset plates, which the brace elements are attached to. Where cover plates have been added to strengthen columns, it is assumed that the cover plates are able to prevent fractures in column splices and base plates. Elsewhere, column splices and base plates are not reinforced.

For the braced schemes, the sizes of braces are determined through seismic design conforming to the basic safety objective (BSO) of ASCE-41 Rehabilitation of Existing Buildings [4]. ASTM A500 Grade B steel is assumed for conventional brace elements, and ASTM A36 steel is assumed for buckling-restrained elements. The corresponding expected material properties are given in Table 2.2.

In component testing of buckling-restrained brace elements, the compressive strength of the elements has consistently been reporter greater than their tensile strength. This effect is commonly referred to as the compressive overstrength of buckling-restrained brace elements, and it has been reported to be as great as 20% [55]. In STEEL the same material properties are assumed in compression and tension, and the program is therefore not capable of capturing this overstrength in compression. To compensate, the ultimate strength of the material model is increased by half the value of the compressive overstrength such that the tensile strength of the elements is overshot by half the value of the compressive overstrength, and the brace compressive strength is underpredicted by half the value of the compressive overstrength. This gives similar hysteresis loops as observed in experiments as demonstrated in Section 3.4. In this study, a compressive overstrength of 10% is assumed. The ultimate strength listed in Table 2.2 for the material model used to model buckling-retrained braces (ASTM A36) includes considerations of compressive overstrength, as described above.

End-conditions for both conventional and buckling-restrained brace elements are assumed to be

pinned. The details of the designs are presented in the following section.

Table 2.2: STEEL material model parameters used for modeling ASTM A500, Grade B steel, which is assumed for conventional brace elements, and ASTM A36 steel, which is assumed for buckling-restrained elements.

Steel Material	σ_y (MPa)	σ_u (MPa)	E (GPa)	E_{sh} (GPa)	ε_{sh} (-)	ε_u (-)	ε_{rup} (-)
ASTM A500 Grade B	444.0	519.9	199.9	4.0	0.0120	0.1000	0.19
ASTM A36	289.6	441.3	199.9	4.0	0.0040	0.1500	0.30

To quantify the strength of the building models, push-over analyses are performed using a similar procedure as described by Hall [33]. In these analyses, the building models are subjected to horizontal ground acceleration that increases linearly at a rate of 0.3 g per minute, and the building responses are computed dynamically.

The building models are identical to those used in the earthquake analyses except that the masses of the horizontal degrees of freedom are recalculated to the total seismic design mass of the base line model W_{BLM}/g with a distribution given by the following equations:

$$w_i^p = C_i^p \frac{W_{BLM}}{g}, \quad C_i^p = \frac{w_i^{BLM} h_i}{\sum_{k=1}^{n} w_k^{BLM} h_k}$$

Where w_i^{BLM} is the actual floor mass of the i^{th} floor of the base line model, w_i^p is the floor mass of the i^{th} floor used in the push-over analyses, h_i is the elevation (from ground level) of the i^{th} floor, and n is the number of floors above ground. In addition, the masses in the vertical degrees of freedom are omitted in the push-over analyses.

Results are presented in Figures 2.5 and 2.6. The vertical scale is the building base shear normalized by the seismic design weight of the base line model W_{BLM}. The base shear is calculated by summing the horizontal foundation reaction forces. The horizontal scale is the building overall drift ratio, which refers to the ratio of the horizontal roof displacement relative to the displacement at ground level and the height of the building above ground. Push-over curves are presented for three runs per building model. Each run uses a different realization of the strengths of the beam-to-column moment resisting connections, column splices, and column base plates. For reference, the plots also show push-over curves for the base line model.

The curves are linear up to a yielding or fracture point of the building model. Beyond those points, the building models either show some strain hardening that is followed by strength degrading behavior, or directly show a strength degrading behavior. Some curves show a drop to zero base shear and are indicative of failure mechanisms that include the first few stories. Other curves show a more moderate drop in base shear and are indicative of failure mechanisms higher up in the building models. These curves suggest that estimating the global ductility of the building models based on push-over curves can be misleading. Since the push-over analyses are performed dynamically, stiffness changes that result from yielding of structural elements and, especially, fracturing of connections cause vibrations. The resulting vibrational oscillations are apparent in the figures.

2.3 Design Criteria for Brace Retrofit Schemes

A nonlinear dynamic procedure is used to ensure that retrofit schemes satisfy the Basic Safety Objective (BSO) as defined in $ASCE$ Seismic Rehabilitation of Existing Buildings [4]. The BSO rehabilitation objective achieves the dual performance levels of Life Safety (LS) and Collapse Prevention (CP) for the Basic Safety Earthquake-1 (BSE-1) and BSE-2 earthquake hazard levels, respectively. The BSE-1 and BSE-2 earthquake hazard levels essentially refer to seismic hazard levels that have a 10% and 2% probability of exceedance in 50 years, respectively. Seismic loading for design purposes in the Los Angeles greater metropolitan area is obtained by taking the maximum considered earthquake (MCE) maps prepared by NEHRP [21] and making corrections for site-amplifications using the site-condition map prepared by Wills and Clahan [74]. Then, the resulting short-period (0.2 sec) and long-period (1 sec) design spectral response acceleration parameters (S_{XS} and S_{X1}, respectively) are sampled evenly over the region of interest, and for design purposes S_{XS} and S_{X1} are taken as the expected values plus one standard deviation (STD) of log normal probability density function (PDF) fits to the two datasets. The resulting values for S_{XS} and S_{X1} for the greater Los Angeles area are 2.09g and 1.07g, respectively, where g refers to the acceleration due to gravity. Maps for S_{XS} and S_{X1} and histograms of the sampled values overlaid by the log normal PDFs are presented in Figure 2.7 and Figure 2.8, respectively. The locations where S_{XS} and S_{X1} are sampled are shown as white triangles.

From the obtained S_{XS} and S_{X1} values, a 5%-damped design response spectrum corresponding to the BSE-2 earthquake hazard level is derived. Then the design spectrum is uploaded to the PEER

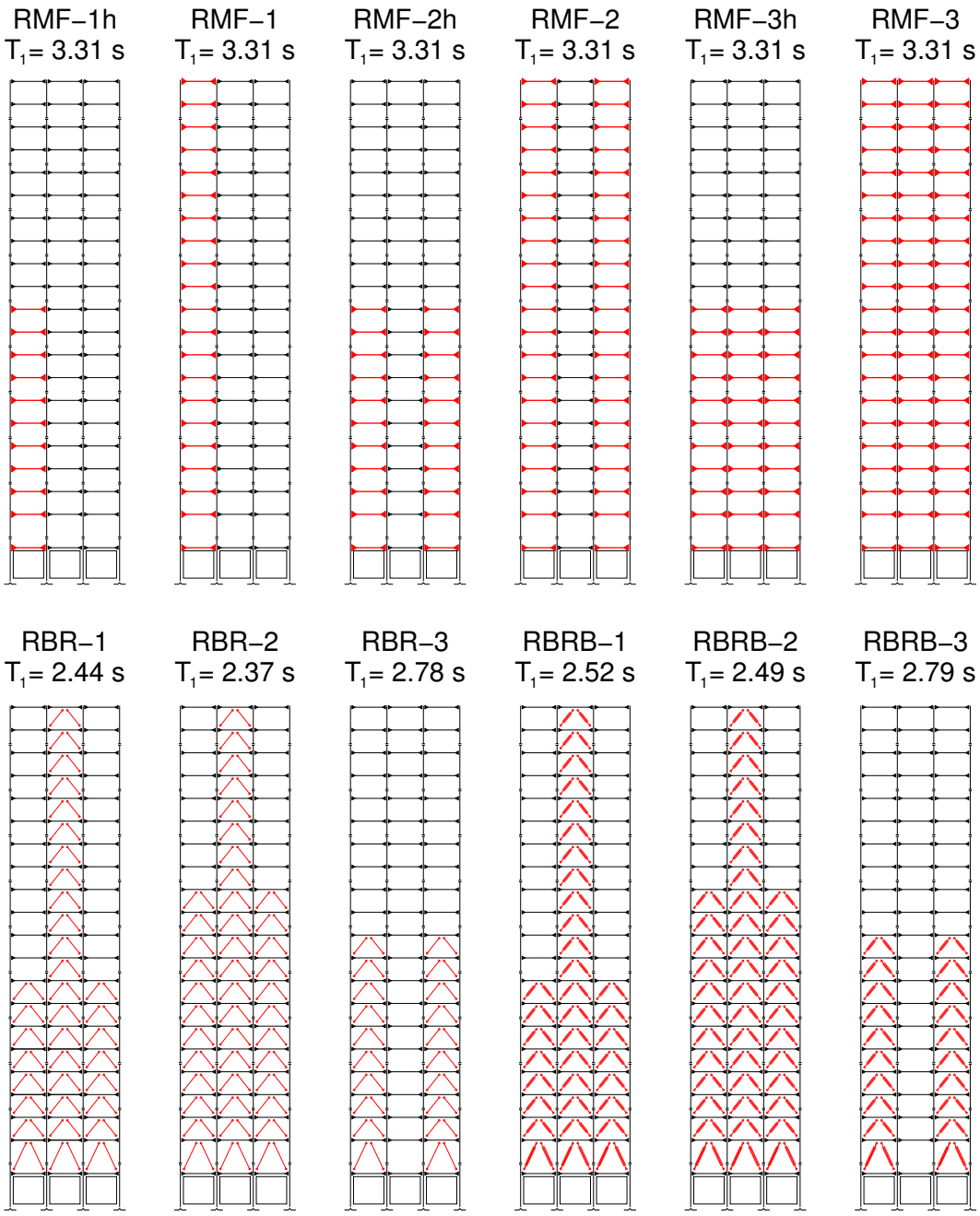

Figure 2.4: A schematic overview of the retrofit schemes considered in this study and associated first mode natural periods. RMF refers to retrofit schemes that consist of upgrading the brittle moment-resisting beam-to-column connections, RBR refers to retrofit schemes that employ conventional brace elements, and RBRB refers to retrofit schemes that employ buckling-restrained brace elements. Black triangles indicate pre-Northridge beam-to-column moment resisting connections. Upgraded connections are indicated by enlarged triangles in red and the affected beams are indicated by thick red lines. Added conventional and buckling-restrained braces are shown in red as well.

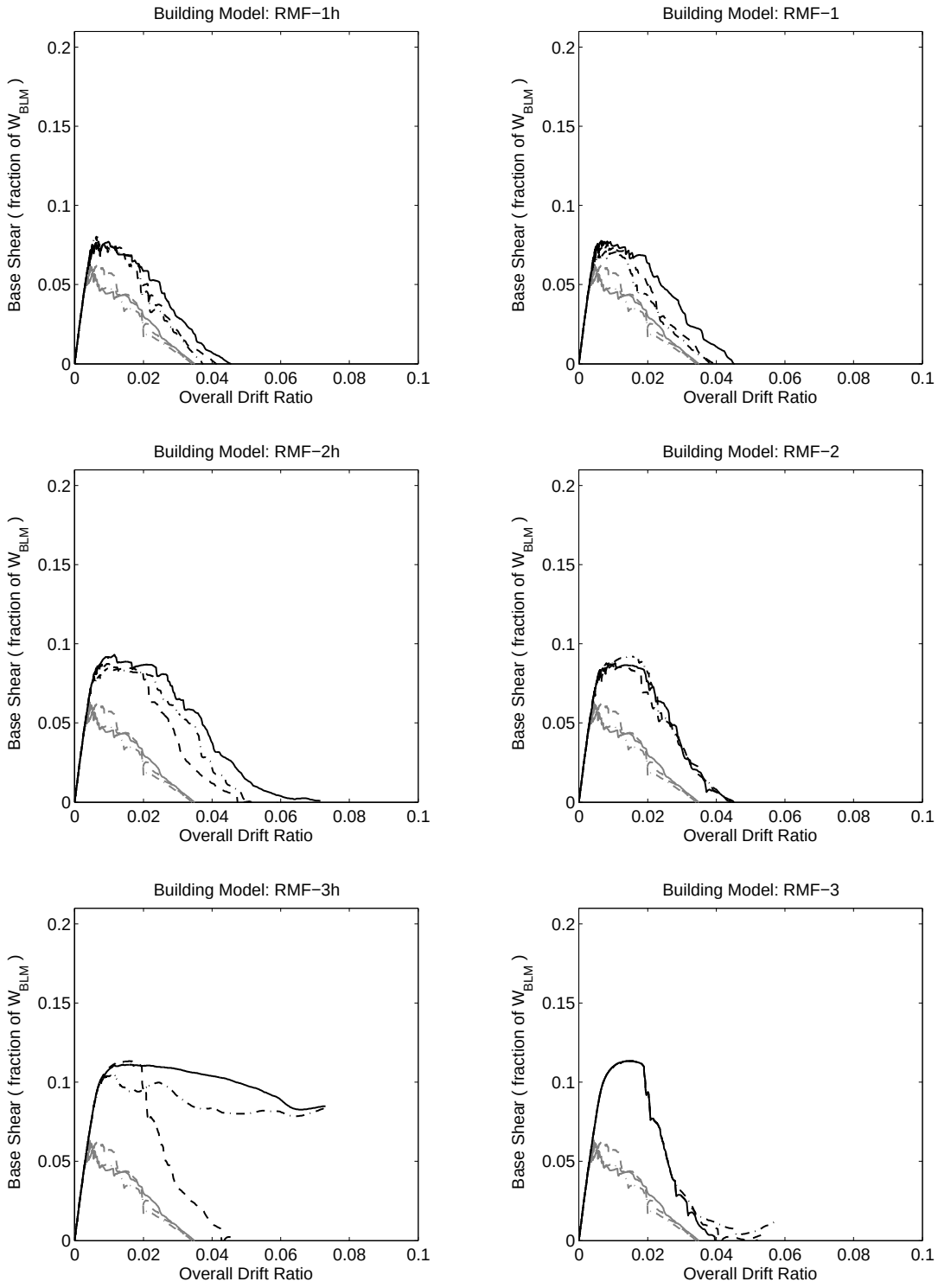

Figure 2.5: Push-over curves for the retrofit schemes that consider upgrading the brittle beam-to-column moment resisting connections (black curves), and for the base line model (gray curves). Three curves are shown for each building model that result from three runs that use different realizations of the strengths of the beam-to-column moment resisting connections, column splices, and column base plates.

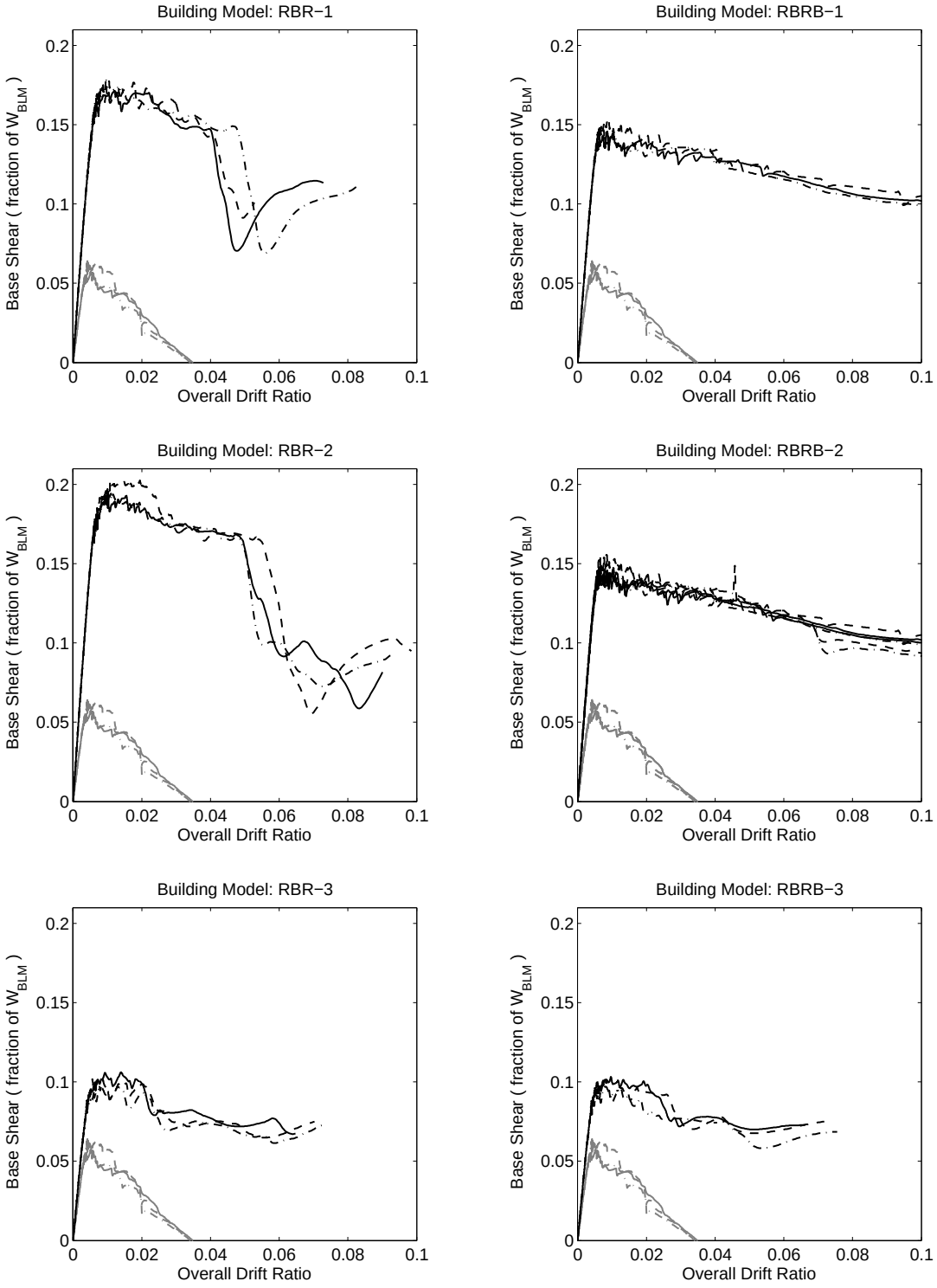

Figure 2.6: Push-over curves for the retrofit schemes that consider implementing either conventional or buckling-restrained brace elements (black curves), and for the base line model (gray curves). Three curves are shown for each building model that result from three runs that use different realizations of the strengths of the beam-to-column moment resisting connections, column splices, and column base plates.

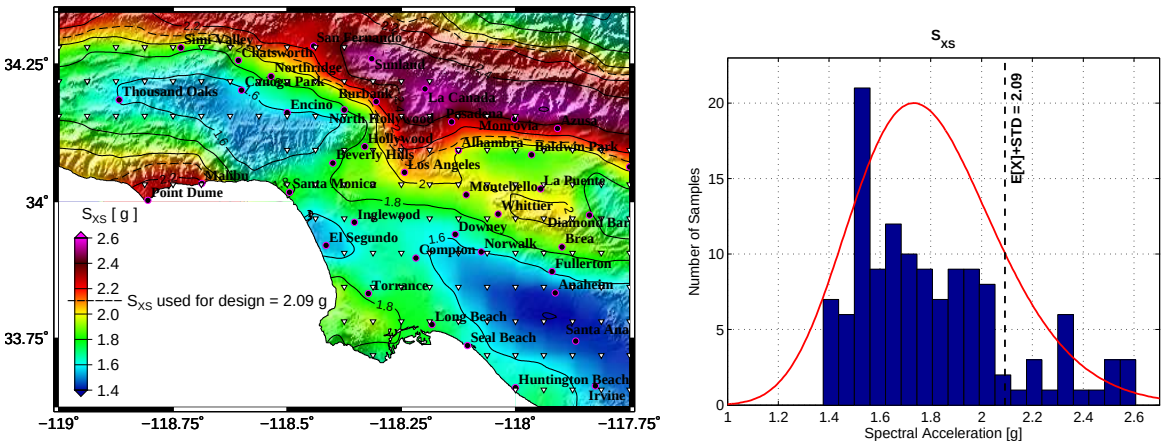

(a) (b)

Figure 2.7: (a) Map for the short-period (0.2 sec) spectral response acceleration parameter, S_{XS}, in the region of interest. The locations where S_{XS} is sampled are shown as white triangles. (b) Histogram of the S_{XS} samples overlaid with a log normal PDF fit to the data set. For design purposes, S_{XS} is taken to be the expected value plus one standard deviation (STD) of the log normal PDF (black dashed line).

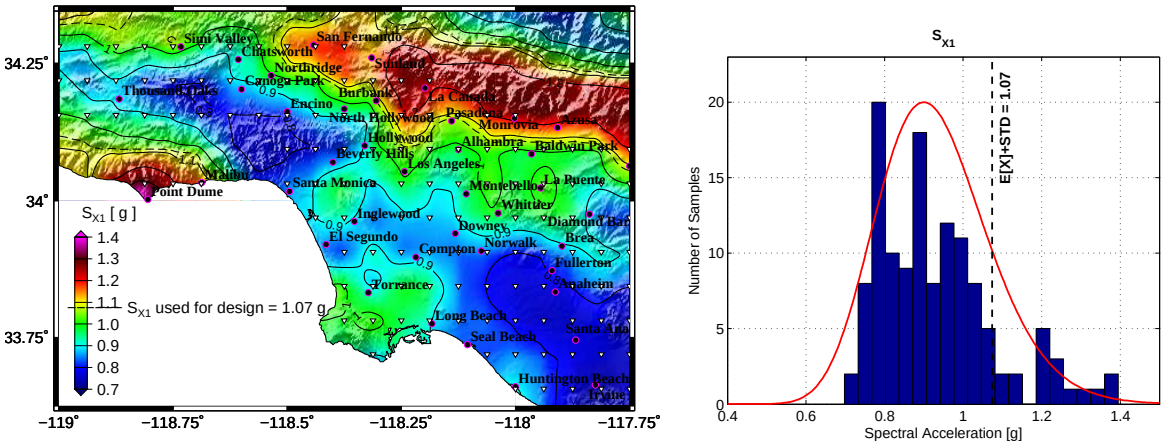

(a) (b)

Figure 2.8: (a) Map for the long-period (1 sec) spectral response acceleration parameter, S_{X1}, in the region of interest. The locations where S_{X1} is sampled are shown as white triangles. (b) Histogram of the S_{X1} samples overlaid with a log normal PDF fit to the data set. For design purposes, S_{X1} is taken to be the expected value plus one standard deviation (STD) of the log normal PDF (black dashed line).

ground motion database user-interface [62], and seven records and corresponding scaling factors that give a close fit to the design spectrum are selected from the database. For each record, a square root of the sum of the squares (SRSS) 5%-damped response spectra is constructed from the scaled horizontal components. The records are then uniformly re-scaled such that the average of the seven SRSS response spectra does not fall below 1.3 times the design response spectrum for

periods from 0.2T to 1.5T (where T is the fundamental period of the building model), as prescribed in $ASCE$ Seismic Rehabilitation of Existing Buildings [4]. The BSE-1 design spectrum is the BSE-2 spectrum scaled down by a factor of 2/3. As a consequence, in this study the same set of seven records is used for the BSE-1 earthquake hazard level with the scaling factors reduced by 2/3. The building model is then subjected to the scaled fault normal component of the ground motion records, which is usually the dominant component. The braces added to frame A and cover plates added to strengthen the columns are sized to achieve a target peak transient inter-story drift ratio of 1.5% and 2.0% for the BSE-1 and BSE-2 seismic hazard levels, respectively, and such that the average peak element responses in the seven records is less than the limits required to achieve the Basic Safety Objective (BSO) for the two seismic hazard levels. The element deformation limits are summarized in Table 2.3. The "expected" realization of the foundation interactions is used for the design, but the sensitivity of the solution is also checked using the "soft" and "stiff" realization. The two partial brace retrofit schemes (RBR-3 and RBRB-3) are designed such that the lower braced portions of the buildings conform to the BSO design criteria, but large beam rotations and beam-to-column connection fractures are expected in the upper portions.

In the design phase, fracture susceptibility of pre-Northridge connections, column base plates, and column splices are modeled assuming fiber fracture strains equal to the geometric means of the probability functions described in Section 3.2, or as 3.5 times the yield strain for beam bottom flange fibers and 8.0 times the yield strain for beam top flange fibers, and all column fibers of column base plates and column splices. This is comparable to suggested modeling in $ASCE$ Rehabilitation of Existing Buildings [4] and $FEMA$ State of the Art Report on Connection Performance [20]. Contributions of floor live loads to the seismic mass are omitted from the design process. The weight of added structural members and column cover plates are calculated and added to the dead loads. As designs are only carried out in the narrow dimension of the building, the weight of the retrofit elements in the long dimension cannot be calculated. Instead, the added weight in the long dimension is assumed to be the same as that calculated for the narrow dimension, and is added to the dead load applied on the exterior columns of the lumped frames B and C. Analyses are performed twice for different gravity loads, once for gravity loads taken as 1.1 times the sum of the dead loads and 30% of the floor live loads, and again for gravity loads taken as 0.9 times the dead loads only.

Because the six brace retrofit schemes have comparable first mode periods, the same set of seven ground motion records are used in their design, and for all six schemes, the same scaling factors are needed to satisfy the ground motion scaling criteria prescribed in $ASCE$ Rehabilitation of Existing

Table 2.3: Summary of design deformation limits for the Life Safety (LS) and Collapse Prevention (CP) performance levels [4].

Component/Action	CP	CP
Beams/Flexure[a]		
a. $\frac{b_f}{2t_f} \leq \frac{52}{\sqrt{F_{ye}}}$ and $\frac{h}{t_w} \leq \frac{418}{\sqrt{F_{ye}}}$	$6\theta_y$	$8\theta_y$
b. $\frac{b_f}{2t_f} \geq \frac{65}{\sqrt{F_{ye}}}$ and $\frac{h}{t_w} \geq \frac{640}{\sqrt{F_{ye}}}$	$2\theta_y$	$3\theta_y$
c. Other	Linear interpolation between the values on lines a and b for both flange slenderness (first term) and web slenderness (second term) shall be performed, and the lower resulting value shall be used.	
Column/Flexure[b]		
For $P/P_{CL} \leq 0.2$		
a. $\frac{b_f}{2t_f} \leq \frac{52}{\sqrt{F_{ye}}}$ and $\frac{h}{t_w} \leq \frac{300}{\sqrt{F_{ye}}}$	$6\theta_y$	$8\theta_y$
b. $\frac{b_f}{2t_f} \geq \frac{65}{\sqrt{F_{ye}}}$ and $\frac{h}{t_w} \geq \frac{460}{\sqrt{F_{ye}}}$	$2\theta_y$	$3\theta_y$
c. Other	Linear interpolation between the values on lines a and b for both flange slenderness (first term) and web slenderness (second term) shall be performed, and the lower resulting value shall be used.	
For $0.2 \leq P/P_{CL} \leq 0.5$		
a. $\frac{b_f}{2t_f} \leq \frac{52}{\sqrt{F_{ye}}}$ and $\frac{h}{t_w} \leq \frac{260}{\sqrt{F_{ye}}}$	$8(1-\frac{5}{3}\frac{P}{P_{CL}})\theta_y$	$11(1-\frac{5}{3}\frac{P}{P_{CL}})\theta_y$
b. $\frac{b_f}{2t_f} \geq \frac{65}{\sqrt{F_{ye}}}$ and $\frac{h}{t_w} \geq \frac{400}{\sqrt{F_{ye}}}$	$0.5\theta_y$	$0.8\theta_y$
c. Other	Linear interpolation between the values on lines a and b for both flange slenderness (first term) and web slenderness (second term) shall be performed, and the lower resulting value shall be used.	
For $P/P_{CL} \geq 0.5$	No yielding is allowed	
Column Panel Zones[c]	$8\theta_y$	$11\theta_y$
HSS Braces/Compression[d]		
a. Slender $\frac{Kl}{r} \geq 4.2\sqrt{\frac{E}{F_{ye}}}$	$5\Delta_c$	$7\Delta_c$
b. Stocky[e] $\frac{Kl}{r} \leq 2.1\sqrt{\frac{E}{F_{ye}}}$	$4\Delta_c$	$6\Delta_c$
c. Other	Linear interpolation between the values for slender and stock braces (after application of all applicable modifiers) shall be used.	
Braces/Tension[f]	$7\Delta_T$	$9\Delta_T$
Pre-Northridge Connections[g]	0.0337-0.00086d	0.0284-0.00040d
Buckling-Restrained Braces	Modeled strains in the yielding core need to be less than the maximum strains that have been previously been demonstrated in experiments.	

[a] Beams: $\theta_y = \frac{ZF_{ye}l_b}{6EI_b}$

[b] Columns: $\theta_y = \frac{ZF_{ye}l_c}{6EI_c}\left(1-\frac{P}{P_{ye}}\right)$; P_{CL} is the "lower-bound" critical axial loading.

[c] Panel Zones: $\theta_y = \frac{\tau_y}{G}$

[d] Δ_c is the axial deformation at expected buckling load.

[e] Section compactness: Where the brace section is noncompact according to Table B5.1 of *AISC* LRFD Specifications [1], the acceptance criteria shall be multiplied by 0.5. For intermediate compactness conditions, the acceptance criteria shall be multiplied by a value determined by linear interpolation between the seismically compact and the noncompact cases.

[f] Δ_T is the axial deformation at expected tensile yielding load.

[g] d is the beam depth.

[*] b_f - width of beam/column flange; t_f - thickness of beam/column flange; h - height of beam/column web; t_w - thickness of beam/column web; F_{ye} - expected yield strength; $\frac{Kl}{r}$ - slenderness ratio; l - length of beam/column memeber; I - moment of inertia; E - Young's modulus; τ_y - shear yield strength; G - shear modulus; P - member axial load; P_y - axial load at yield.

Buildings [4]. The SRSS spectras of the set of seven ground motion records and corresponding scaling factors are shown in Figure 2.9. The unscaled fault-normal component ground accelerations, velocities, and displacements of the recorded ground motions used in the design are shown in Figures 2.10 and 2.11. The seismic design weights, the design first mode periods, the average peak base shears from the nonlinear analyses under the BSE-1 and BSE-2 earthquake hazard levels (V_{BSE-1} and V_{BSE-2}, respectively), the average peak inter-story drift ratios from the nonlinear analyses under the BSE-1 and BSE-2 earthquake hazard levels (IDR_{BSE-1} and IDR_{BSE-2}, respectively), and the designed brace sizes are presented in Table 2.4. Elevation views of frames A of the retrofit schemes showing the brace cross-sections and the locations and thicknesses of added column cover plates are shown in Figures 2.12, 2.13 and 2.14.

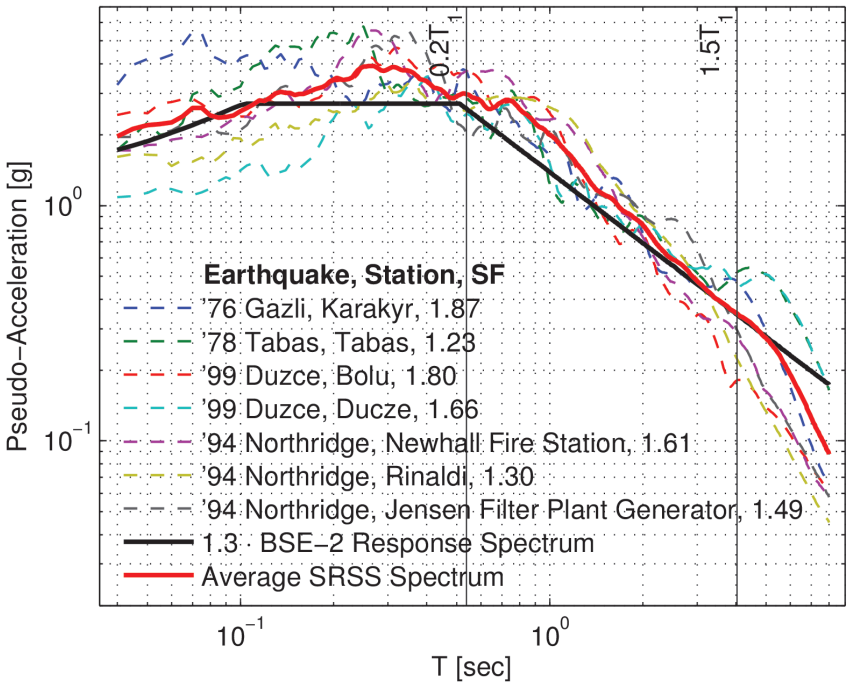

Figure 2.9: Response spectra of the seven ground motion records selected for retrofit schemes RBR-1, RBR-2, RBRB-1, and RBRB-2, scaled accordingly to fit to the BSE-2 seismic hazard level.

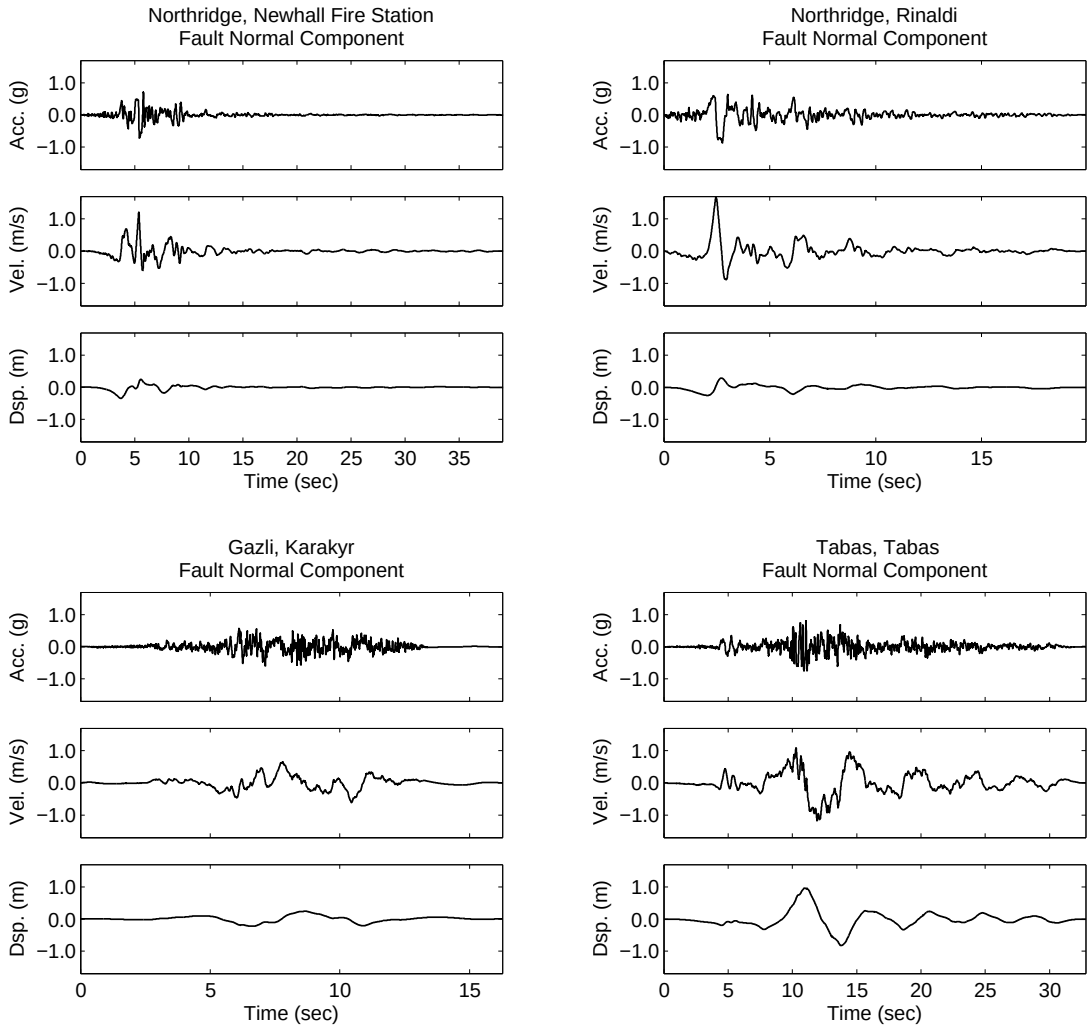

Figure 2.10: Recorded ground motion accelerations, velocities, and displacements (fault-normal component) used in the seismic design of retrofit schemes.

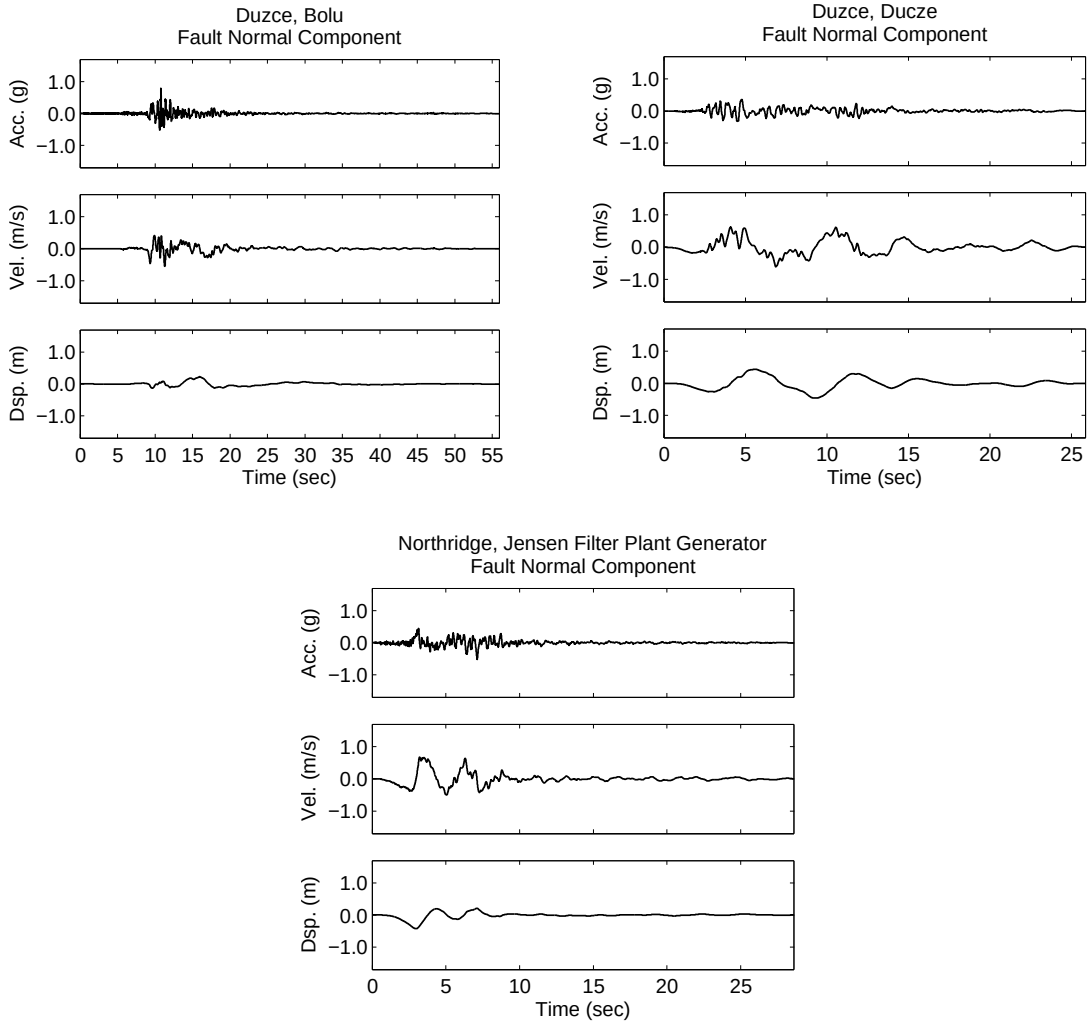

Figure 2.11: Recorded ground motion accelerations, velocities, and displacements (fault-normal component) used in the seismic design of retrofit schemes (continued).

Table 2.4: Design overview of the braced retrofit schemes.

	RBR-1		**RBR-2**		**RBR-3**		**RBRB-1**		**RBRB-2**		**RBRB-3**	
	W=32,247.1 kN $T_{1(design)}$=2.36 sec V_{BSE-1}=8,511.4 kN V_{BSE-2}=9,652.0 kN IDR_{BSE-1}=0.88% IDR_{BSE-2}=1.91%		W=32,282.0 kN $T_{1(design)}$=2.29 sec V_{BSE-1}=8,619.1 kN V_{BSE-2}=9,821.8 kN IDR_{BSE-1}=0.99% IDR_{BSE-2}=2.05%		W=31,832.5 kN $T_{1(design)}$=2.68 sec V_{BSE-1}=6,321.8 kN V_{BSE-2}=7,664.3 kN IDR_{BSE-1}=0.70% * IDR_{BSE-2}=1.46% *		W=32,493.2 kN $T_{1(design)}$=2.43 sec V_{BSE-1}=7,301.6 kN V_{BSE-2}=8,493.3 kN IDR_{BSE-1}=1.13% IDR_{BSE-2}=1.92%		W=32,516.5 kN $T_{1(design)}$=2.41 sec V_{BSE-1}=7,350.7 kN V_{BSE-2}=8,424.5 kN IDR_{BSE-1}=1.09% IDR_{BSE-2}=1.99%		W=32,050.7 kN $T_{1(design)}$=2.70 sec V_{BSE-1}=6,064.0 kN V_{BSE-2}=7,234.9 kN IDR_{BSE-1}=0.80% * IDR_{BSE-2}=1.77% *	
Story	No. of Braces	Brace Cross-Section	No. of Braces	Brace Cross-Section	No. of Braces	Brace Cross-Section	No. of Braces	Yielding Core Area, A_{sc} (cm^2)	No. of Braces	Yielding Core Area, A_{sc} (cm^2)	No. of Braces	Yielding Core Area, A_{sc} (cm^2)
20	2	HSS5x5x1/4	2	HSS5x5x1/4	0	-	2	9.7	2	9.7	0	-
19	2	HSS5x5x1/4	2	HSS5x5x1/4	0	-	2	9.7	2	9.7	0	-
18	2	HSS5x5x1/4	2	HSS5x5x1/4	0	-	2	9.7	2	9.7	0	-
17	2	HSS5x5x1/4	2	HSS5x5x1/4	0	-	2	9.7	2	9.7	0	-
16	2	HSS6x6x3/8	2	HSS6x6x3/8	0	-	2	22.6	2	22.6	0	-
15	2	HSS6x6x3/8	2	HSS6x6x3/8	0	-	2	22.6	2	22.6	0	-
14	2	HSS6x6x3/8	2	HSS6x6x3/8	0	-	2	32.3	2	32.3	0	-
13	2	HSS6x6x3/8	2	HSS6x6x3/8	0	-	2	32.3	2	32.3	0	-
12	2	HSS7x7x3/8	6	HSS5x5x1/4	0	-	2	38.7	6	12.9	0	-
11	2	HSS7x7x3/8	6	HSS5x5x1/4	0	-	2	38.7	6	12.9	0	-
10	2	HSS7x7x3/8	6	HSS5x5x1/4	4	HSS5x5x1/4	2	48.4	6	16.1	4	19.4
9	2	HSS7x7x3/8	6	HSS5x5x1/4	4	HSS5x5x1/4	2	48.4	6	16.1	4	19.4
8	6	HSS5x5x3/8	6	HSS5x5x3/8	4	HSS5x5x1/4	6	19.4	6	19.4	4	22.6
7	6	HSS5x5x3/8	6	HSS5x5x3/8	4	HSS5x5x1/4	6	19.4	6	19.4	4	22.6
6	6	HSS5x5x3/8	6	HSS5x5x3/8	4	HSS5x5x1/4	6	22.6	6	22.6	4	22.6
5	6	HSS5x5x3/8	6	HSS5x5x3/8	4	HSS5x5x1/4	6	22.6	6	22.6	4	22.6
4	6	HSS5x5x1/2	6	HSS5x5x1/2	4	HSS5x5x3/8	6	29.0	6	29.0	4	29.0
3	6	HSS5x5x1/2	6	HSS5x5x1/2	4	HSS5x5x3/8	6	29.0	6	29.0	4	29.0
2	6	HSS5x5x1/2	6	HSS5x5x1/2	4	HSS5x5x3/8	6	29.0	6	29.0	4	29.0
1	6	HSS8x8x1/2	6	HSS8x8x1/2	4	HSS8x8x1/2	6	41.9	6	41.9	4	41.9

* Average peak inter-story drift ratios from the nonlinear analyses under the BSE-1 and BSE-2 earthquake hazard levels in the lower braced portion of the building models. The corresponding inter-story drift ratios for the upper un-retrofitted portion of the building models resulted as 3.00% and 4.51%, respectively, for the RBR-3 retrofit scheme, and 2.73% and 3.76%, respectively, for the RBRB-3 retrofit scheme.

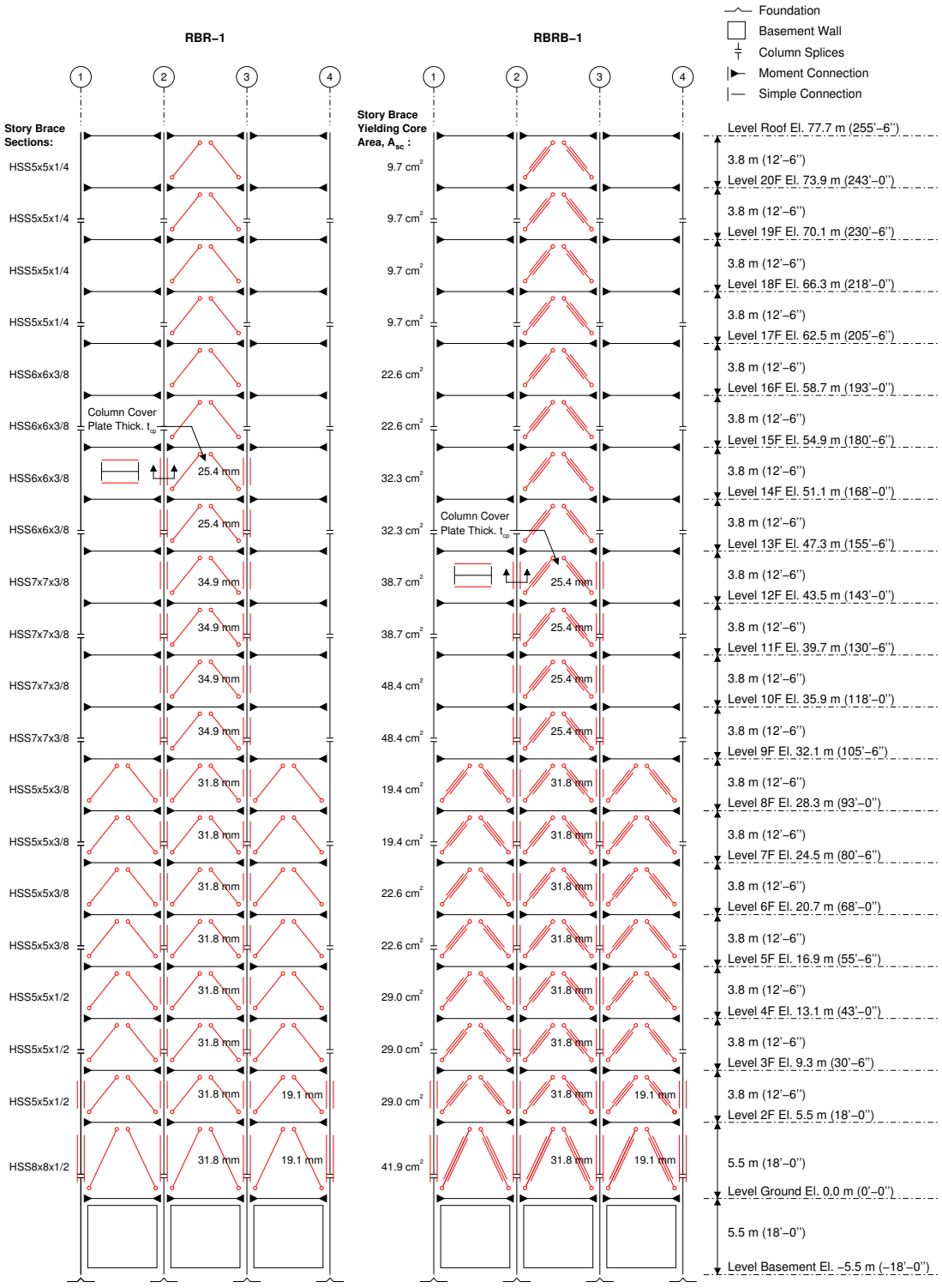

Figure 2.12: Elevation view of frames A of retrofit schemes RBR-1 and RBRB-1.

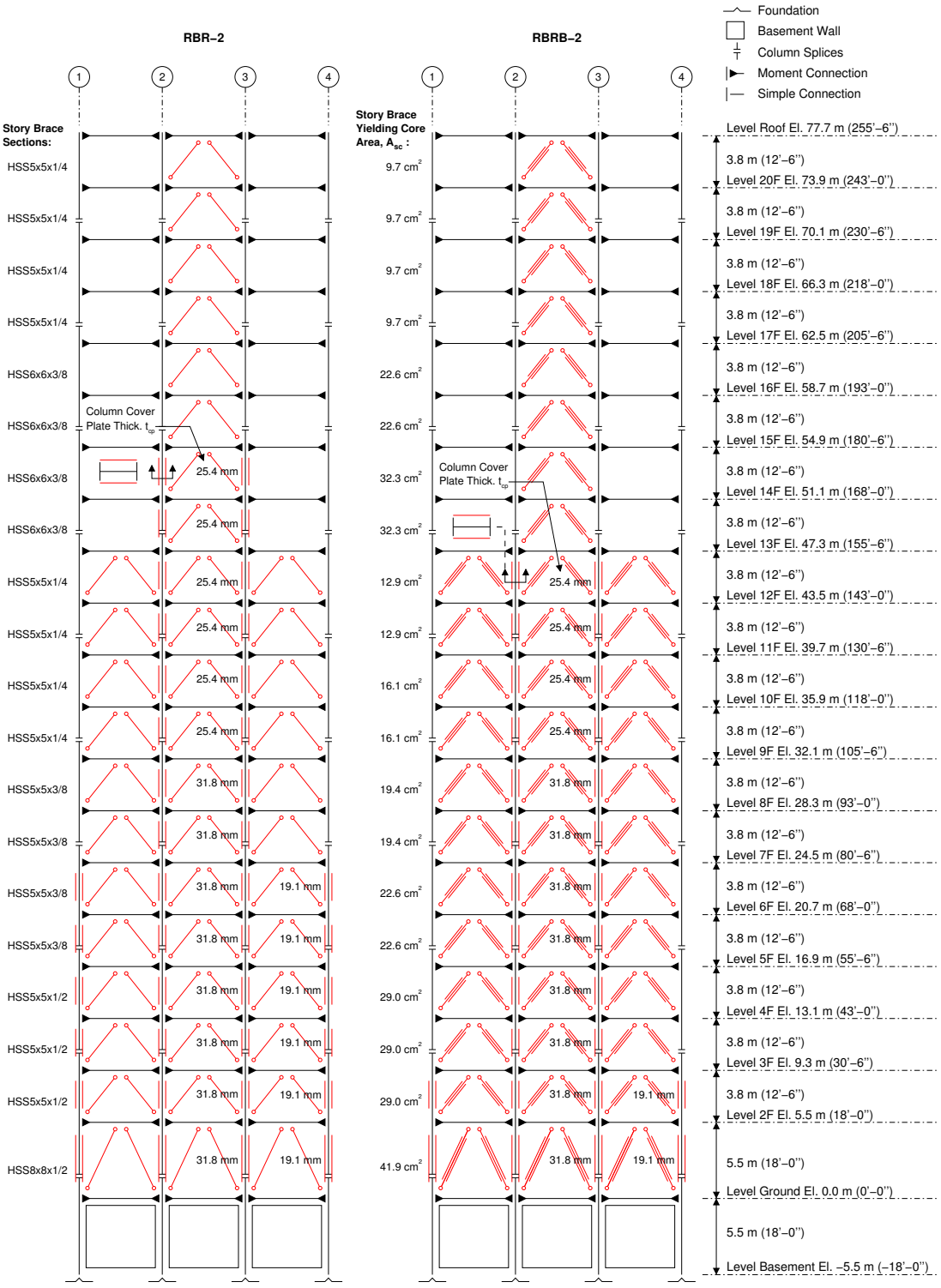

Figure 2.13: Elevation view of frames A of retrofit schemes RBR-2 and RBRB-2.

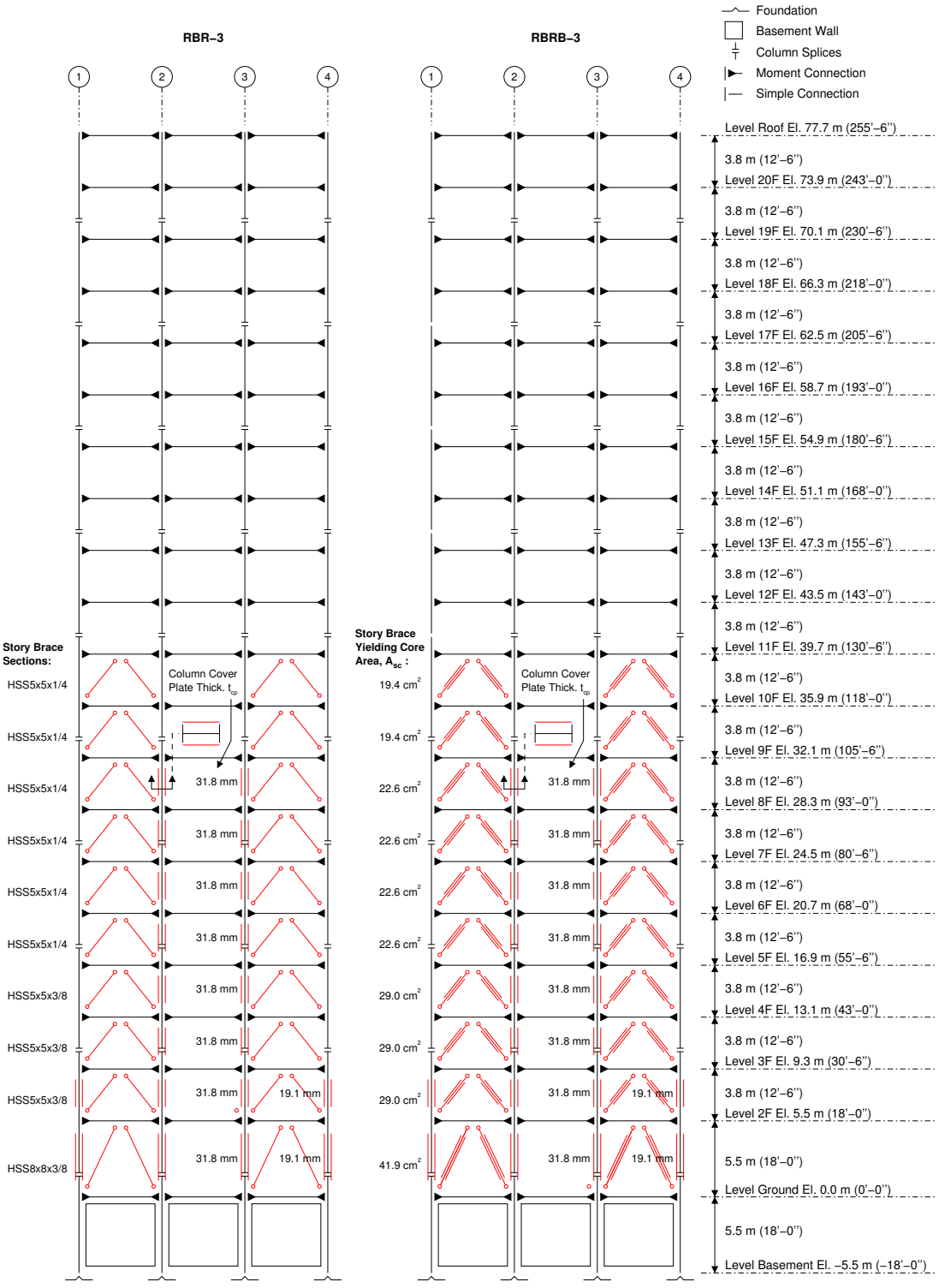

Figure 2.14: Elevation view of frames A of retrofit schemes RBR-3 and RBRB-3.

Chapter 3

Modeling Considerations

Building analyses are carried out with a planar frame analysis program developed at Caltech called STEEL (also referred to as FRAME-2D). A brief summary that describes the capabilities and features of the program is included herein. Details of the formulation can be found in [9] and [36]. Several studies have been conducted to validate the program. Challa and Hall [9] showed that the behavior of a panel zone element which is used to model "joints" in STEEL agrees well with experimental data from a moment-frame subassembly test. Hall et al. [36] demonstrated a good aggreement with experimental data of a cantilever beam and a slender brace element under cyclic loading. Krishnan [43] extended the planar program into three dimensions and showed that both programs give similar results for a two dimensional moment-frame configuration, as well as good agreement with experimental data. In Section 3.3 we demonstrate further the ability of the program to model hysteretic buckling, postbuckling and tension yield of conventional brace elements. In section 3.4 we demonstrate the ability of the program to model cyclic loading of buckling-restrained brace elements.

3.1 Finite Element Modeling in STEEL

A finite element model in STEEL consists of a planar arrangement of beam, column (and brace) elements that connect into panel zone elements (Figure 3.1). Columns attach to the top and bottom of the panel zone, beams connect to the left and right sides of the panel zone, and brace elements connect to the nearest corner of the panel zone.

Beam, column, and brace elements are divided into segments that are further discretized into fibers within their cross-section (Figure 3.2). Associated with each fiber is a nonlinear hysteretic stress-strain law. The hysteretic behavior is fully defined by a virgin backbone curve that consists

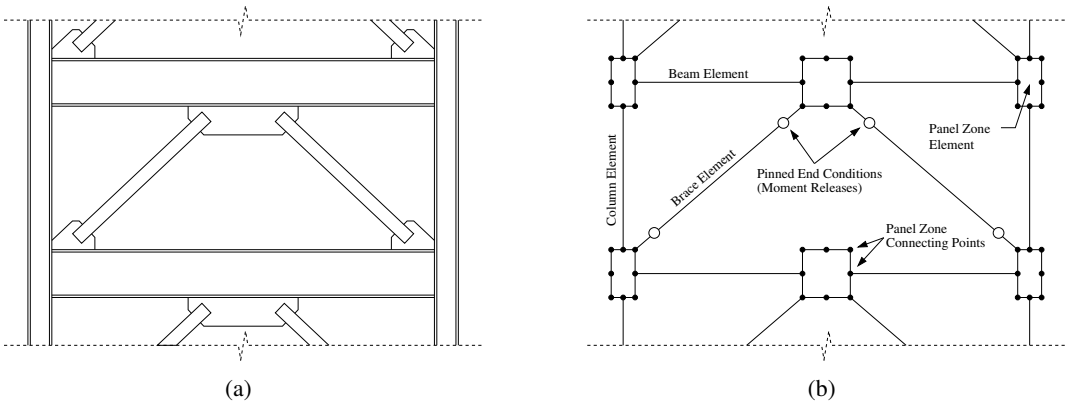

Figure 3.1: (a) An example of a moment-frame retrofitted with brace elements in a chevron configuration. (b) Idealization of the example braced frame in the mathematical modeling.

of a linear-elastic region, a yield plateau, a strain-hardening region, which is described by a cubic ellipse, and a strain-softening region described by a continuation of the same cubic ellipse culminating in fiber rupture (Figure 3.3). Hysteresis loops similarly consist of linear segments and cubic ellipses, and the hysteretic rules to define the cyclic response of each fiber are given by [8]. The backbone curve is fully defined by six parameters: yield stress, σ_y; ultimate stress, σ_u; Young's modulus, E; strain at initiation of strain hardening, ε_{sh}; strain at ultimate stress, ε_u; and the tangent modulus at initiation of strain hardening, E_{sh}. Identical behavior is assumed in compression and tension.

When oriented by their strong axis, beam members have two optional fibers to account for composite action of the beam with the overlying floor slab. One fiber represents the steel deck and takes the same material properties as the steel fibers of the beam cross-section, and one fiber represents the concrete slab (fibers nine and ten in Figure 3.2, respectively). The stress-strain behavior of the concrete fiber is elastic-perfectly plastic in compression and elastic to cracking in tension (Figure 3.4). The concrete behavior is defined by three parameters: compressive strength, σ_{YC}; tensile strength, σ_{FC}; and Young's modulus, E_C. Once the tensile strength is reached and a crack has formed, the fiber can no longer carry tension, but if the loading is reversed the crack can close and carry compression. Residual stress, σ_{RES}, can be distributed over the cross-section as tensile stress in the web-flange junction area, and as compressive stress in the mid-web and flange-tip areas. In this study, σ_{RES} is taken as 41.4 MPa (6.0 ksi). Shear deformations of the segments are included. The shear stiffness is assumed to be linear, and is based on the area of the plates in the plane of the frame and the shear modulus of steel, G.

Eight segments are used for beam and column elements and seven segments are used for conventional brace elements, as shown in Figure 3.5 (a) and (b), respectively. The segments are proportioned such that shorter segments are used where plastic hinges occur. For beam and column elements, plastic hinges are expected to form towards the ends of the element where they connect into joints and where moments are the greatest. For conventional brace elements, plastic hinges form at the mid-span subsequent to lateral buckling of the element. Hall et al. [36] found this discretization to be sufficient to obtain close resemblance with experiments.

Three segments are used to model buckling-restrained brace elements, as shown in Figure 3.5 (c). Two segments are used to model the yielding core of the element, one shorter segment (about 254 mm long) to account for necking in the steel core towards the limit state of the element, and another longer. One segment is used for the remainder of the element and is given a larger area. The yielding core is assumed to occupy 70% of the brace length, and the cross-sectional area of the non-yielding zone is assumed 4.125 times larger than that of the yielding core. The brace length is taken as the distance between the points of panel zones that the brace element is connected to (Figure 3.1). This is comparable to the assumptions made by Sabelli et al. [63] and gives an effective brace stiffness of about 1.5 times the stiffness of a brace assuming the cross-sectional area of the yielding core between the center of the joints that the brace elements frame into. To prevent the element from buckling out of plane, linear rotational springs of 100 times the elastic rotational stiffness of the cross-section (EI) are attached to each interior segment node. Based on observations made when modeling sub-assemblage experiments (Section 3.4), a slight modification of the hysteresis rules of the steel fibers is made for buckling-restrained brace elements in that the unloading stiffness, which is equal to the initial linear-elastic loading stiffness, is extended some beyond the zero stress axis to produce fuller hysteresis loops.

Panel zone elements are used to model "joints", i.e., where either beam (and brace) elements frame into columns or brace elements frame into beams. The panel zone element is rectangular in shape and deforms in shear. The shear strain in the panel zone is the difference between the end rotation of the beams and the end rotation of the connected columns. Two connected beams have the same end rotation, and similarly two connected columns have the same end rotation. The hysteretic stress-strain law is given in panel zone moment, M^{pz}, and shear strain, γ^{pz}. The backbone curve is linear up to 0.8 times the yield moment M_y^{pz}. Following the linear segment is a quadratic ellipse that is tangent to the preceding linear segment and reaches zero slope at $\gamma_u^{pz} = 100\gamma_u^{pz}$ and $M_u^{pz} = 2.35M_y^{pz}$. Beyond γ_u^{pz} the backbone curve is flat and does not degrade (Figure 3.6).

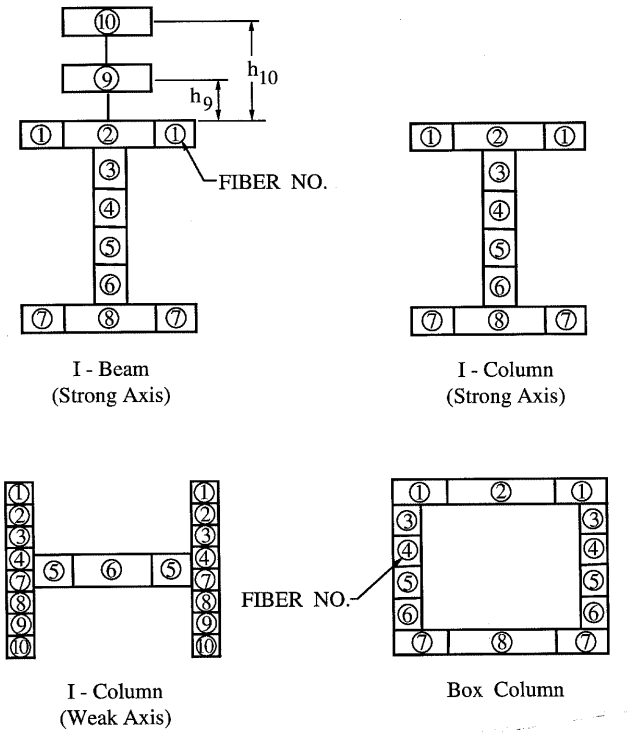

Figure 3.2: Fiber layout for beams and columns [33].

The hysteresis rules that define the cyclic response of a panel zone are similar to those of a steel fiber. The panel zone shear stiffness is given by the product of the volume of the panel zone and the shear modulus of steel, G. The yield moment is given by the product of the volume of the panel zone and the steel shear strength, $\tau_y = \frac{\sigma_y}{\sqrt{3}}$. The dimensions and material properties of the panel zone elements are taken from the joining elements. Where beam (and brace) elements connect to columns oriented by their strong axis the material properties are taken from the column, the width of the panel zone is taken as the column depth, the height is taken as the larger depth of the connecting beam, and the thickness is taken as the column web thickness. Panel zones are omitted if the column is oriented by its weak axis. Panel zone doubler plates can be included. If included, the doubler plate thickness is automatically increased such that the panel zone strength is 0.8 times the plastic capacity of the connecting beams. In the absence of columns (for instance, where brace elements frame into beams in a chevron brace configuration), material properties are taken from the beam, the depth and height of the panel zone is taken as the beam depth, and the thickness is taken as the beam web thickness.

Planar wall elements can be included at basement levels. The wall elements resist shear and provide some axial stiffness to the beam and column members of the frame on the perimeter of

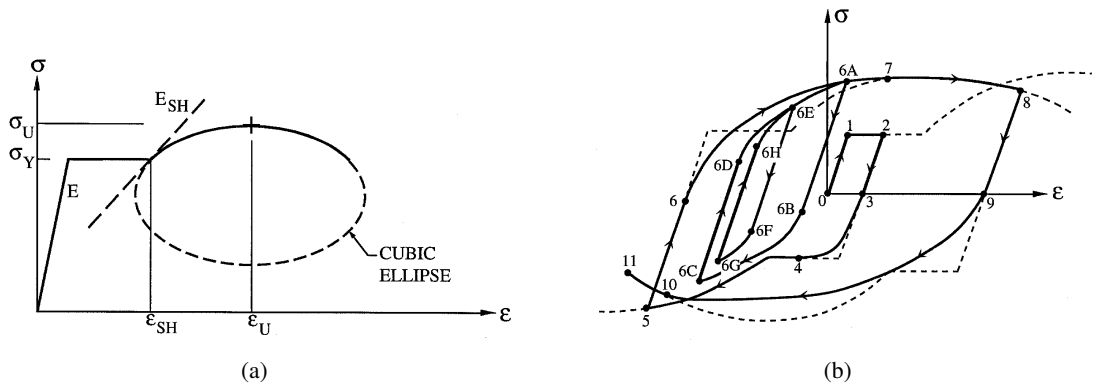

Figure 3.3: (a) A virgin backbone curve and (b) associated axial stress-strain hysteretic relation for steel fibers [33].

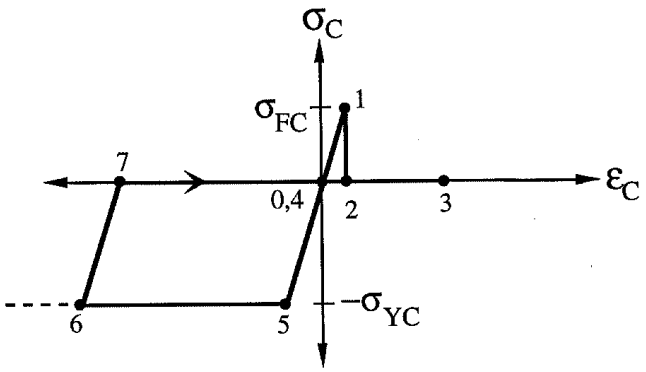

Figure 3.4: Axial stress-strain hysteretic relation for concrete fibers [33].

the wall element. All features are assumed linearly elastic. The wall elements connect to the top and bottom joint nodes of two adjacent columns. If wall elements are oriented perpendicular to the modeled frames, only the vertical degrees of freedom of the top and bottom joint nodes of the two adjacent columns are affected by the presence of the wall element.

Foundation interactions are modeled with bilinear translational springs. The behavior of the foundation springs is defined by six parameters (Figure 3.7): vertical compressive strength, F_{YD}; vertical tensile strength, F_{YU}; horizontal compressive and tensile strength, F_{YH}; vertical spring elastic stiffness, K_V; horizontal spring elastic stiffness, K_H; and fraction of the elastic stiffness to be used for post yield stiffness, α.

Program analysis starts with applying the gravity loads followed by the earthquake loading. The Constant Average Acceleration method (Newmark's method with $\gamma = 0.50$ and $\beta = 0.25$) is used for time integration. Model coordinates, global coordinates at the junction of beams, columns, and

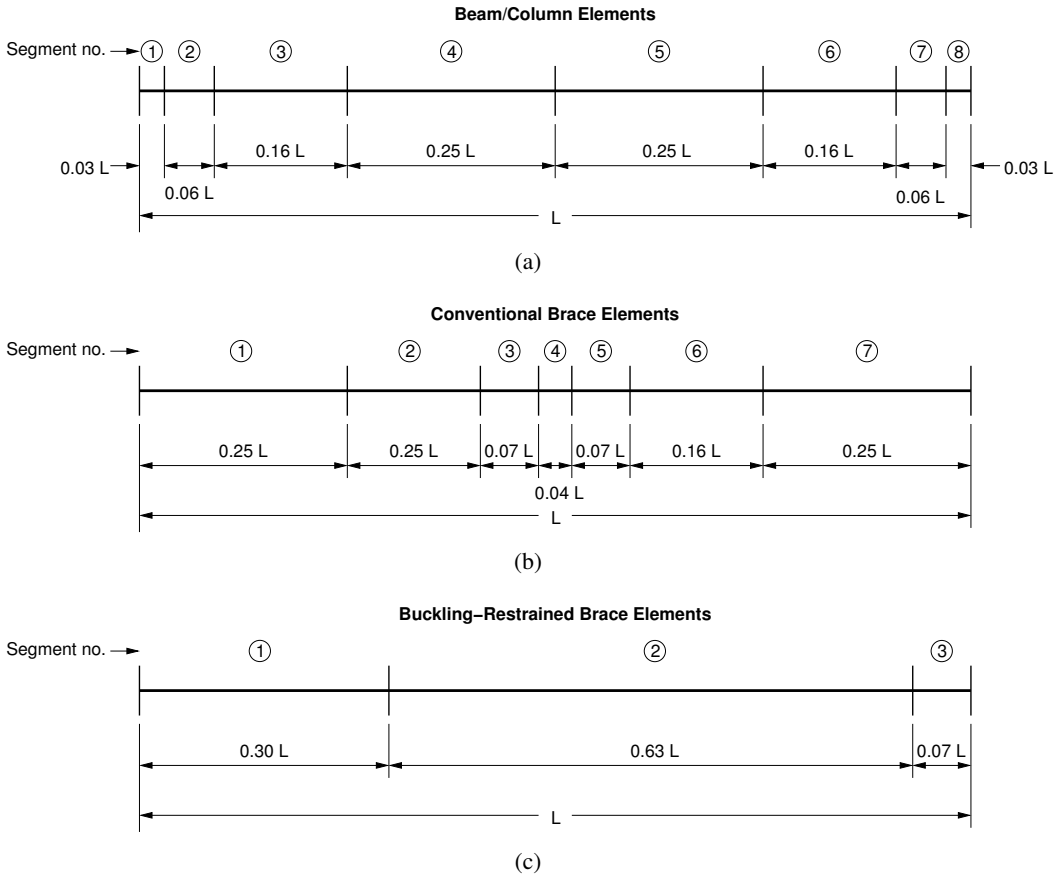

Figure 3.5: Segment layouts for (a) beams and columns, (b) conventional braces, and (c) buckling-restrained braces.

brace elements, and local coordinates in between segments of each element are updated during each iteration of a single time step and the dynamic equations of equilibrium are solved in the deformed configuration. This automatically accounts for local $P-\Delta$ effects such as element buckling as well as global $P-\Delta$ effects.

Model damping can be provided through traditional mass and stiffness proportional Rayleigh damping. Elastic-perfectly plastic viscous inter-story dampers can also be defined. As stated in Section 2.1, in this study, viscous damping is taken as a small amount (0.5%) of stiffness proportional damping at the fundamental mode plus a larger amount of inter-story damping. In this way, unrealistically large damping forces encountered in the use of Rayleigh damping, as demonstrated by Hall [35], are avoided.

Parallel modeled frames are constrained through connecting elements. A single connecting element constrains the horizontal joint degrees of freedom of one floor of one frame and the horizontal joint degrees of freedom of the same floor of another frame such that the average displacement of

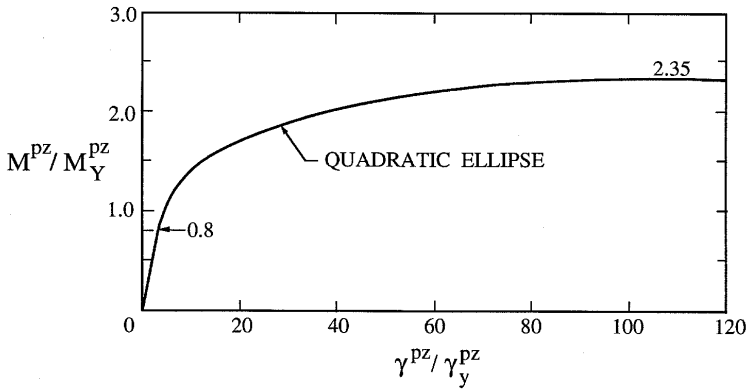

Figure 3.6: A virgin backbone curve for panel zone elements. The associated moment-shear strain hysteretic relation for panel zones is similar to that of steel fibers [33].

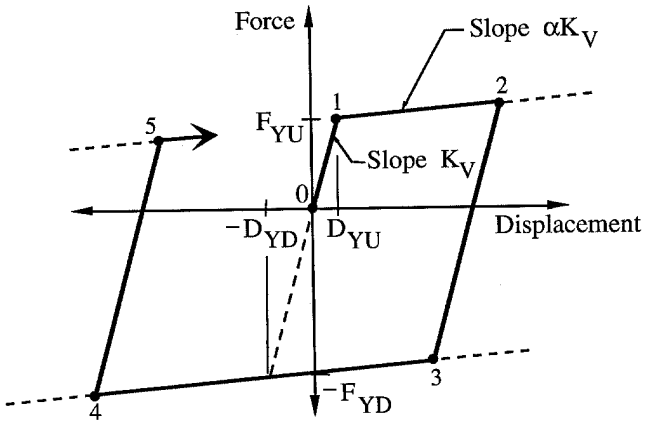

Figure 3.7: Vertical load-deflection hysteretic relation for vertical foundation springs [33].

the nodes of the first frame is equal to that of the second frame.

3.2 Modeling of Connections

The analysis program employs a feature to reduce the area of individual fibers. It also includes a feature to assign fracture strains to a group of fibers. These features are used to model both moment-resisting and simple (non-moment-resisting) beam-to-column connections, beam-to-column connection fractures, column base plate fractures, and column splice fractures.

The fiber fracture strains are assigned through fracture strain categories. For each fiber fracture strain category, the segments and fibers within each segment that should adhere to the category need to be specified along with a probabilistic distribution for fracture strains. The probabilistic distribution consists of ten values for fracture strain, ε_F, as multiples of the yield strain, ε_y, which all

have the same probability of being realized in a simulation. Then the fracture categories are assigned to the desired elements. At the beginning of an analysis the program loops over all segments of all elements and draws randomly from the pool of fracture strains values and assigns the drawn values to all fibers of the same category in that segment.

A "simple" bolted shear tab connection is modeled by zeroing the areas of beam bottom and top flange fibers in the two adjacent segments closest to the column face. In addition, the areas of the web fibers are reduced by a factor of 0.3. This yields a connection stiffness comparable to experimentally tested bolted shear tab connections (Table 5.12 in FEMA 355D [20]). The same area reduction is applied to beam web fibers for moment-resisting beam-to-column connections, but the full areas of bottom and top flange fibers are used.

To model fracture susceptibility of pre-Northridge beam-to-column connections, column base plate connections and column splices, two probability distributions for fiber fracture strains, are defined for use in the present study:

D1: $\varepsilon_F/\varepsilon_y = 0.7$, 1, 10, 50, 100 with likelihood of 20%, 40%, 20%, 10%, and 10%, respectively.

D2: $\varepsilon_F/\varepsilon_y = 1$, 10, and 100 with likelihood of 40%, 30%, and 30%, respectively.

For pre-Northridge beam-to-column connections, the distribution D1 is applied to beam top flange fibers (fibers 1 through 4) and distribution D2 is applied to beam bottom flange fibers (fibers 5 through 8) of the segment closest to the column face. For column base plate fractures, distribution D1 is applied to all fibers of the bottom most segment of all basement columns. For column splices, distribution D1 is applied to all fibers of the fourth segment (from the bottom) of all columns at every alternate story, or as shown in Figure 2.3. Hall found this fracture criteria to be consistent with the experiences in the 1994 Northridge earthquake [34]. No fractures are permitted for braces in the present study.

If all the fibers of a column splice fracture, the column is assumed incapable of carrying any loads thereafter. The assumption is that the lateral offset of the story would be sufficient to bring the web and flange plates out of alignment, and so the load carrying capacity would be dramatically diminished. If all fibers of a beam-to-column connection fracture, however, the shear transfer capacity is assumed to be retained. Also, for beam-to-column connections and partially fractured column splices, a fractured fiber is capable of regaining contact and carry compression. Column base plate connection fractures are treated in the same fashion as for beam-to-column connections.

If all fibers of a segment rupture, the element that contains the segment is assumed incapable of carrying any load thereafter.

3.3 Modeling of Conventional Brace Elements

The ability of STEEL to accurately capture buckling and post-buckling, tension yield, and hysteretic effects of conventional brace elements is validated against data from cyclic load tests by Black et al. [6] and Fell et al. [15, 16].

The Black et al. testing program was comprised of twenty-four steel struts with cross-sectional shapes and slenderness ratios commonly encountered in practice. The tested structural shapes were wide-flanges, double-angles, double-channels, and both thick and thin round and square tubes. Eighteen specimens were pinned at both ends, and had slenderness rations of 40, 80, and 120, while six specimens were pinned at one end and fixed at the other end, and had slenderness ratios of 40 and 80. True pinned end-conditions were realized in these tests by employing clevis-pins and clevises to allow free rotations at the brace ends in the plane of buckling. The Fell et al. testing program tested a total of nineteen struts. Eight specimens were square tube sections, eight were round tubes, and three specimens were wide-flanges. The slenderness ratios of the tube sections ranged from 63 to 102. The slenderness ratios of the wide-flange specimens were 153 (all specimens had the same cross-section and were of the same length of 3124.2 mm). Among the differences between the two testing programs is that Fell et al. employed typical brace connections with the specimens welded to gusset plates that were bolted to a movable constraint frame and a stationary reaction block (as opposed to the ideal pinned (or fixed) end-conditions employed by Black et al.). The brace connections are designed such that during buckling, a yield line forms in the gusset plates to accommodate large rotations associated with lateral buckling of the braces. For the tube sections, whose out-of-plane stiffness is substantially greater than the out-of-plane stiffness of the yielded gusset plates, this effectively resulted in pinned end-conditions. However, for the wide flange sections, the connections provided some partial fixity.

Another important difference is that the specimens in the Black et al. testing program were generally not loaded to failure (at least not documented), while Fell et al. carefully documented onset of local buckling of the cross-section at mid-span of the specimens, initiation of fractures in the cross-sections, and ultimately the complete failure of the specimens. In both testing programs the specimens were subjected to cyclic quasi-statically applied loads simulating earthquake effects

on braced frame structures in the axial direction only. A schematic view of the experimental set up in the Black et al. testing program and the Fell et al. testing program with the brace connections idealized as pinned end-conditions, as well as the computer model used for analysis, is shown in Figure 3.8.

In this study, square hollow structural sections (HSS) or square tubes are employed in the retrofit schemes. Therefore, validation efforts are mostly focused on this type of cross-section. Also, since braces are assumed pinned, experiments that realized fixed end-conditions are of less interest. Four struts from the Black et al. testing program are modeled: Strut 01, Strut 03, Strut 17, and Strut 18. Strut 01 was a W8x20 wide-flange section with slenderness ratio of 120. Strut 03 was a W6x20 wide-flange section with slenderness ratio of 80. Strut 17 was a HSS4x4x1/4 square tube section with slenderness ratio of 79. Strut 18 was a HSS4x4x1/2 square tube section with slenderness ratio of 77. The material for the wide-flanges was specified as ASTM A36 steel, and ASTM A501 steel was specified for the square tube sections. Hall et al. [36] demonstrated good agreement for Strut 03 and the results are reproduced here. Another five square tube sections from the Fell et al. testing program (out of eight) are modeled as well. Two of the square tube sections were filled with grout meant to delay local buckling and another specimen was reinforced at midspan and these are precluded. Three out of the five modeled specimens were HSS4x4x1/4 square tube sections with slenderness ratios of 81, and two were HSS4x4x3/8 square tube sections with slenderness ratios of 84. ASTM A500 Grade B steel was specified for all five specimens.

Material coupons were taken from the specimens and actual mechanical properties were measured in a standard tensile test. The measured material monotonic stress-strain curves are shown in Figures 3.9, 3.10, 3.11, 3.12, and 3.14. Experiment specifications and measured properties are summarized in Table 3.1.

As mentioned earlier in this chapter, brace elements are discretized using seven fiber segments. The axial loads are applied at small eccentricities that are adjusted to realize the same buckling loads as observed in the experiments (except for the HSS1-2 specimen, which was first loaded and yielded in tension for which a buckling load of 110 kips was modeled, compared to a measured buckling load of 119 kips). The material models were set to be similar to what was observed in the coupon tests but then tuned to realize similar hysteretic features that were observed in the experiments. The material model backbone curves used in modeling the Black et al. specimens are shown in Figure 3.13. The material model backbone curves used in modeling the Fell et al. specimens are shown in Figure 3.14 (same figure that shows the measured mechanical properties). The model parameters

Table 3.1: Experimental parameters of the modeled specimens from the Black et al. and Fell et al. testing programs.

Test Program	Specimen Tag	Cross Section	L (cm)	A (cm^2)	I_{min} (cm^4)	KL/r (-)	P_{cr} (kN)	σ_y (MPa)	σ_u (MPa)	ε_{rup} (-)
Black et al.	Strut 01	W8x20	381.00	37.51	383.76	119	423	289.6	481.3	0.28
	Strut 03	W6x20	306.93	37.53	552.75	80	899	277.2	446.1	0.28
	Strut 17	HSS4x4x1/4	304.80	24.19	367.43	78	547	397.1	457.8	0.13
	Strut 18	HSS4x4x1/2	276.45	45.16	606.97	75	1210	565.4	565.4	0.12
Fell et al.	HSS1-1	HSS4x4x1/4	312.42	21.74	334.57	80	698	497.8	528.8	0.12
	HSS1-2	HSS4x4x1/4	312.42	21.74	334.57	80	529	497.8	528.8	0.12
	HSS1-3	HSS4x4x1/4	312.42	21.74	334.57	80	716	497.8	528.8	0.12
	HSS2-1	HSS4x4x3/8	312.42	30.99	453.19	82	827	521.9	559.9	0.11
	HSS2-2	HSS4x4x3/8	312.42	30.99	453.19	82	818	521.9	559.9	0.11

for all models are summarized in Table 3.2. Excellent agreement with experimental data is achieved for all specimens using material backbone curves reasonably close to the measured mechanical properties. Note that although local buckling is not modeled in STEEL, the models deteriorate at similar points as the specimens in the Fell et al. testing program. The axial displacement histories applied to the modeled specimens from the Black et al. testing program are shown in Figure 3.15. Corresponding modeled and measured brace element responses are shown in Figures 3.16 and 3.17. Displacement histories applied to the modeled Fell et al. specimens are shown in Figure 3.18, and corresponding brace element responses (modeled and measured) are shown in Figures 3.19 and 3.20.

In the building analyses axial loads are applied to conventional brace elements at an eccentricity of 4.3 mm (0.17 in). That yields similar initial buckling loads as predicted by equations E2-2 and E2-3 in $AISC$ Manual of Steel Construction [1] using a reduction factor, ϕ, of 0.85.

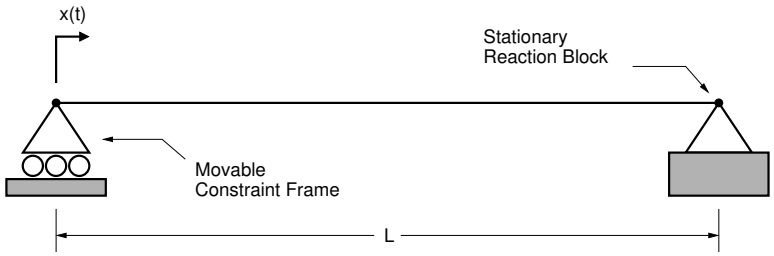

Figure 3.8: A schematic view of the experimental set-up in the Black et al. testing program and the Fell et al. testing program with the brace connections idealized as pinned end-conditions, and the STEEL model used for analysis. The location where displacement loading protocols are applied is implied by x(t).

Table 3.2: STEEL model parameters of the modeled specimens from the Black et al. and Fell et al. testing programs.

Test Program	Specimen Tag	σ_y (MPa)	σ_u (MPa)	E (GPa)	E_{sh} (GPa)	ε_{sh} (-)	ε_u (-)	ε_{rup} (-)	$ecc.$ (mm)
Black et al.	Strut 01	288.9	481.3	199.9	4.4	0.0160	0.1480	0.28	1.24e+00
	Strut 03	314.9	457.8	199.9	4.0	0.0150	0.1475	0.28	3.28e-02
	Strut 17	397.1	457.8	199.9	4.0	0.0120	0.0800	0.15	1.68e+00
	Strut 18	561.9	565.4	199.9	4.0	0.0030	0.1000	0.20	1.22e+00
Fell et al.	HSS1-1	468.8	548.1	199.9	55.2	0.0035	0.0690	0.13	7.62e-03
	HSS1-2	479.2	537.8	199.9	103.4	0.0025	0.0800	0.16	1.27e-07
	HSS1-3	475.7	558.5	199.9	137.9	0.0024	0.0530	0.10	7.62e-03
	HSS2-1	455.1	541.0	199.9	165.5	0.0023	0.1250	0.25	2.54e-01
	HSS2-2	455.1	551.6	199.9	165.5	0.0023	0.1100	0.22	3.05e-01

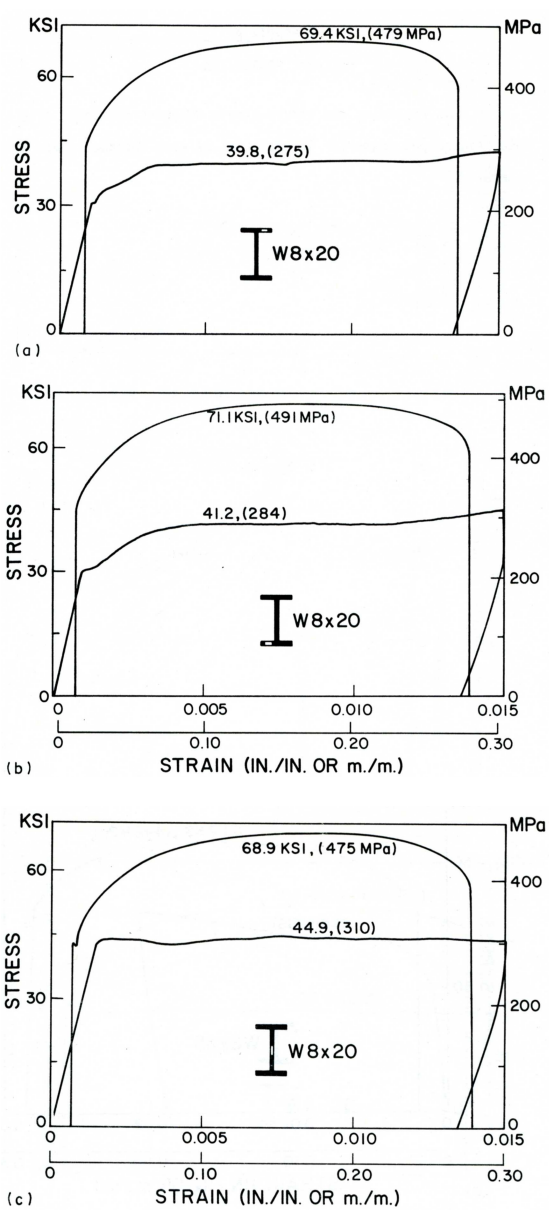

Figure 3.9: Measured material mechanical properties of coupons taken from Strut 01 of the Black et al. testing program [6].

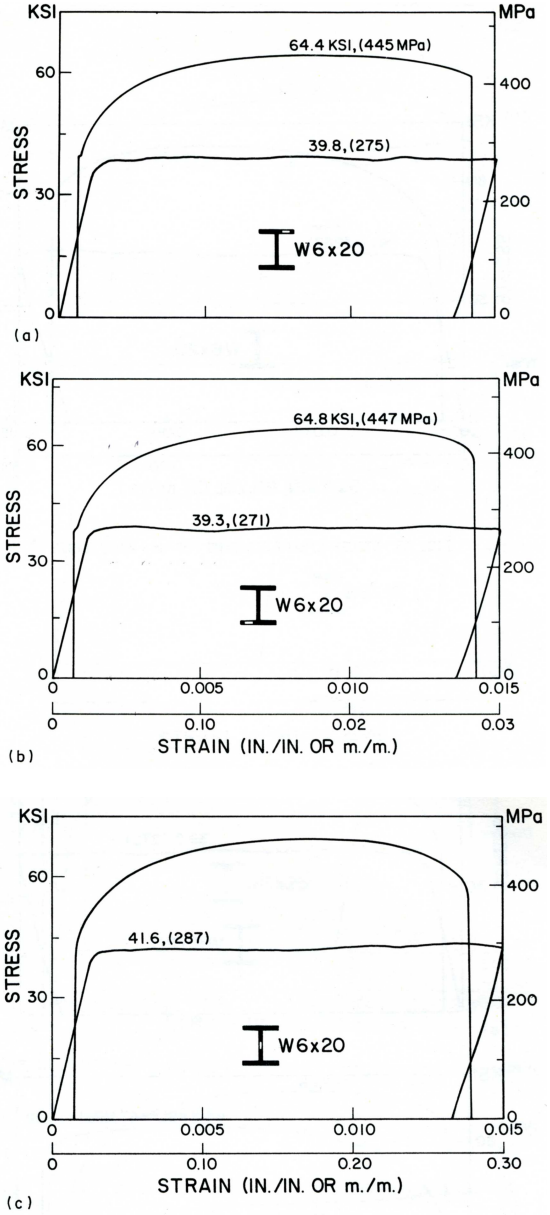

Figure 3.10: Measured material mechanical properties of coupons taken from Strut 03 of the Black et al. testing program [6].

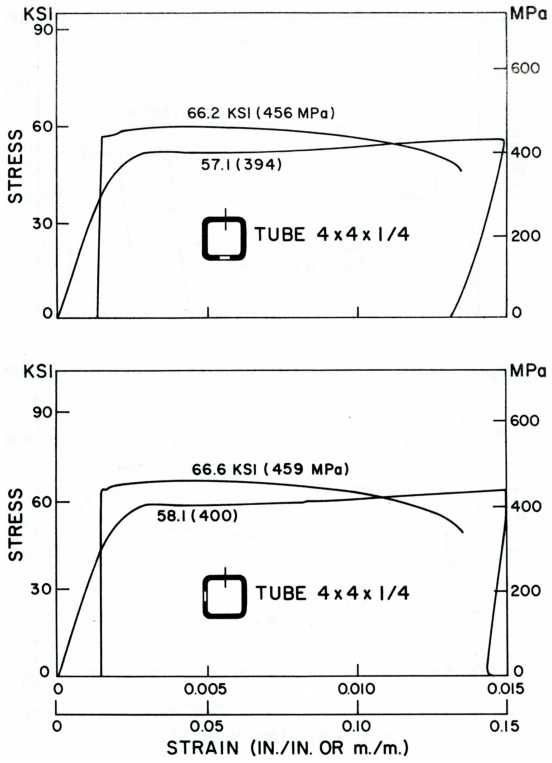

Figure 3.11: Measured material mechanical properties of coupons taken from Strut 17 of the Black et al. testing program [6].

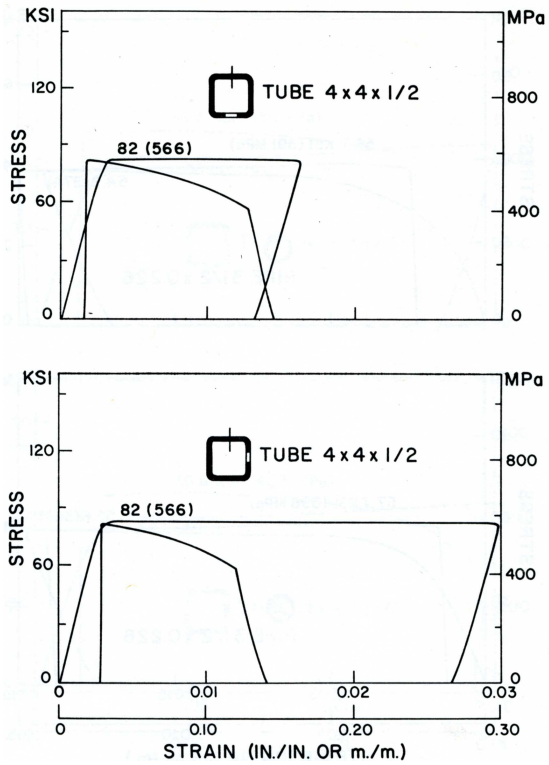

Figure 3.12: Measured material mechanical properties of coupons taken from Strut 18 of the Black et al. testing program [6].

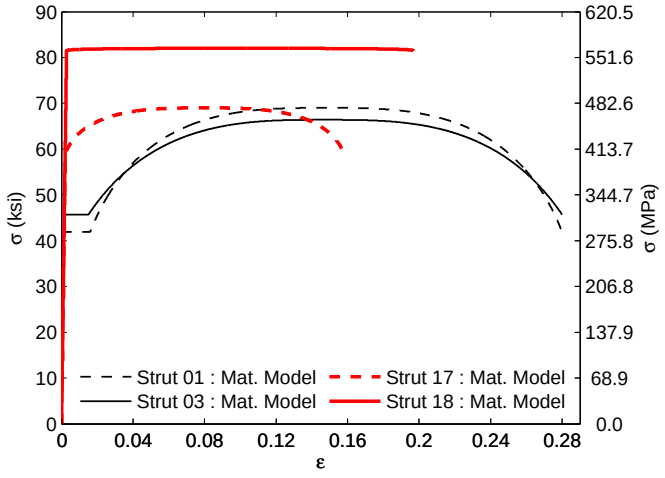

Figure 3.13: Material models used in STEEL for modeling of the specimens from the Black et al. testing program.

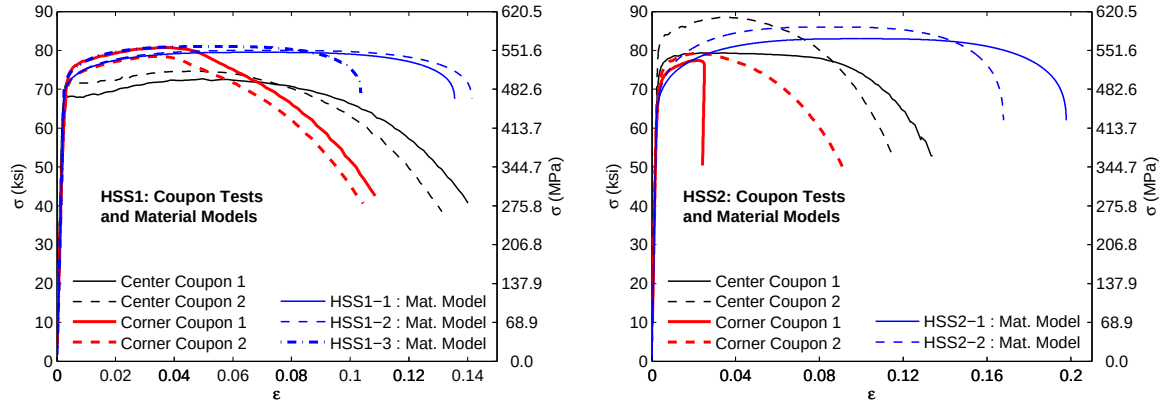

Figure 3.14: Measured material mechanical properties and corresponding material models used in STEEL for (a) the HSS1 specimens and (b) the HSS2 specimens of the Fell et al. testing program. Four material coupons were sampled for each cross-section type. Two material coupons were sampled from the corners of the cross-sections, and two material models were sampled from the center of the walls of the cross-sections.

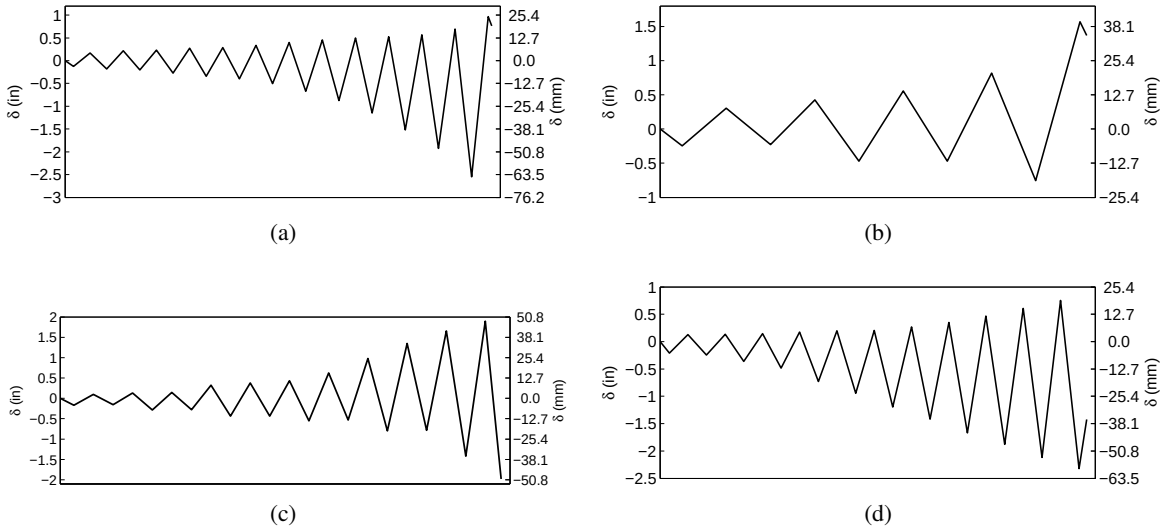

Figure 3.15: Displacement loading histories applied axially to specimen (a) Strut 01, (b) Strut 03, (c) Strut 17, and (d) Strut 18 of the Black et al. testing program. Compression is negative.

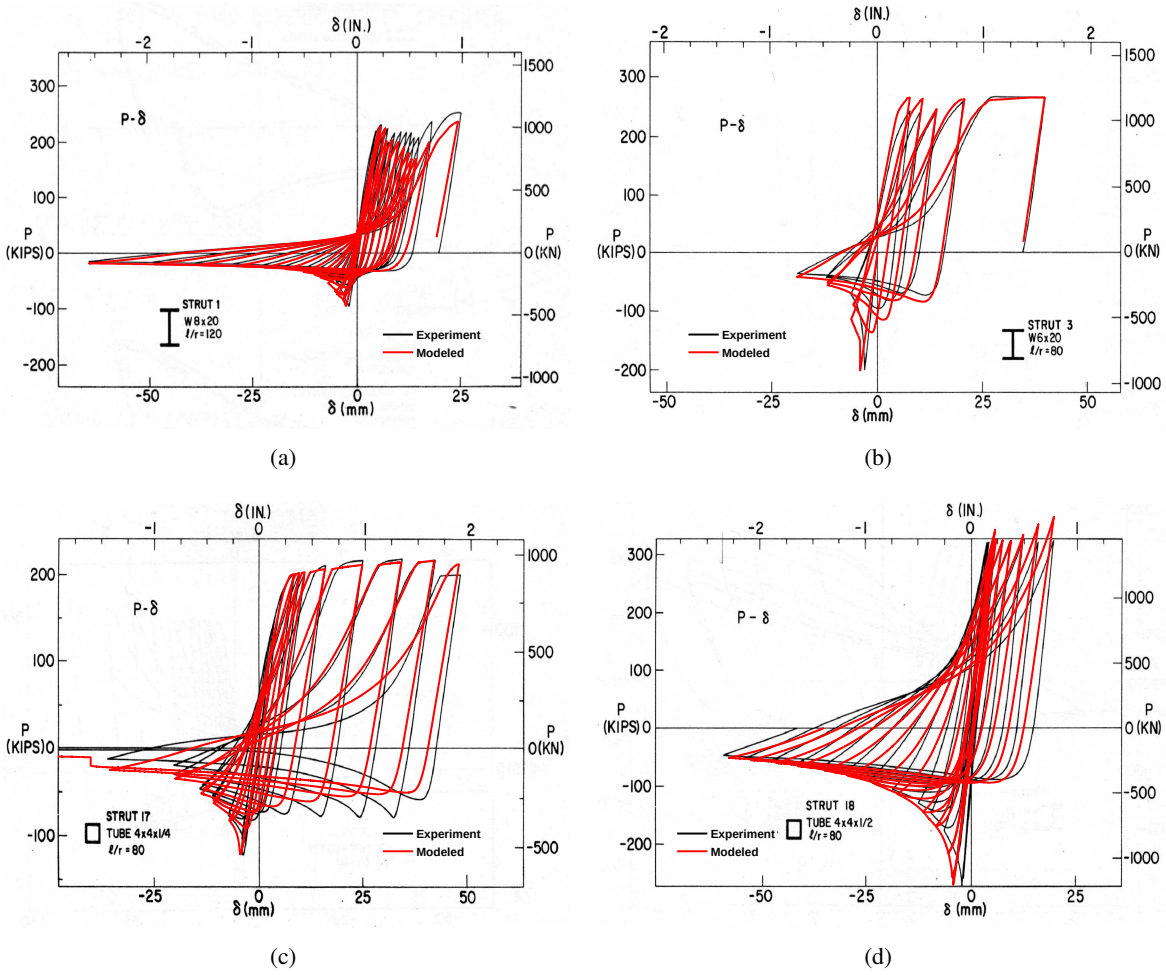

Figure 3.16: Measured and modeled brace axial displacement versus axial force responses of specimen (a) Strut 01, (b) Strut 03, (c) Strut 17, and (d) Strut 18 of the Black et al. testing program.

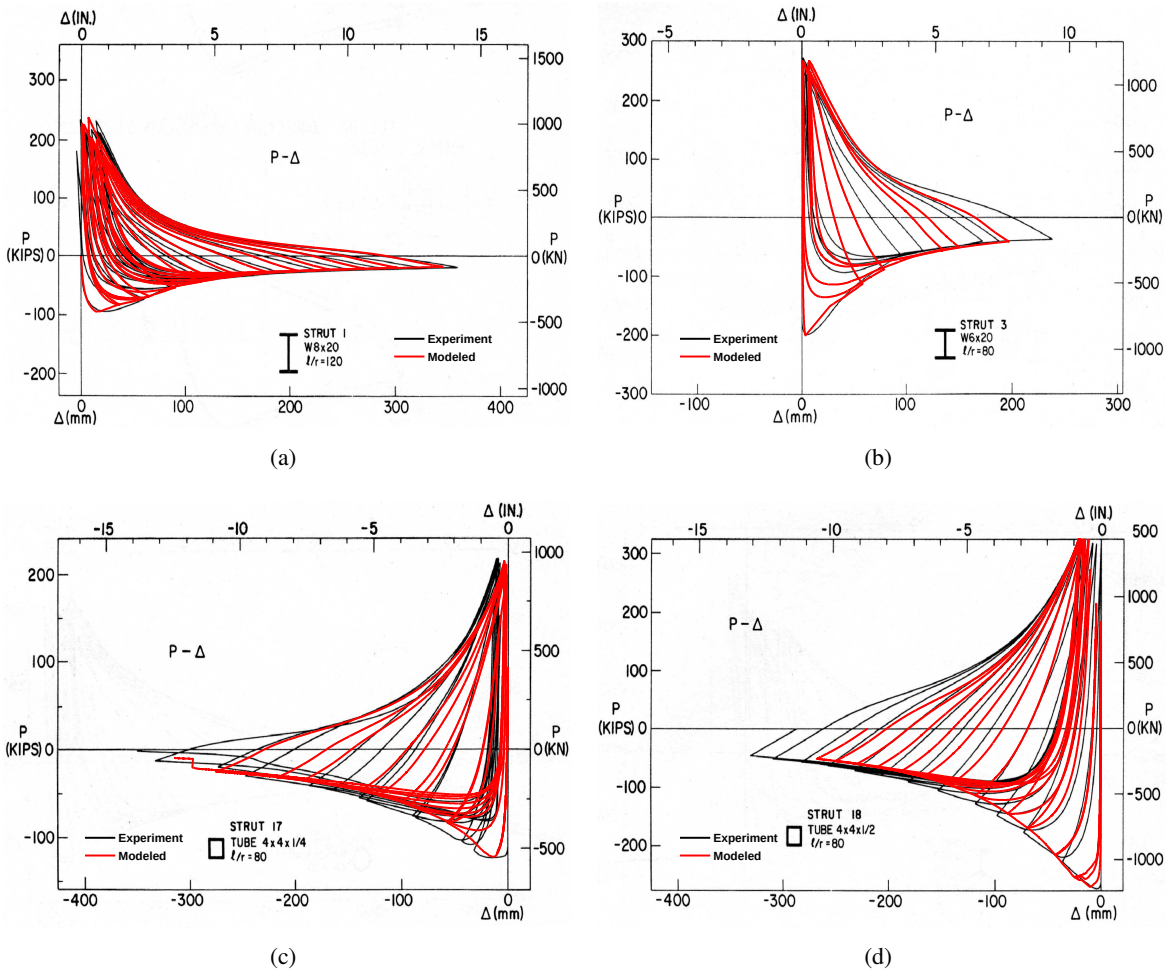

Figure 3.17: Measured and modeled brace lateral displacement versus axial force responses of specimen (a) Strut 01, (b) Strut 03, (c) Strut 17, and (d) Strut 18 of the Black et al. testing program.

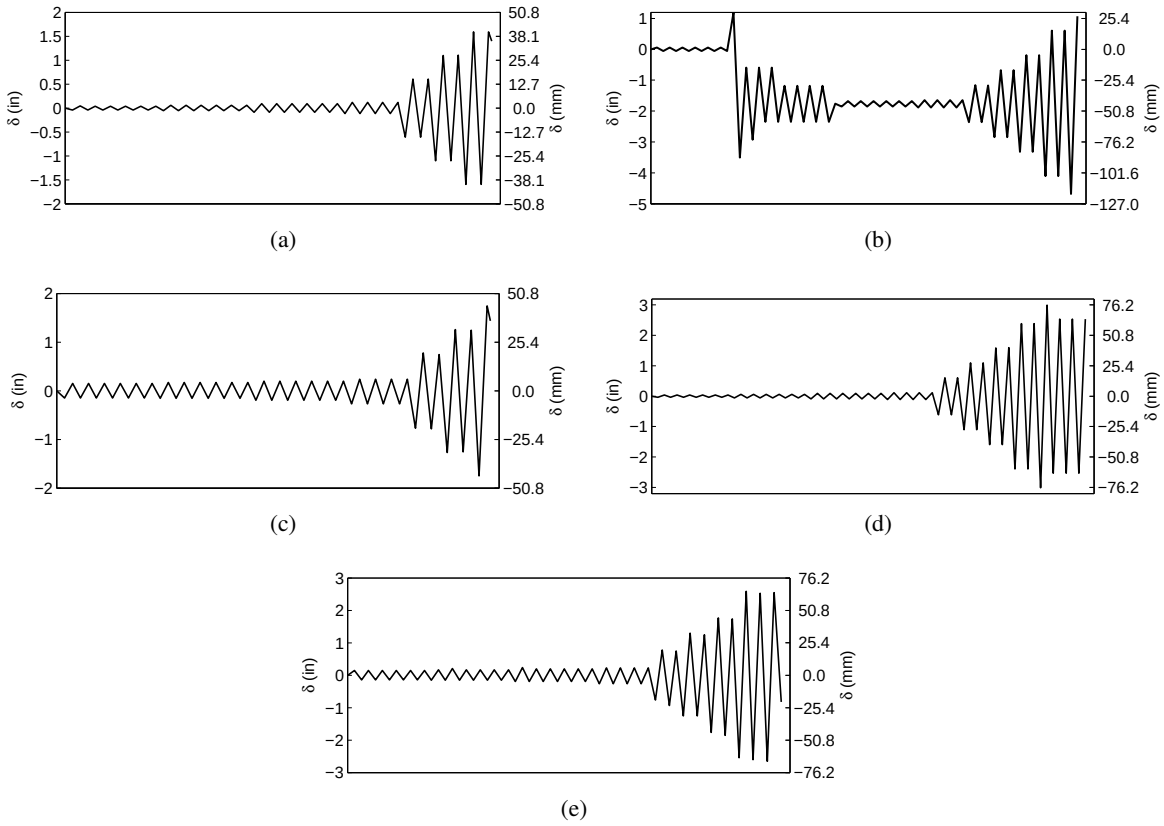

Figure 3.18: Displacement loading histories applied axially to specimen (a) HSS1-1, (b) HSS1-2, (c) HSS1-3, (d) HSS2-1, and (e) HSS2-2 of the Fell et al. testing program. Compression is negative.

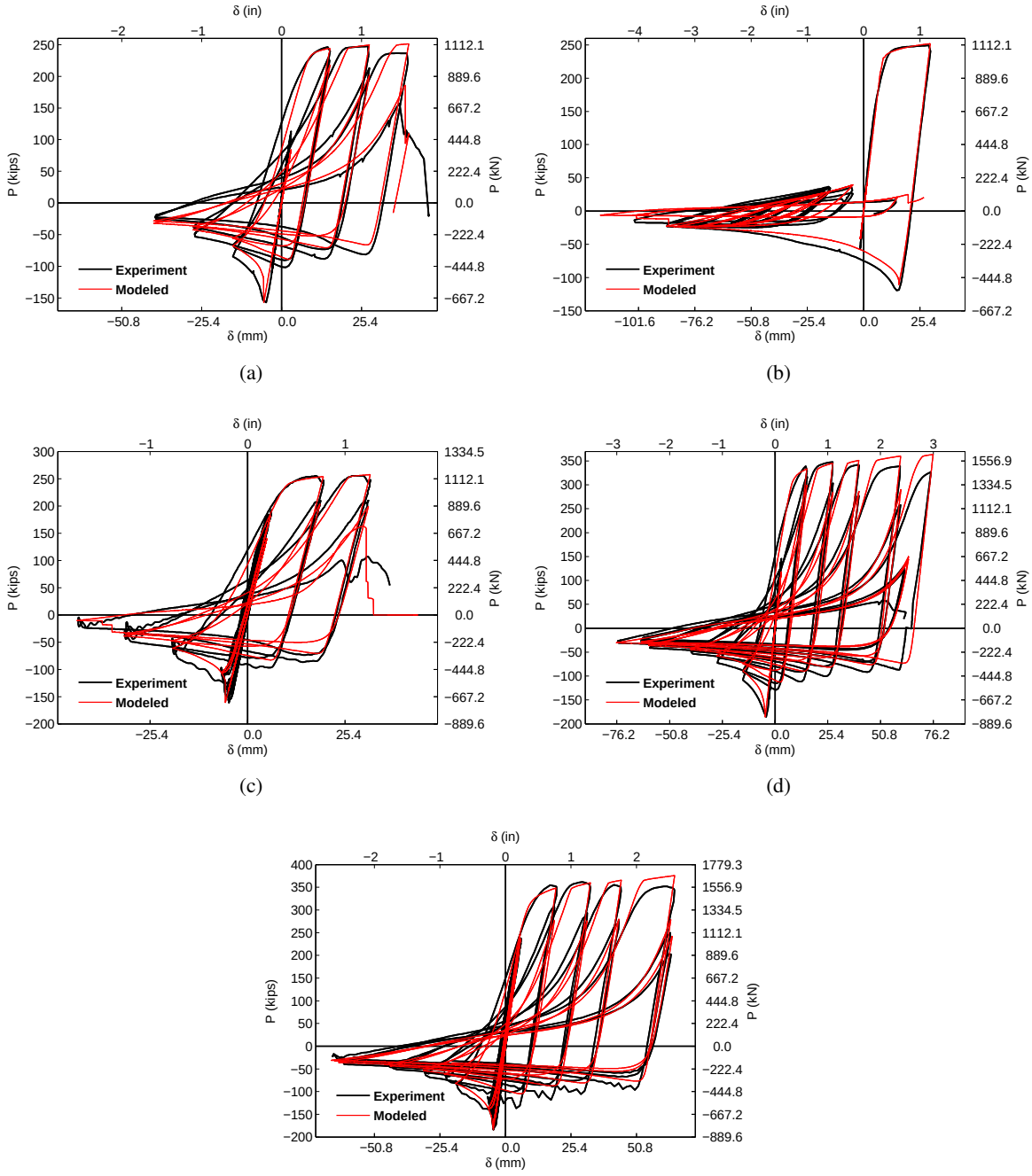

Figure 3.19: Measured and modeled brace axial displacement versus axial force responses of specimen (a) HSS1-1, (b) HSS1-2, (c) HSS1-3, (d) HSS2-1, and (e) HSS2-2 of the Fell et al. testing program.

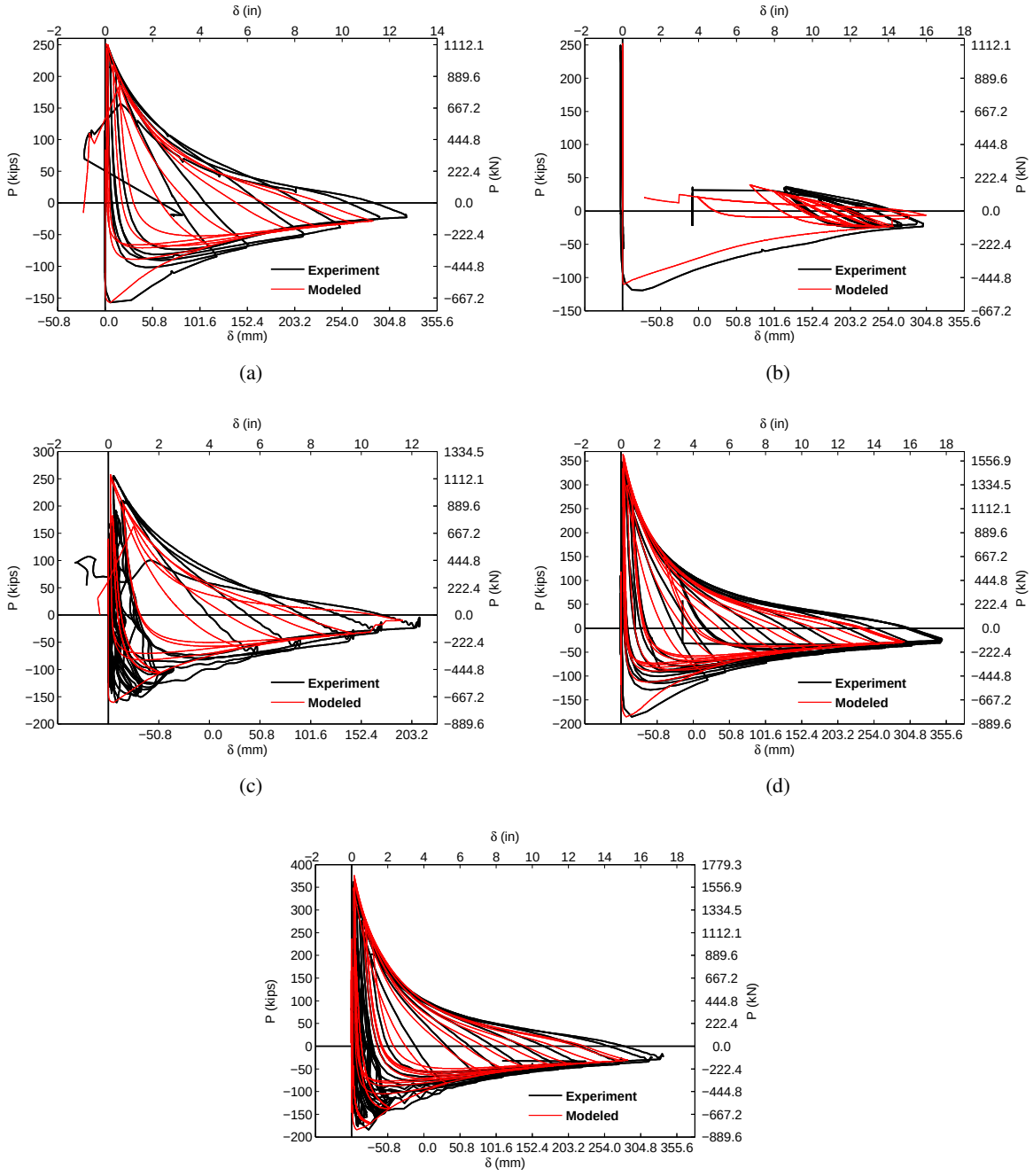

Figure 3.20: Measured and modeled brace lateral displacement versus axial force responses of specimen (a) HSS1-1, (b) HSS1-2, (c) HSS1-3, (d) HSS2-1, and (e) HSS2-2 of the Fell et al. testing program.

3.4 Modeling of Buckling-Restrained Brace Elements

The different types of available buckling-restrained brace elements generally share the same concept, i.e., a central portion of the brace element that has a smaller cross-sectional area compared to the remainder of the element is restrained from lateral and local buckling by an external mechanism, and is detailed such that the central yielding core can deform longitudinally independently from the external mechanism. Modeling a buckling-restrained brace element, therefore, requires at least two segments. In addition, to account for necking in the yielding core towards the limit state of the element, the yielding core needs to be further discretized into one long segment and another short segment with only a marginally smaller cross sectional area than the "long" segment.

A number of experiments have been performed on the different types of buckling-restrained elements, including [5, 54, 55, 58]. Interestingly, compressive strength of buckling-restrained braces has been reported to be greater than the tensile strength. This effect is commonly referred to as compressive overstrength. Compressive overstrength has been reported as great as 20% [55]. In STEEL the same material properties are assumed in compression and tension and the program is therefore not capable of capturing this overstrength in compression. To compensate, both compressive and tensile strength of the material can be increased such that the tensile strength of a buckling-restrained brace is overshot by half the value of the compressive overstrength, and the brace compressive strength is underpredicted by half the value of the compressive overstrength. In this way, the modeled brace dissipates the same amount of energy in a complete loading cycle as an actual buckling-restrained brace. Also, for a brace pair, as in a chevron bracing configuration, this method accurately predicts the total lateral strength of the brace pair. However, the imbalance of forces at beam mid-span where the brace elements connect to the beam is not accounted for.

To demonstrate the adequacy of these modeling assumptions, three buckling-restrained brace sub-assemblage experiments by Newell el al. [58] and one by Merrit et al. [55] are modeled in STEEL, and the modeled brace behavior is compared against experimental data.

Newell et al. tested two pairs of nominally identical buckling-restrained brace elements manufactured by CoreBrace, LLC. The central yielding cores of the first pair of specimens (1G and 2G) were composed of flat plates of cross-sectional area of 77.4 cm^2 (12.0 in^2), but crusiform core shapes of cross-sectional area of 174.2 cm^2 (27.0 in^2) were used for the second pair (3G and 4G). The yielding cores of the specimens were confined in grout filled steel square tube sections. The braces were spliced to gusset brackets with a steel connection plate that was welded to the brace core

plate and bolted to the gusset bracket. Some slipping of bolts was experienced in the experiments. Specimen 2G experienced problems with the core centering mechanism and showed "non-typical" brace behavior and is therefore not modeled. The steel core of specimen 3G ruptured during the experiment and that is not captured in the modeling. The rupture may have occurred due to fatigue, which is not modeled in STEEL, or due to material defect. For instance, specimen 4G, which was identical to specimen 3G, was loaded to greater strains without rupturing.

The Merrit et al. testing program tested eight specimens of varying capacity manufactured by Star Seismic, LLC. All specimens were composed of flat yielding core plates confined in grout filled steel square tube sections. The braces were pin-connected to gusset plates. The gusset plate was thickened around the pin hole, but plastic elongation of the pin hole was still experienced.

In both testing programs, the specimens were subjected to cyclic quasi-statically applied loads in both axial and transverse directions (to simulate rotational demands on the brace connections). The experimental setup is similar to the schematic figure presented for conventional brace element experiments (Figure 3.8), except that the moving end is put through a transverse displacement time-history simultaneously with an axial displacement time-history. Axial deformations of the brace specimens as well as axial deformations over the gusset plates, which the brace specimens were connected to, were measured and peak displacements of each loading cycle were reported. Newell et al. also presented hysteresis plots of brace specimen axial force versus brace deformation. Merrit et al. presented similar plots, but generally plotted brace specimen axial force versus total deformation (gusset plate deformation plus brace deformation), except for specimen S7. For specimen S7, hysteretic brace axial force versus brace deformations was presented as well. In the present study, modeling of bolt slip or pin hole elongation is neglected, and therefore brace axial force versus brace deformation responses are of most interest. Hence, specimen S7 is the only specimen modeled from the Merrit et al. testing program.

ASTM A36 steel was specified for the yielding cores in both testing programs. Material coupons were taken from the specimens and the actual mechanical properties were measured. The brace specimen lengths, L, yielding core lengths, L_{yc}, and yielding core cross-sectional areas, A_{yc}, are presented in Table 3.3, along with measured yield stresses, σ_y, ultimate stresses, σ_u, rupture strains, ε_{rup}, and maximum compressive overstrength factors, β, realized in the experiments. The material model constants used for the STEEL models are presented in Table 3.4. The ultimate strength, σ_u, of the material models used in STEEL include considerations of compressive overstrength as described previously.

Table 3.3: Experiment parameters of the modeled specimens from the Newell et al. and Merrit et al. testing programs.

Test Program	Specimen Tag	L (cm)	L_{yc} (cm)	A_{yc} (cm^2)	σ_y (MPa)	σ_u (MPa)	ε_{rup} (-)	β (-)
Newell et al.	1G	660.72	336.55	77.42	258.6	484.7	0.32	1.17
	3G	635.48	366.87	174.19	258.6	484.7	0.32	1.10
	4G	635.48	366.87	174.19	258.6	484.7	0.32	1.13
Merrit et al.	S7	695.96	470.41	184.06	289.3	435.6	0.26	1.20

Table 3.4: STEEL material model parameters of the modeled specimens from the Newell et al. and Merrit et al. testing programs.

Test Program	Specimen Tag	σ_y (MPa)	σ_u (MPa)	E (GPa)	E_{sh} (GPa)	ε_{sh} (-)	ε_u (-)	ε_{rup} (-)
Newell et al.	1G	258.6	546.1	199.9	13.8	0.0020	0.1600	0.32
	3G	261.3	506.8	199.9	13.8	0.0020	0.1600	0.32
	4G	261.3	511.6	199.9	13.8	0.0020	0.1600	0.32
Merrit et al.	S7	289.6	477.8	199.9	13.8	0.0040	0.1320	0.26

The axial displacement histories applied to the modeled buckling-restrained brace specimens are shown in Figure 3.21. Corresponding modeled and measured brace element responses are shown in Figure 3.22. The modeled element responses show close agreement with the experiment.

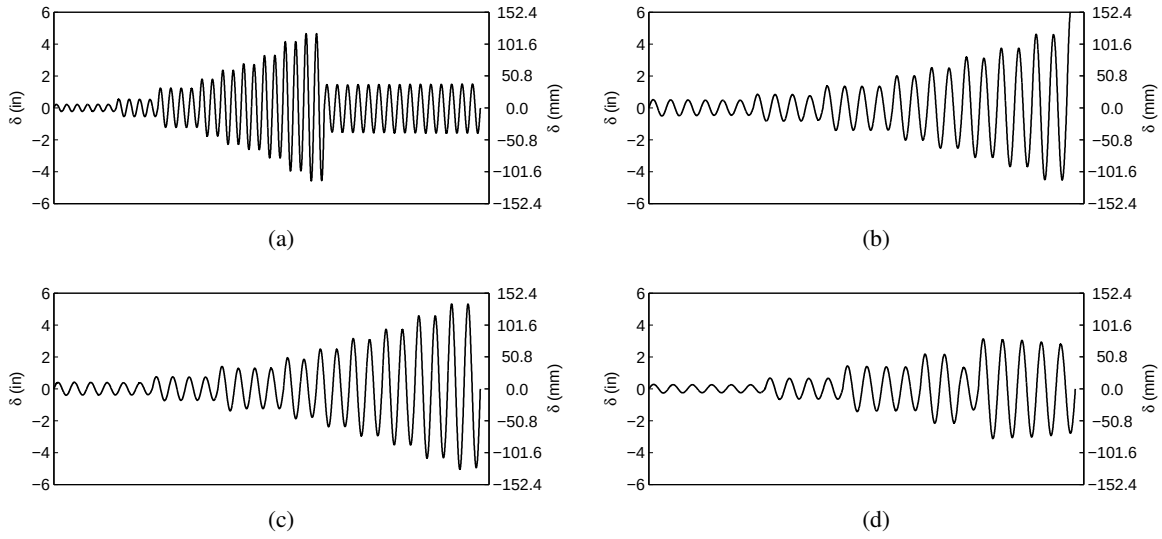

Figure 3.21: Displacement loading histories applied axially to specimen (a) 1G, (b) 3G, and (c) 4G of the Newell et al. testing program, and (d) specimen S7 of the Merrit et al. testing program. Compression is negative.

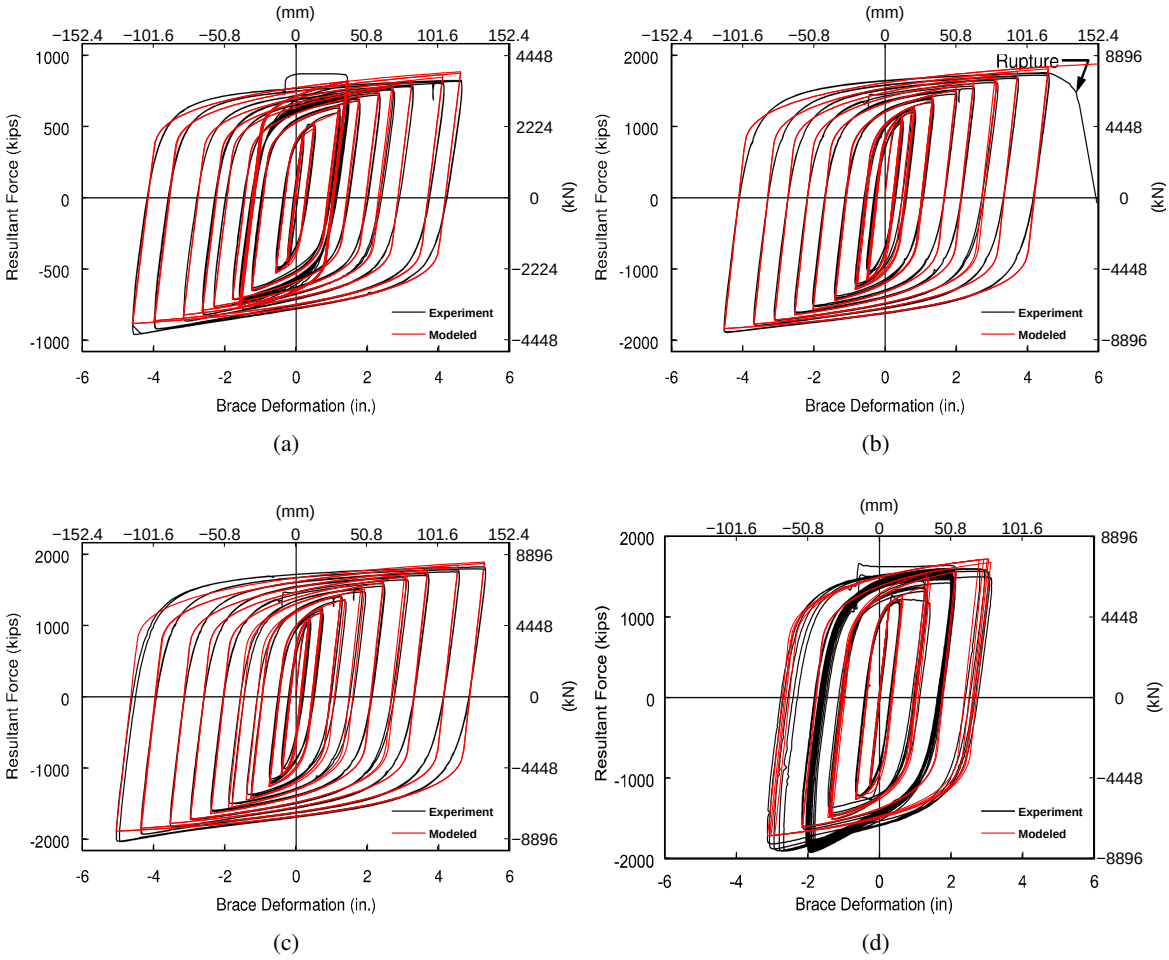

Figure 3.22: Measured and modeled isolated brace displacement versus axial force responses of specimen (a) 1G, (b) 3G, and (c) 4G of the Newell et al. testing program, and (d) specimen S7 of the Merrit et al. testing program.

Chapter 4

Ground Motions

The greater Los Angeles metropolitan area, which is the geographic focus of this study, is built in a highly seismically active region. A complex network of faults surrounds, cuts through, and is buried underneath the urban area. Some faults have surface expressions and are well mapped, such as the San Andreas, Santa Monica-Hollywood-Raymond, and Newport-Inglewood faults. Other blind-thrust faults are burried underneath the earth's surface. such as the Puente Hills fault system that lies underneath downtown Los Angeles and the Northridge fault that ruptured on January 17 1994 and caused 57 deaths and economic losses in excess of $40 billion [14, 60]. The San Andreas fault has the potential of producing large ($M_w \sim 8$) earthquakes, typically every 200-300 years [67, 68]. Blind-thrust faults have the potential for more moderate ($M_w \sim 7$) earthquakes [66], but their proximity to heavily urbanized areas render them a major threat as well.

In this study we use simulated ground motions from three hypothetical earthquake scenarios that cause strong shaking in the Los Angeles metropolitan area: motions from a simulated M_w 7.9 1857-like San Andreas fault earthquake produced by Krishnan et al. [46, 47, 44], motions from the M_w 7.8 ShakeOut scenario earthquake on the San Andreas fault produced by Graves et al. [27, 26], and motions from a simulated M_w 7.2 Puente Hills earthquake produced by Graves and Somerville [25, 30]. In addition, the sets of synthetic ground motions are complemented with a collection of recorded ground motion time histories from actual earthquakes that have occurred around the world.

The ground motions from the simulated scenario earthquakes all consist of three components: an east-west (EW) component, a north-south (NS) component, and a vertical component. Each set of recorded ground motions consists of a component normal to the fault rupture (fault-normal), a component parallel to the fault rupture (fault-parallel), and all but one record, from the Superstition Hills earthquake, includes a vertical component as well. Both EW and NS orientations of the planar building models are considered in the simulated scenario earthquakes. The recorded ground motions

from actual earthquakes are applied in incremental dynamic analyses of the building models. In the incremental dynamic analyses, the fault-normal and vertical components (if available) are scaled by scaling factors ranging from 0.6 to 2.0 with increments of 0.2. The scaled ground motion records are then applied to the building models.

4.1 M_w 7.9 1857-Like San Andreas Fault Earthquake

This earthquake scenario is a computational re-creation of a M_w 7.9 earthquake that occurred on the San Andreas fault in 1857. In the 1857 event, a rupture nucleated near Parkfield in Central California and progressed 360 km south-east along the fault [69]. The computational recreation of this event was first presented by Krishnan et al. [46, 47], and was later updated by Krishnan et al. [44] in order to incorporate advances made to the Southern California Earthquake Center (SCEC) Community Velocity Model, which is used in mathematically propagating the seismic waves through the earth structure.

The earthquake source model used in the simulations was generated by mapping a source model of the 2002 M_w 7.9 Denali earthquake that occurred on the Denali fault system, produced by Ji et al. [40], onto the San Andreas fault with the rupture initiating at Parkfield. The 2002 Denali earthquake initiated as a thrust event on the Susitna Glacier fault, but quickly transitioned into strike-slip mode on the main Denali fault and propagated 218 km south-east along the Denali fault before jumping onto the Totschunda fault, where the rupture continued in a strike-slip mode for another 76 km [13]. The Denali fault is geometrically similar to and has similar rupture mechanics (right lateral strike-slip) as the San Andreas fault, which allows the mapping of this event onto the San Andreas fault and it gives an earthquake scenario comparable to the 1857 event.

The seismic waves generated by the San Andreas fault source model are propagated through the earth structure using a seismic wave propagation software called SPECFEM3D (V2.0 SESAME), and ground motion time histories are produced at 636 geographic sites evenly distributed over the greater Los Angeles metropolitan area. Each site represents an area of 10 km^2. The SCEC Community Velocity Model, version H11.9 [61], is used to characterize the earth structure and contains seismic wave speeds, densities, topography, bathymetry, and attenuations. The methodology adopted in SPECFEM3D is based on the spectral-element method [42, 72] and it has been shown, using earlier versions of the SCEC Community Velocity Model, to accurately model basin responses up to frequencies of approximately 0.5 Hz [41, 52]. A spectral-element mesh of the Southern Cal-

ifornia region that is compatible with the SCEC Community Velocity model is created using an advanced unstructured mesher, CUBIT, developed by Sandia National Laboratory [64] and adapted as GeoCubit for large-scale geological applications [7]. The limitation on the frequency content of the simulated ground motions is primarily due to insufficient resolution of the model of the seismic wave speed structure of the earth for propagating high-frequency waves, and the higher frequency waveforms need to be obtained differently. In this ground motion simulation, a variant of the classical Empirical Green's Function (EGF) method presented by Mourhatch and Krishnan [56] is applied at each of the 636 sites to produce high-frequency (0.5 - 5 Hz) ground motion waveforms. Then, using a matching pair of low-pass and high-pass Butterworth filters, the two sets of ground motion time histories are synthesized to give broadband (0 - 5 Hz) ground motion waveforms.

Amplification due to site-specific geology is not considered in the low-frequency portion of the simulations. However, Krishnan et al. [46, 47] suggest that site amplification is likely to be minimal for low-frequency ($<$0.5 Hz) waves, and consequently the effects on long-period (low-frequency) structures such as the ones considered in this study are also likely to be minimal. As for the high-frequency (0 - 5 Hz) portion of the simulations, the generated ground motion time histories are basically constructed from real ground motions that are recorded at the ground surface at sites reasonably close to the target site, and contain potential amplifications due to site-specific geology.

In Figure 4.1, a map of the greater Los Angeles metropolitan area is presented, showing the locations of the 636 sites where ground motion time histories are generated and the building models are analyzed. The relation of the study area to the 290 km hypothetical rupture of the San Andreas fault is shown in the inset. Maps of peak ground acceleration (PGA), peak ground velocities (PGV), and peak ground displacements (PGD) realized in the earthquake scenario are shown for EW and NS directions in Figure 4.2. Peak ground velocities are in the range of 1-2 m/s in the San Fernando Valley, 0.25-0.75 m/s in the Los Angeles basin, and 0.25-1 m/s in the San Gabriel Valley. Ground acceleration, velocity, and displacement time-histories for four sites located near downtown Los Angeles, Pasadena, Santa Monica, and Long Beach are shown in Figures 4.3 and 4.4.

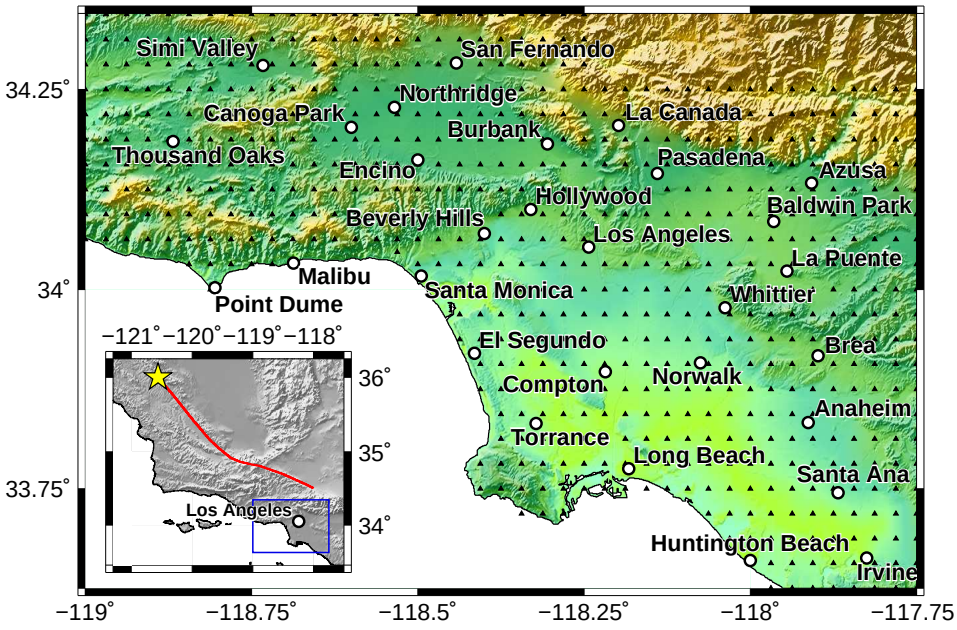

Figure 4.1: Geographic scope of the 1857-like scenario earthquake simulations. Black triangles represent the 636 sites where ground motion time histories are generated and the building models are analyzed. The color scheme reflects topography with green representing low elevation and yellow representing high elevations. The red line in the inset shows the surface trace of the hypothetical 290 km rupture of the San Andreas fault. The nucleation point of the rupture is indicated by a yellow star. In the inset, the extent of the greater Los Angeles metropolitan region, which is the geographic focus of this study, is indicated by a blue rectangle.

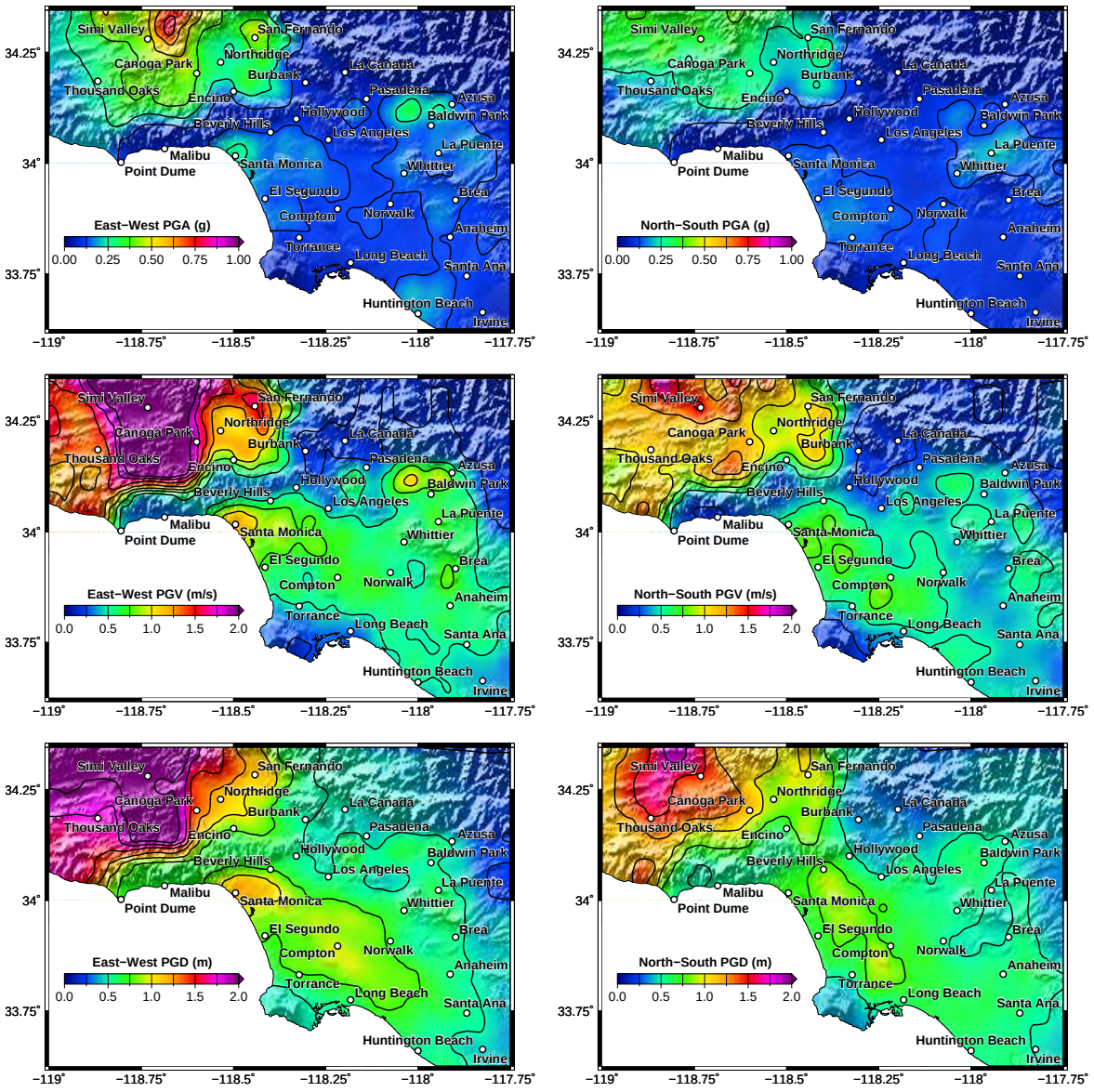

Figure 4.2: Peak ground accelerations (PGA), peak ground velocities (PGV), and peak ground displacements (PGD) realized in the greater Los Angeles metropolitan area for the east-west and north-south directions in the simulated 1857-like scenario earthquake.

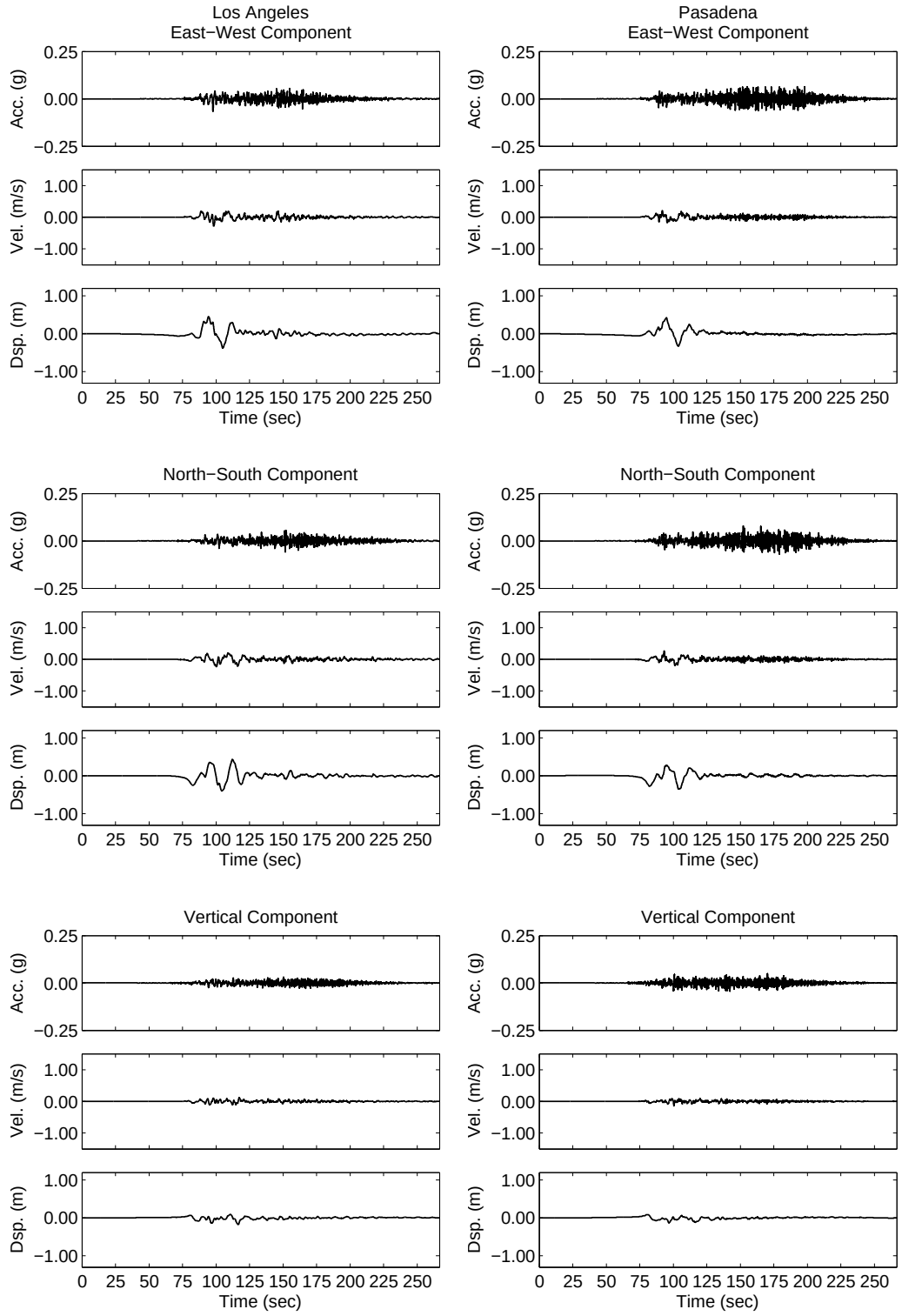

Figure 4.3: East-west, north-south, and vertical component ground acceleration, velocity, and displacement time histories realized in Los Angeles and Pasadena in the 1857-like earthquake scenario.

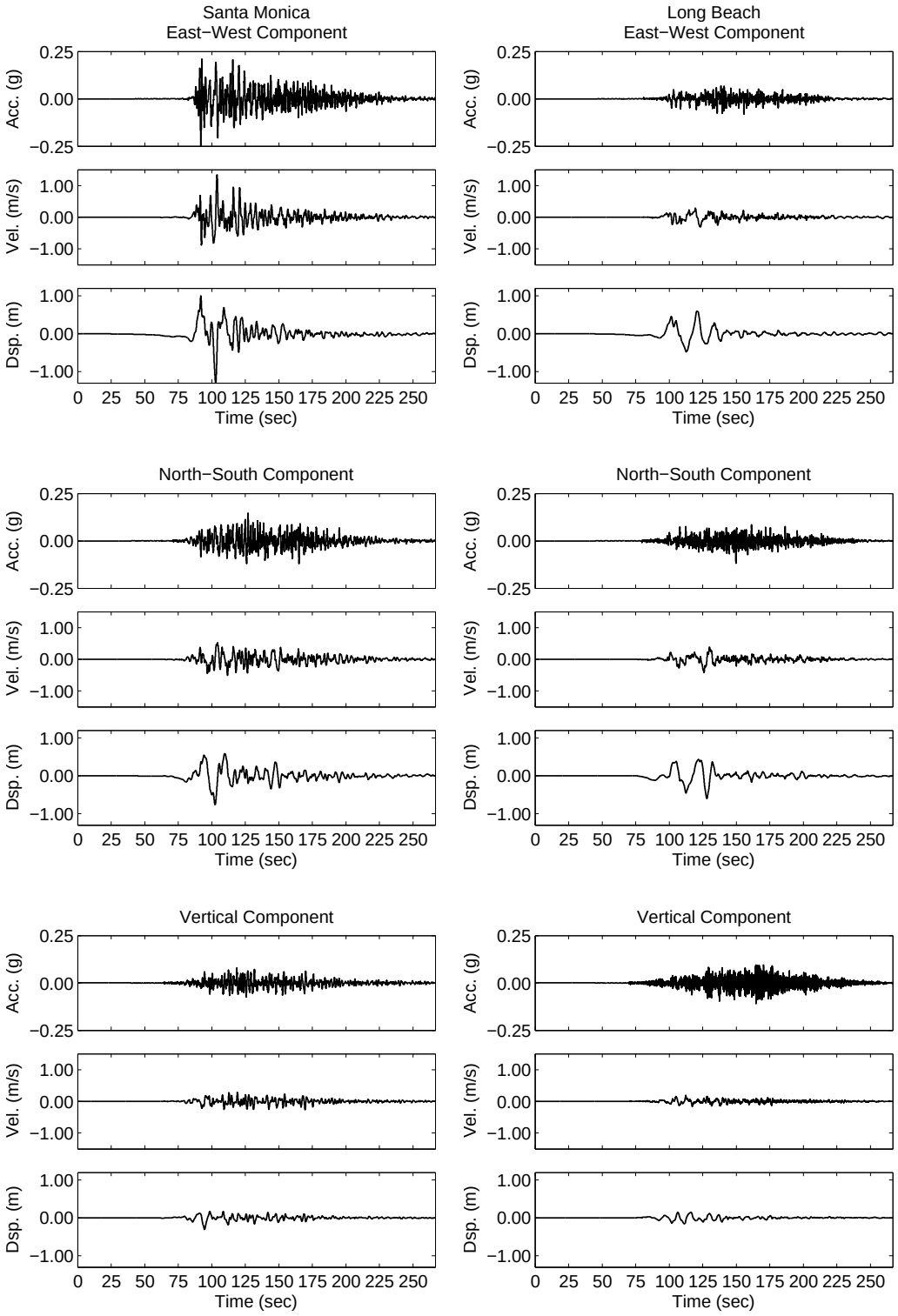

Figure 4.4: East-west, north-south, and vertical component ground acceleration, velocity, and displacement time histories realized in Santa Monica and Long Beach in the 1857-like earthquake scenario.

4.2 M_w 7.8 ShakeOut Scenario Earthquake on San Andreas Fault

The ShakeOut Scenario considers a M_w 7.8 earthquake on the southern part of the San Andreas fault. The model of the earthquake source is described in [26]. It was developed through expert discussion at multiple meetings and workshops, and is constrained by available geologic, geodetic, paleoseismic, and seismological observations [26]. The rupture nucleates at Bombay Beach and propagates 305 km north-west along the fault, and terminates at Lake Hughes near Palmdale, as shown in the inset of Figure 4.5.

The ground motion simulations use a hybrid approach by Graves and Pitarka [28] and updated by Graves and Pitarka [29] to produce broadband (0-10 Hz) three-component ground motions time histories at 25,500 geographic sites covering a large portion of Southern California. In this study, a subset of 784 sites evenly distributed over the greater Los Angeles metropolitan area is used for building analyses. Each site represents an area of 8 km^2. The hybrid approach is similar to the 1857-like scenario simulations. It combines a deterministic approach at long periods ($T > 1$ sec) with a semi-stochastic approach at short periods ($T < 1$ sec). The calculations of the long period part of the ground motions use a 3-D viscoelastic, finite difference algorithm [10, 24] with 3-D velocity structure derived from the SCEC Community Velocity Model, version S4.0. The short period part of the ground motions is obtained using a methodology that sums the response of each subfault assuming a random phase, a wave-number squared source spectrum, and simplified Green's functions [28].

Amplification due to site-specific geology is considered through application of frequency-dependent, nonlinear amplification factors based on V_{S30} [26]. V_{S30} is the travel-time-weighted shear speed in the upper 30 m at a given site.

In Figure 4.5, a map of the greater Los Angeles metropolitan area is presented, showing the locations of the subset of 784 sites from the ShakeOut earthquake scenario simulations considered in this study, where ground motion time histories are generated and the building models are analyzed. The relation of the study area to the 305 km hypothetical rupture of the San Andreas fault is shown in the inset. Maps of peak ground acceleration (PGA), peak ground velocities (PGV), and peak ground displacements (PGD) realized in the earthquake scenario are shown for EW and NS directions in Figure 4.6. Peak ground velocities are in the range of 0-1 m/s in the San Fernando Valley, 0.6-1.5 m/s in the Los Angeles basin, and 0.5-2.0 m/s in the San Gabriel Valley. Ground acceleration, velocity, and displacement time-histories for four sites located near downtown Los Angeles, Pasadena, Santa

Monica, and Long Beach are shown in Figures 4.7 and 4.8.

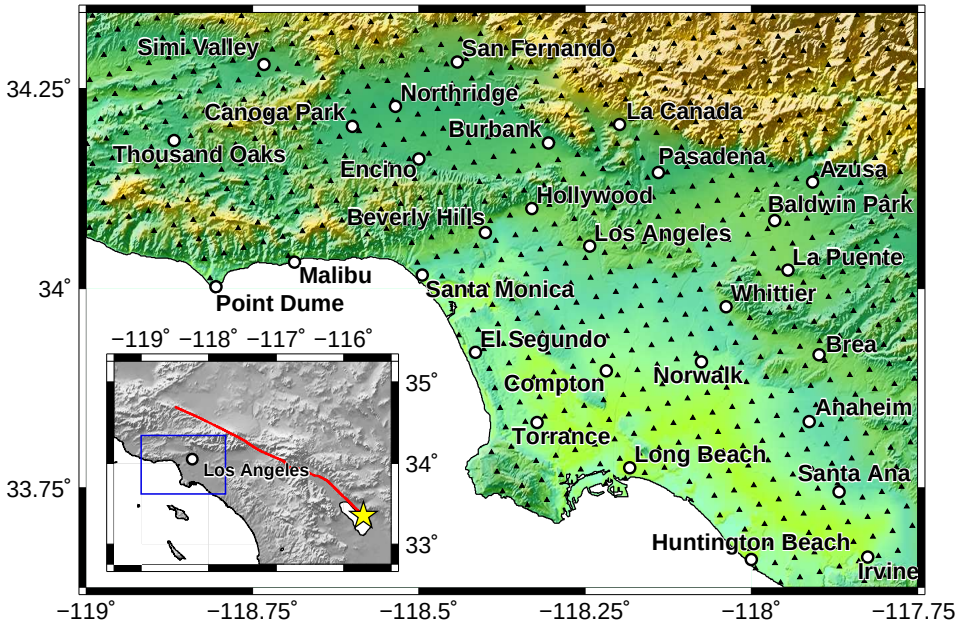

Figure 4.5: Geographic scope of the subset of 784 sites from the ShakeOut scenario earthquake simulations considered in this study. Black triangles represent the sites where ground motion time histories are generated and the building models are analyzed. The color scheme reflects topography with green representing low elevation and yellow representing high elevations. The red line in the inset shows the surface trace of the hypothetical 305 km rupture of the San Andreas fault. The nucleation point of the rupture is indicated by a yellow star. In the inset, the extent of the greater Los Angeles metropolitan region, which is the geographic focus of this study, is indicated by a blue rectangle.

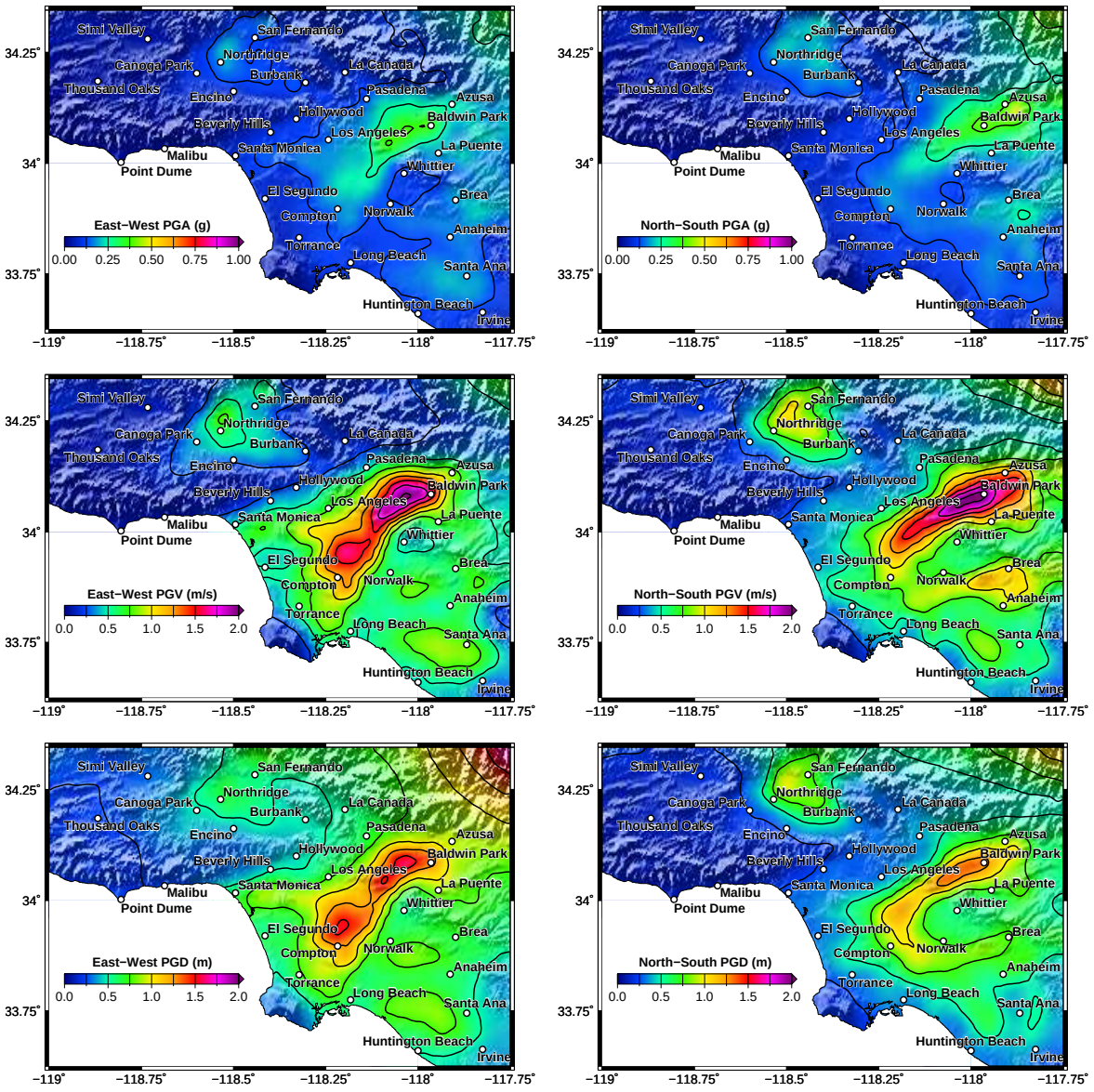

Figure 4.6: Peak ground accelerations (PGA), peak ground velocities (PGV), and peak ground displacements (PGD) realized in the greater Los Angeles metropolitan area for the east-west and north-south directions in the simulated ShakeOut scenario earthquake.

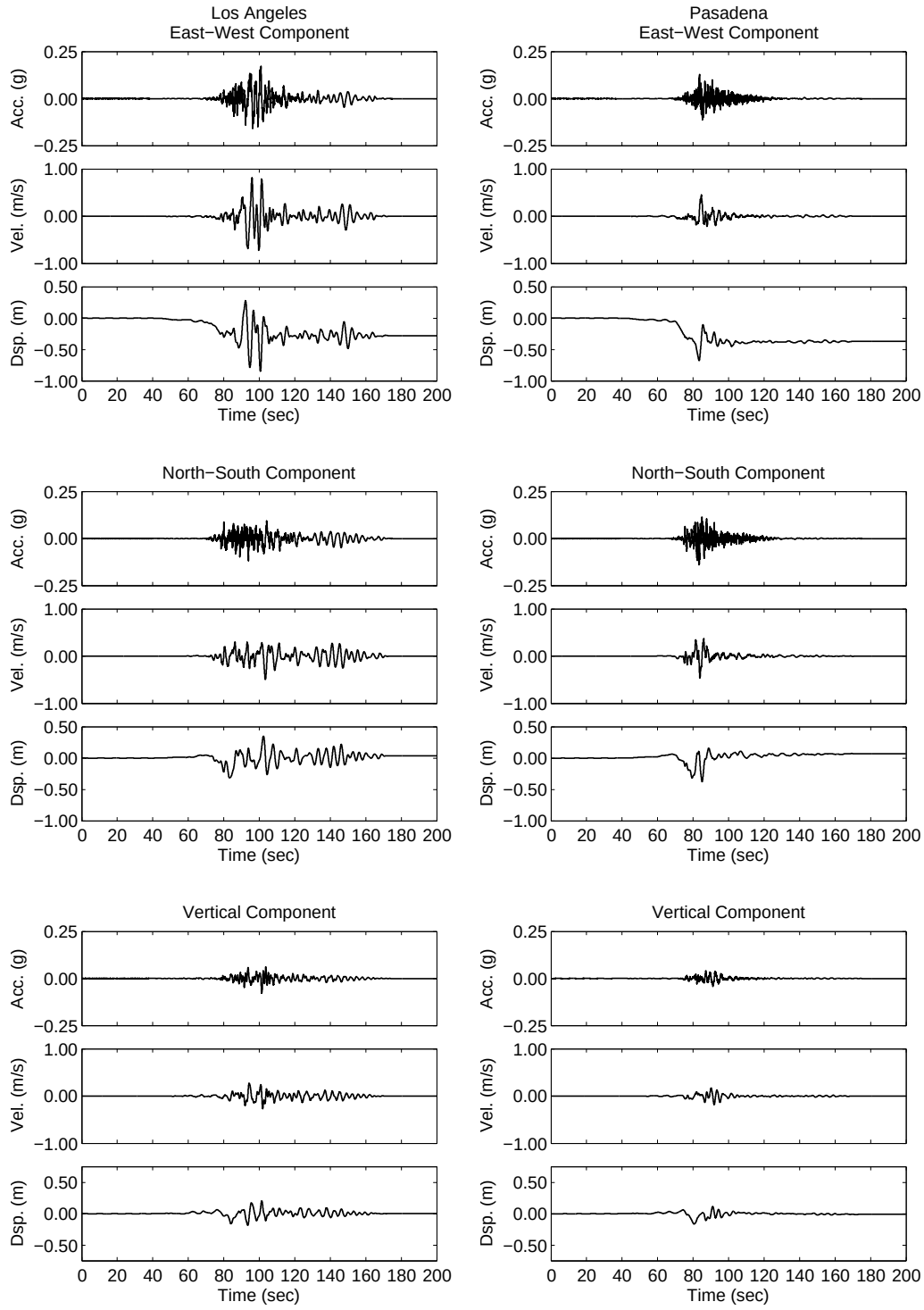

Figure 4.7: East-west, north-south, and vertical component ground acceleration, velocity, and displacement time histories realized in Los Angeles and Pasadena in the ShakeOut scenario earthquake.

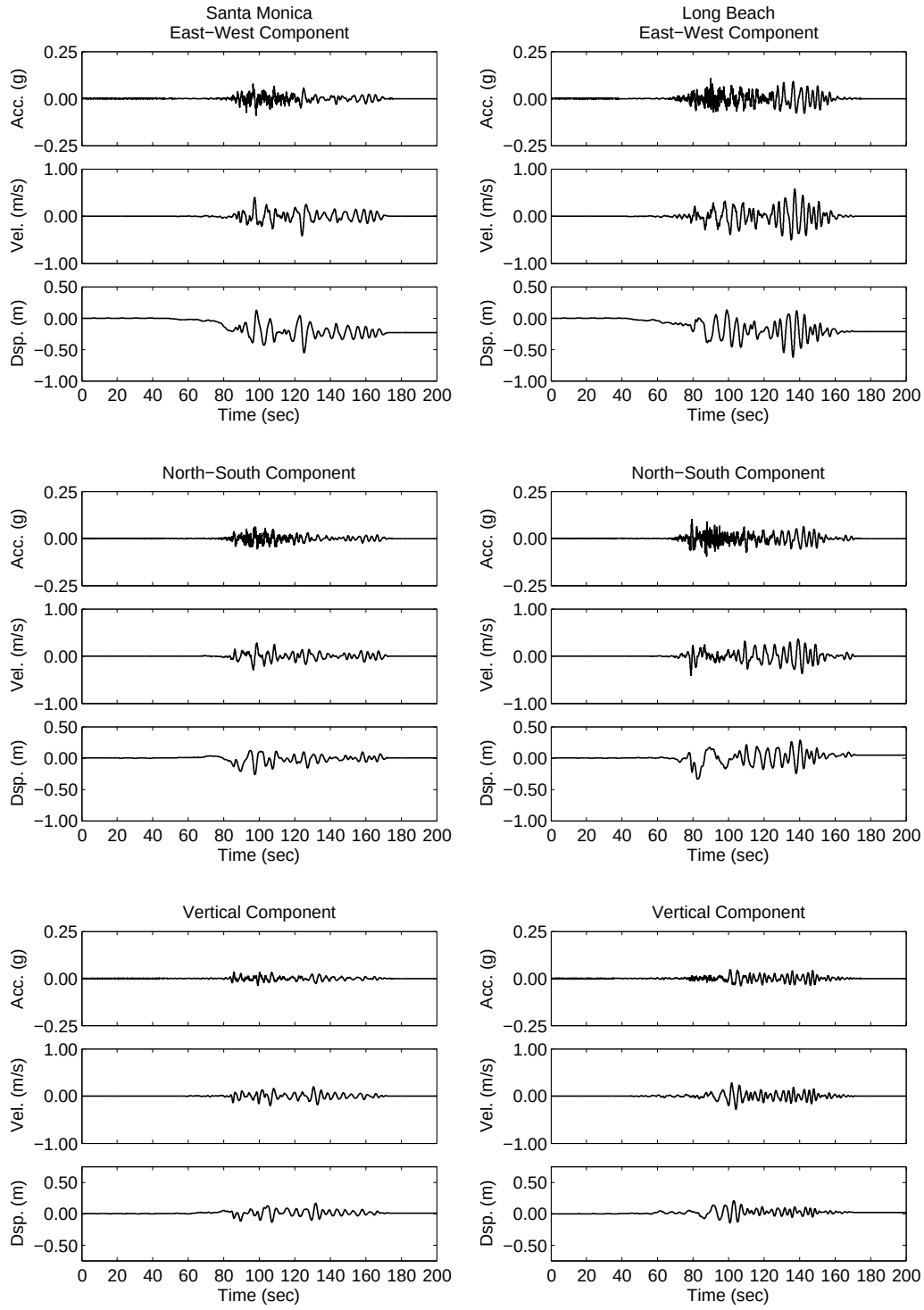

Figure 4.8: East-west, north-south, and vertical component ground acceleration, velocity, and displacement time histories realized in Santa Monica and Long Beach in the ShakeOut scenario earthquake.

4.3 M_w 7.2 Puente Hills Earthquake

The Puente Hills fault system lies directly beneath downtown Los Angeles. It is composed of three segments: a northern segment, referred to as the Los Angeles segment, and two southern segments (shown as one segment in Figure 4.9), referred to as the Santa Fe and Coyote hills segments. The geometry and the slip rate of the system were mapped by Shaw et al. [65], and Dolan et al. [12] identified four large (M_w 7.2-7.5) paleoearthquakes that had occurred on the fault system.

The Puente Hills earthquake simulations are based on the original parameterization presented by Graves and Somerville [30], with the rupture details updated to be consistent with the methodology of Graves and Pitarka [29]. Graves and Somerville considered three hypothetical earthquakes on the Puente Hills fault system, and simulated broadband (0 - 10 Hz) ground motion time histories over a uniform grid of 66,000 sites covering most of the greater Los Angeles metropolitan area. The first scenario (R-1) considered a rupture on the Los Angeles segment only and resulted in a magnitude M_w 6.7. The second scenario considered a rupture of the entire fault system resulting in a magnitude M_w 7.2. The third scenario considered the same fault segments as R-2 but was designed to represent a low dynamic stress drop event. It resulted in significantly lowered ground motion levels while maintaining the same slip distribution and total moment.

In this study, we consider the second scenario (R-2) and a subset of 587 sites in the greater Los Angeles metropolitan area. Each site represents an area of 9 km^2. Similar to the ShakeOut scenario, the ground motions simulations applied a hybrid procedure by Graves and Pitarka [28, 29]. It combines a deterministic approach at long periods ($T > 1$ sec) with a semi-stochastic approach at short periods ($T < 1$ sec). The calculations of the long period part of the ground motions use a 3-D viscoelastic, finite difference algorithm [10, 24] with 3-D velocity structure derived from the SCEC Community Velocity Model,version S4.0. The short period part of the ground motions is obtained using a methodology that sums the response of each subfault assuming a random phase, a wave-number squared source spectrum, and simplified Green's functions [28].

Amplification due to site-specific geology is considered through application of frequency-dependent, nonlinear amplification factors based on V_{S30} [26]. V_{S30} is the travel-time-weighted shear speed in the upper 30 m at a given site.

In Figure 4.9, a map of the greater Los Angeles metropolitan area is presented, showing the locations of the subset of 587 sites from the Puente Hills earthquake scenario simulations considered in this study, where ground motion time histories are generated and the building models are

analyzed. The extent of the Puente Hills fault system is indicated by red rectangles. Maps of peak ground acceleration (PGA), peak ground velocities (PGV), and peak ground displacements (PGD) realized in the earthquake scenario are shown for EW and NS directions in Figure 4.10. Peak ground velocities are in the range of 0.25-0.75 m/s in the San Fernando Valley, 1-2 m/s in the Los Angeles basin, and 0.5-2.0 m/s in the San Gabriel Valley. Ground acceleration, velocity, and displacement time-histories for four sites located near downtown Los Angeles, Pasadena, Santa Monica, and Long Beach are shown in Figures 4.11 and 4.12.

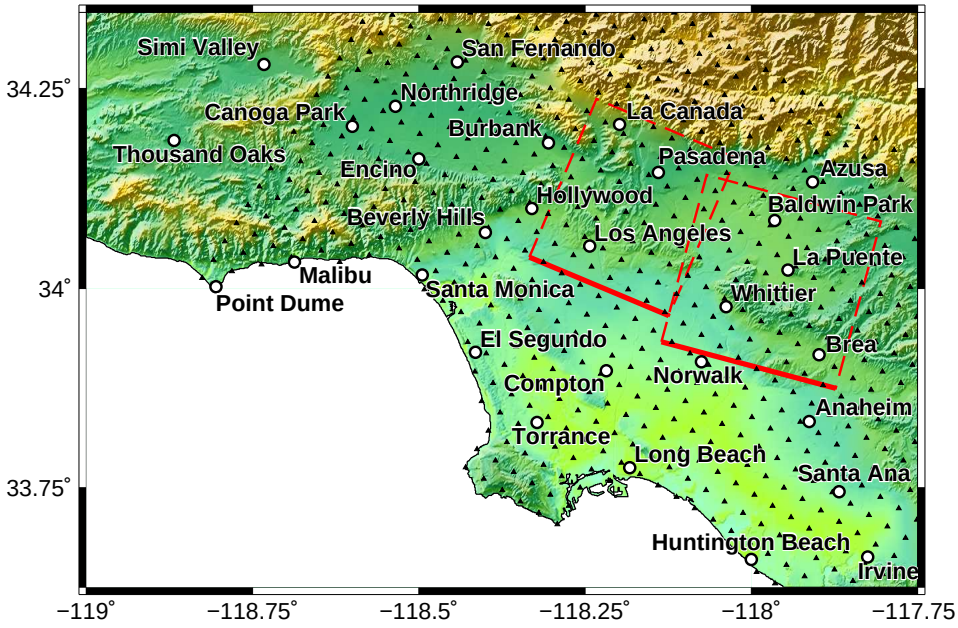

Figure 4.9: Geographic scope of the subset of 587 sites from the Puente Hills earthquake scenario simulations considered in this study. Black triangles represent sites where ground motion time histories are generated and the building models are analyzed. The color scheme reflects topography with green representing low elevation and yellow representing high elevations. The extent of the Puente Hills fault system is indicated by red rectangles. The upper rectangle represents the Los Angeles segment and the lower rectangle represents the Santa Fe and Coyote Hills segments.

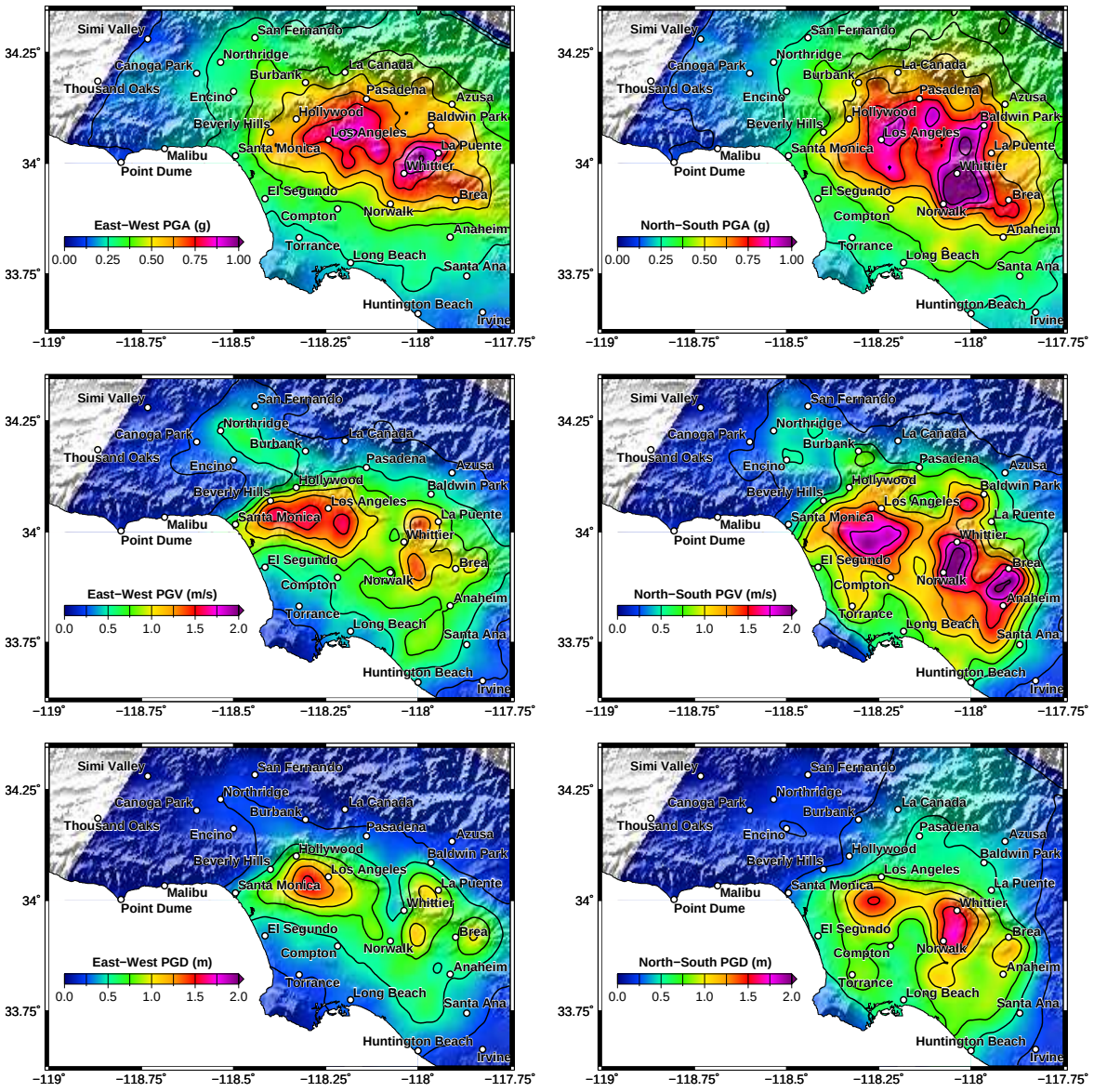

Figure 4.10: Peak ground accelerations (PGA), peak ground velocities (PGV), and peak ground displacements (PGD) realized in the greater Los Angeles metropolitan area for the east-west and north-south directions in the simulated earthquake scenario (R-2) on the Puente Hills fault system.

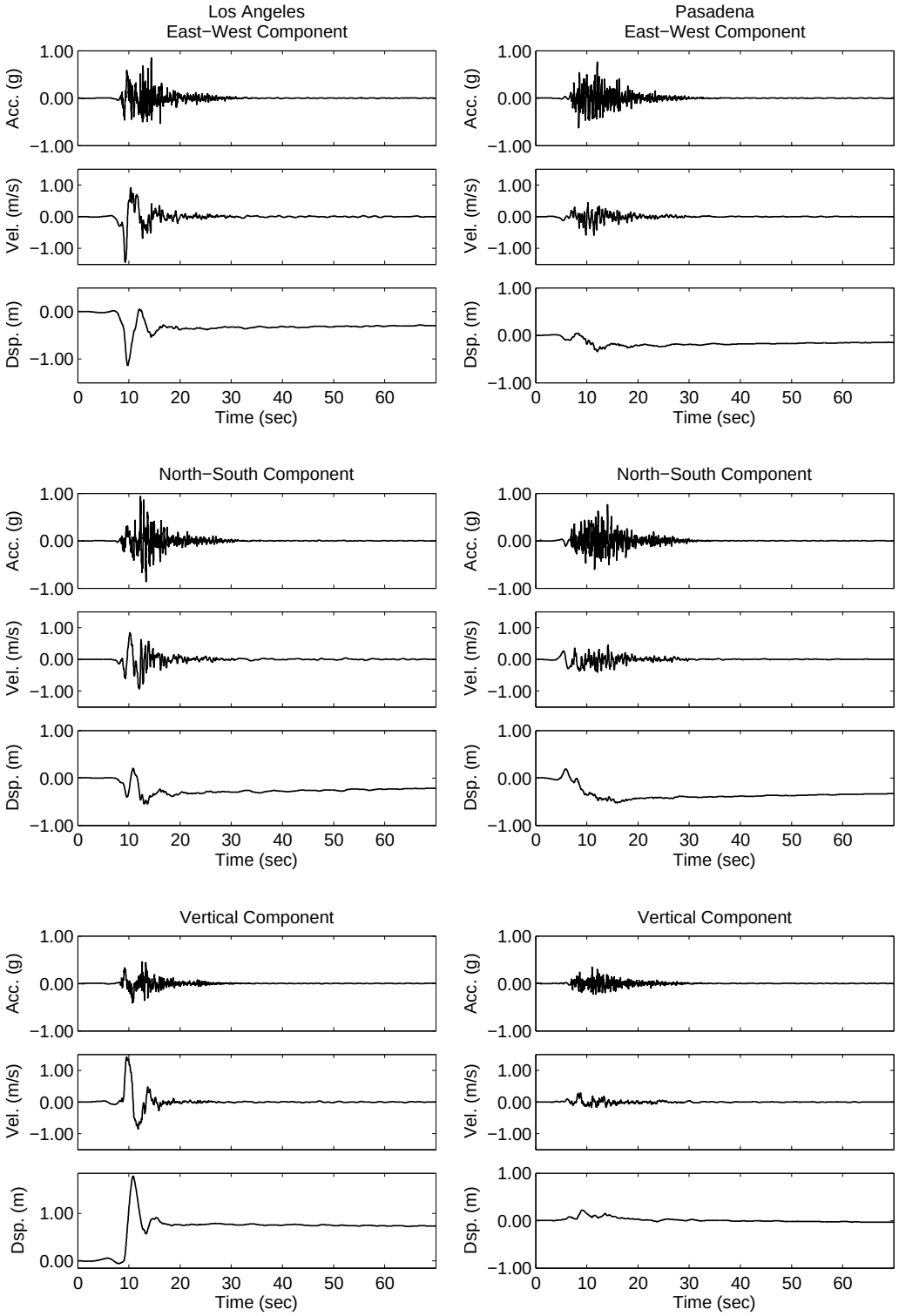

Figure 4.11: East-west, north-south, and vertical component ground acceleration, velocity, and displacement time histories realized in Los Angeles and Pasadena in the earthquake scenario on the Puente Hills fault system.

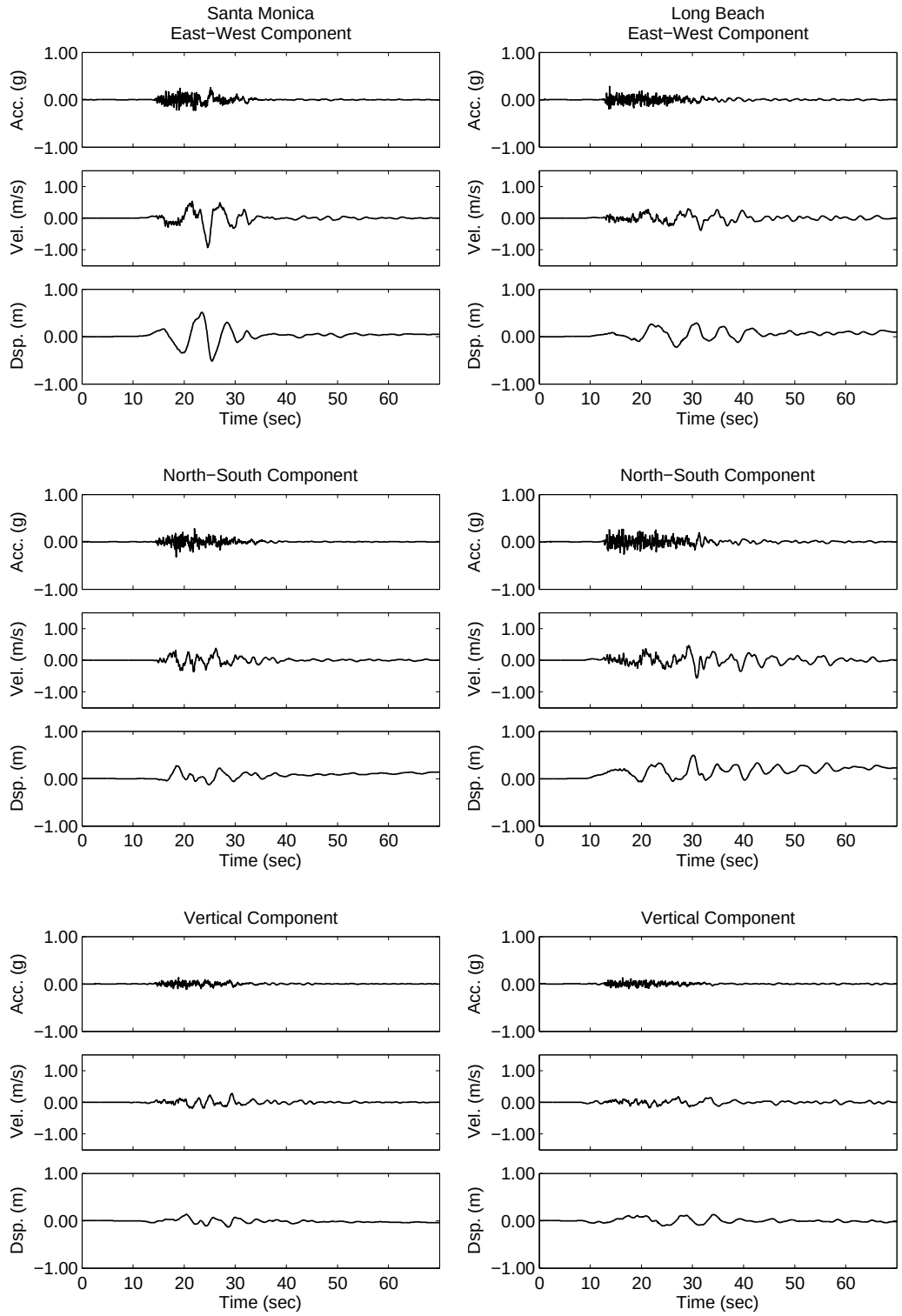

Figure 4.12: East-west, north-south, and vertical component ground acceleration, velocity, and displacement time histories realized in Santa Monica and Long Beach in the earthquake scenario on the Puente Hills fault system.

4.4 Recorded Real Strong Ground Motions

A collection of twenty recorded ground motion time histories from eleven actual earthquakes is applied in incremental analyses of the building models. Each ground motion record consists of a fault-normal and a fault-parallel component, and all but one, the record from the Superstition Hills earthquake, includes a vertical component as well. In the incremental analyses the fault-normal and vertical components (if available) are scaled with scaling factors ranging from 0.6 to 2.0 with increments of 0.2. The scaled ground motion time histories are then applied to the building models. The recorded ground motion time histories are listed in Table 4.1. Unscaled fault-normal and vertical component ground acceleration, velocity and displacement time histories and associated 5% damped pseudo-acceleration response spectra are presented in Figures 4.13 through 4.21.

Table 4.1: List of the ground motion records from actual earthquakes applied to the building models in the incremental dynamic analyses.

Event	**Location**	**Year**	**Moment Magnitude**	**Station/Record**	**PGV*** **(m/s)**	**Figure**
Cape Mendocino	CA, USA	1992	7.2	Petrolia	1.33	4.13
Chi-Chi	Taiwan	1999	7.6	CWBC101	1.07	4.13
				CWBT063	0.83	4.14
				CWBT120	0.62	4.14
				TCU052	1.83	4.15
				TCU068	2.80	4.15
Denali	AK, USA	2002	7.9	Pump Station #10	1.09	4.16
Imperial Valley	CA, USA	1979	6.5	El Centro Array #6	1.13	4.16
				El Centro Array #7	1.13	4.17
				Meloland Overpass	0.95	4.17
Kobe	Japan	1995	6.9	JMA	1.07	4.18
				Takatori	1.54	4.18
Landers	CA, USA	1992	7.3	Lucern Valley	1.47	4.19
Loma Prieta	CA, USA	1989	6.9	Lexington Dam	1.19	4.19
				Los Gatos Presentation Center	1.05	4.20
Northridge	CA, USA	1994	6.7	Rinaldi	1.63	4.20
				Sylmar	1.32	4.21
San Fernando	CA, USA	1971	6.6	Pacoima Dam	1.15	4.21
Superstition Hills	CA, USA	1987	6.7	Superstition Mountain	1.12	4.22
Tabas (Iran)	Iran	1978	7.4	Tabas	1.28	4.22

* Fault-normal component.

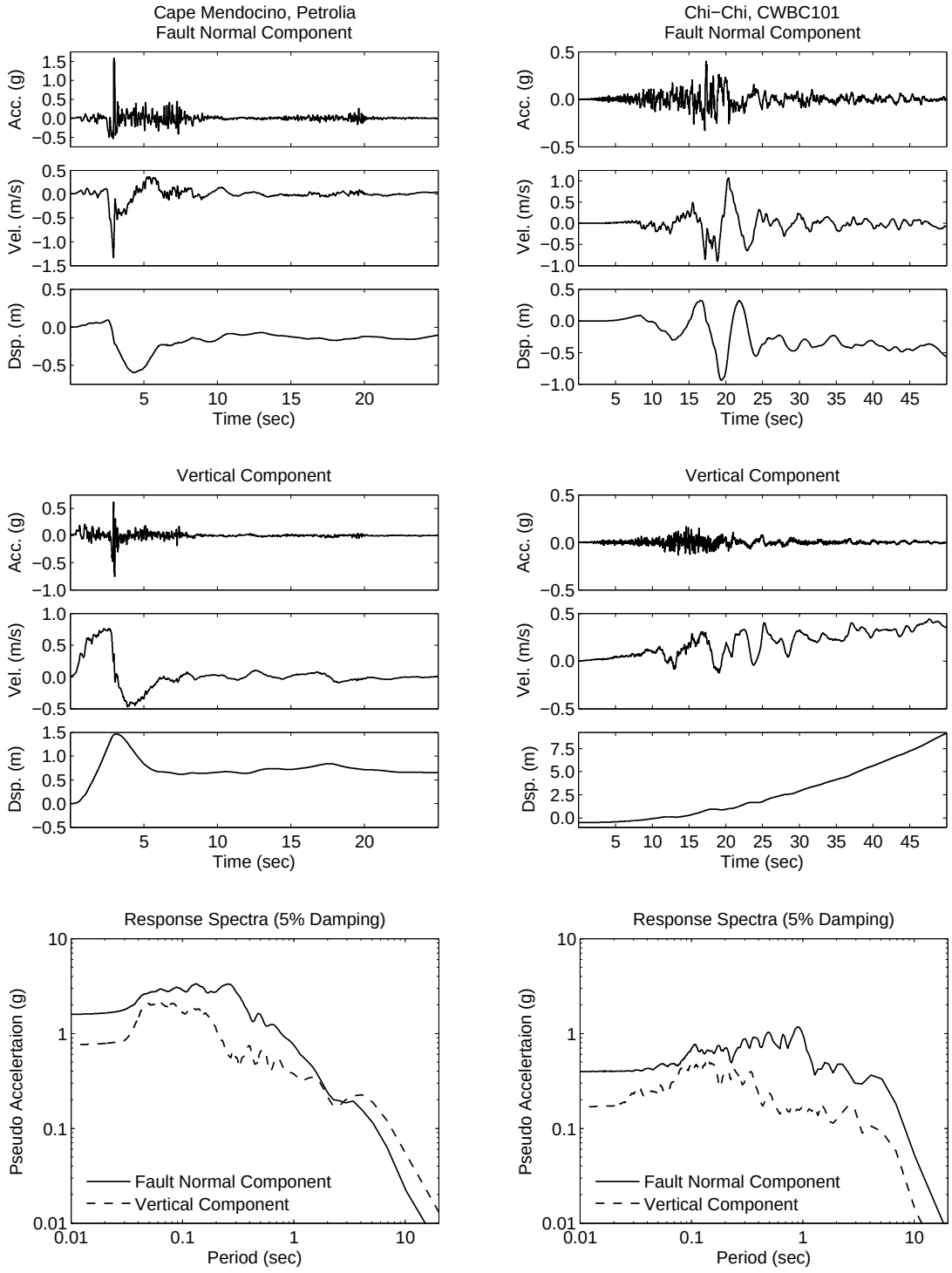

Figure 4.13: Unscaled fault-normal and vertical component ground acceleration, velocity, and displacement time histories and associated 5% damped pseudo-acceleration response spectra from the Cape Mendocino earthquake, Petrolia station, and the Chi-Chi earthquake, CWBC101 station.

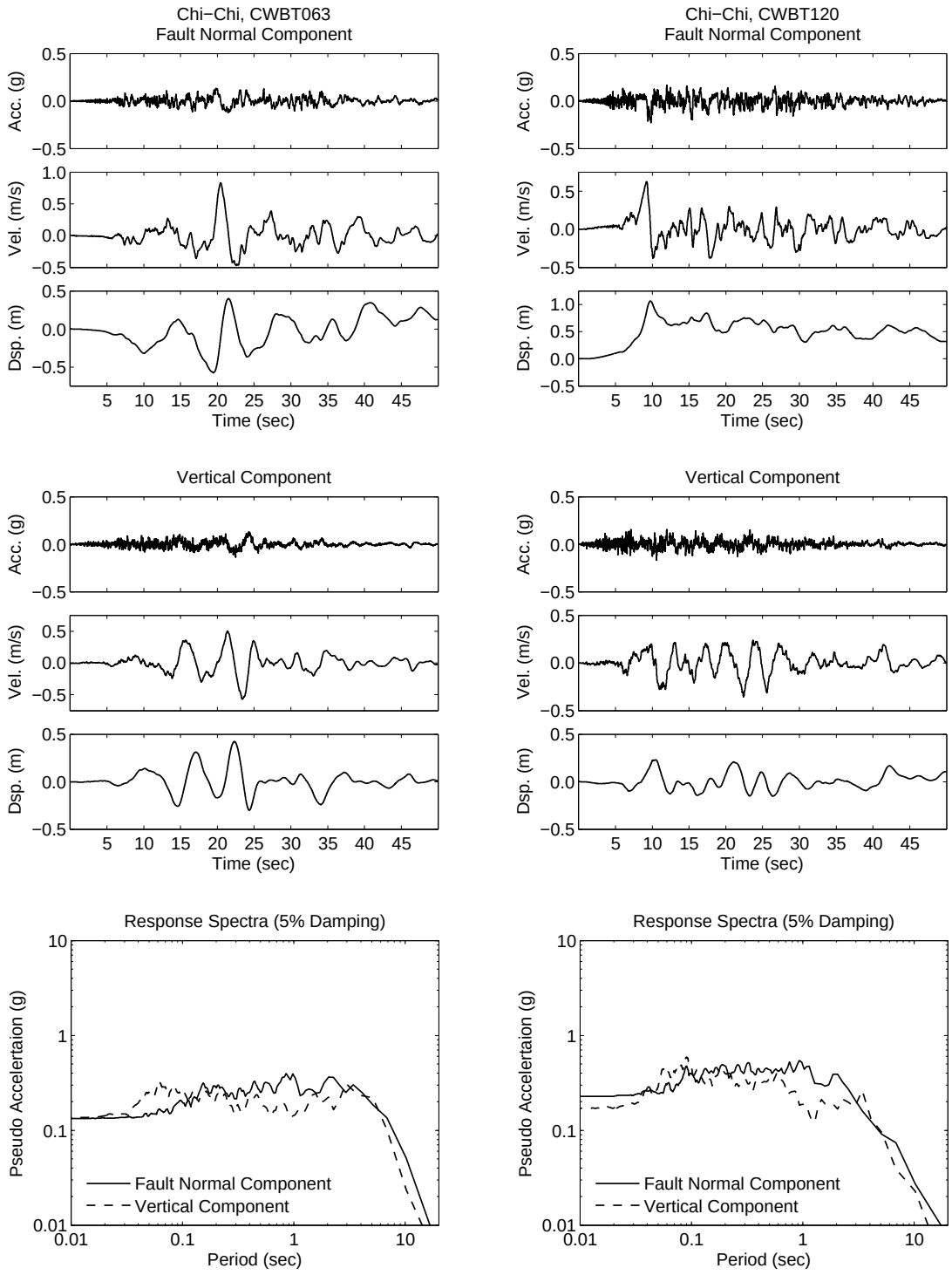

Figure 4.14: Unscaled fault-normal and vertical component ground acceleration, velocity, and displacement time histories and associated 5% damped pseudo-acceleration response spectra from the Chi-Chi earthquake, CWBT063 and CWBT120 stations.

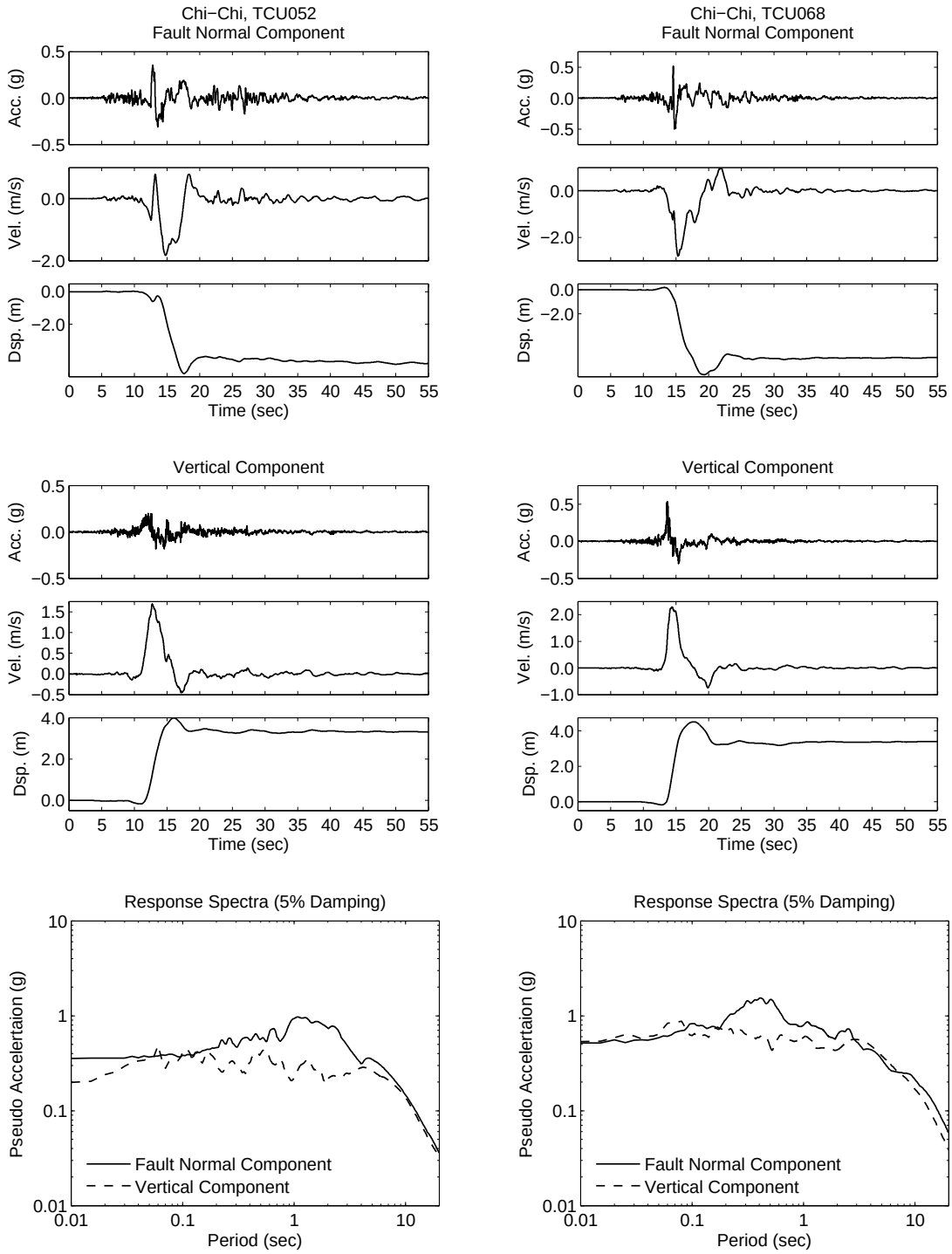

Figure 4.15: Unscaled fault-normal and vertical component ground acceleration, velocity, and displacement time histories and associated 5% damped pseudo-acceleration response spectra from the Chi-Chi earthquake, TCU052 and TCU068 stations.

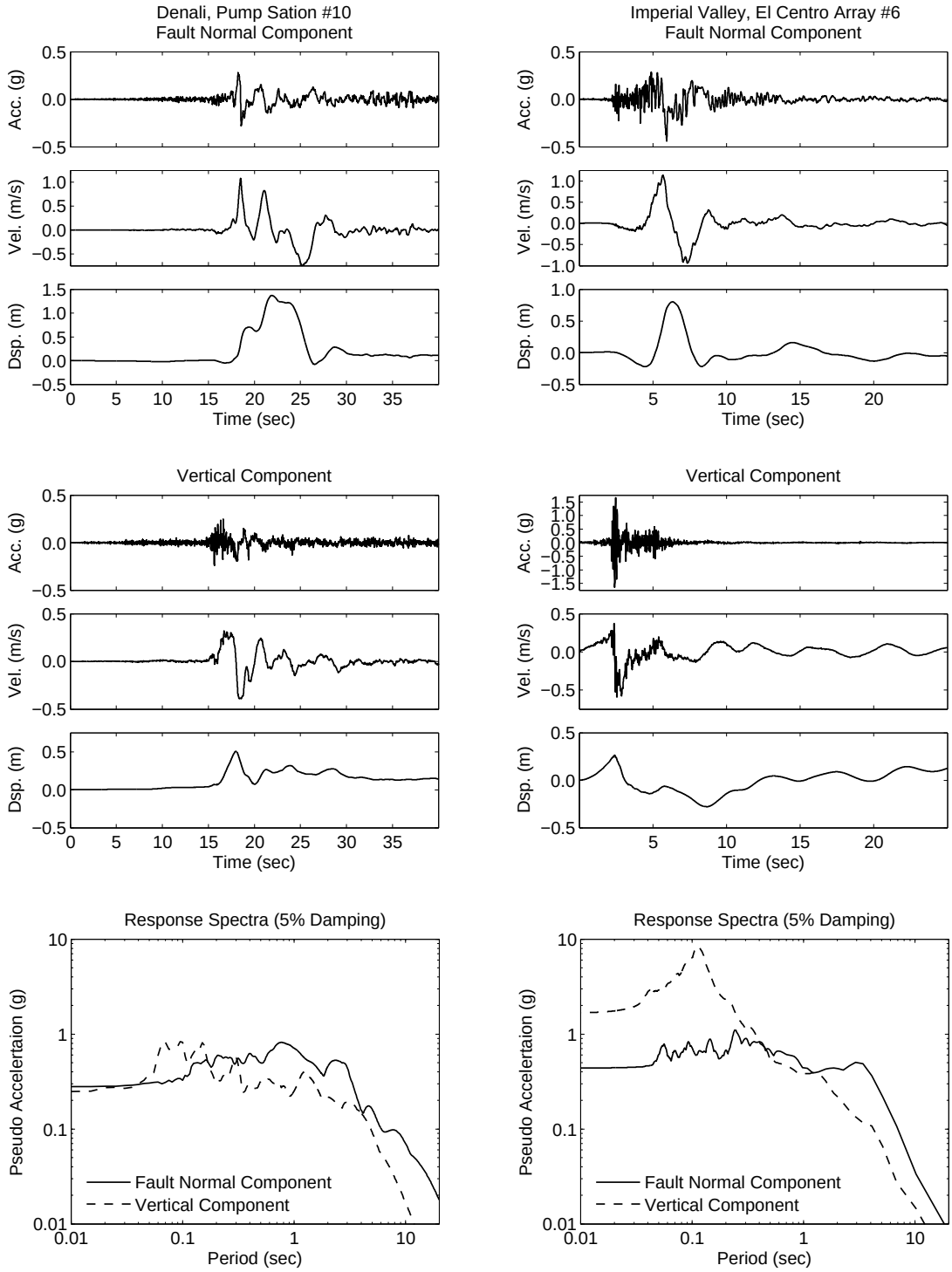

Figure 4.16: Unscaled fault-normal and vertical component ground acceleration, velocity, and displacement time histories and associated 5% damped pseudo-acceleration response spectra from the Denali earthquake, PS #10 station, and the El Centro earthquake, Array #6 station.

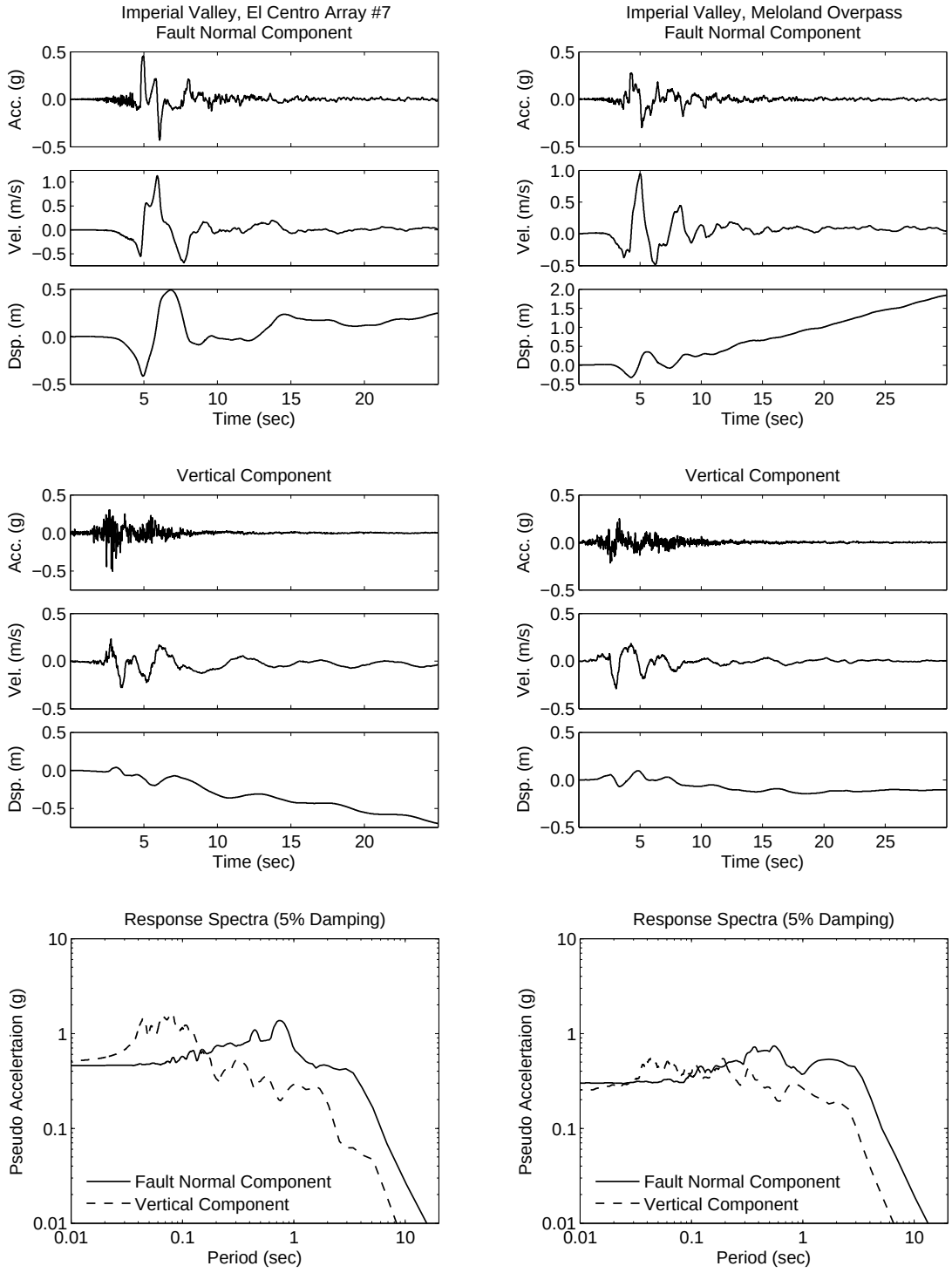

Figure 4.17: Unscaled fault-normal and vertical component ground acceleration, velocity, and displacement time histories and associated 5% damped pseudo-acceleration response spectra from the El Centro earthquake, Array #7 and Meloland Overpass stations.

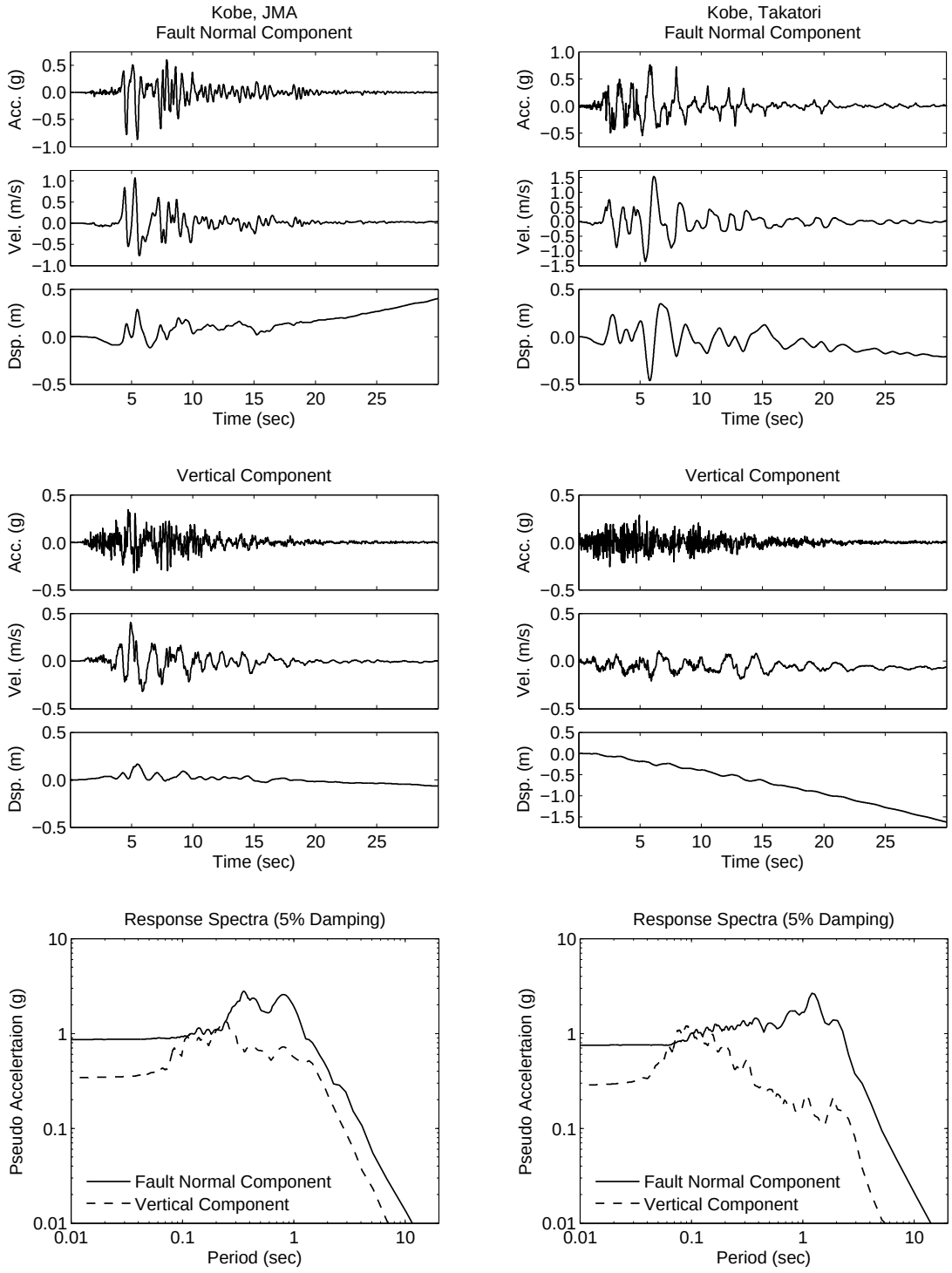

Figure 4.18: Unscaled fault-normal and vertical component ground acceleration, velocity, and displacement time histories and associated 5% damped pseudo-acceleration response spectra from the Kobe earthquake, JMA and Takatori stations.

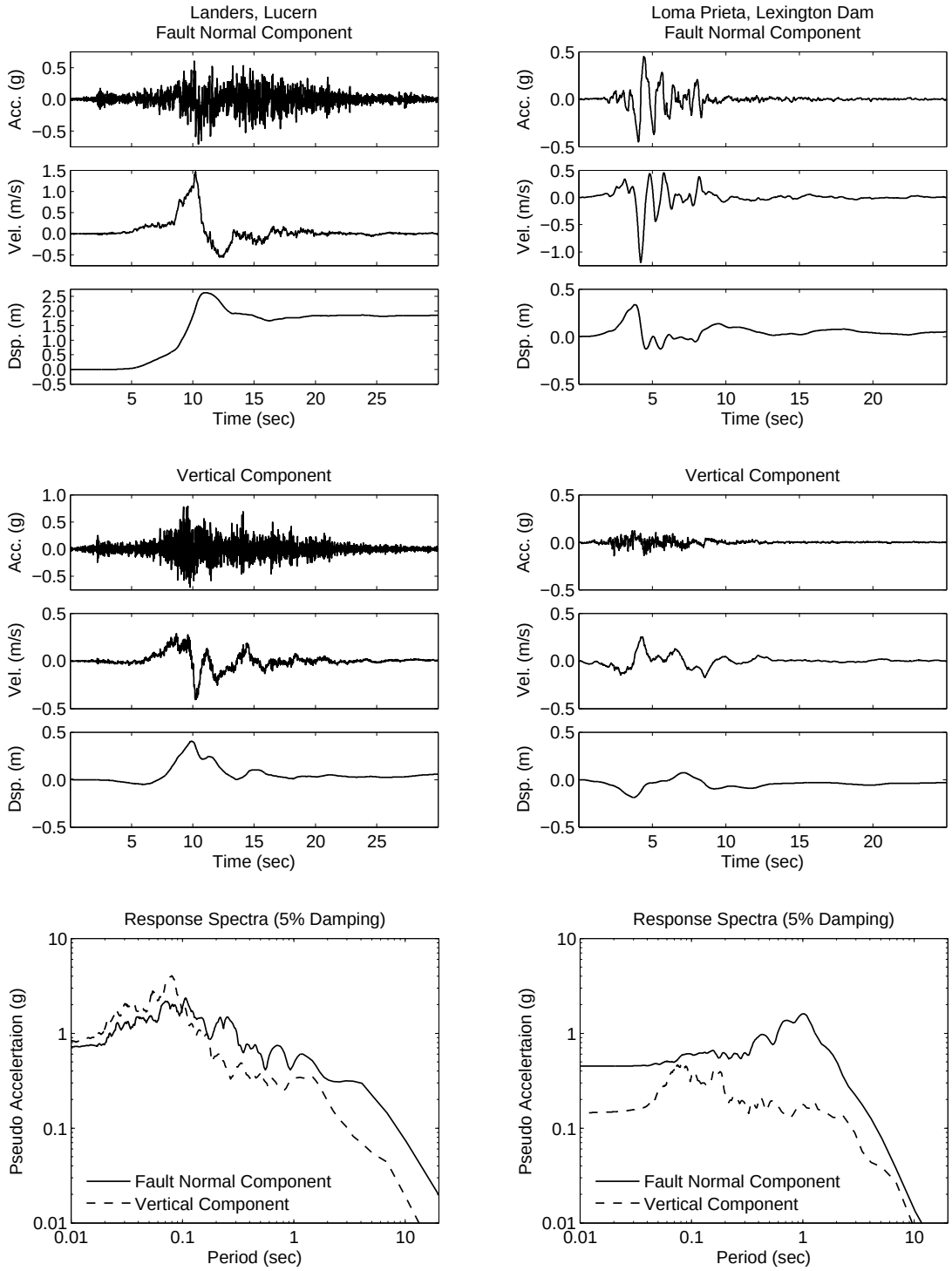

Figure 4.19: Unscaled fault-normal and vertical component ground acceleration, velocity, and displacement time histories and associated 5% damped pseudo-acceleration response spectra from the Landers earthquake, Lucern Valley station, and the Loma Prieta earthquake, Lexington dam station.

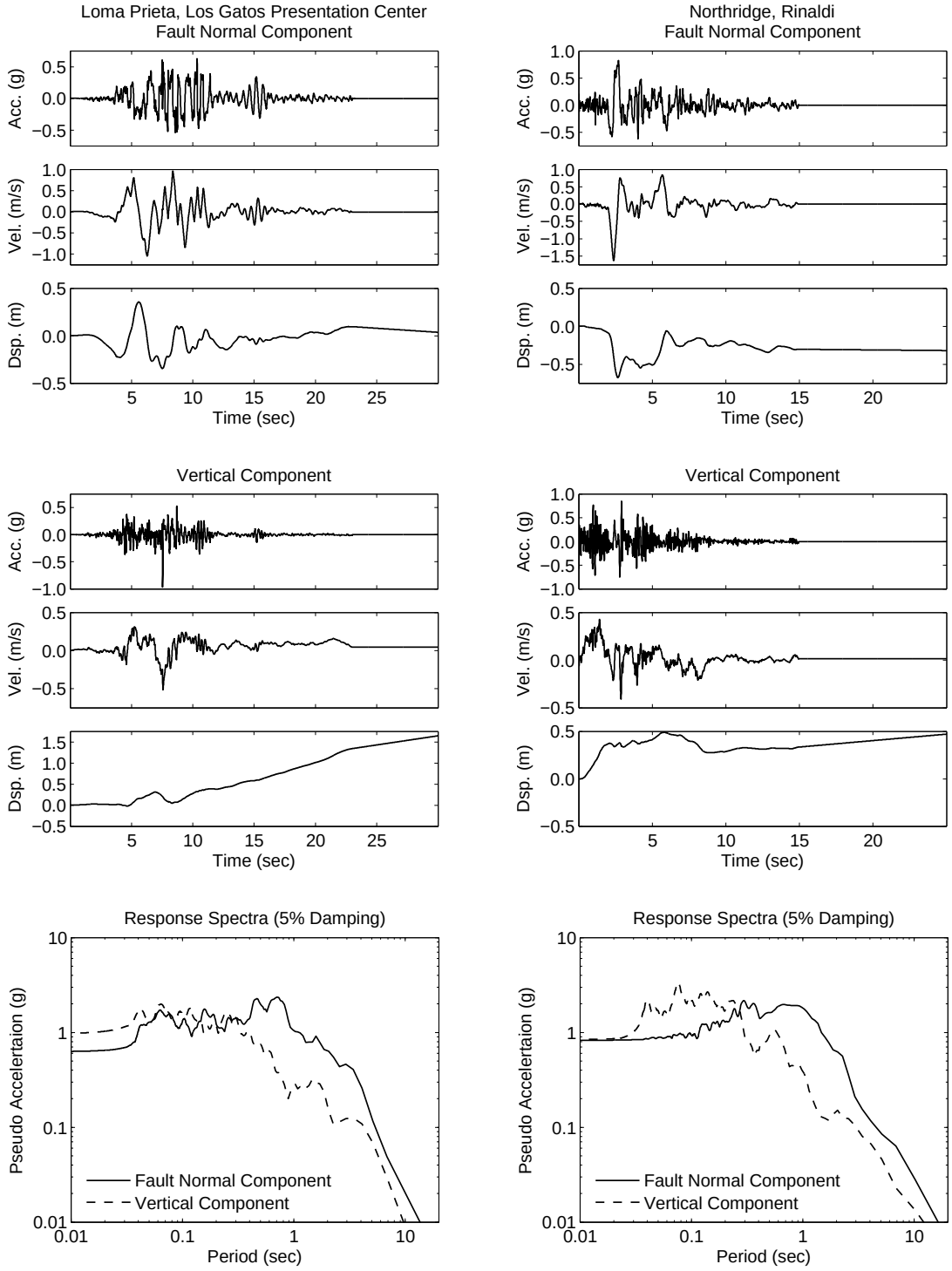

Figure 4.20: Unscaled fault-normal and vertical component ground acceleration, velocity, and displacement time histories and associated 5% damped pseudo-acceleration response spectra from the Loma Prieta earthquake, Los Gatos presentation center station, and the Northridge earthquake, Rinaldi station.

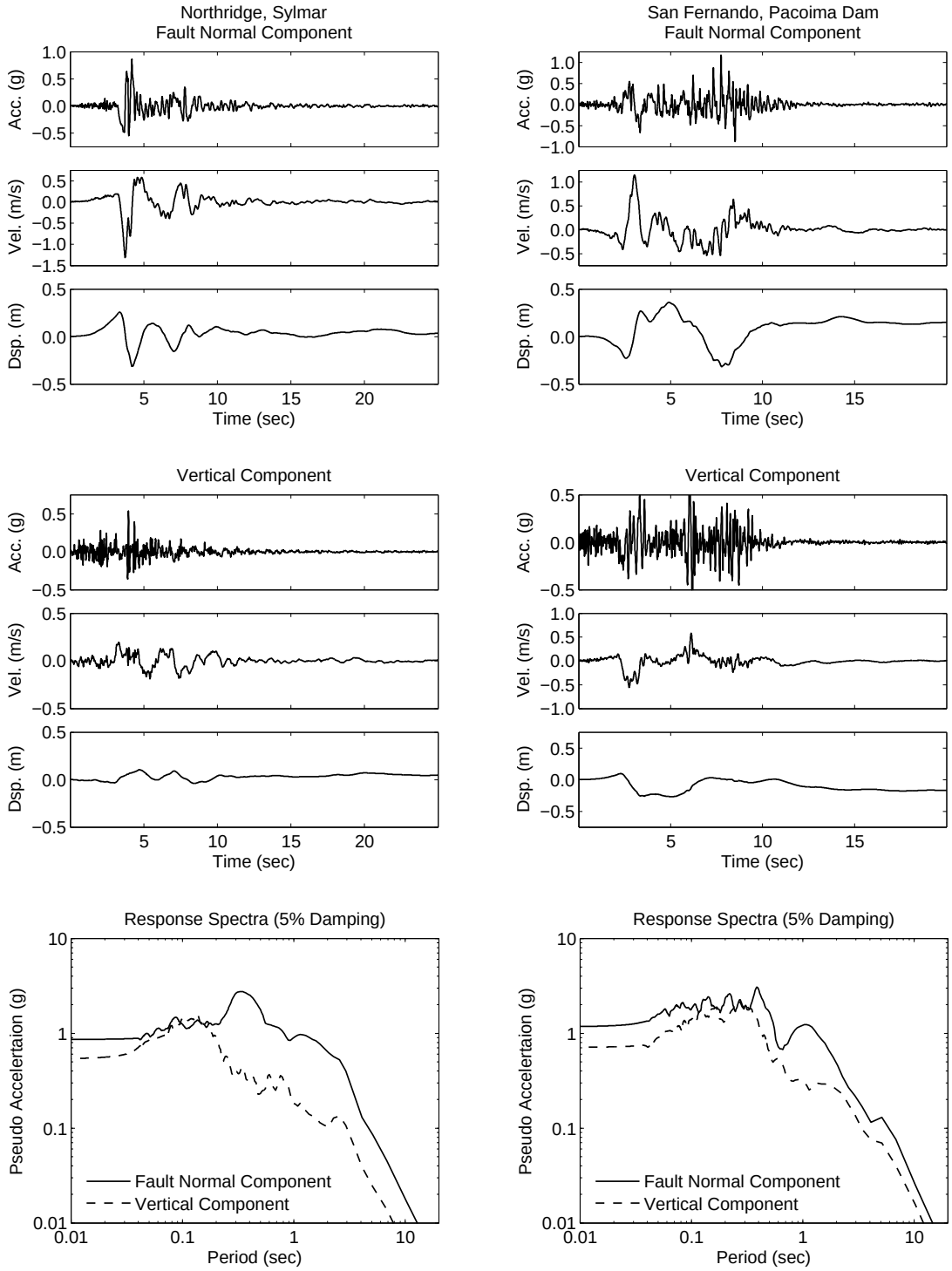

Figure 4.21: Unscaled fault-normal and vertical component ground acceleration, velocity, and displacement time histories and associated 5% damped pseudo-acceleration response spectra from the Northridge earthquake, Sylmar station, and the San Fernando earthquake, Pacoima Dam station.

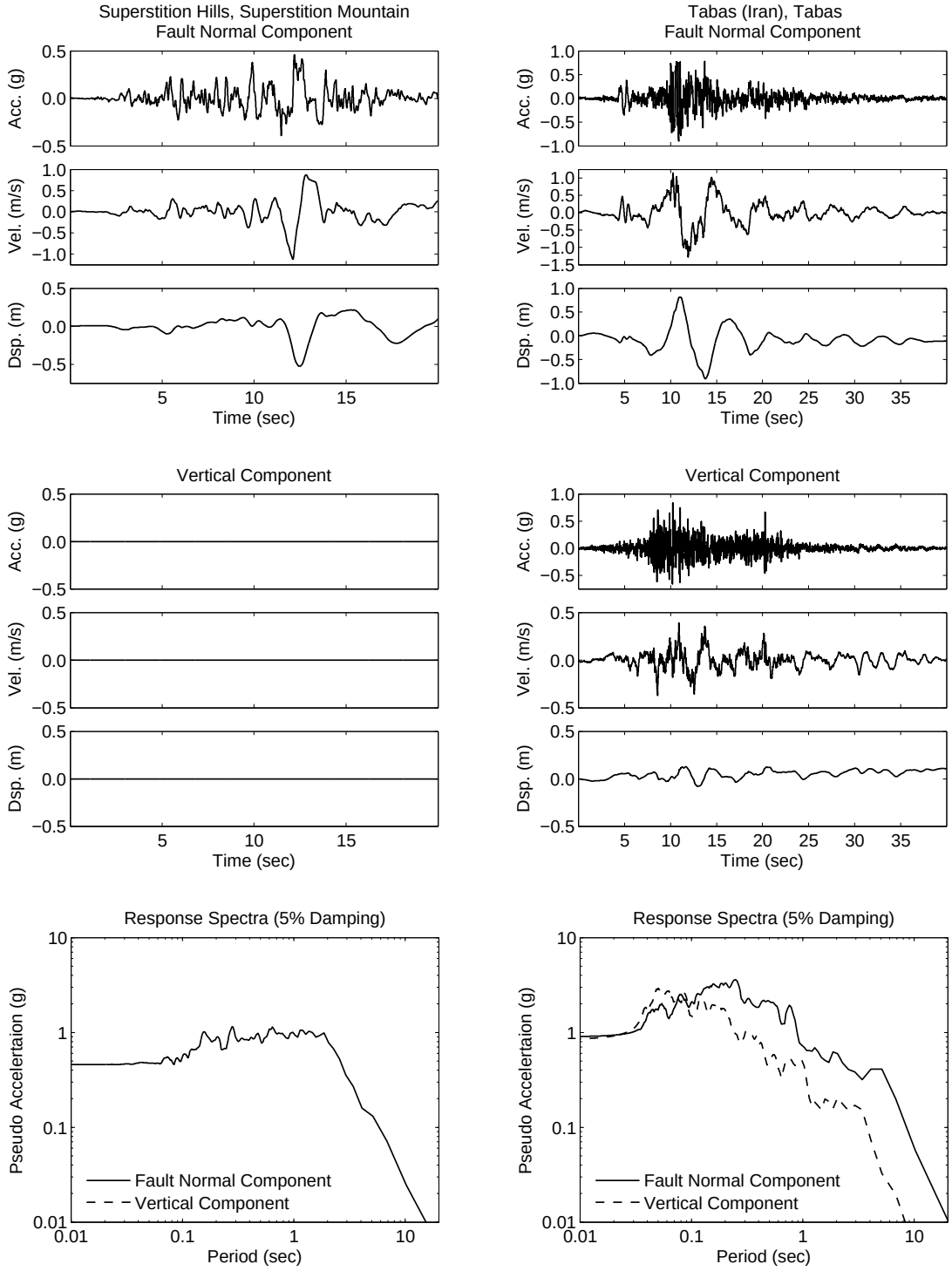

Figure 4.22: Unscaled fault-normal and vertical component ground acceleration, velocity, and displacement time histories and associated 5% damped pseudo-acceleration response spectra from the Superstition Hills earthquake, Superstition Mountain station, and the Tabas (Iran) earthquake, Tabas station.

Chapter 5

Results

All thirteen building models are analyzed for the ground motions described in the previous chapter. Simulated building performance is cataloged into four performance categories: “immediate occupancy”, “repairable”, “unrepairable”, and “collapse”. The distinction of the performance categories is drawn from simulated residual inter-story drift ratio (IDR), residual building overall drift ratio (ODR), and residual foundation rotation angle.

Inter-story drift ratio refers to the ratio of relative horizontal displacement of two adjacent floors and the height of the story defined by the two floors. Building overall drift ratio refers to the ratio of the horizontal roof displacement relative to the horizontal displacement at ground level and the height of the building above ground. Foundation rotation angle is measured as the angle made by the basement level walls and horizonal. The concrete walls at the basement level are rigid in comparison to the upper structure and the foundation springs. As a result, they primarily rotate as a rigid body as opposed to deforming in shear. Inter-story drift ratio and building overall drift ratio are corrected for floor incline. Inclination at floor levels can result from either rotation of the foundation or accumlated lengthening of columns in tension and shortening of columns in compression.

“Immediate occupancy” performance category is defined in FEMA 356 [17] as building performance where residual drift is negligible and the structure retains its original strength and stiffness. In the present work, “immediate occupancy” category is assumed if residual inter-story drift and residual foundation rotation angle is less than $\frac{1}{2000}$.

The next concern is whether the simulated building responses would indicate structural damage beyound economical repair. Iwata et al. [39] analyzed twelve steel frame buildings that suffered damage in the 1995 Kobe earthquake in Japan and established limits on residual deformation beyond which a building would not be repaired but demolished. In the study two sets of “repairability limits” are presented: one based on whether rehabilitation could be achieved “without any difficult

straightening repair construction or large-scale reinforcing construction" (if residual inter-story drift ratio exceeds $\frac{1}{71}$, or if residual overall building drift exceeds $\frac{1}{110}$), and the second based on direct and indirect repair cost to the building owner (if residual inter-story drift ratio exceeds $\frac{1}{90}$, or if residual overall building drift exceeds $\frac{1}{200}$).

McCormick et al. [53] studied one occupied building at Kyoto University in Japan and performed a review of previous research in Japan, including considerations of psychological and physiological effects of residual drifts on occupants. They concluded that incline of floors or tilt of vertical elements of $\frac{1}{200}$ are generally perceivable by occupants, and occupants of a building experience dizziness and nausea as the incline or tilt approaches $\frac{1}{100}$.

In the present work a building model is deemed "unrepairable" if residual inter-story drift ratio exceeds $\frac{1}{71}$, or if residual overall building drift exceeds $\frac{1}{110}$, or if foundation residual rotation angle exceeds $\frac{1}{200}$. A building model is assumed "repairable" if residual deformations are in between "immediate occupancy" and "unrepairable". Finally, "collapse" is defined as the complete loss of the lateral force-resisiting system. The performance categories are summarized in Table 5.1. This grading scheme is similar to the methodology presented by Olsen et al. [59].

Table 5.1: Performance categories used to catalog simulated model performance, and associated limits on selected model response parameters used to distinguish between them.

Performance Category	Residual IDR Limit	Residual ODR Limit	Residual Foundation Tilt Limit
Immediate Occcupancy	$\frac{1}{2000}$	N/A	$\frac{1}{2000}$
Repairable	$\frac{1}{71}$	$\frac{1}{110}$	$\frac{1}{200}$
Unrepairable			
Collapse	Complete loss of the lateral force-resisting system.		

The results in the simulated scenario earthquakes (sections 5.1, 5.2, and 5.3) are presented in three types of graphics: bar plots that summarize the number of simulations for each building model that resulted in the "repairable", "unrepairable", and "collapse" performance categories; fragility plots that show the probability of the building models realizing the "repairable" performance category or worse, the "unrepairable" performance category or worse, or model collapse, given horizontal peak ground velocity; and maps that geographically show for each building model the distribution of simulated performance categories in the greater Los Angeles metropolitan area.

The fragility plots are constructed by sorting the data into bins based on horizontal peak ground velocities. For each bin, the fraction of the simulations that exceed a particular performance category

is calculated. Then, a cumulative log-normal distribution function is fitted to the data by using a method of least squares. In some instances, the data is not well represented by a cumulative log-normal distribution function, and the calculated fractions of the simulations that exceeded that particular performance category are plotted instead, with the data points alligned at the median velocity of each bin.

The results in the incremental dynamic analyses using recorded ground motions from actual earthquakes (section 5.4) are presented in two types of graphics: bar plots that summarize the number of simulations for each building model that resulted in the "repairable", "unrepairable", and "collapse" performance categories; and in table-figures that show the simualted performance cateogries for each of the ground motion records and the range of applied ground motion scaling factors.

In Section 5.5 the data is gathered from all three simulated scenario earthquakes, and from the incremental dynamic analyses using recorded ground motions from actual earthquakes, and the number of simulations that resulted in "repairable", "unrepairable", and "collapse" performance categories for each building model are summarized in bar plots. Also, the data from all three simulated earthquake scenarios is used to construct fragility plots that show the probability of the building models realizing the "repairable" performance category or worse, the "unrepairable" performance category or worse, or model collapse, given horizontal peak ground velocity.

In Section 5.6 the most frequently observed collapse mechanisms in the builing models are described.

Some simulations failed to converge before showing a clear sign of model collapse. Those simulations are labeled as "non-convergent", and are presented where they occur. In addition, the "non-convergent" simulations are removed from the dataset before fragility plots are constructed.

5.1 Building Performance: M_w 7.9 1857-Like San Andreas Fault Earthquake

The results in the simulated 1857-like San Andreas fault earthquake scenario are presented in three types of graphics. The number of simulations that resulted in the "repairable", "unrepairable", and "collapse" performance categories is summarized in Figure 5.1. Fragility plots that show the probability of the building models realizing "repairable" performance category or worse, "unrepairable" performance category or worse, or model collapse, given horizontal peak ground velocity are presented in Figures 5.2, 5.3, and 5.4, respectively. Finally, maps that geographically show the distribution of simulated performance categories in the greater Los Angeles metropolitan area for each building model are presented in Figures 5.5 to 5.17 as follows:

	Figure:		Figure:
Base Line Model	5.5	RBR-1	5.12
RMF-1h	5.6	RBR-2	5.13
RMF-1	5.7	RBR-3	5.14
RMF-2h	5.8	RBRB-1	5.15
RMF-2	5.9	RBRB-2	5.16
RMF-3h	5.10	RBRB-3	5.17
RMF-3	5.11		

When employing the "expected" foundation model, the base line model is simulated to collapse at 226 sites (out of 636) when the building model is oriented in the east-west direction and at 200 sites when oriented in north-south. Each site represents an area of 10 km^2. A majority of these sites are located in the San Fernando Valley and to the east of the San Fernando Valley, but model collapse is also simulated at a number of sites near Santa Monica and throughout the Los Angeles and San Gabriel basins. Furthermore, complete economic loss ("unrepairable" or "collapse" performance categories) of the base line model is simulated at 278 sites when the building model is oriented in the east-west direction, and at 252 sites when oriented in north-south.

Retrofit schemes RBR-2, RBRB-1, and RBRB-2 achieve the greatest reduction in number of simulated collapses, or to a range of 68-75 sites when the building models are oriented in the east-west direction and to only a few sites (1-4) when oriented in north-south. Retrofit scheme RBR-1 is simulated to collapse at a slightly greater number of sites. Scheme RBR-1 is observed to

localize deformations in a few stories just above the 8th story, or where the bracing configuration is tapered. In contrast, schemes RBR-2, RBRB-1, and RBRB-2 deform more uniformly over the height, resulting in better performance.

As for complete economic losses, scheme RBR-2 performs best, with complete economic losses being simulated at 115 sites when the building model is oriented in the east-west direction, and at 42 sites when oriented in north-south. Complete economic losses of schemes RBR-1, RBRB-1, and RBRB-2 are simulated at a total (both orientations) of 184-194 sites. It appears that braced-frames that employ buckling-restrained braces tend to have greater residual drifts. However, the buckling-restrained braces are likely to store significant residual forces, and the residual drifts may be recovered to some extent by replacing the deformed braces. Conventional brace elements are not expected to store residual forces to the same degree.

Out of the retrofit schemes that consider retrofitting the brittle beam-to-column moment resisting connections (RMF schemes), scheme RMF-3 performs best, with model collapse being simulated at 130 sites when the building model is oriented in the east-west direction, and at 81 sites when oriented in north-south. Furthermore, complete economic loss of the building model is simulated at 155 sites when it is oriented in the east-west direction, and at 113 sites when oriented in north-south. Interestingly, schemes RMF-2h and RMF-2 are simulated to collapse at a total number of sites (both orientations) comparable to scheme RMF-3, but complete economic loss of the building models is simulated at around 300 sites in total. Model collapse and complete economic loss of scheme RMF-3h is simulated at total (both orientations) of 264 and 337 sites, respectively.

These results suggest that at a certain point, upgrading additional beam-to-column connections will result in minimal additional improvement in performance.

The two retrofit schemes that implement brace elements in the lower half of the building model while leaving the upper half unaltered (schemes RBR-3 and RBRB-3) are somewhat successful in that the schemes are more effective in limiting deformations in the lower half of the building model, compared to the moment-frame half-height retrofit schemes (RMF-1h, RMF-2h, and RMF-3h), and thus reduce to a greater extent global P-delta overturning moments. However, the resulting structures are stiffer than the moment-frame configurations and consequently attract larger seismic forces, which often results in excessive drifts in the upper half. A retrofit scheme that implements brace elements in the lower half of the building model in conjunction with upgrading beam-to-column moment connections in the upper half may present some additional improvement in building

performance while keeping architectural impact low. Retrofit schemes RBR-3 and RBRB-3 are simulated to collapse at a total (both orientations) of 275 and 247 sites, respectively, and complete economic loss of the building models is simulated at a total (both orientations) of 348 and 336 sites, respectively.

From the fragility curves constructed from the data, the simulated building performances can be related to horizontal peak ground velocities (PGV). For instance, the base line model realizes a 20% chance of simulated collapse at PGV of around 0.6 m/s. In comparison, a 20% chance of simulated collapse is realized at PGV around 1.6 m/s for retrofit schemes RBR-2, RBRB-1, and RBRB-2, and at PGV just shy of 1 m/s for schemes RMF-2h, RMF-2, and RMF-3.

The horizontal peak ground velocities at which the building models realize a 20% chance of simulated "repairable" performance category or worse, "unrepairable" performance category or worse, and model collapse are summarized in Table 5.2.

The "expected" and "stiff" foundation models resulted in very similar building performances. When employing the "stiff" foundation model, foundation reactions were in the elastic range for all building models. When employing the "expected" foundation model, foundation reactions were in the elastic range for all but two building models. Yielding of the foundation springs was observed for retrofit scheme RBR-1 and more noticeably for scheme RBR-2, with residual foundation rotations up to around 1%. When employing the "soft" foundation model, unfortunately, some simulations for schemes RBR-1, RBR-2, and RBRB-2 failed to converge before showing a clear sign of collapse, which prevents a just comparison of the building models. It can still be seen that employing the "soft" (and weak) foundation model has little impact on the collapse potential of the building models. Also, the capacities of the soft and weak foundation springs were frequently exceeded in all building models at only moderate levels of seismicity. As a result, all building models realized similar potential for exceeding the "immediate occupancy" foundation residual rotation limit, and only moderate reduction in number of simulated complete economic losses of the building models is observed for the retrofit schemes. However, the foundations were never simulated to loose stability, although residual foundation rotations were observed to be as large as 10%.

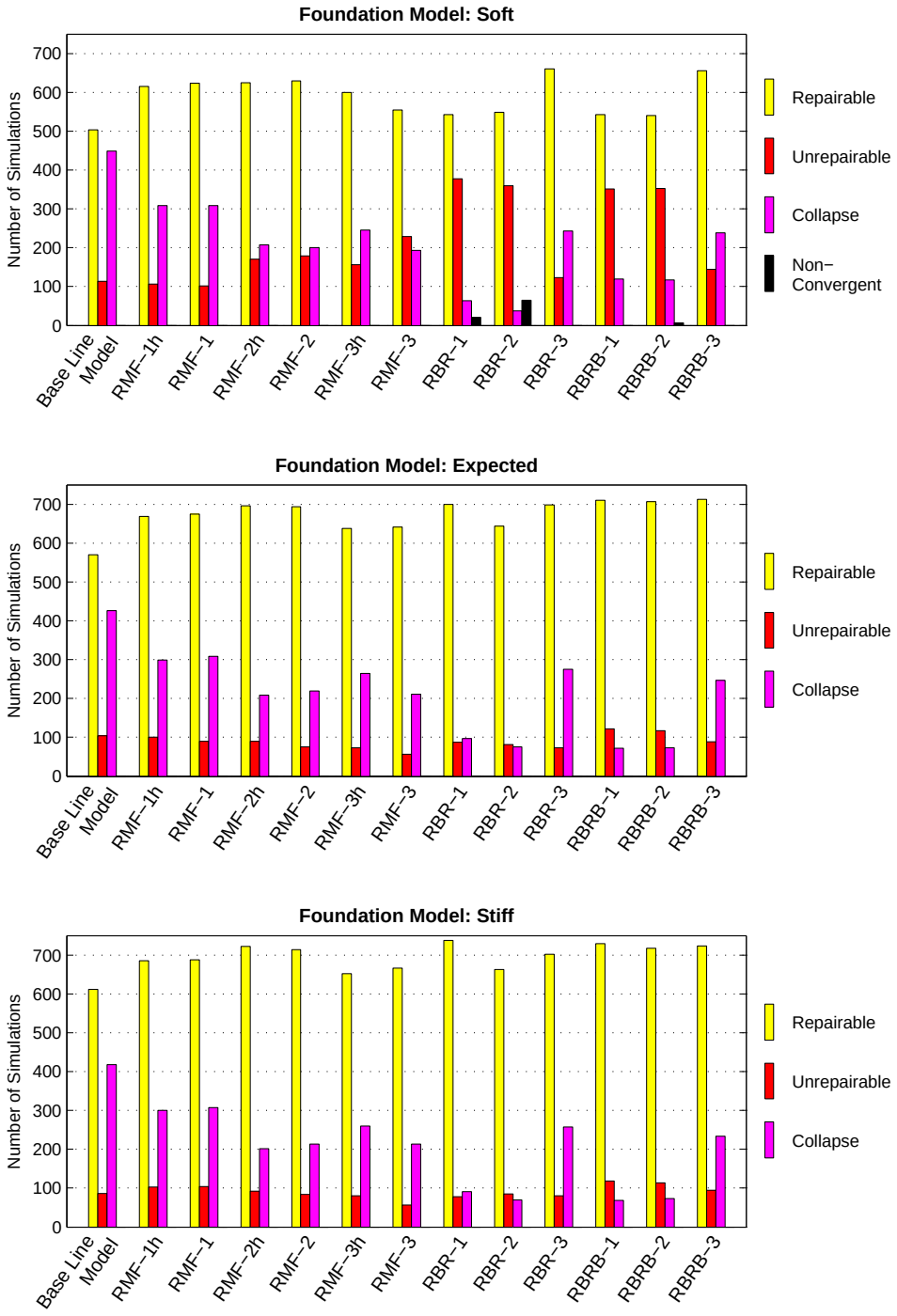

Figure 5.1: Summary of the number of simulations that resulted in the "repairable", "unrepairable", and "collapse" performance categories in the M_w 7.9 1857-like San Andreas fault earthquake scenario, assuming the "soft" (top figure), "expected" (middle figure), and "stiff" (bottom figure) foundation spring stiffnesses. The total number of simulations carried out for each building model, for each assumption on foundation spring stiffnesses, is 1272. Some simulations for retrofit schemes RBR-1, RBR-2, and RBRB-2, assuming the "soft" foundation spring stiffnesses, failed to converge before showing a clear sign of model collapse. These simulations are labeled as "non-convergent" and are removed from the data sets before constructing associated fragility curves.

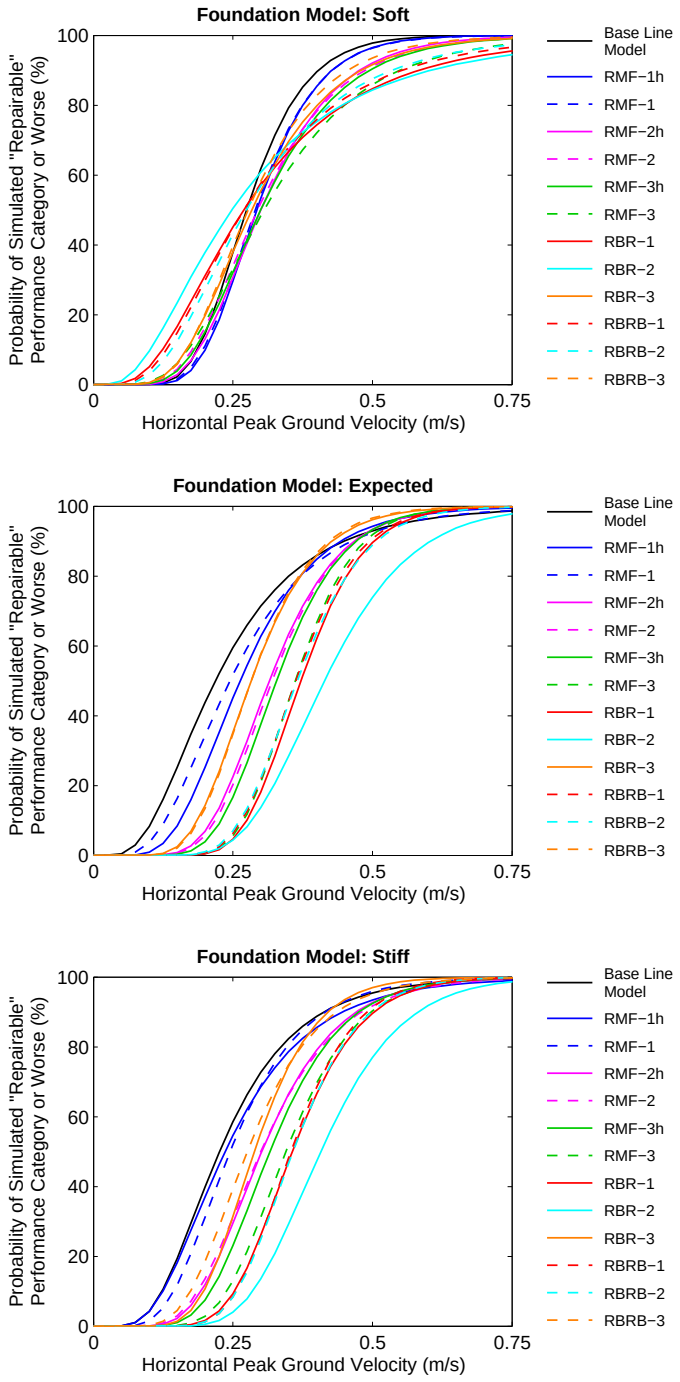

Figure 5.2: Fragility curves showing the probability of the building models realizing the "repairable" performance category or worse, given horizontal peak ground velocity in the M_w 7.9 1857-like San Andreas fault earthquake scenario, assuming the "soft" (top figure), "expected" (middle figure), and "stiff" (bottom figure) foundation spring stiffnesses.

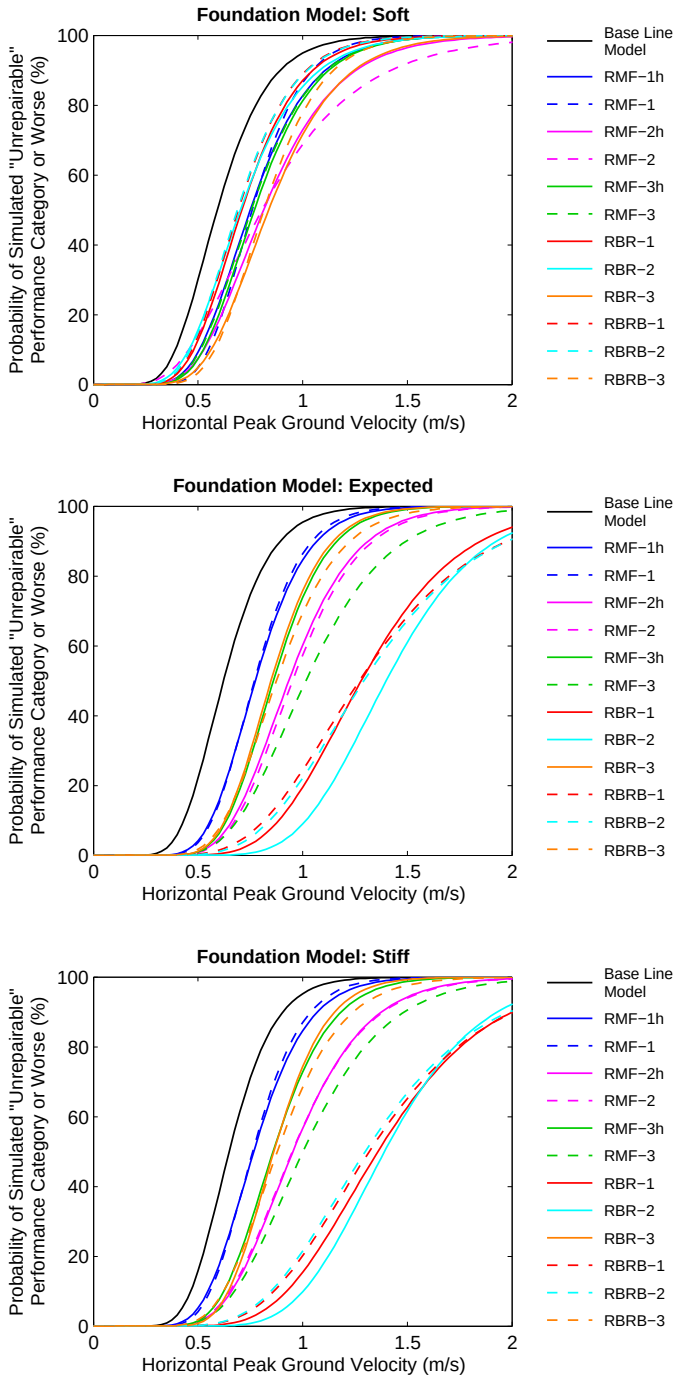

Figure 5.3: Fragility curves showing the probability of the building models realizing the "unrepairable" performance category or worse, given horizontal peak ground velocity in the M_w 7.9 1857-like San Andreas fault earthquake scenario, assuming the "soft" (top figure), "expected" (middle figure), and "stiff" (bottom figure) foundation spring stiffnesses.

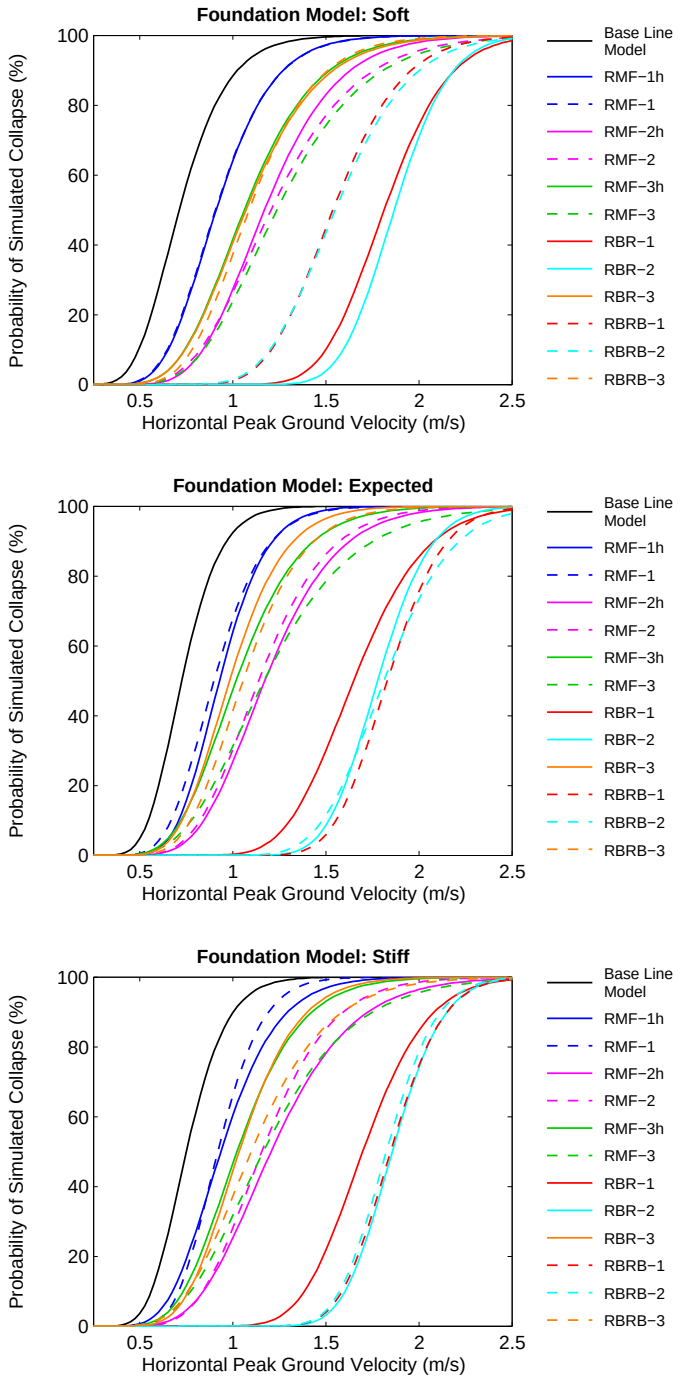

Figure 5.4: Fragility curves showing the probability of the building models realizing model collapse, given horizontal peak ground velocity in the M_w 7.9 1857-like San Andreas fault earthquake scenario, assuming the "soft" (top figure), "expected" (middle figure), and "stiff" (bottom figure) foundation spring stiffnesses.

Table 5.2: Horizontal peak ground velocities in meters per second at which the building models realize a 20% chance of simulated "repairable" performance category or worse, "unrepairable" performance category or worse, and model collapse in the M_w 7.9 1857-like San Andreas fault earthquake.

Building Performance:	"Repairable" or Worse			"Unrepairable" or Worse			Collapse		
Building Model: / **Foundation Model:**	"Soft"	"Expected"	"Stiff"	"Soft"	"Expected"	"Stiff"	"Soft"	"Expected"	"Stiff"
BLM[a]	0.23	0.12	0.15	0.45	0.50	0.53	0.55	0.60	0.62
RMF-1h	0.23	0.18	0.15	0.58	0.62	0.62	0.73	0.78	0.75
RMF-1	0.23	0.15	0.18	0.62	0.62	0.62	0.73	0.75	0.78
RMF-2h	0.23	0.25	0.23	0.60	0.75	0.75	0.95	0.95	0.95
RMF-2	0.20	0.25	0.23	0.55	0.75	0.75	0.95	0.93	0.93
RMF-3h	0.23	0.25	0.25	0.60	0.70	0.70	0.85	0.80	0.83
RMF-3	0.20	0.30	0.28	0.58	0.78	0.78	0.95	0.90	0.90
RBR-1	0.15[b]	0.30	0.28	0.55[b]	1.00	1.05	1.60[b]	1.43	1.48
RBR-2	0.15[b]	0.33	0.33	0.53[b]	1.12	1.12	1.68[b]	1.60	1.68
RBR-3	0.20	0.23	0.23	0.65	0.70	0.70	0.85	0.80	0.85
RBRB-1	0.18	0.30	0.28	0.53	0.95	1.00	1.30	1.65	1.68
RBRB-2	0.18[b]	0.30	0.28	0.53[b]	0.98	0.98	1.30[b]	1.58	1.65
RBRB-3	0.20	0.23	0.20	0.65	0.70	0.70	0.88	0.85	0.85

[a] Base Line Model

[b] Some simulations for retrofit schemes RBR-1, RBR-2, and RBRB-2 failed to converge before showing a clear sign of collapse, which may have an effect on these presented values.

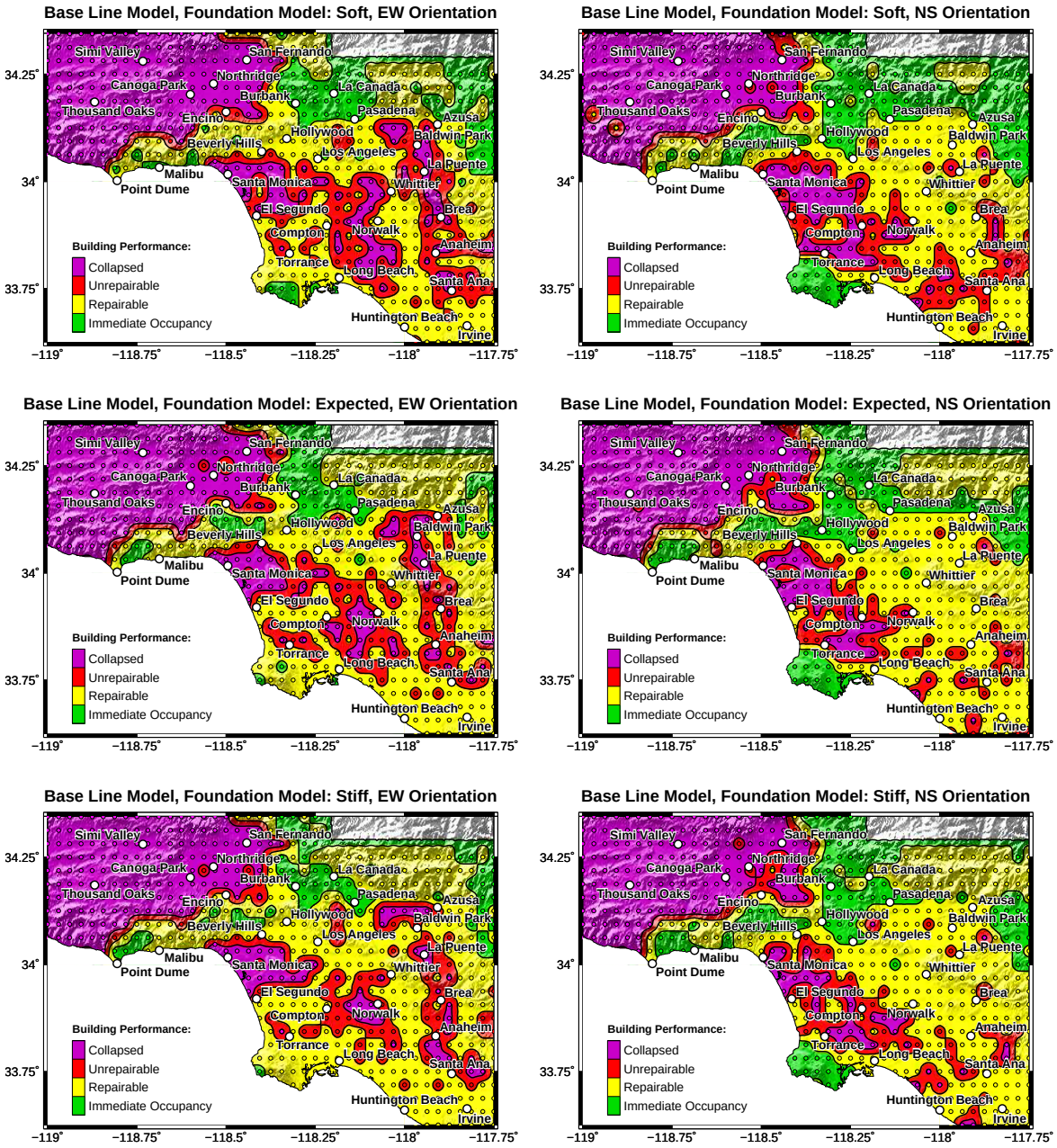

Figure 5.5: Maps of simulated building performance of the Base Line Model in the M_w 7.9 1857-like scenario earthquake on the San Andreas fault oriented in east-west (EW) direction (left column) and north-south (NS) direction (right column). The maps in the top row show the model performance using the "soft" realization of the foundations, the maps in the center row show model performance using the "expected" realization of the foundations, and the maps in the bottom row show the model performance using the "stiff" realization of the foundations. The small circles show the simulated building performance at each site. A nearest neighbor method is used to interpolate the building performance between sites.

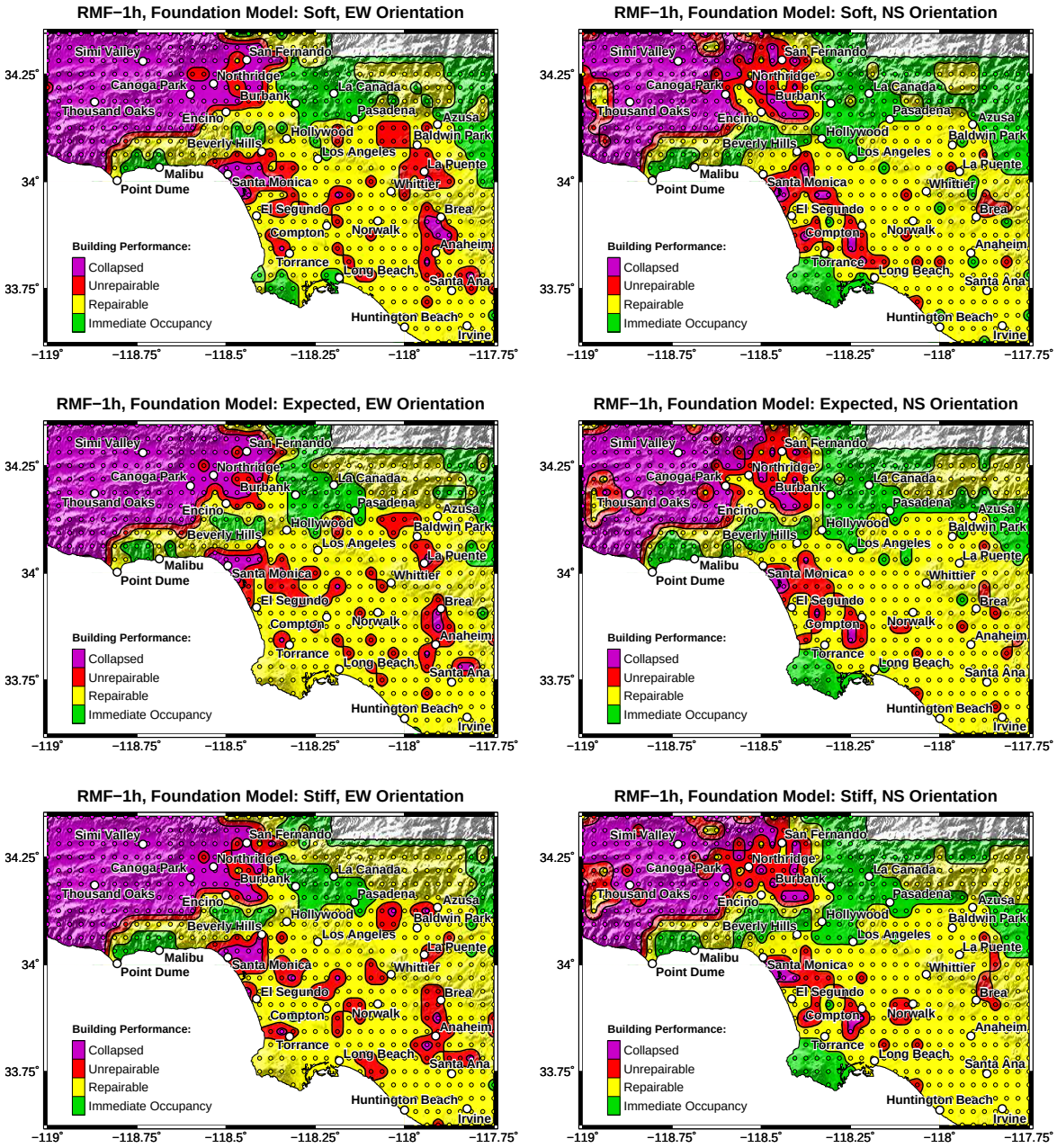

Figure 5.6: Maps of simulated building performance of retrofit scheme RMF-1h in the M_w 7.9 1857-like scenario earthquake on the San Andreas fault oriented in east-west (EW) direction (left column) and north-south (NS) direction (right column). The maps in the top row show the model performance using the "soft" realization of the foundations, the maps in the center row show model performance using the "expected" realization of the foundations, and the maps in the bottom row show the model performance using the "stiff" realization of the foundations. The small circles show the simulated building performance at each site. A nearest neighbor method is used to interpolate the building performance between sites.

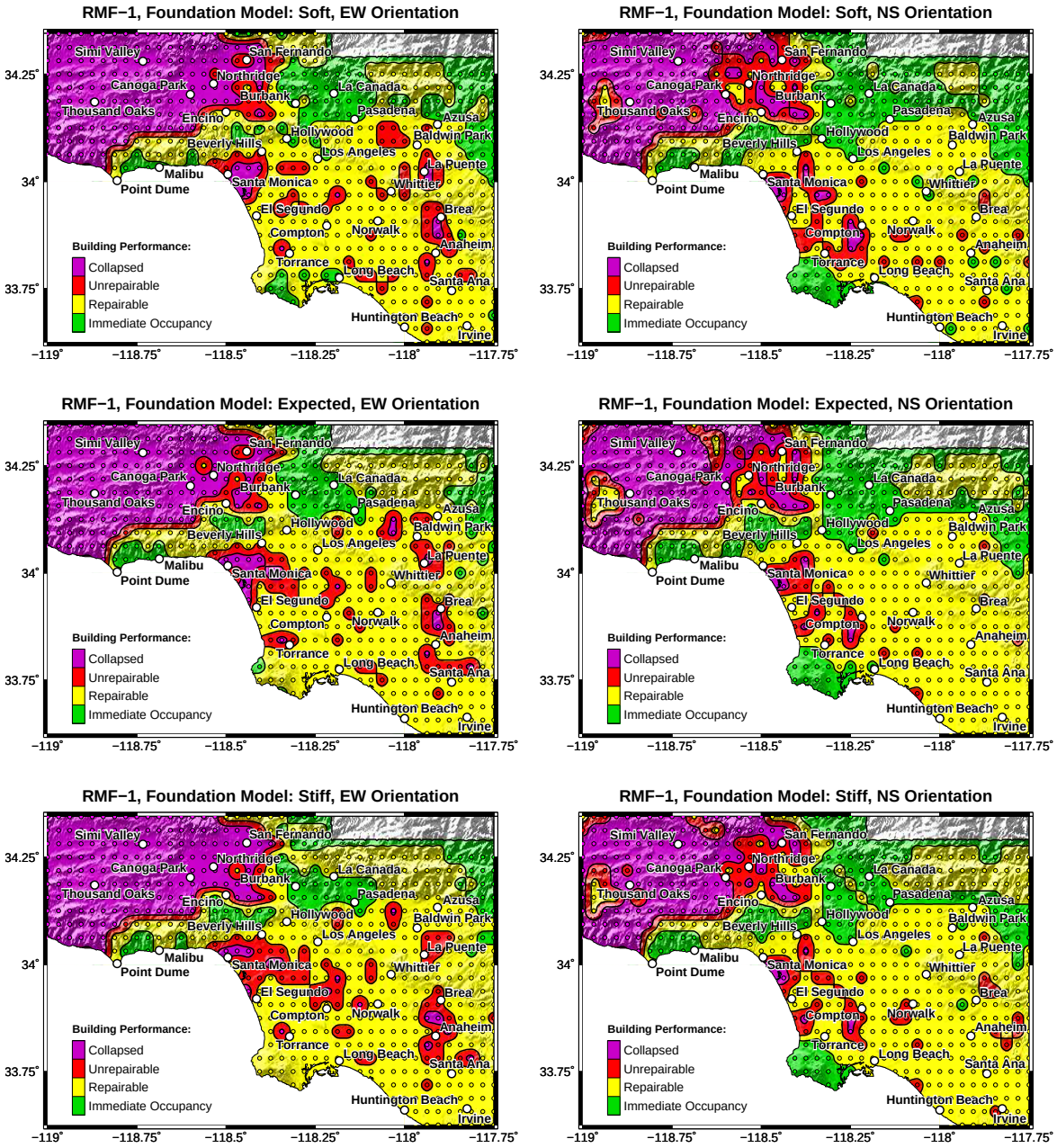

Figure 5.7: Maps of simulated building performance of retrofit scheme RMF-1 in the M_w 7.9 1857-like scenario earthquake on the San Andreas fault oriented in east-west (EW) direction (left column) and north-south (NS) direction (right column). The maps in the top row show the model performance using the "soft" realization of the foundations, the maps in the center row show model performance using the "expected" realization of the foundations, and the maps in the bottom row show the model performance using the "stiff" realization of the foundations. The small circles show the simulated building performance at each site. A nearest neighbor method is used to interpolate the building performance between sites.

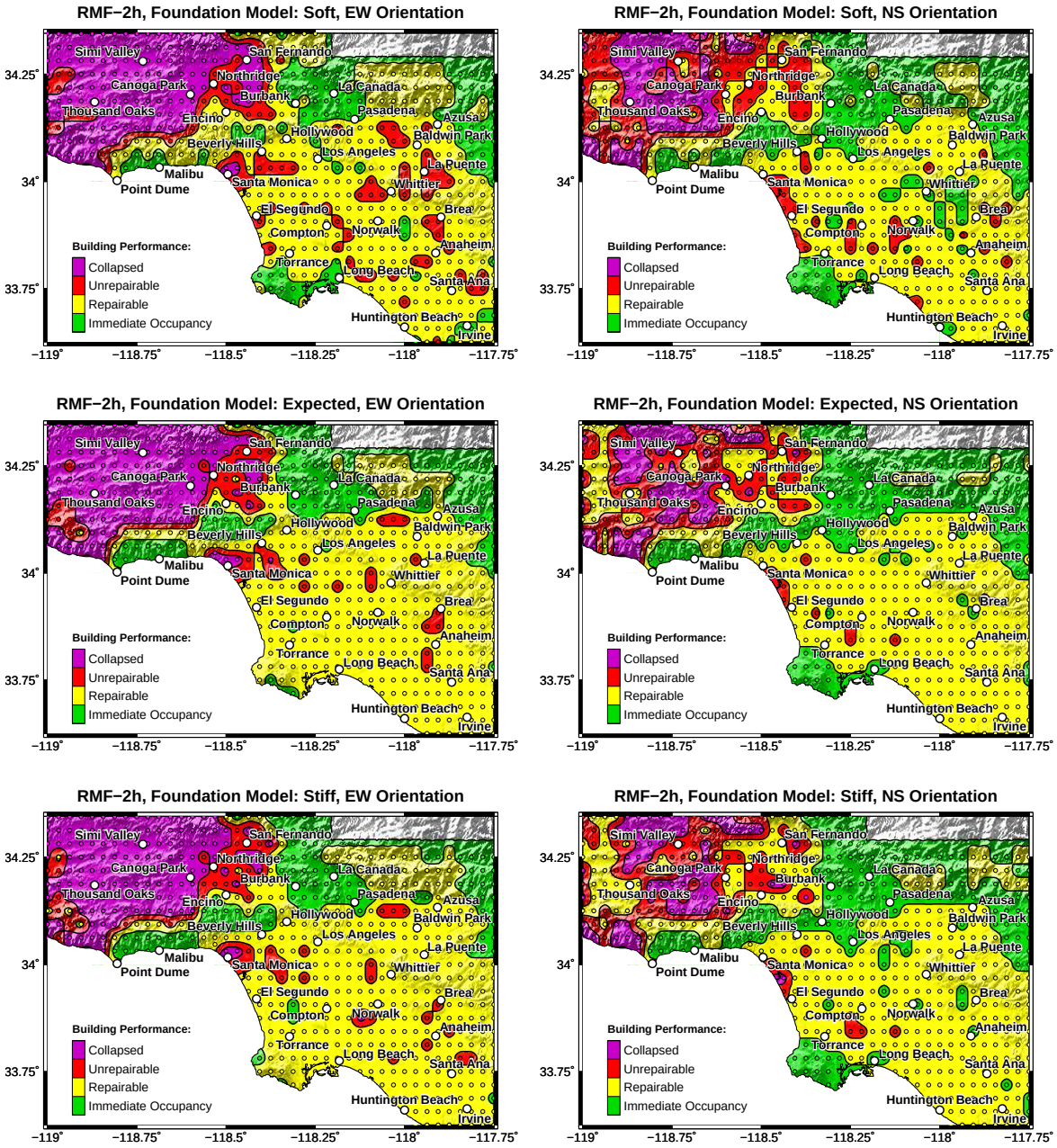

Figure 5.8: Maps of simulated building performance of retrofit scheme RMF-2h in the M_w 7.9 1857-like scenario earthquake on the San Andreas fault oriented in east-west (EW) direction (left column) and north-south (NS) direction (right column). The maps in the top row show the model performance using the "soft" realization of the foundations, the maps in the center row show model performance using the "expected" realization of the foundations, and the maps in the bottom row show the model performance using the "stiff" realization of the foundations. The small circles show the simulated building performance at each site. A nearest neighbor method is used to interpolate the building performance between sites.

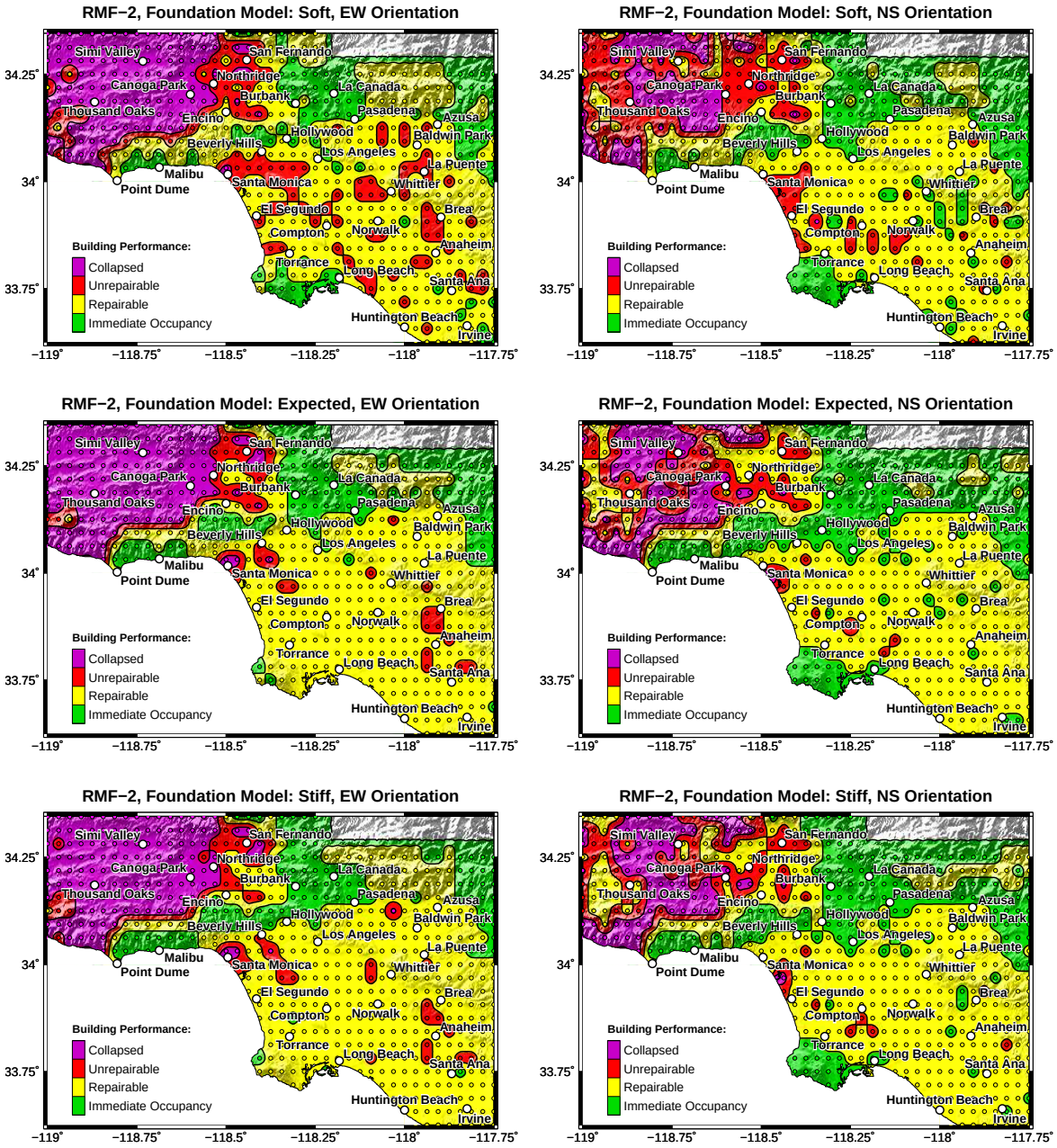

Figure 5.9: Maps of simulated building performance of retrofit scheme RMF-2 in the M_w 7.9 1857-like scenario earthquake on the San Andreas fault oriented in east-west (EW) direction (left column) and north-south (NS) direction (right column). The maps in the top row show the model performance using the "soft" realization of the foundations, the maps in the center row show model performance using the "expected" realization of the foundations, and the maps in the bottom row show the model performance using the "stiff" realization of the foundations. The small circles show the simulated building performance at each site. A nearest neighbor method is used to interpolate the building performance between sites.

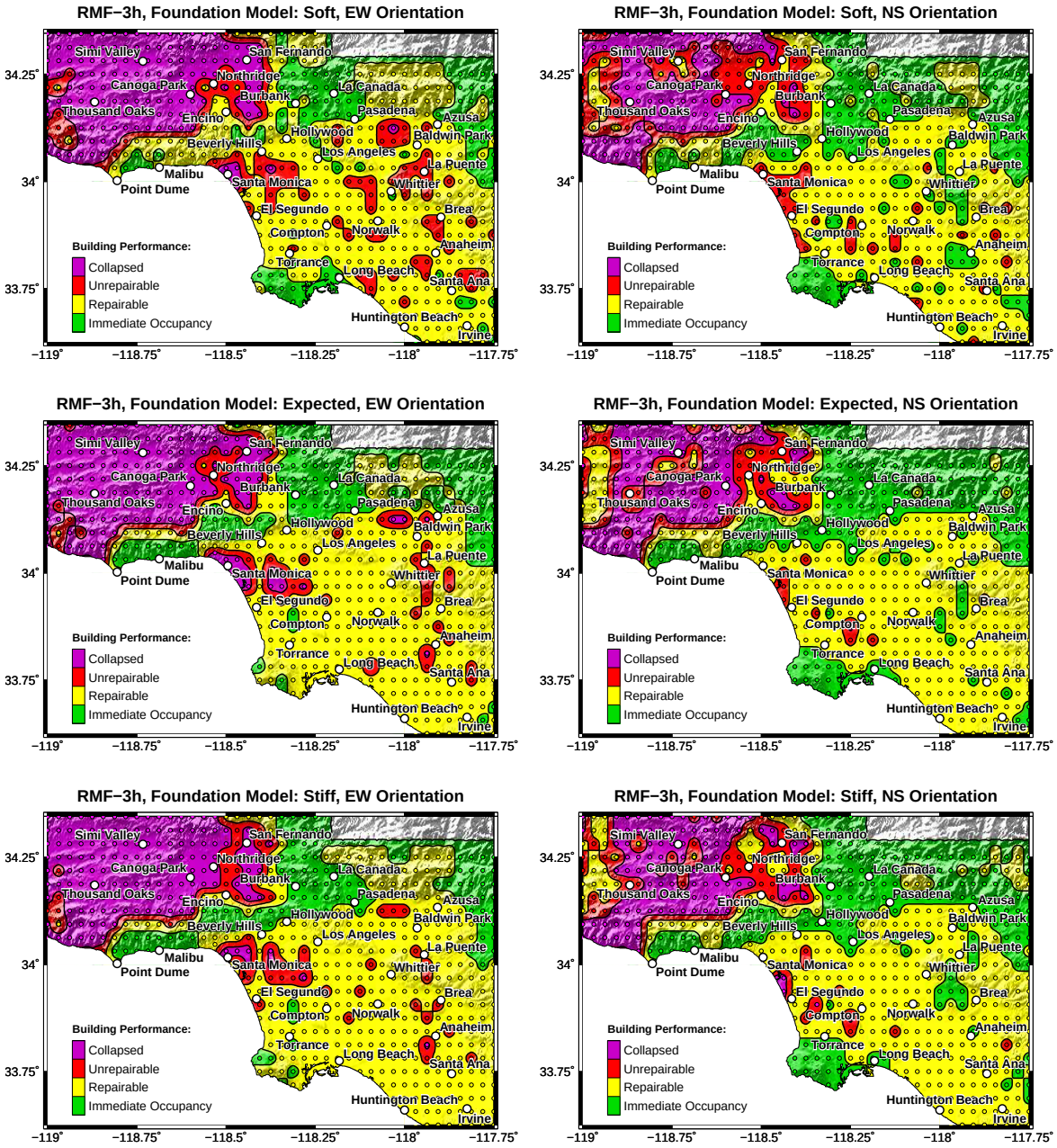

Figure 5.10: Maps of simulated building performance of retrofit scheme RMF-3h in the M_w 7.9 1857-like scenario earthquake on the San Andreas fault oriented in east-west (EW) direction (left column) and north-south (NS) direction (right column). The maps in the top row show the model performance using the "soft" realization of the foundations, the maps in the center row show model performance using the "expected" realization of the foundations, and the maps in the bottom row show the model performance using the "stiff" realization of the foundations. The small circles show the simulated building performance at each site. A nearest neighbor method is used to interpolate the building performance between sites.

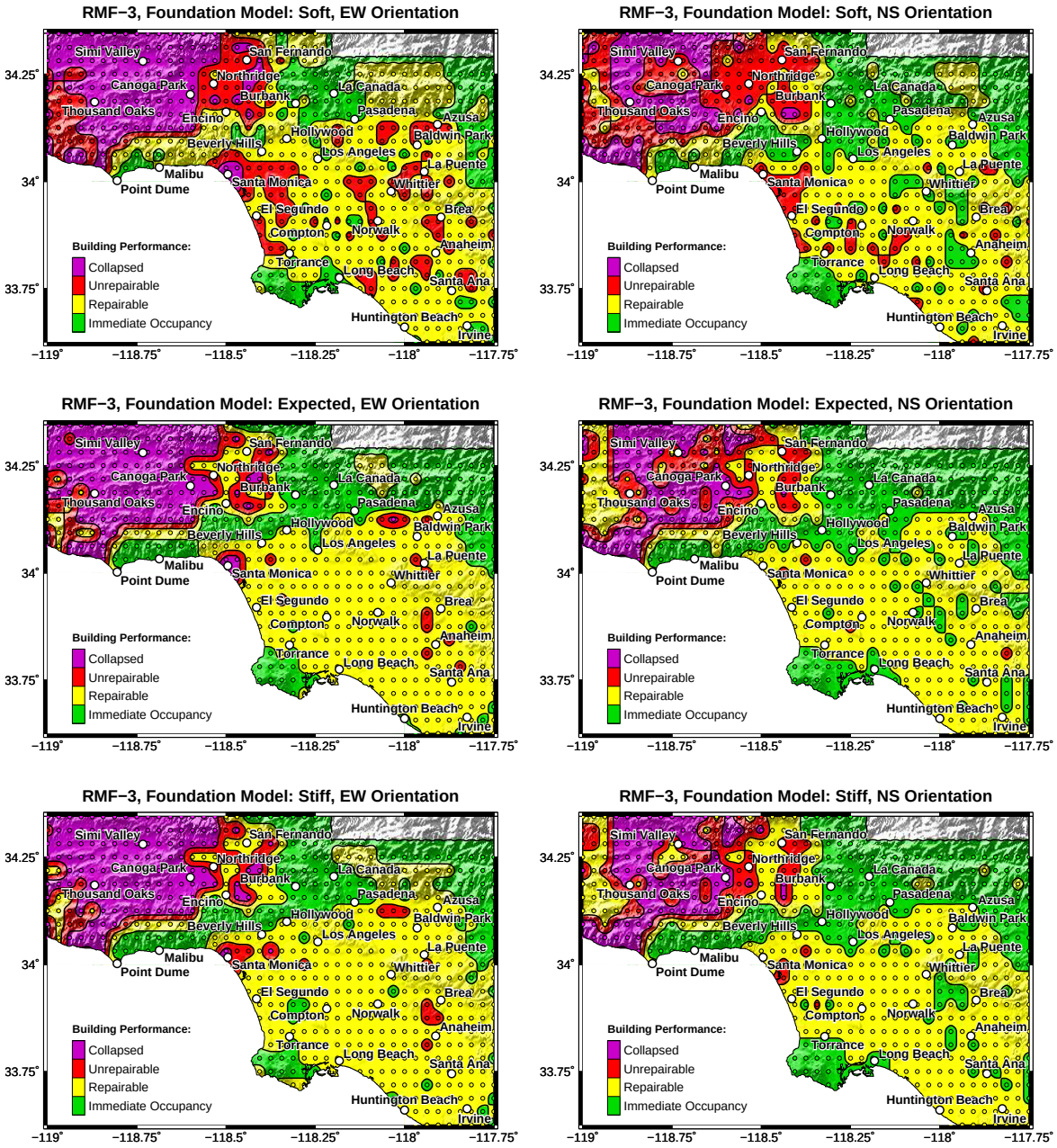

Figure 5.11: Maps of simulated building performance of retrofit scheme RMF-3 in the M_w 7.9 1857-like scenario earthquake on the San Andreas fault oriented in east-west (EW) direction (left column) and north-south (NS) direction (right column). The maps in the top row show the model performance using the "soft" realization of the foundations, the maps in the center row show model performance using the "expected" realization of the foundations, and the maps in the bottom row show the model performance using the "stiff" realization of the foundations. The small circles show the simulated building performance at each site. A nearest neighbor method is used to interpolate the building performance between sites.

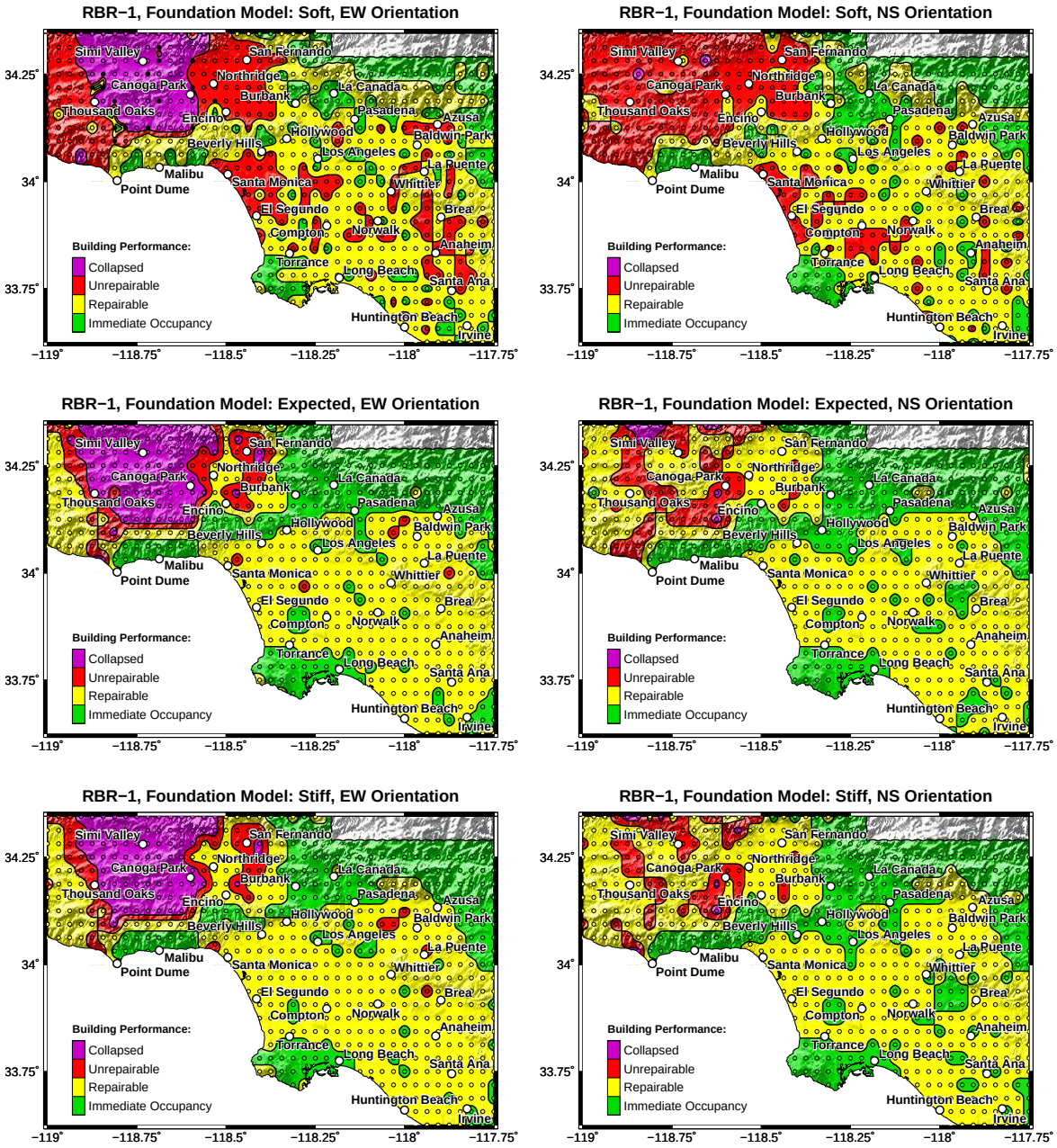

Figure 5.12: Maps of simulated building performance of retrofit scheme RBR-1 in the M_w 7.9 1857-like scenario earthquake on the San Andreas fault oriented in east-west (EW) direction (left column) and north-south (NS) direction (right column). The maps in the top row show the model performance using the "soft" realization of the foundations, the maps in the center row show model performance using the "expected" realization of the foundations, and the maps in the bottom row show the model performance using the "stiff" realization of the foundations. The small circles show the simulated building performance at each site. Sites where simulations failed to converge before showing a clear sign of model collapse are shown as small black circles. A nearest neighbor method is used to interpolate the building performance between sites.

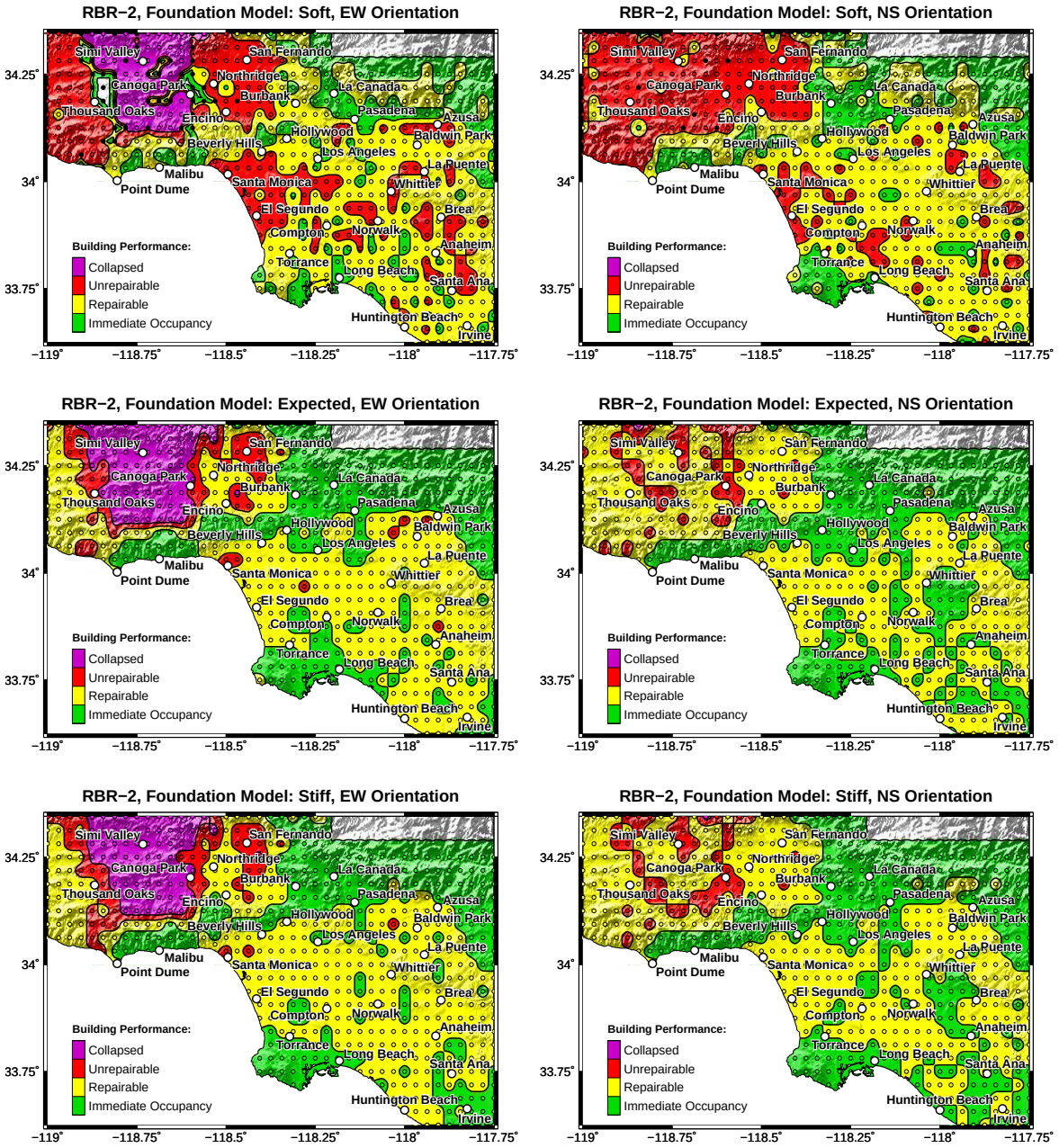

Figure 5.13: Maps of simulated building performance of retrofit scheme RBR-2 in the M_w 7.9 1857-like scenario earthquake on the San Andreas fault oriented in east-west (EW) direction (left column) and north-south (NS) direction (right column). The maps in the top row show the model performance using the "soft" realization of the foundations, the maps in the center row show model performance using the "expected" realization of the foundations, and the maps in the bottom row show the model performance using the "stiff" realization of the foundations. The small circles show the simulated building performance at each site. Sites where simulations failed to converge before showing a clear sign of model collapse are shown as small black circles. A nearest neighbor method is used to interpolate the building performance between sites.

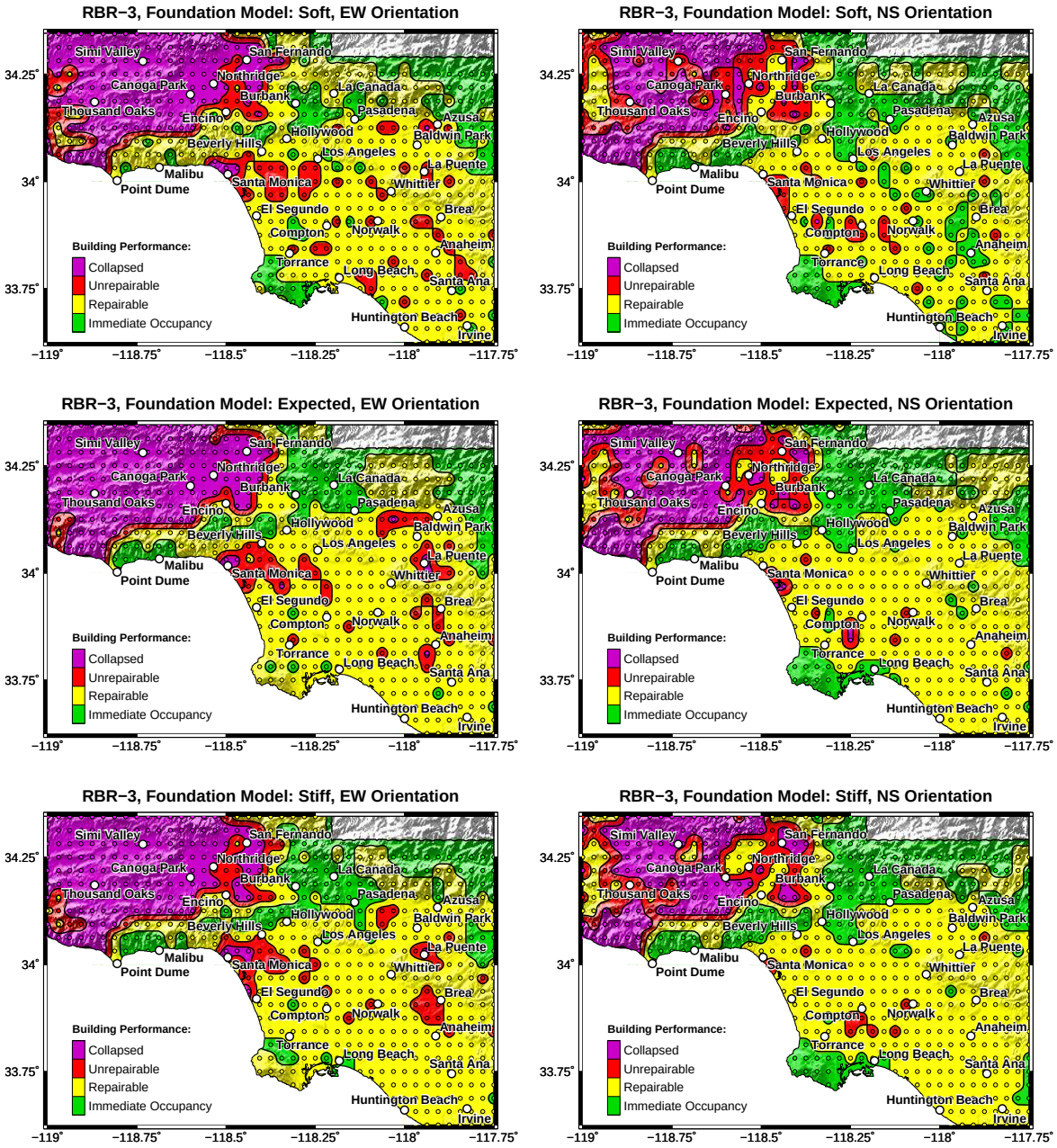

Figure 5.14: Maps of simulated building performance of retrofit scheme RBR-3 in the M_w 7.9 1857-like scenario earthquake on the San Andreas fault oriented in east-west (EW) direction (left column) and north-south (NS) direction (right column). The maps in the top row show the model performance using the "soft" realization of the foundations, the maps in the center row show model performance using the "expected" realization of the foundations, and the maps in the bottom row show the model performance using the "stiff" realization of the foundations. The small circles show the simulated building performance at each site. A nearest neighbor method is used to interpolate the building performance between sites.

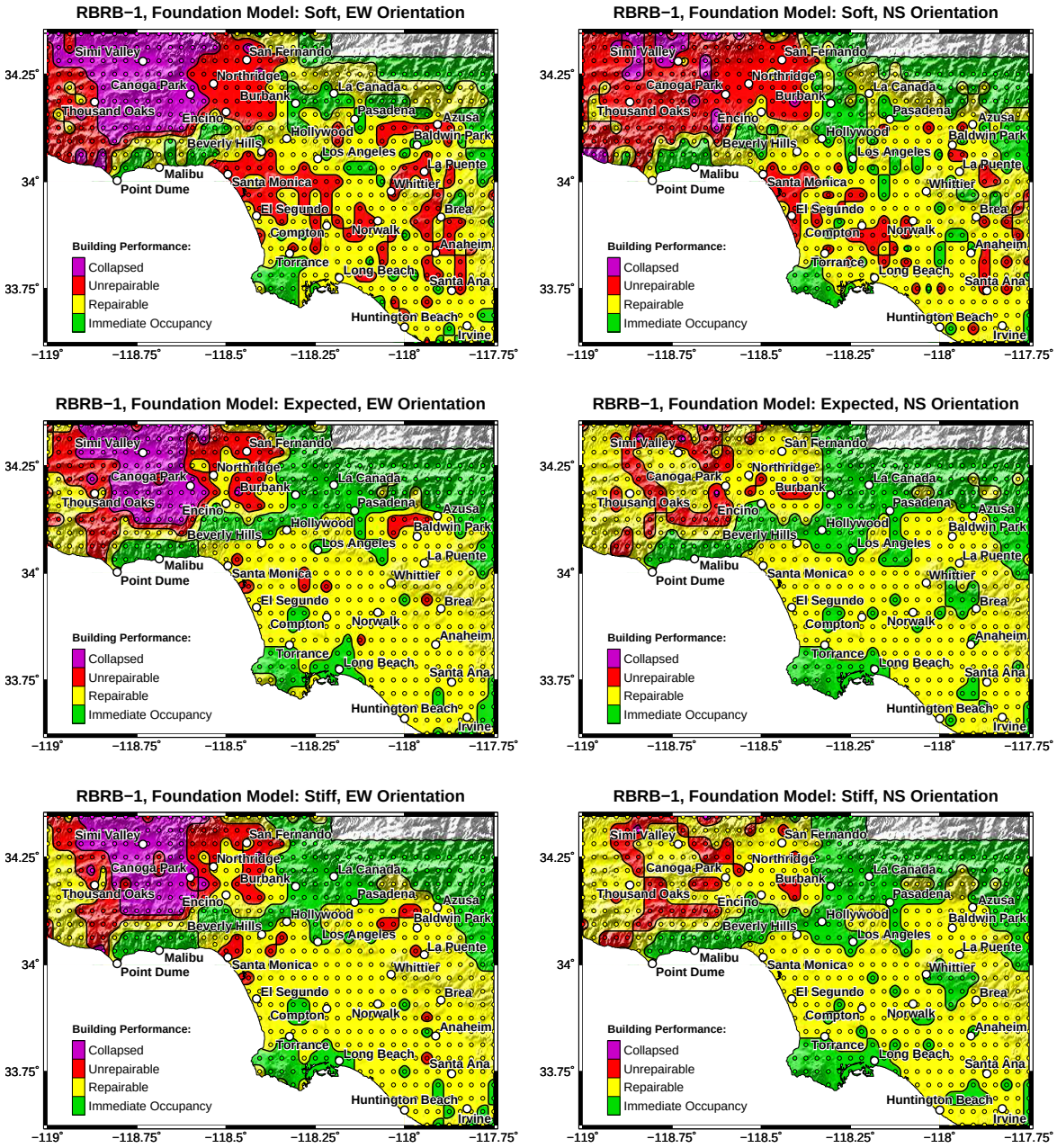

Figure 5.15: Maps of simulated building performance of retrofit scheme RBRB-1 in the M_w 7.9 1857-like scenario earthquake on the San Andreas fault oriented in east-west (EW) direction (left column) and north-south (NS) direction (right column). The maps in the top row show the model performance using the "soft" realization of the foundations, the maps in the center row show model performance using the "expected" realization of the foundations, and the maps in the bottom row show the model performance using the "stiff" realization of the foundations. The small circles show the simulated building performance at each site. A nearest neighbor method is used to interpolate the building performance between sites.

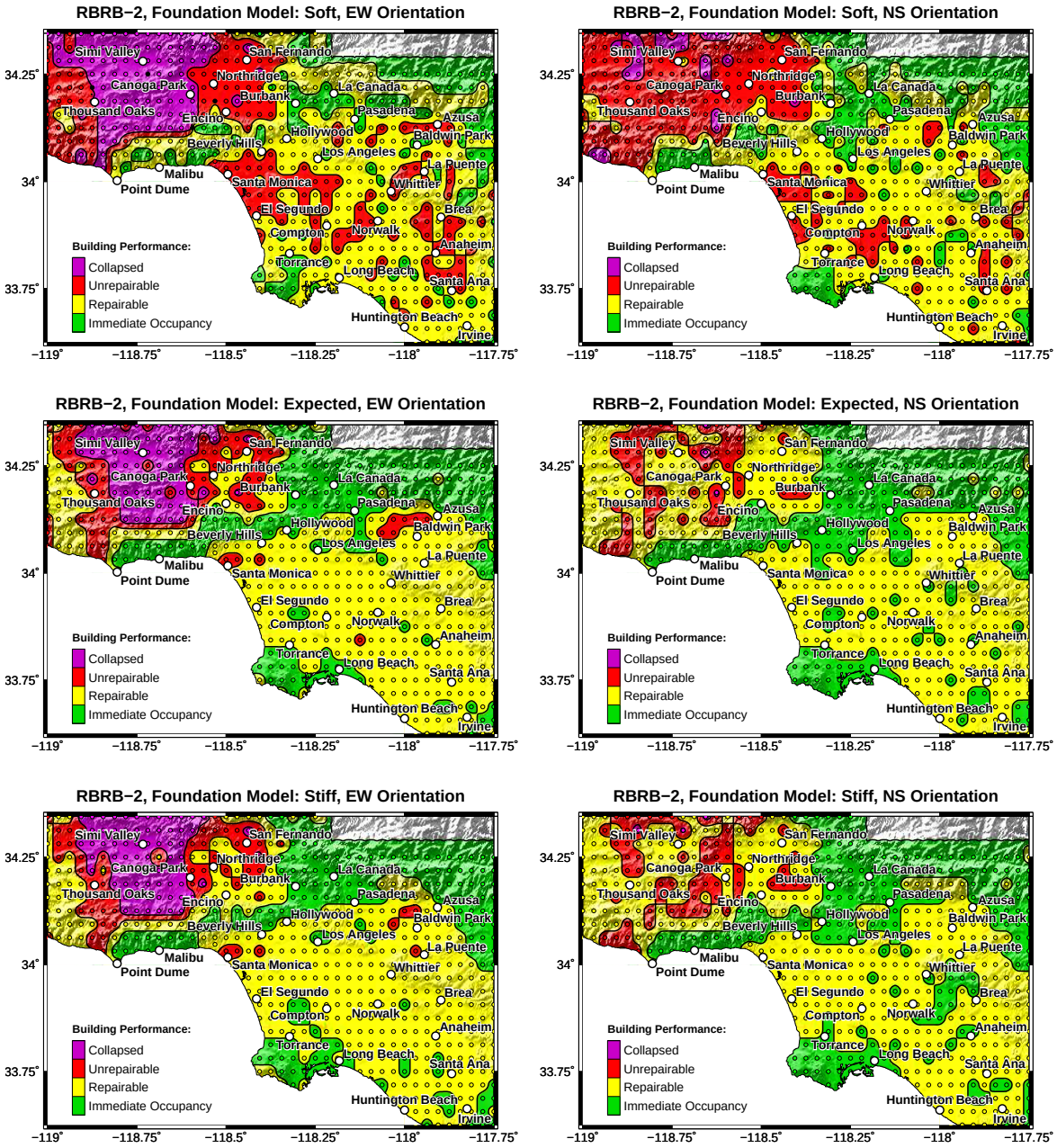

Figure 5.16: Maps of simulated building performance of retrofit scheme RBRB-2 in the M_w 7.9 1857-like scenario earthquake on the San Andreas fault oriented in east-west (EW) direction (left column) and north-south (NS) direction (right column). The maps in the top row show the model performance using the "soft" realization of the foundations, the maps in the center row show model performance using the "expected" realization of the foundations, and the maps in the bottom row show the model performance using the "stiff" realization of the foundations. The small circles show the simulated building performance at each site. Sites where simulations failed to converge before showing a clear sign of model collapse are shown as small black circles. A nearest neighbor method is used to interpolate the building performance between sites.

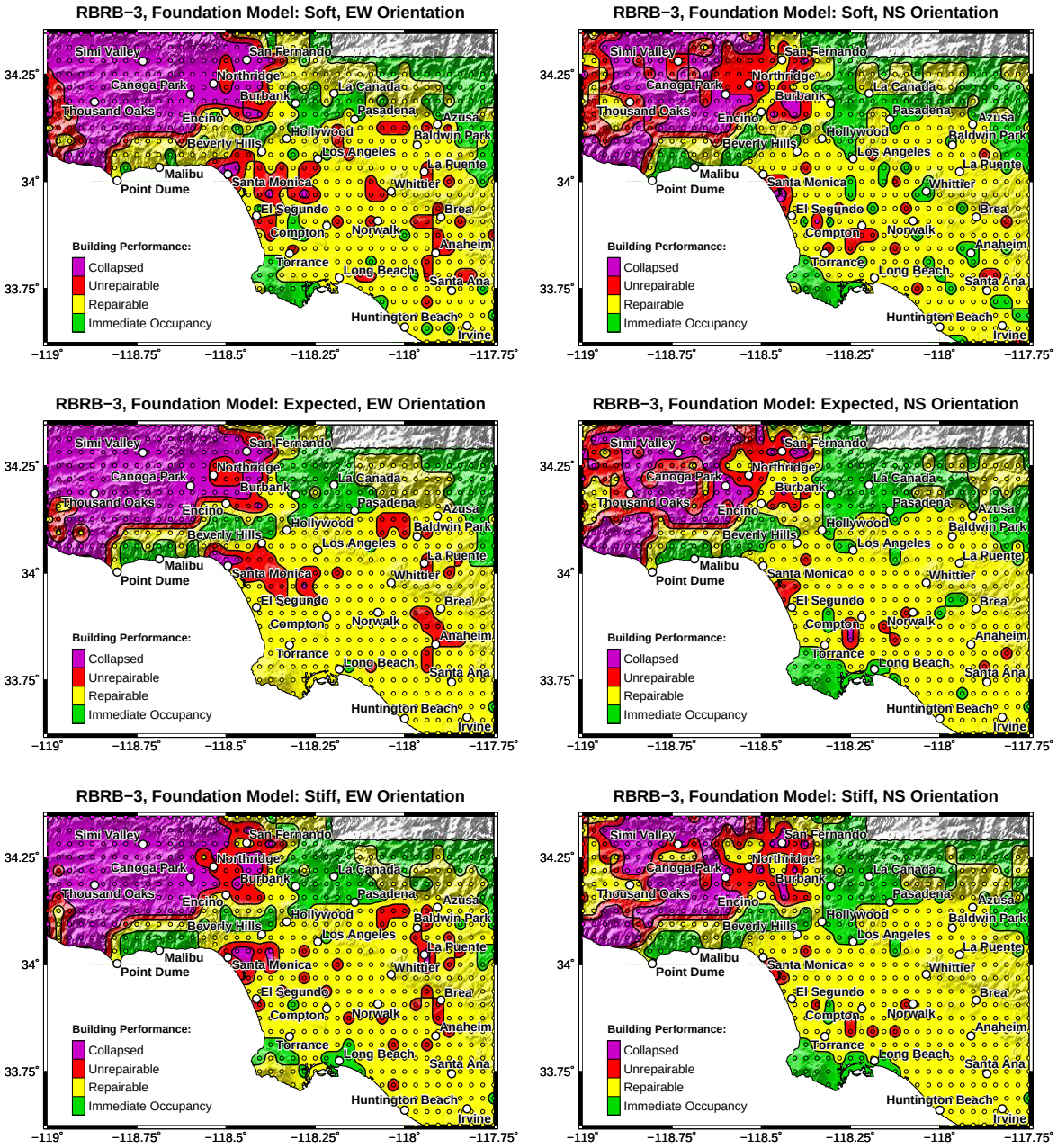

Figure 5.17: Maps of simulated building performance of retrofit scheme RBRB-3 in the M_w 7.9 1857-like scenario earthquake on the San Andreas fault oriented in east-west (EW) direction (left column) and north-south (NS) direction (right column). The maps in the top row show the model performance using the "soft" realization of the foundations, the maps in the center row show model performance using the "expected" realization of the foundations, and the maps in the bottom row show the model performance using the "stiff" realization of the foundations. The small circles show the simulated building performance at each site. A nearest neighbor method is used to interpolate the building performance between sites.

5.2 Building Performance: M_w 7.8 ShakeOut Scenario Earthquake on San Andreas Fault

Results in the ShakeOut scenario earthquake on the San Andreas fault are presented in a similar fashion as the results in the 1857-like San Andreas fault earthquake scenario. The number of simulations per building model that resulted in the "repairable", "unrepairable", and "collapse" performance categories are summarized in Figure 5.18. Fragility plots that show the probability of the building models realizing "repairable" performance category or worse, "unrepairable" performance category or worse, or model collapse, given horizontal peak ground velocity, are presented in Figures 5.19, 5.20, and 5.21, respectively. Finally, maps that geographically show the distribution of simulated performance categories in the greater Los Angeles metropolitan area for each building model are presented in Figures 5.22 to 5.34 as follows:

	Figure:		Figure:
Base Line Model	5.22	RBR-1	5.29
RMF-1h	5.23	RBR-2	5.30
RMF-1	5.24	RBR-3	5.31
RMF-2h	5.25	RBRB-1	5.32
RMF-2	5.26	RBRB-2	5.33
RMF-3h	5.27	RBRB-3	5.34
RMF-3	5.28		

The results in the ShakeOut scenario earthquake on the San Andreas fault show similar trends to what was observed in the simulated 1857-like San Andreas fault earthquake scenario.

When employing the "expected" foundation model, the base line model is simulated to collapse at 134 sites (out of 784) when the building model is oriented in the east-west direction and at 140 sites when oriented in north-south. Each site represents an area of 8 km^2. These sites cover a large portion of the Los Angeles and San Gabriel basins, and model collapse is also simulated in the near region of Santa Monica as well as in the San Fernando basin. Furthermore, complete economic loss ("unrepairable" or "collapse" performance categories) of the base line model is simulated at 219 sites when the building model is oriented in the east-west direction, and at 274 sites when oriented in north-south.

Retrofit schemes RBR-2, RBRB-1, and RBRB-2 achieve the greatest reduction in number of simulated collapses, or to a range of 0-6 sites when the building models are oriented in either east-west or north-south directions. Retrofit scheme RBR-1 is simulated to collapse at a slightly greater number of sites, or at a total (both orientations) of 22 sites. As was observed in the 1857-like San Andreas fault earthquake, scheme RBR-1 is observed to localize deformations in a few stories just above the 8^{th} story, or where the bracing configuration is tapered. In contrast, schemes RBR-2, RBRB-1, and RBRB-2 deform more uniformly over the height, resulting in better performance.

As for complete economic losses, scheme RBR-2 performs best, with complete economic losses being simulated at 35-37 sites when the building model is oriented in either east-west or north-south directions. Complete economic losses of schemes RBR-1, RBRB-1, and RBRB-2 are simulated at a total (both orientations) of 93-104 sites. As was mentioned in the previous section, it appears that braced-frames that employ buckling-restrained braces tend to have greater residual drifts. However, the buckling-restrained braces are likely to store significant residual forces, and the residual drifts may be recovered to some extent by replacing the deformed braces. Conventional brace elements are not expected to store residual forces to the same degree.

Out of the retrofit schemes that consider retrofitting the brittle beam-to-column moment resisting connections (RMF schemes), scheme RMF-3 is simulated to collapse at 59 sites when the building model is oriented in the east-west direction, and at 74 sites when oriented in north-south. Furthermore, complete economic loss of the building model is simulated at 110 sites when it is oriented in the east-west direction, and at 152 sites when oriented in north-south. Interestingly, scheme RMF-2h is simulated to collapse at fewer sites, or at 58 sites when the building model is oriented in the east-west direction and at 54 sites when oriented in north-south. However, complete economic loss of scheme RMF-2h is simulated at 137 sites when the building model is oriented in the east-west direction, and at 159 sites when oriented in north-south. Retrofit schemes RMF-2 and RMF-3h are simulated to collapse at a total (both orientations) of 138 and 141 sites, respectively, and complete economic loss of the building models is simulated at a total (both orientations) of 295 and 331 sites, respectively.

Because of the complex nature of building responses under strong ground motions, it is difficult to give an argument that irrefutably justifies that repairing fewer beam-to-column connections will lead to lower collapse potential than if all the connections are upgraded. Also, the ground motion time histories have a similar signature from site-to-site, which is a characteristic of this particular

simulated earthquake. This signature in the ground motions happened to induce fewer simulated collapses for scheme RMF-2h compared to RMF-3, but it may necessarily repeated in other earthquakes. However, these results suggest that at a certain point, upgrading additional beam-to-column connections will result in minimal additional improvement in performance.

The two retrofit schemes that implement brace elements in the lower half of the building model while leaving the upper half unaltered (schemes RBR-3 and RBRB-3), are again somewhat successful in that the schemes are more effective in limiting deformations in the lower half of the building model, compared to the moment-frame half-height retrofit schemes (RMF-1h, RMF-2h, and RMF-3h), and thus reduce to a greater extent global P-delta overturning moments. However, as was mentioned in the previous section, the resulting structures are stiffer than the moment-frame configurations and consequently attract larger seismic forces, which often results in excessive drifts in the upper half. A retrofit scheme that implements brace elements in the lower half of the building model in conjunction with upgrading beam-to-column moment connections in the upper half may present some additional improvement in building performance while keeping architectural impact low. Retrofit schemes RBR-3 and RBRB-3 are simulated to collapse at a total (both orientations) of 166 and 144 sites, respectively, and complete economic loss of the building models is simulated at a total (both orientations) of 375 and 348 sites, respectively.

From the fragility curves constructed from the data, the simulated building performances can be related to horizontal peak ground velocities (PGV). Because there were so few simulated collapses for retrofit schemes RBR-1, RBR-2, RBRB-1, and RBRB-2, fragility curves showing the probability of simulated model collapse given horizontal peak ground velocity are not constructed, and hence, values of horizontal peak velocity at 20% chance of collapse cannot be reported. However, retrofit schemes RMF-2h, RMF-2, RMF-3h, and RMF-3 realize a 20% of simulated model collapse at a horizontal peak ground velocity of 0.9 m/s (slightly less than what was realized for schemes RMF-2h, RMF-2, and RMF-3 in the 1857-like San Andreas fault earthquake scenario), and the base line model realized a 20% chance of simulated model collapse at a horizontal peak ground velocity of 0.6 m/s (the same as was realized in the 1857-like San Andreas fault earthquake scenario).

The horizontal peak ground velocities at which the building models realize a 20% chance of simulated “repairable” performance category or worse, “unrepairable” performance category or worse, and model collapse, are summarized in Table 5.3.

The “expected” and “stiff” foundation models resulted in very similar building performances. When employing the “stiff” foundation model, foundation reactions were in the elastic range for all building models. When employing the “expected” foundation model, foundation reactions were in the elastic range for all but two building models. Yielding of the foundation springs was observed for retrofit scheme RBR-1 and more noticeably for scheme RBR-2, with residual foundation rotations up to around 1%. When employing the “soft” foundation model, the capacities of the foundation springs were frequently exceeded in all building models at only moderate levels of seismicity. As a result, all building models realized similar potential for exceeding the “immediate occupancy” foundation residual rotation limit, and only moderate reduction in number of simulated complete economic losses of the building models is observed for the retrofit schemes. However, the foundations were never simulated to loose stability, although residual foundation rotations were observed to be as large as 9%, and the retrofit schemes achieve even more dramatic reduction in collapse potential, compared to when the “expected” and “stiff” foundation models are employed.

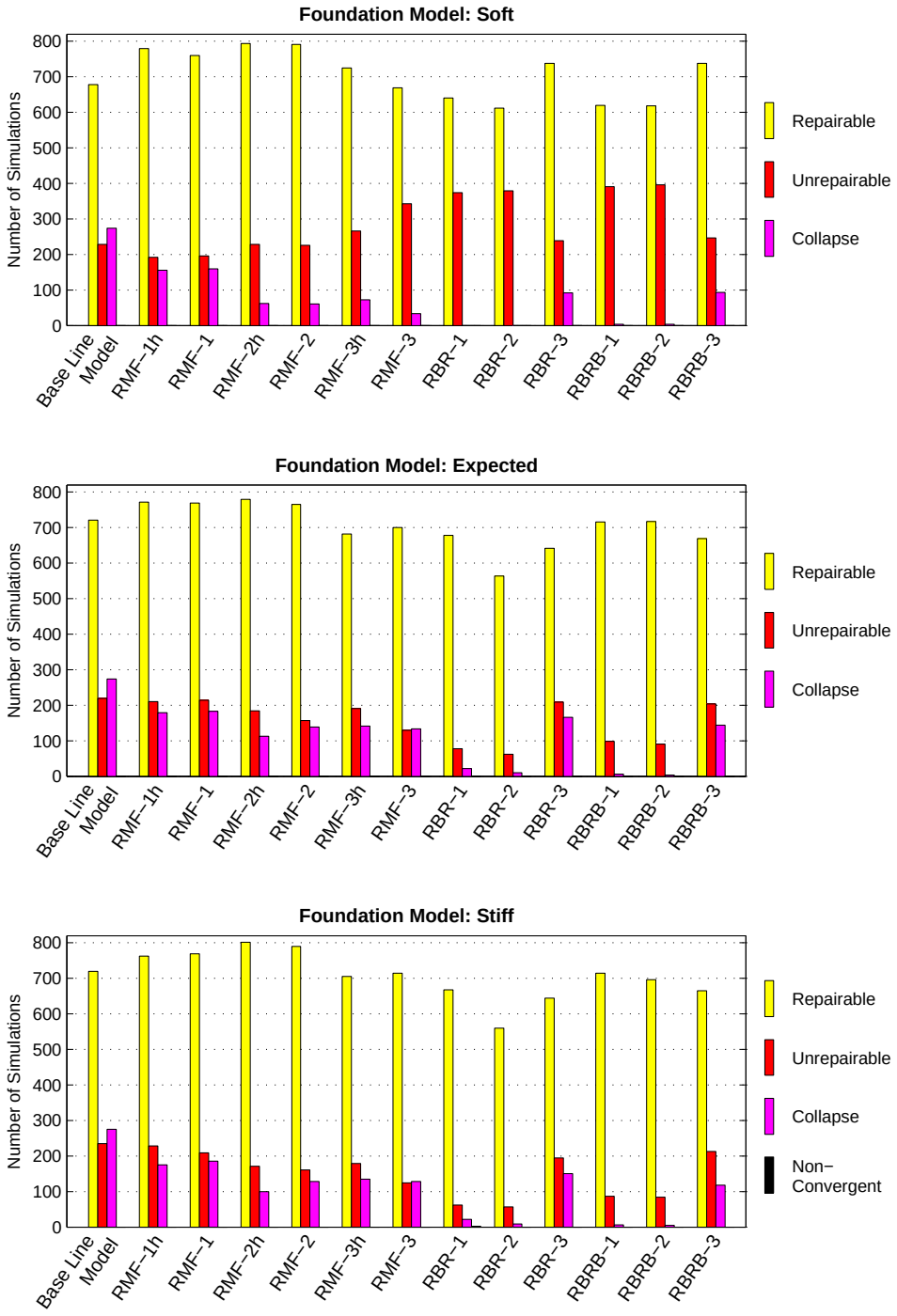

Figure 5.18: Summary of the number of simulations that resulted in the "repairable", "unrepairable", and "collapse" performance categories in the M_w 7.8 ShakeOut scenario earthquake on the San Andreas fault, assuming the "soft" (top figure), "expected" (middle figure), and "stiff" (bottom figure) foundation spring stiffnesses. The total number of simulations carried out for each building model, for each assumption on foundation spring stiffnesses, is 1568. A couple of simulations for retrofit scheme RBR-1 assuming the "stiff" foundation spring stiffnesses failed to converge before showing a clear sign of model collapse. These simulations are labeled as "non-convergent" and are removed from the data sets before constructing associated fragility curves.

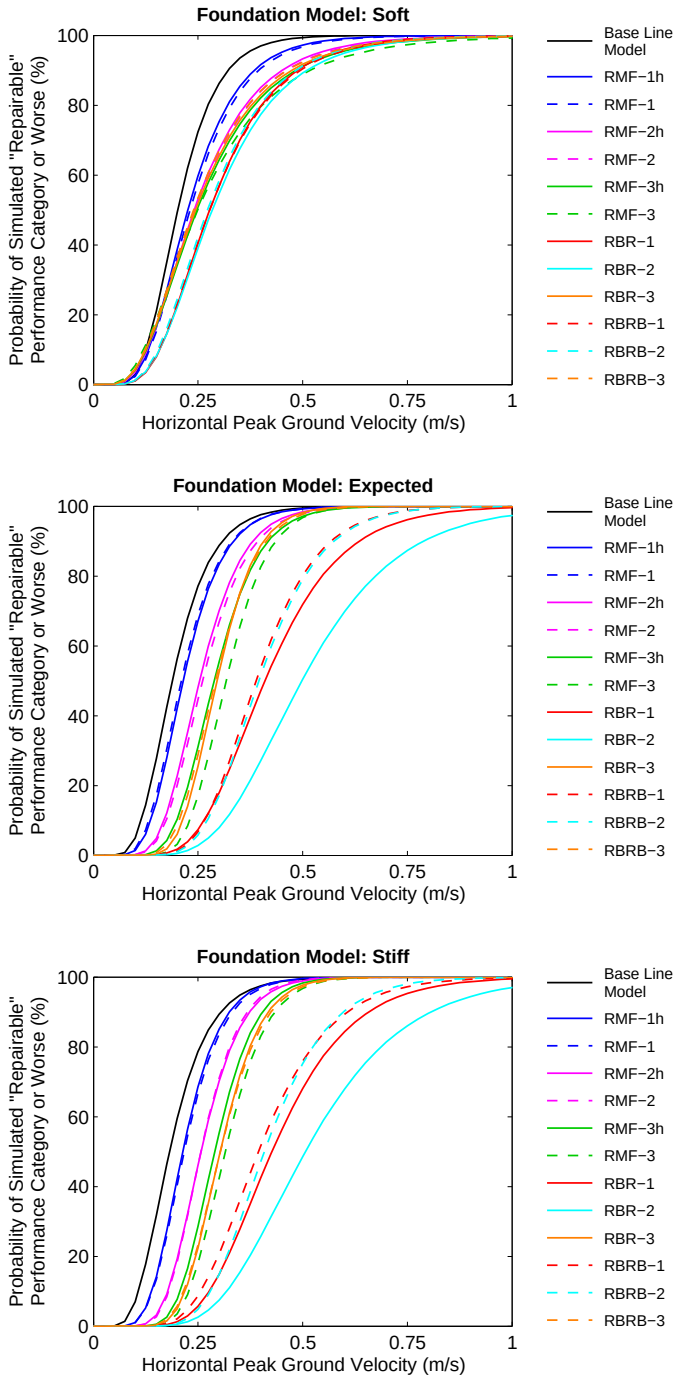

Figure 5.19: Fragility curves showing the probability of the building models realizing the "repairable" performance category or worse given horizontal peak ground velocity in the M_w 7.8 ShakeOut scenario earthquake on the San Andreas fault, assuming the "soft" (top figure), "expected" (middle figure), and "stiff" (bottom figure) foundation spring stiffnesses.

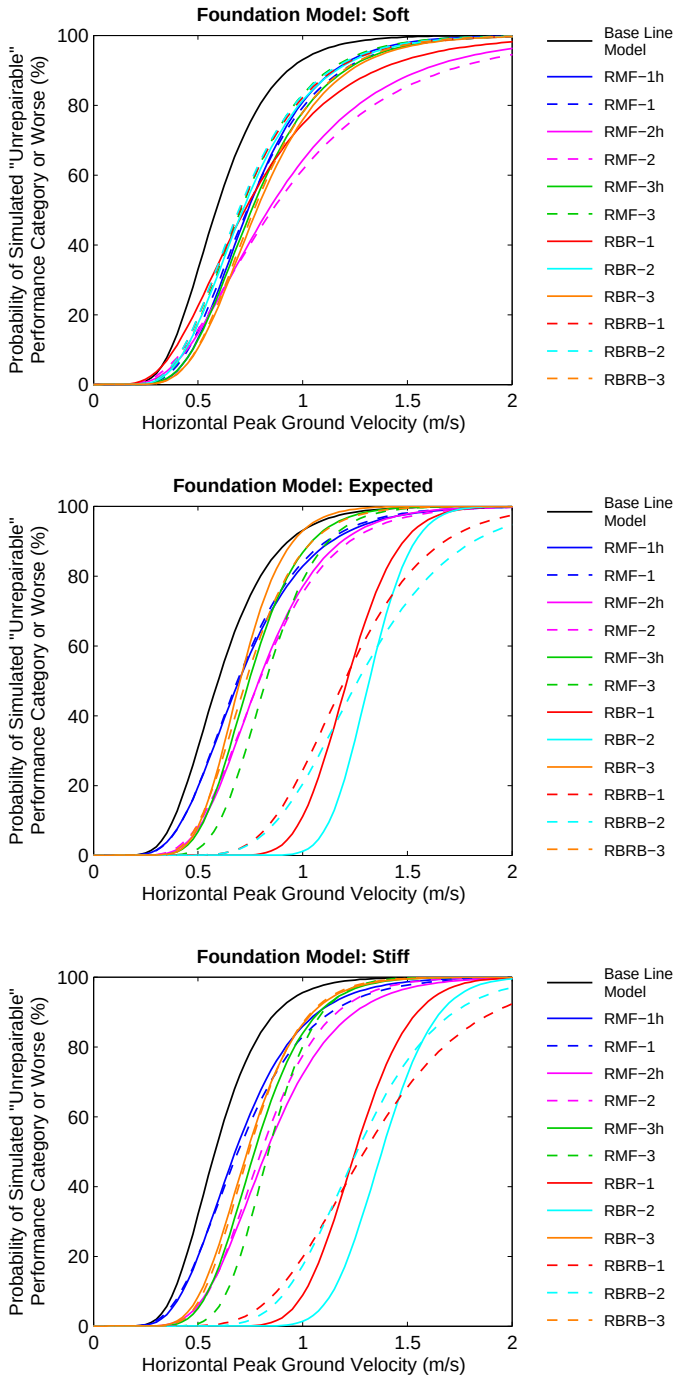

Figure 5.20: Fragility curves showing the probability of the building models realizing the "unrepairable" performance category or worse given horizontal peak ground velocity in the M_w 7.8 ShakeOut scenario earthquake on the San Andreas fault, assuming the "soft" (top figure), "expected" (middle figure), and "stiff" (bottom figure) foundation spring stiffnesses.

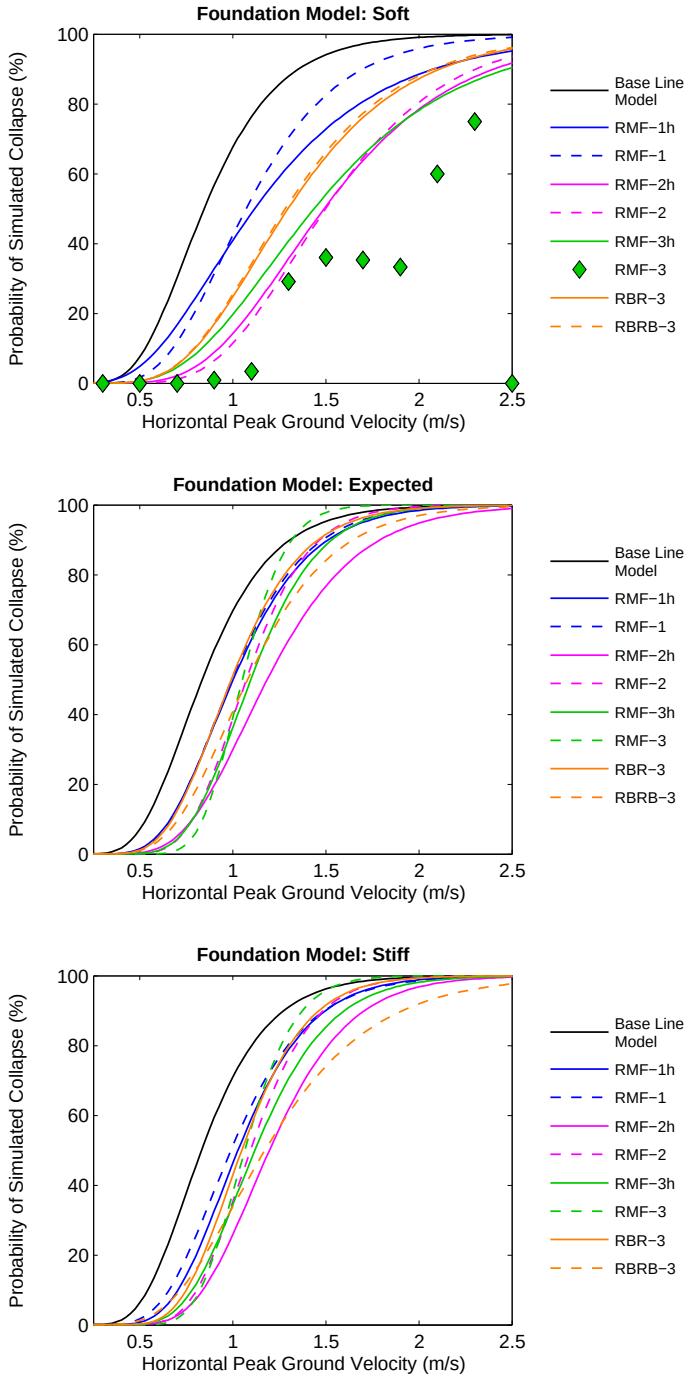

Figure 5.21: Fragility curves showing the probability of the building models realizing model collapse given horizontal peak ground velocity in the M_w 7.8 ShakeOut scenario earthquake on the San Andreas fault, assuming the "soft" (top figure), "expected" (middle figure), and "stiff" (bottom figure) foundation spring stiffnesses. Because of the small number of simulations that resulted in model collapse of retrofit schemes RBR-1, RBR-2, RBRB-1, and RBRB-2, fragility curves are not constructed for those schemes. The data for retrofit scheme RMF-3, assuming the "soft" foundation spring stiffnesses, is not well represented by a cumulative log-normal distribution function, and the actual fractions of the simulations that resulted in simulated model collapse for each interval of 0.2 m/s horizontal peak ground velocity are plotted instead.

Table 5.3: Horizontal peak ground velocities in meters per second at which the building models realize a 20% chance of simulated "repairable" performance category or worse, "unrepairable" performance category or worse, and model collapse in the M_w 7.8 ShakeOut scenario earthquake on the San Andreas fault.

Building Performance:	"Repairable" or Worse			"Unrepairable" or Worse			Collapse		
Building Model: / **Foundation Model:**	"Soft"	"Expected"	"Stiff"	"Soft"	"Expected"	"Stiff"	"Soft"	"Expected"	"Stiff"
BLM[a]	0.15	0.12	0.12	0.43	0.45	0.45	0.62	0.62	0.62
RMF-1h	0.15	0.15	0.15	0.55	0.50	0.50	0.75	0.78	0.80
RMF-1	0.15	0.15	0.18	0.53	0.50	0.50	0.80	0.78	0.75
RMF-2h	0.15	0.20	0.20	0.55	0.60	0.62	1.10	0.90	0.95
RMF-2	0.15	0.20	0.20	0.55	0.60	0.62	1.12	0.88	0.90
RMF-3h	0.15	0.23	0.23	0.55	0.60	0.62	1.00	0.88	0.88
RMF-3	0.15	0.25	0.25	0.53	0.68	0.70	-[b]	0.90	0.90
RBR-1	0.20	0.30	0.33	0.48	1.05	1.10	-[c]	-[c]	-[c]
RBR-2	0.20	0.38	0.38	0.53	1.20	1.23	-[c]	-[c]	-[c]
RBR-3	0.15	0.25	0.25	0.58	0.58	0.58	0.95	0.78	0.85
RBRB-1	0.20	0.30	0.30	0.50	0.95	1.00	-[c]	-[c]	-[c]
RBRB-2	0.18	0.30	0.33	0.50	1.00	1.03	-[c]	-[c]	-[c]
RBRB-3	0.15	0.23	0.25	0.58	0.58	0.60	0.93	0.83	0.85

[a] Base Line Model

[b] Fragility curve was not constructed because the data was not well represented by a cumulative log-normal distribution function.

[c] Fragility curve was not constructed because there were so few simulated collapses.

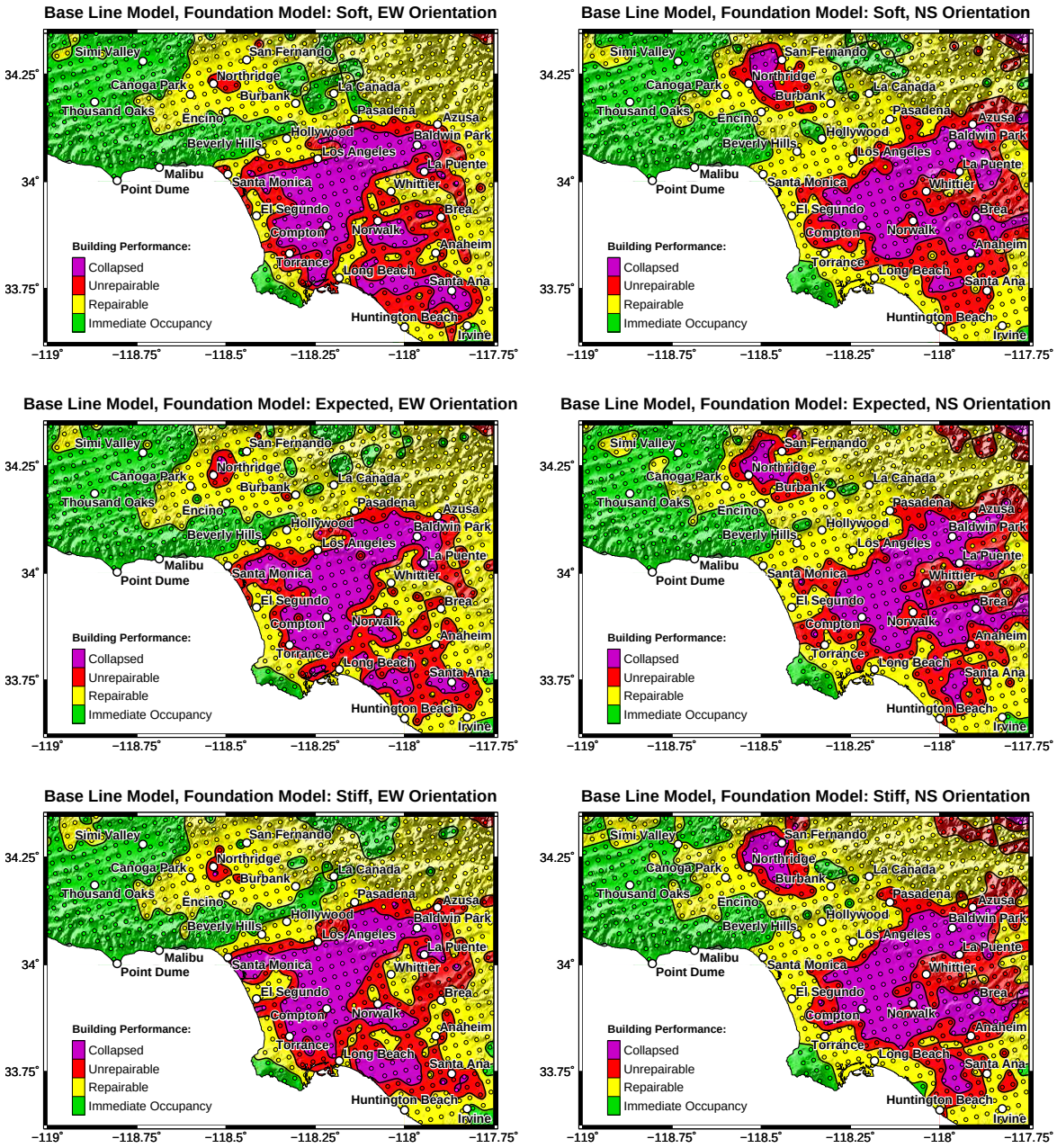

Figure 5.22: Maps of simulated building performance of the Base Line Model in the M_w 7.8 ShakeOut scenario earthquake on the San Andreas fault oriented in east-west (EW) direction (left column) and north-south (NS) direction (right column). The maps in the top row show the model performance using the "soft" realization of the foundations, the maps in the center row show model performance using the "expected" realization of the foundations, and the maps in the bottom row show the model performance using the "stiff" realization of the foundations. The small circles show the simulated building performance at each site. A nearest neighbor method is used to interpolate the building performance between sites.

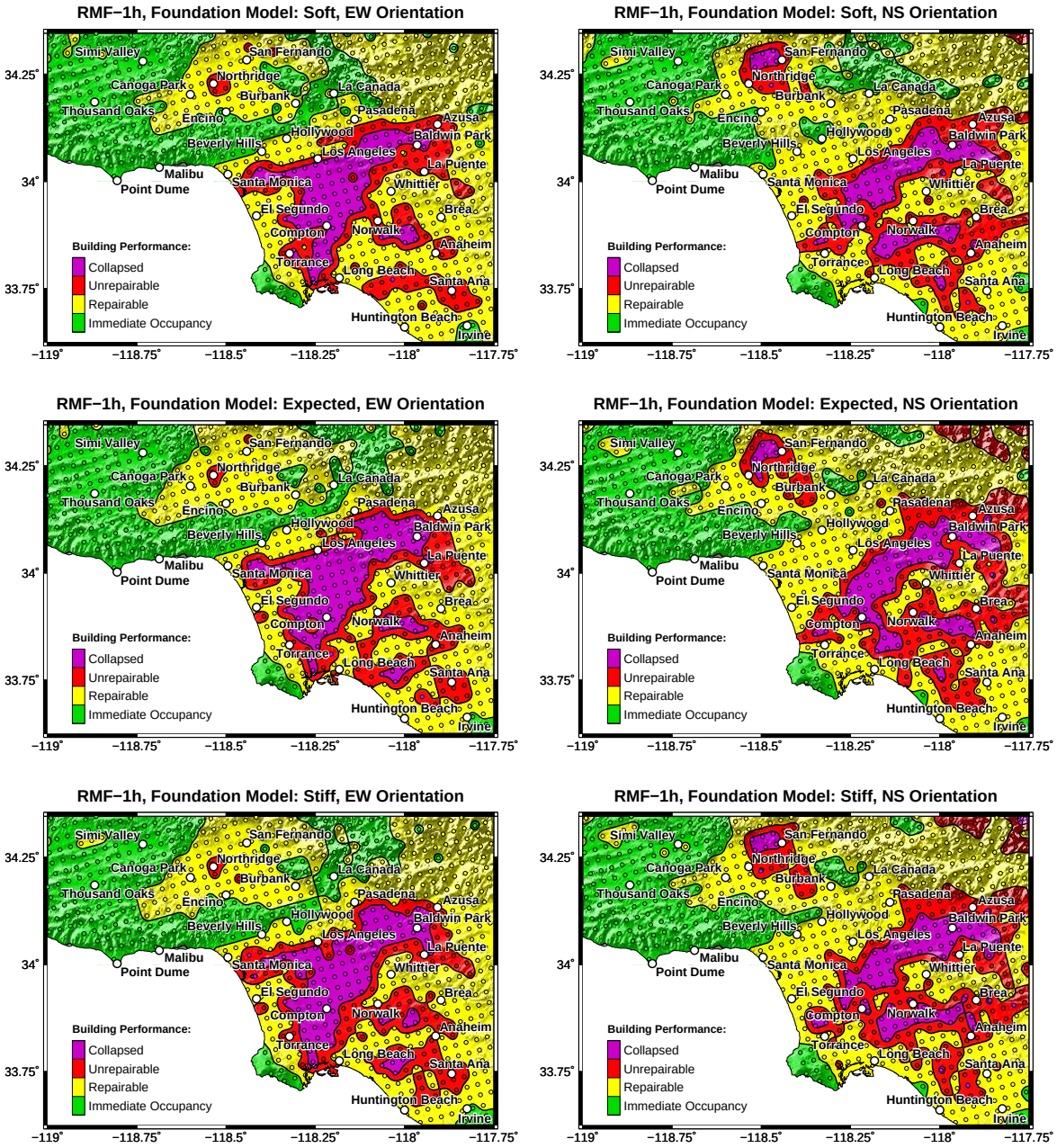

Figure 5.23: Maps of simulated building performance of retrofit scheme RMF-1h in the M_w 7.8 ShakeOut scenario earthquake on the San Andreas fault oriented in east-west (EW) direction (left column) and north-south (NS) direction (right column). The maps in the top row show the model performance using the "soft" realization of the foundations, the maps in the center row show model performance using the "expected" realization of the foundations, and the maps in the bottom row show the model performance using the "stiff" realization of the foundations. The small circles show the simulated building performance at each site. A nearest neighbor method is used to interpolate the building performance between sites.

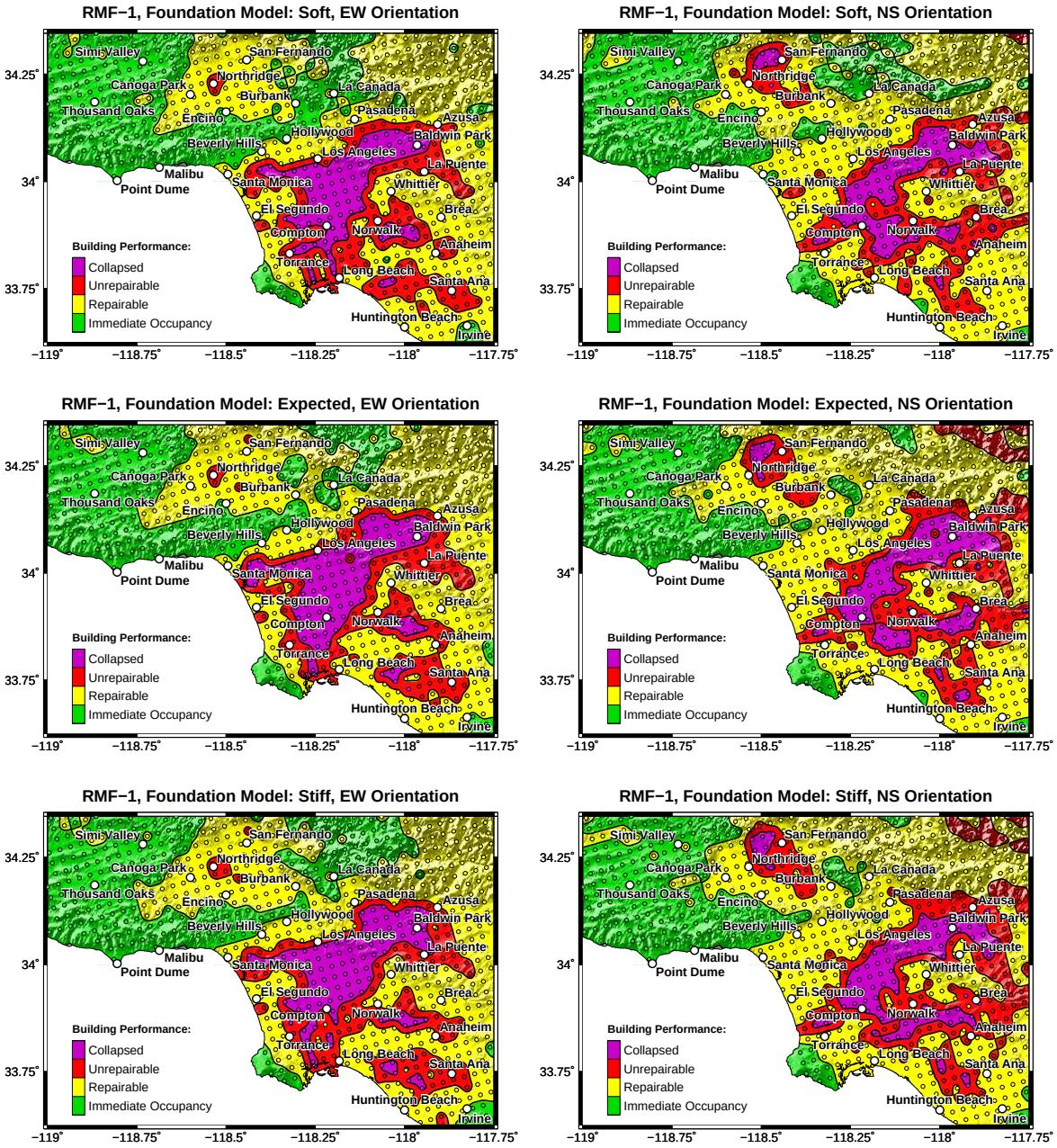

Figure 5.24: Maps of simulated building performance of retrofit scheme RMF-1 in the M_w 7.8 ShakeOut scenario earthquake on the San Andreas fault oriented in east-west (EW) direction (left column) and north-south (NS) direction (right column). The maps in the top row show the model performance using the "soft" realization of the foundations, the maps in the center row show model performance using the "expected" realization of the foundations, and the maps in the bottom row show the model performance using the "stiff" realization of the foundations. The small circles show the simulated building performance at each site. A nearest neighbor method is used to interpolate the building performance between sites.

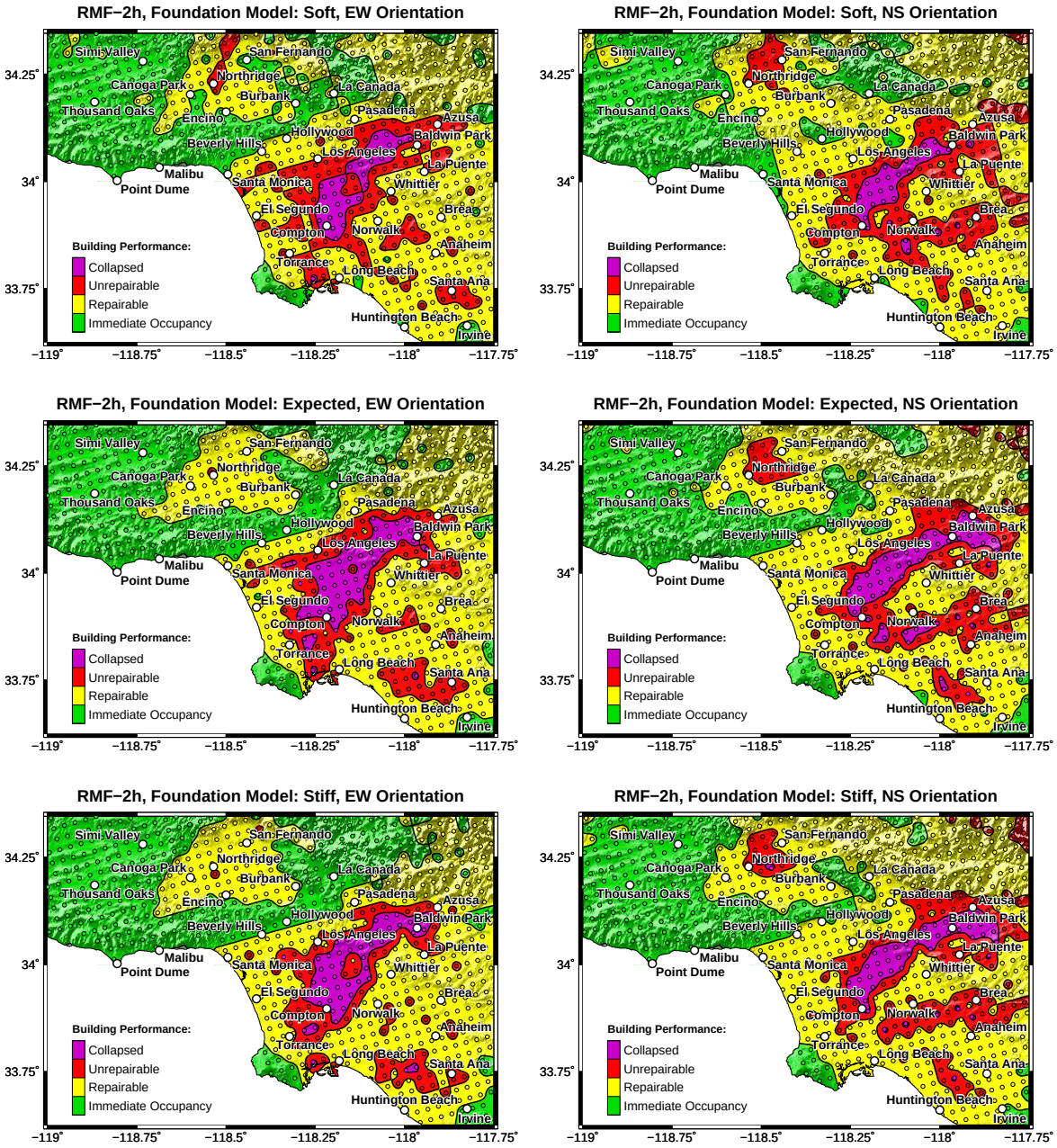

Figure 5.25: Maps of simulated building performance of retrofit scheme RMF-2h in the M_w 7.8 ShakeOut scenario earthquake on the San Andreas fault oriented in east-west (EW) direction (left column) and north-south (NS) direction (right column). The maps in the top row show the model performance using the "soft" realization of the foundations, the maps in the center row show model performance using the "expected" realization of the foundations, and the maps in the bottom row show the model performance using the "stiff" realization of the foundations. The small circles show the simulated building performance at each site. A nearest neighbor method is used to interpolate the building performance between sites.

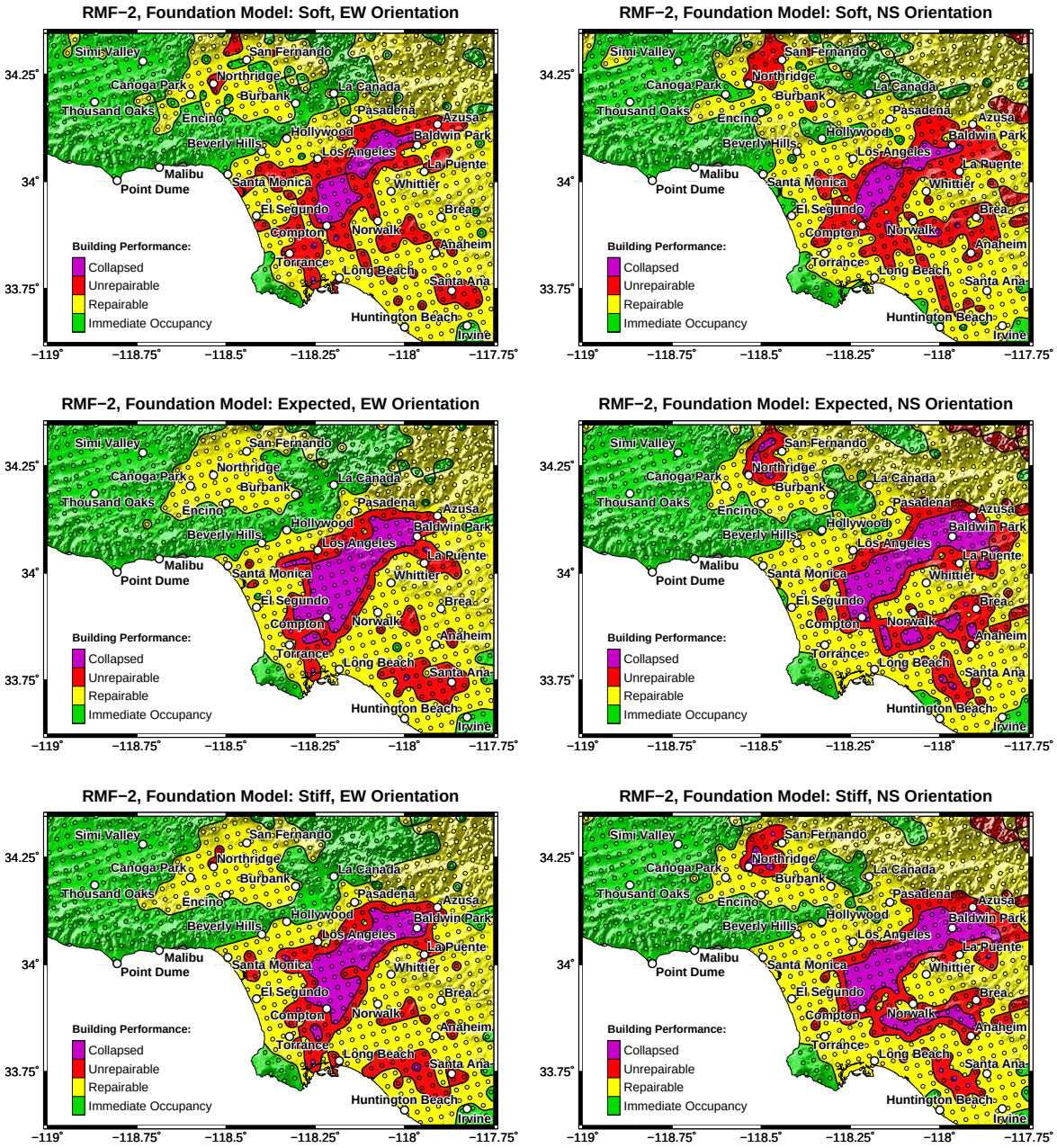

Figure 5.26: Maps of simulated building performance of retrofit scheme RMF-2 in the M_w 7.8 ShakeOut scenario earthquake on the San Andreas fault oriented in east-west (EW) direction (left column) and north-south (NS) direction (right column). The maps in the top row show the model performance using the "soft" realization of the foundations, the maps in the center row show model performance using the "expected" realization of the foundations, and the maps in the bottom row show the model performance using the "stiff" realization of the foundations. The small circles show the simulated building performance at each site. A nearest neighbor method is used to interpolate the building performance between sites.

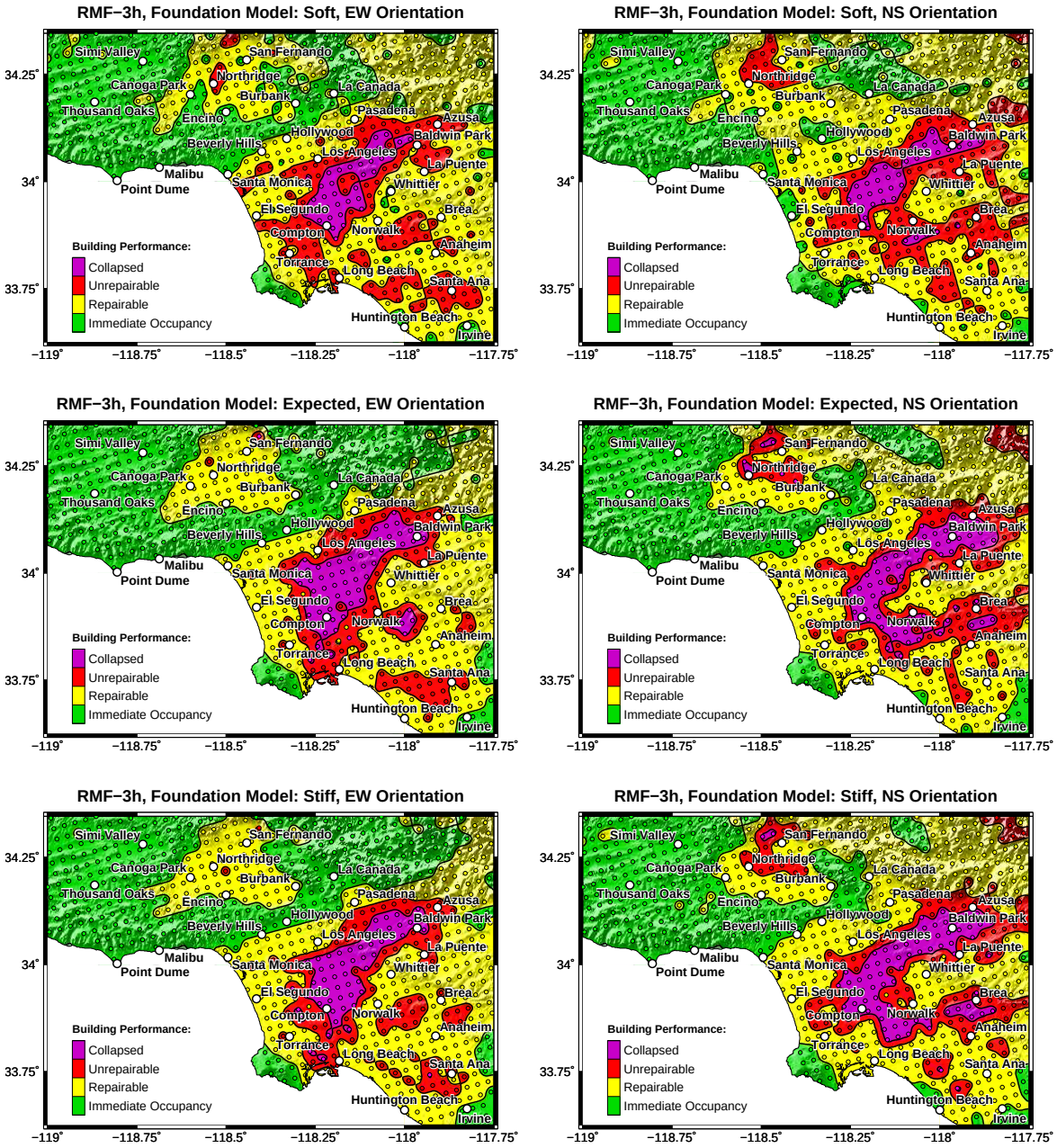

Figure 5.27: Maps of simulated building performance of retrofit scheme RMF-3h in the M_w 7.8 ShakeOut scenario earthquake on the San Andreas fault oriented in east-west (EW) direction (left column) and north-south (NS) direction (right column). The maps in the top row show the model performance using the "soft" realization of the foundations, the maps in the center row show model performance using the "expected" realization of the foundations, and the maps in the bottom row show the model performance using the "stiff" realization of the foundations. The small circles show the simulated building performance at each site. A nearest neighbor method is used to interpolate the building performance between sites.

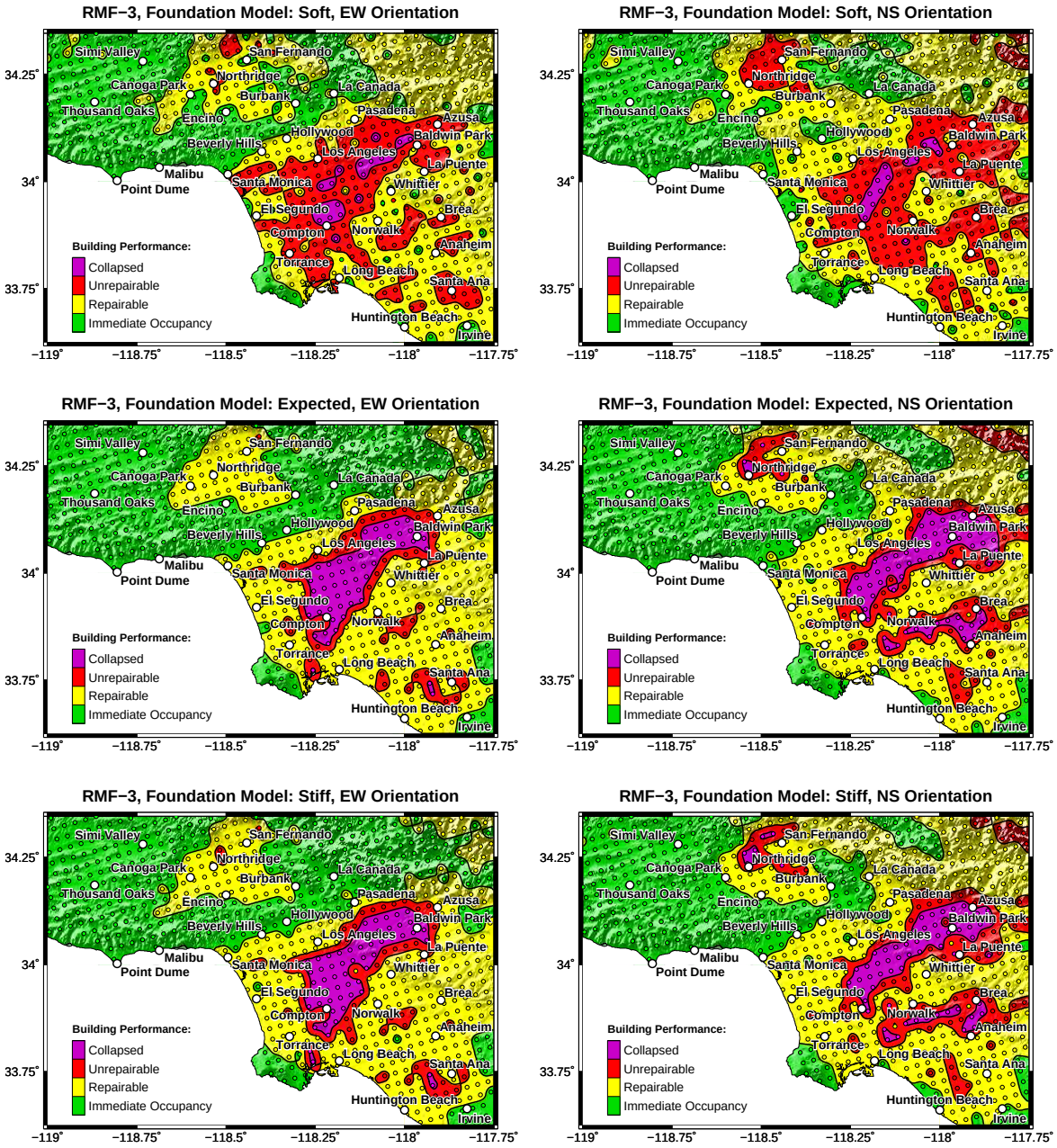

Figure 5.28: Maps of simulated building performance of retrofit scheme RMF-3 in the M_w 7.8 ShakeOut scenario earthquake on the San Andreas fault oriented in east-west (EW) direction (left column) and north-south (NS) direction (right column). The maps in the top row show the model performance using the "soft" realization of the foundations, the maps in the center row show model performance using the "expected" realization of the foundations, and the maps in the bottom row show the model performance using the "stiff" realization of the foundations. The small circles show the simulated building performance at each site. A nearest neighbor method is used to interpolate the building performance between sites.

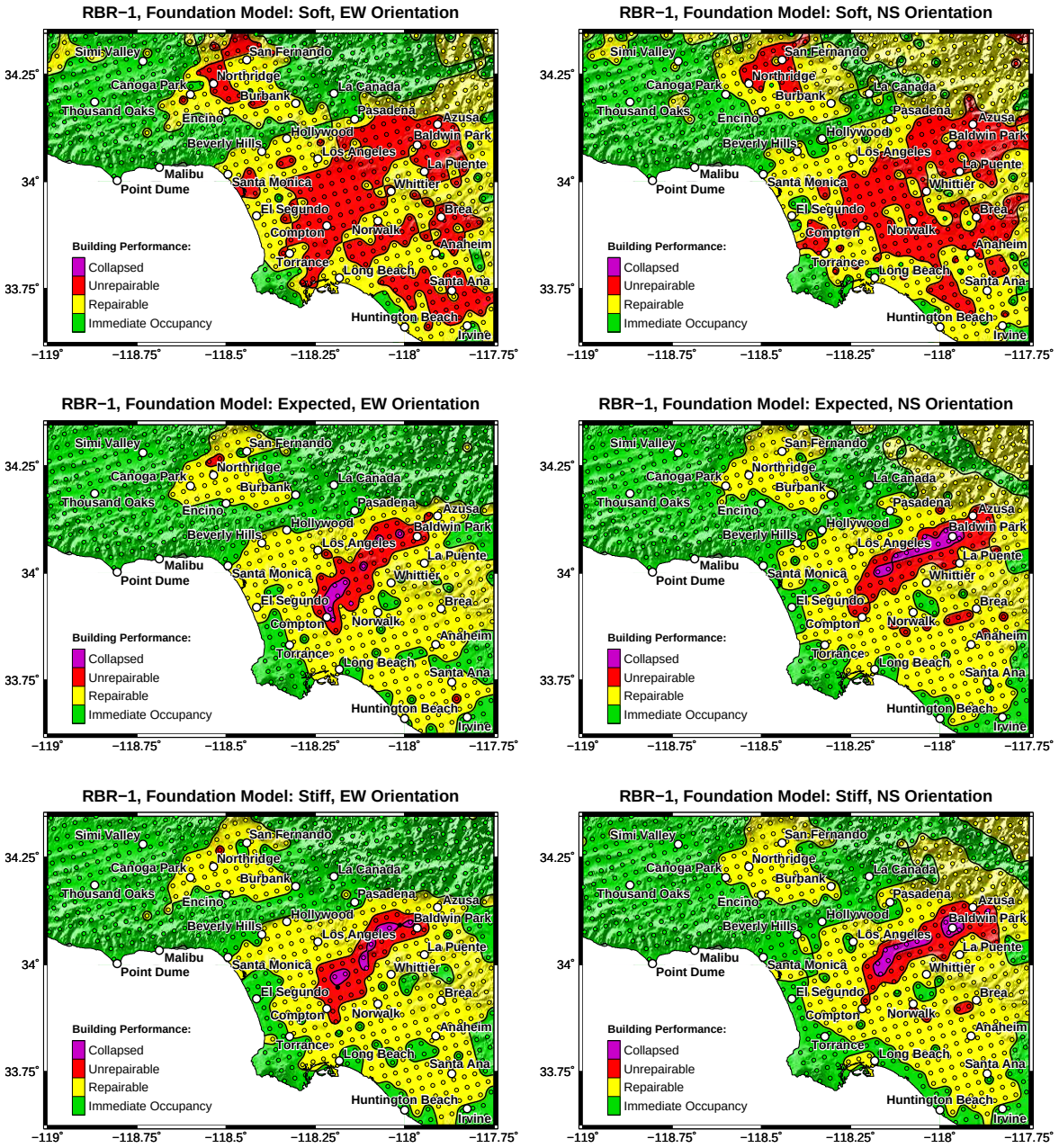

Figure 5.29: Maps of simulated building performance of retrofit scheme RBR-1 in the M_w 7.8 ShakeOut scenario earthquake on the San Andreas fault oriented in east-west (EW) direction (left column) and north-south (NS) direction (right column). The maps in the top row show the model performance using the "soft" realization of the foundations, the maps in the center row show model performance using the "expected" realization of the foundations, and the maps in the bottom row show the model performance using the "stiff" realization of the foundations. The small circles show the simulated building performance at each site. Sites where simulations failed to converge before showing a clear sign of model collapse are shown as small black circles. A nearest neighbor method is used to interpolate the building performance between sites.

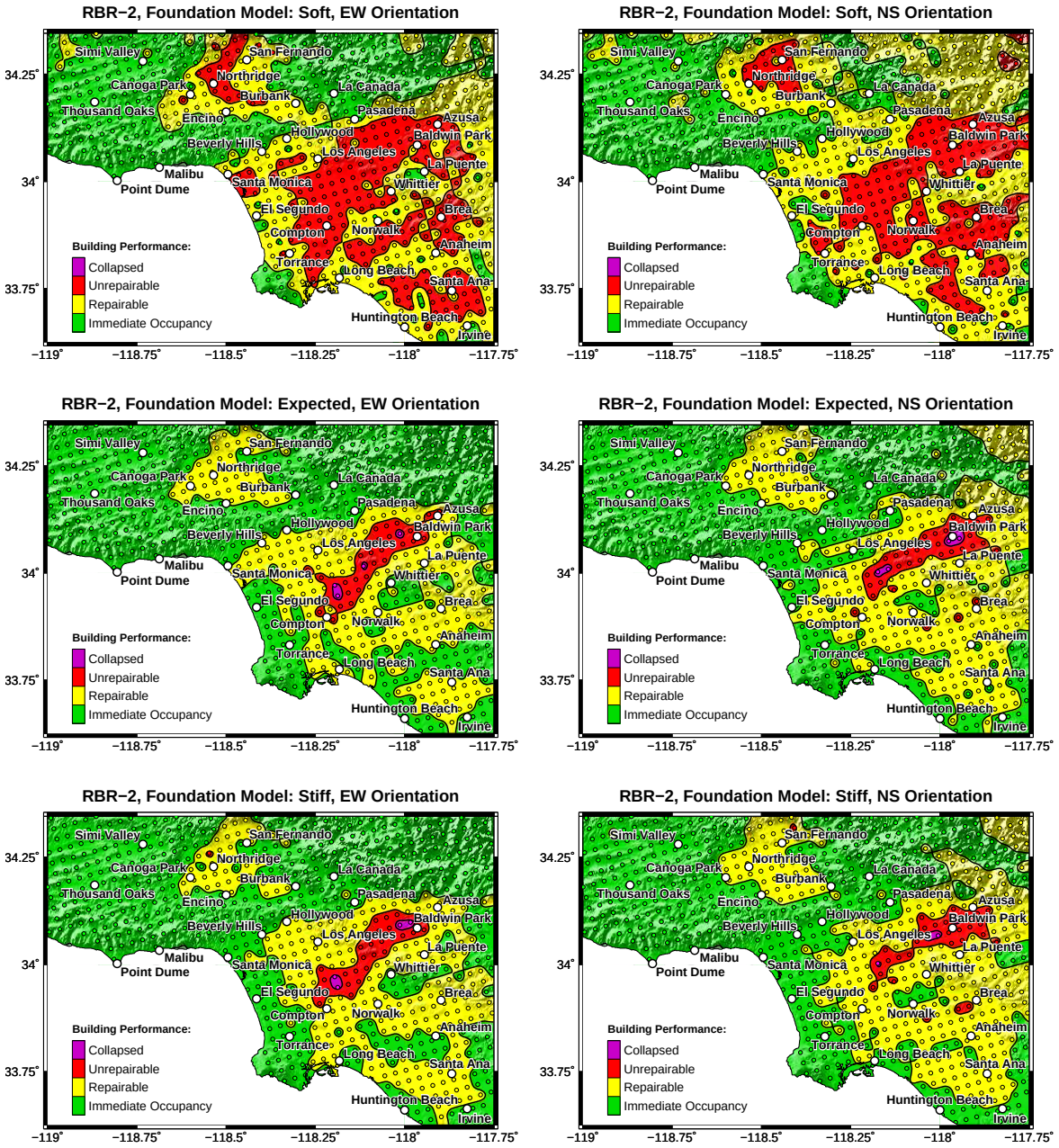

Figure 5.30: Maps of simulated building performance of retrofit scheme RBR-2 in the M_w 7.8 ShakeOut scenario earthquake on the San Andreas fault oriented in east-west (EW) direction (left column) and north-south (NS) direction (right column). The maps in the top row show the model performance using the "soft" realization of the foundations, the maps in the center row show model performance using the "expected" realization of the foundations, and the maps in the bottom row show the model performance using the "stiff" realization of the foundations. The small circles show the simulated building performance at each site. A nearest neighbor method is used to interpolate the building performance between sites.

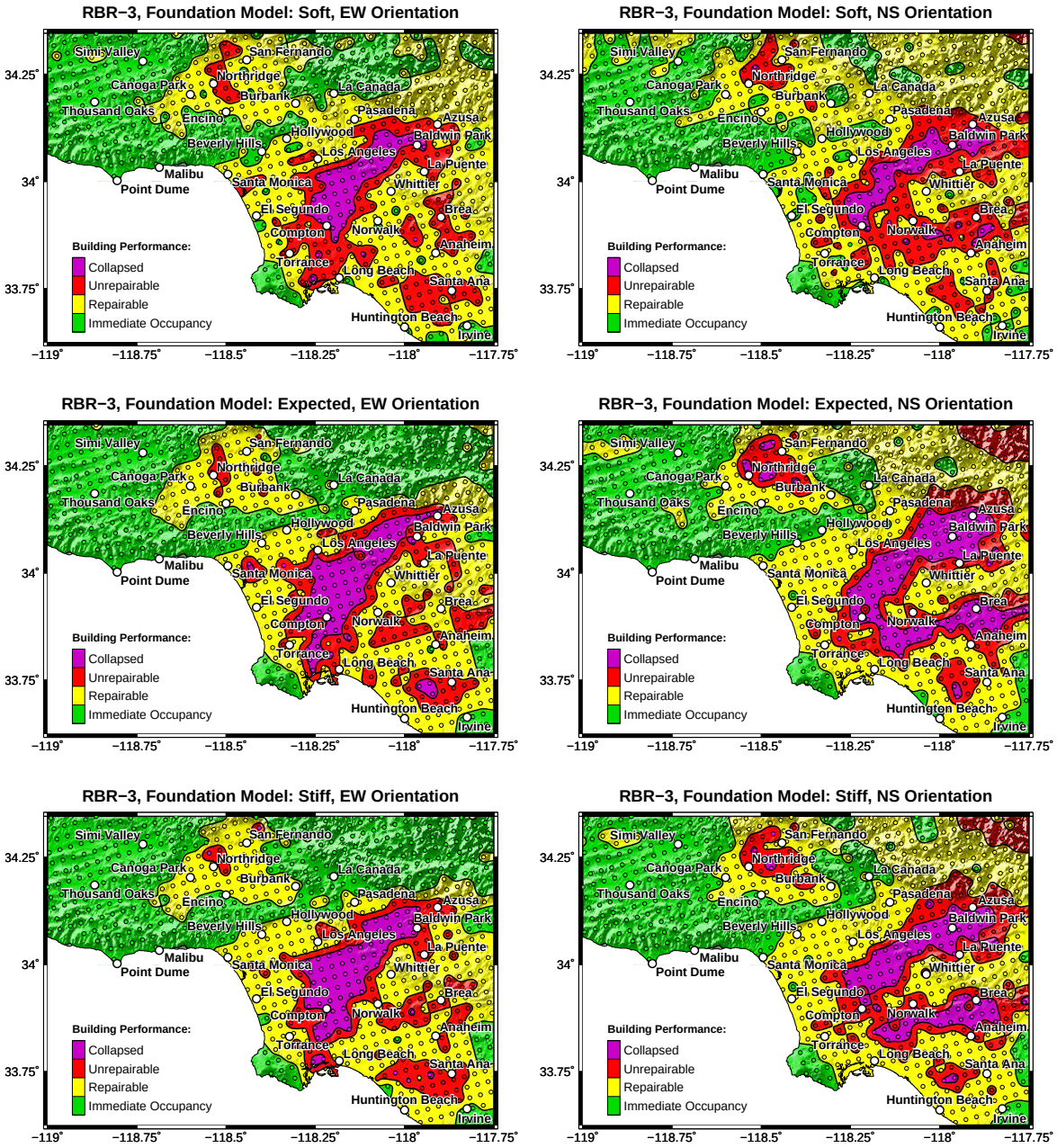

Figure 5.31: Maps of simulated building performance of retrofit scheme RBR-3 in the M_w 7.8 ShakeOut scenario earthquake on the San Andreas fault oriented in east-west (EW) direction (left column) and north-south (NS) direction (right column). The maps in the top row show the model performance using the "soft" realization of the foundations, the maps in the center row show model performance using the "expected" realization of the foundations, and the maps in the bottom row show the model performance using the "stiff" realization of the foundations. The small circles show the simulated building performance at each site. A nearest neighbor method is used to interpolate the building performance between sites.

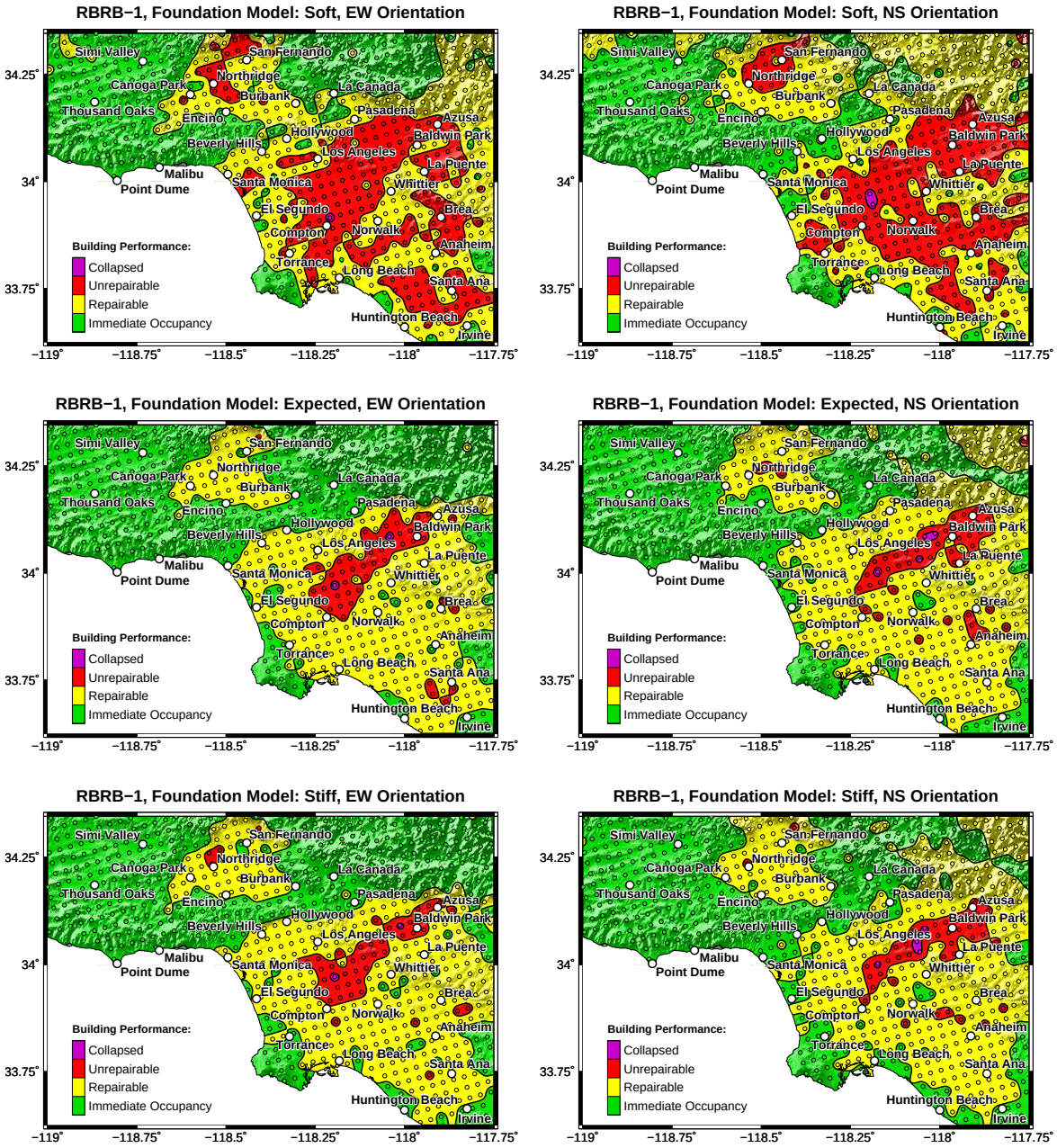

Figure 5.32: Maps of simulated building performance of retrofit scheme RBRB-1 in the M_w 7.8 ShakeOut scenario earthquake on the San Andreas fault oriented in east-west (EW) direction (left column) and north-south (NS) direction (right column). The maps in the top row show the model performance using the "soft" realization of the foundations, the maps in the center row show model performance using the "expected" realization of the foundations, and the maps in the bottom row show the model performance using the "stiff" realization of the foundations. The small circles show the simulated building performance at each site. A nearest neighbor method is used to interpolate the building performance between sites.

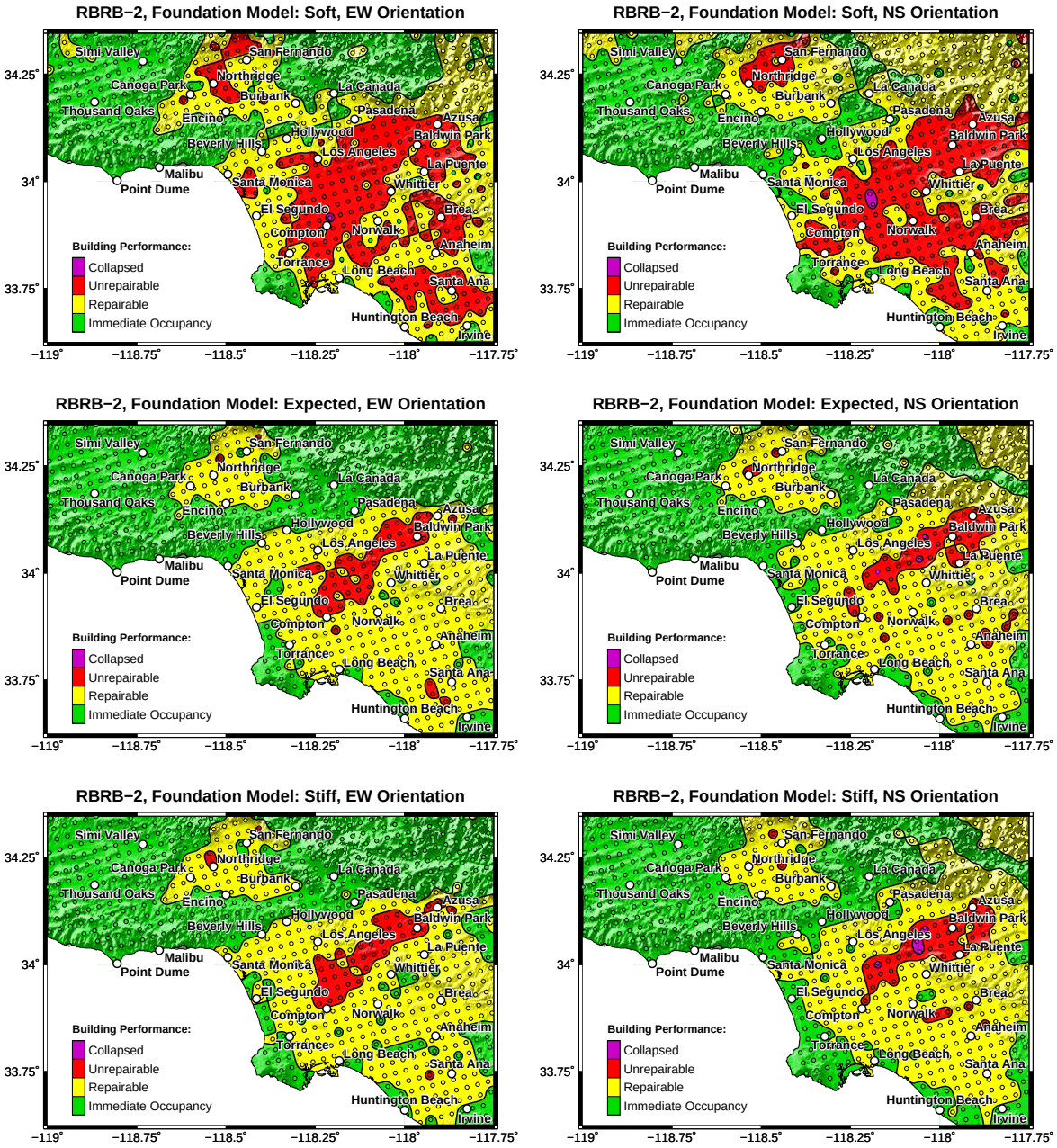

Figure 5.33: Maps of simulated building performance of retrofit scheme RBRB-2 in the M_w 7.8 ShakeOut scenario earthquake on the San Andreas fault oriented in east-west (EW) direction (left column) and north-south (NS) direction (right column). The maps in the top row show the model performance using the "soft" realization of the foundations, the maps in the center row show model performance using the "expected" realization of the foundations, and the maps in the bottom row show the model performance using the "stiff" realization of the foundations. The small circles show the simulated building performance at each site. A nearest neighbor method is used to interpolate the building performance between sites.

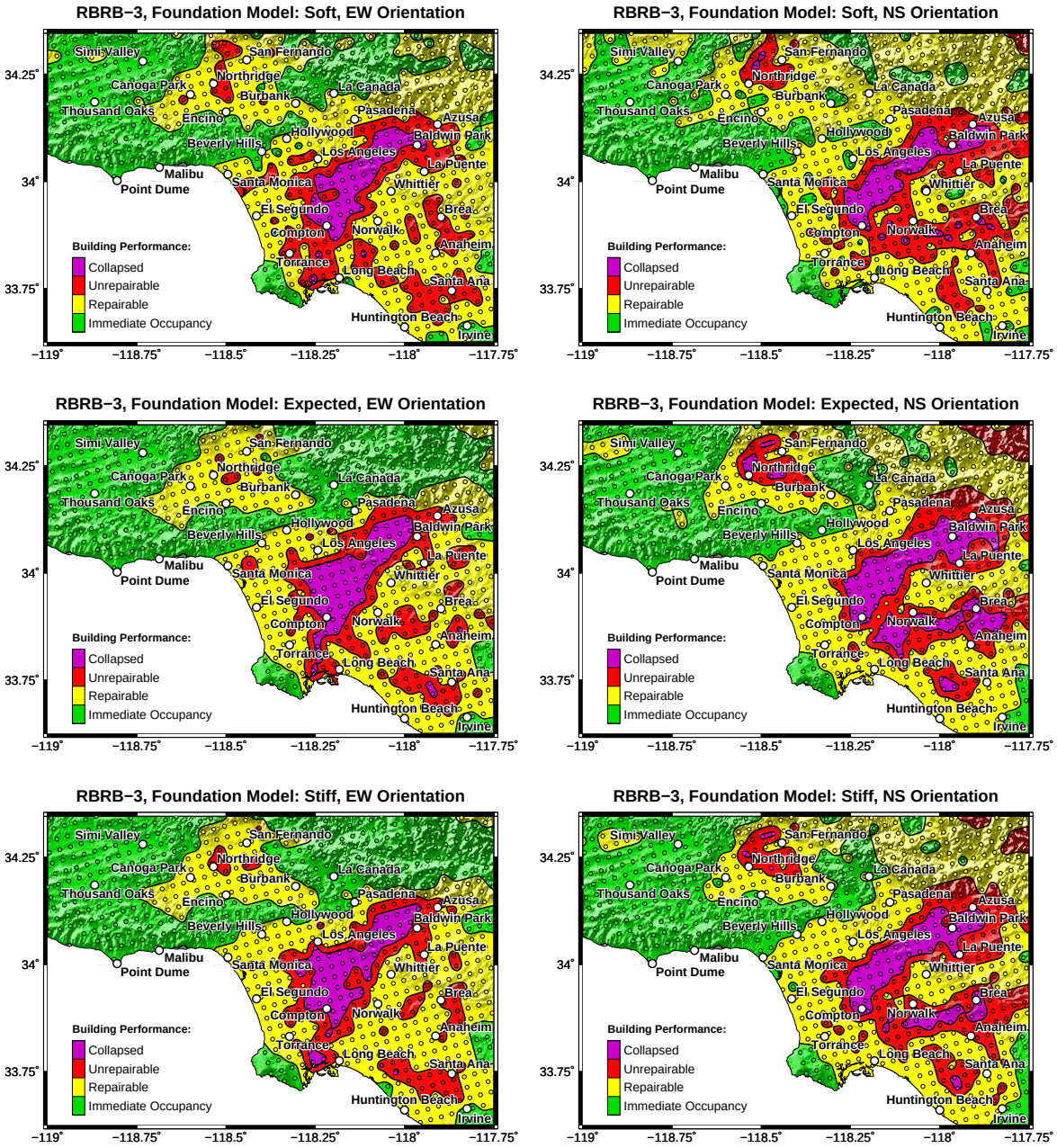

Figure 5.34: Maps of simulated building performance of retrofit scheme RBRB-3 in the M_w 7.8 ShakeOut scenario earthquake on the San Andreas fault oriented in east-west (EW) direction (left column) and north-south (NS) direction (right column). The maps in the top row show the model performance using the "soft" realization of the foundations, the maps in the center row show model performance using the "expected" realization of the foundations, and the maps in the bottom row show the model performance using the "stiff" realization of the foundations. The small circles show the simulated building performance at each site. A nearest neighbor method is used to interpolate the building performance between sites.

5.3 Building Performance: M_w 7.2 Puente Hills Scenario Earthquake

Results in the scenario earthquake on the Puente Hills fault system are presented in a similar fashion as the results in the two simulated San Andreas fault earthquake scenarios. The number of simulations per building model that resulted in the "repairable", "unrepairable", and "collapse" performance categories are summarized in Figure 5.35. Fragility plots that show the probability of the building models realizing "repairable" performance category or worse, "unrepairable" performance category or worse, or model collapse, given horizontal peak ground velocity, are presented in Figures 5.36, 5.37, and 5.38, respectively. Finally, maps that geographically show the distribution of simulated performance categories in the greater Los Angeles metropolitan area for each building model are presented in Figures 5.39 to 5.51 as follows:

	Figure:		Figure:
Base Line Model	5.39	RBR-1	5.46
RMF-1h	5.40	RBR-2	5.47
RMF-1	5.41	RBR-3	5.48
RMF-2h	5.42	RBRB-1	5.49
RMF-2	5.43	RBRB-2	5.50
RMF-3h	5.44	RBRB-3	5.51
RMF-3	5.45		

The results in the scenario earthquake on the Puente Hills fault system show trends similar to what was observed in the two simulated San Andreas fault earthquake scenarios.

When employing the "expected" foundation model, the base line model is simulated to collapse at 69 sites (out of 587) when the building model is oriented in the east-west direction and at 126 sites when oriented in north-south. Each site represents an area of 9 km^2. These sites cover a large portion of the Los Angeles basin, and model collapse is also simulated at several sites in the San Gabriel basin. Furthermore, complete economic loss ("unrepairable" or "collapse" performance categories) of the base line model is simulated at 126 sites when the building model is oriented in the east-west direction, and at 182 sites when oriented in north-south.

A single model collapse is simulated for retrofit scheme RBR-1 (both orientations), and none are simulated for schemes RBR-2, RBRB-1, and RBRB-2.

As for complete economic losses, scheme RBR-2 performs best, with complete economic losses simulated at 16 sites when the building model is oriented in the east-west direction, and at 65 sites when oriented in north-south. Complete economic loss is simulated at a total (both orientations) of 97 sites for scheme RBR-1, and at total (both orientation) of 127-128 sites for schemes RBRB-1 and RBRB-2. As was mentioned in the previous sections, it appears that braced-frames that employ buckling-restrained braces tend to have greater residual drifts. However, the buckling-restrained braces are likely to store significant residual forces, and the residual drifts may be recovered to some extent by replacing the deformed braces. Conventional brace elements are not expected to store residual forces to the same degree.

Interestingly, out of the retrofit schemes that consider retrofitting the brittle beam-to-column moment resisting connections (RMF schemes), scheme RMF-2h performs best, with model collapse simulated at 10 sites when the building model is oriented in the east-west direction, and at 31 sites when oriented in north-south. Furthermore, complete economic loss of the building model is simulated at 52 sites when it is oriented in the east-west direction, and at 123 sites when oriented in north-south. Schemes RMF-2, RMF-3h, and RMF-3 are simulated to collapse at total (both orientations) of 72-74 sites, and complete economic losses of the three schemes are simulated at total (both orientations) of 188, 210, and 177 sites, respectively.

Because of the complex nature of building responses under strong ground motions, it is difficult to give an argument that irrefutably justifies that repairing fewer beam-to-column connections will lead to lower collapse potential than if all the connections are upgraded. Also, the ground motion time histories have a similar signature from site-to-site, which is a characteristic of this particular simulated earthquake. This signature in the ground motions happened to induce fewer simulated collapses for scheme RMF-2h compared to RMF-3, but it may necessarily repeated in other earthquakes. However, these results suggest that at a certain point, upgrading additional beam-to-column connections will result in minimal additional improvement in performance.

The two retrofit schemes that implement brace elements in the lower half of the building model while leaving the upper half unaltered (schemes RBR-3 and RBRB-3), as before, are somewhat successful in that the schemes are more effective in limiting deformations in the lower half of the building model compared to the moment-frame half-height retrofit schemes (RMF-1h, RMF-2h, and RMF-3h), and thus reduce to a greater extent global P-delta overturning moments. However, as was mentioned in the previous sections, the resulting structures are stiffer than the moment-frame

configurations and consequently attract larger seismic forces, which often results in excessive drifts in the upper half. A retrofit scheme that implements brace elements in the lower half of the building model in conjunction with upgrading beam-to-column moment connections in the upper half may present some additional improvement in building performance while keeping architectural impact low. Retrofit schemes RBR-3 and RBRB-3 are simulated to collapse at a total (both orientations) of 82 and 65 sites, respectively, and complete economic loss of the building models is simulated at a total (both orientations) of 243 and 214 sites, respectively.

From the fragility curves constructed from the data, the simulated building performances can be related to horizontal peak ground velocities (PGV). Because there were so few simulated collapses for retrofit schemes RBR-1, RBR-2, RBRB-1, and RBRB-2, fragility curves showing the probability of simulated model collapse given horizontal peak ground velocity are not constructed. In a few other cases, such curves were not constructed because the data was not well represented by a cumulative log-normal distribution function, and instead, the actual fraction of simulations that resulted in simulated model collapse for each interval of 0.2 m/s horizontal peak ground velocity is plotted. However, fragility curves showing the probability of collapse given horizontal peak ground velocity were constructed for retrofit scheme RMF-3 and the base line model. Retrofit scheme RMF-3 realizes a 20% of simulated model collapse at a horizontal peak ground velocity of 1.2 m/s, compared to a velocity of 0.8 m/s for the base line model. These velocities are greater than what was observed in the two San Andreas fault earthquake scenarios. The difference is likely due to the longer duration of ground shaking experienced for the San Andreas fault earthquake scenarios.

The horizontal peak ground velocities at which the building models realize a 20% chance of simulated “repairable” performance category or worse, “unrepairable” performance category or worse, and model collapse are summarized in Table 5.4.

The “expected” and “stiff” foundation models resulted in very similar building performances. When employing the “stiff” foundation model, foundation reactions were in the elastic range for all building models. When employing the “expected” foundation model, foundation reactions were in the elastic range for all but four building models. Yielding of the foundation springs was observed (in a few simulations) for retrofit schemes RBRB-1 and RBRB-2, but more noticeably for schemes RBR-1 and RBR-2, with residual foundation rotations up to around 1%. When employing the “soft” foundation model, the capacities of the foundation springs were frequently exceeded in all building models at only moderate levels of seismicity. As a result, all building models realized

similar potential for exceeding the “immediate occupancy” foundation residual rotation limit, and only modest reduction in number of simulated complete economic losses of the building models is observed for the retrofit schemes. However, the foundations were never simulated to loose stability, although residual foundation rotations were observed to be as large as 7%, and the retrofit schemes achieve even more dramatic reduction in collapse potential, compared to when the “expected” and “stiff” foundation models are employed.

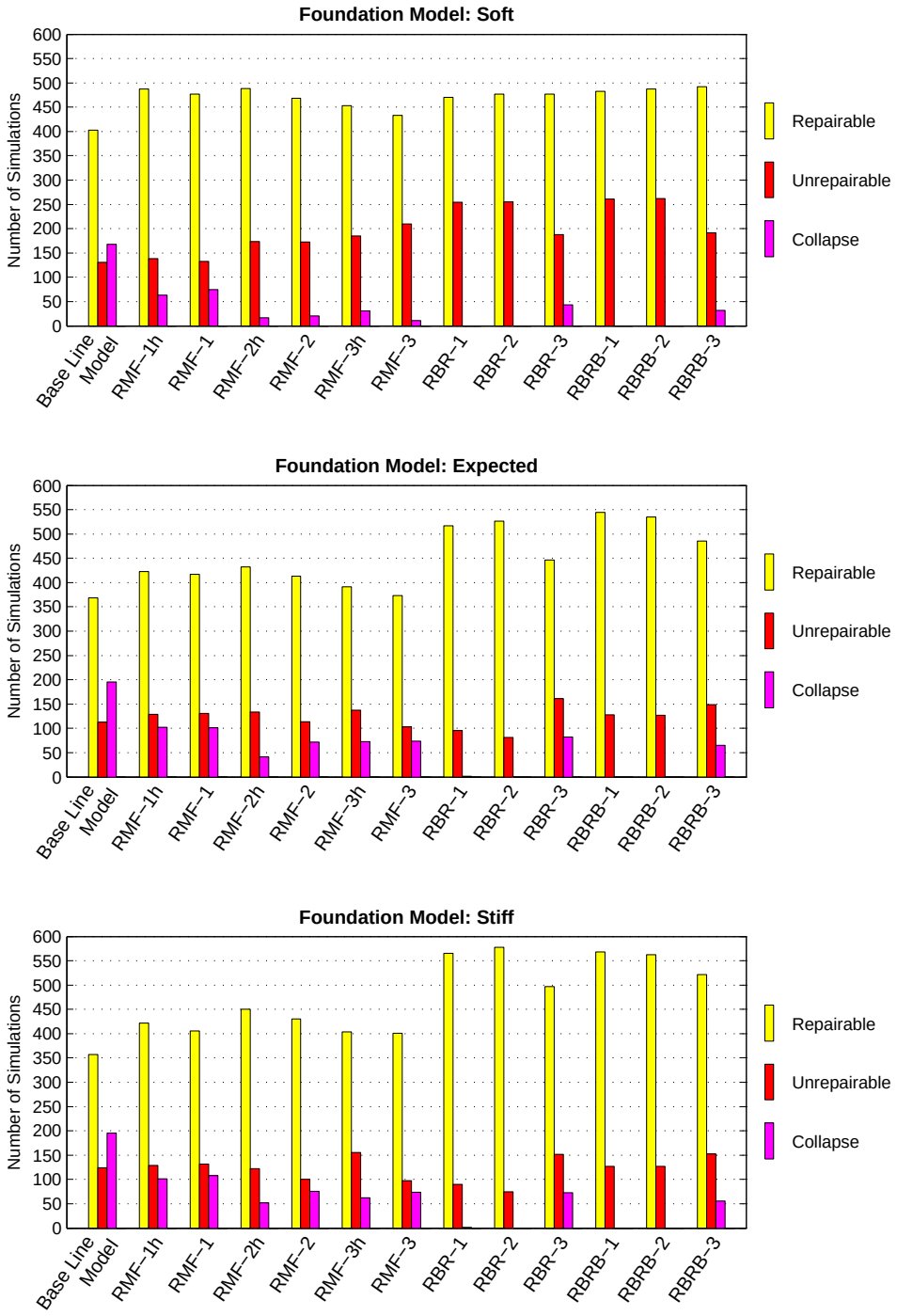

Figure 5.35: Summary of the number of simulations that resulted in the "repairable", "unrepairable", and "collapse" performance categories in the M_w 7.2 scenario earthquake on the Puente Hills fault system, assuming the "soft" (top figure), "expected" (middle figure), and "stiff" (bottom figure) foundation spring stiffnesses. The total number of simulations carried out for each building model, for each assumption on foundation spring stiffnesses, is 1174.

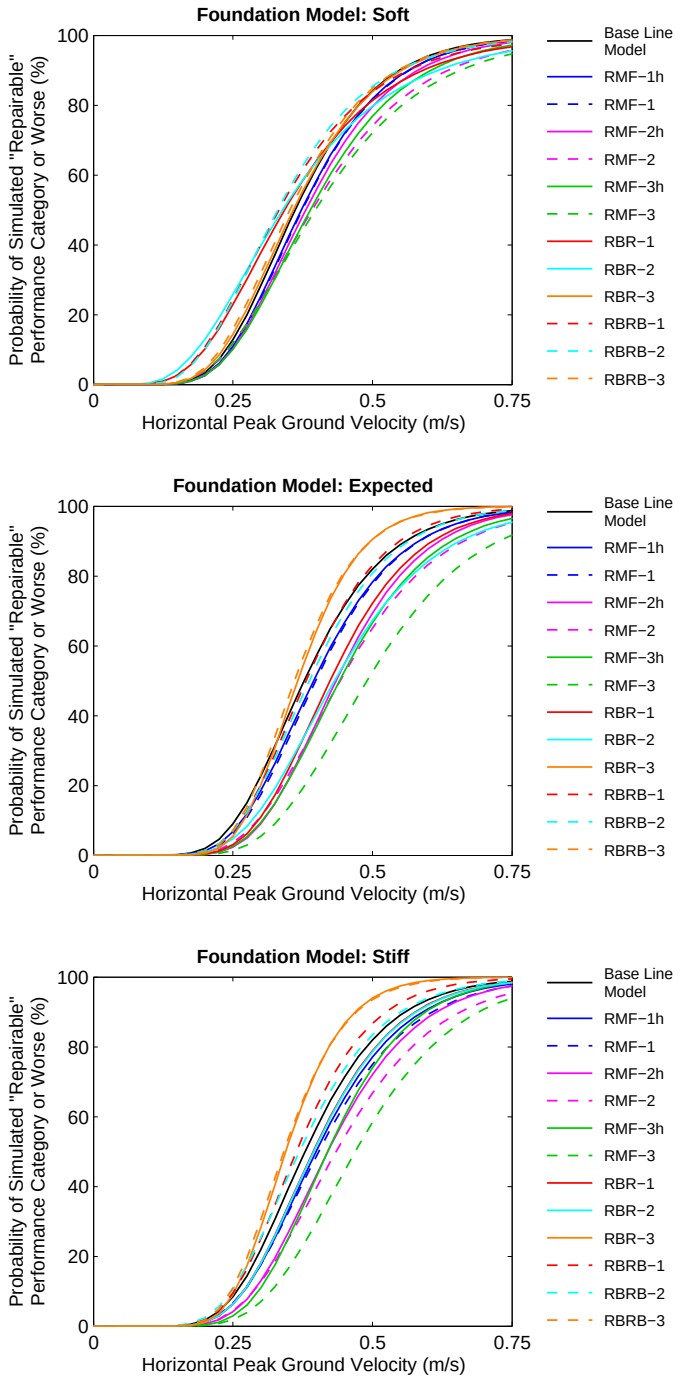

Figure 5.36: Fragility curves showing the probability of the building models realizing the "repairable" performance category or worse given horizontal peak ground velocity in the M_w 7.2 scenario earthquake on the Puente Hills fault system, assuming the "soft" (top figure), "expected" (middle figure), and "stiff" (bottom figure) foundation spring stiffnesses.

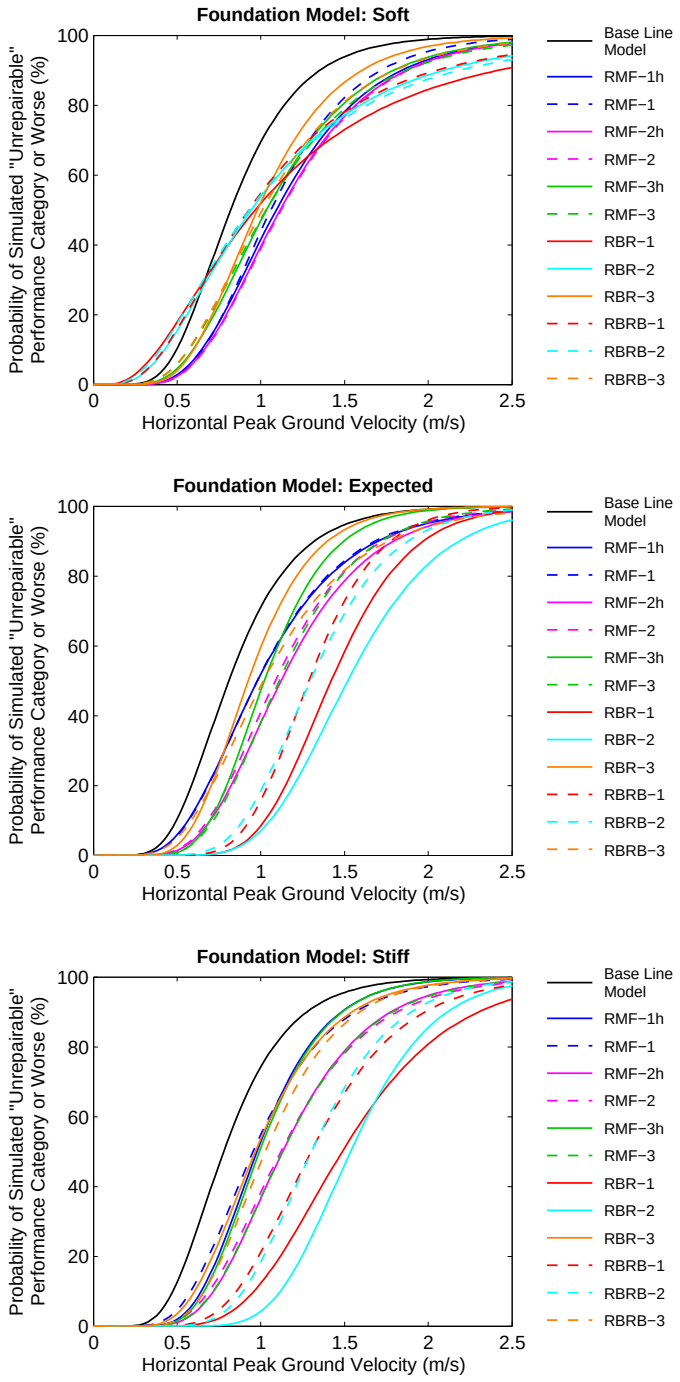

Figure 5.37: Fragility curves showing the probability of the building models realizing the "unrepairable" performance category or worse given horizontal peak ground velocity in the M_w 7.2 scenario earthquake on the Puente Hills fault system, assuming the "soft" (top figure), "expected" (middle figure), and "stiff" (bottom figure) foundation spring stiffnesses.

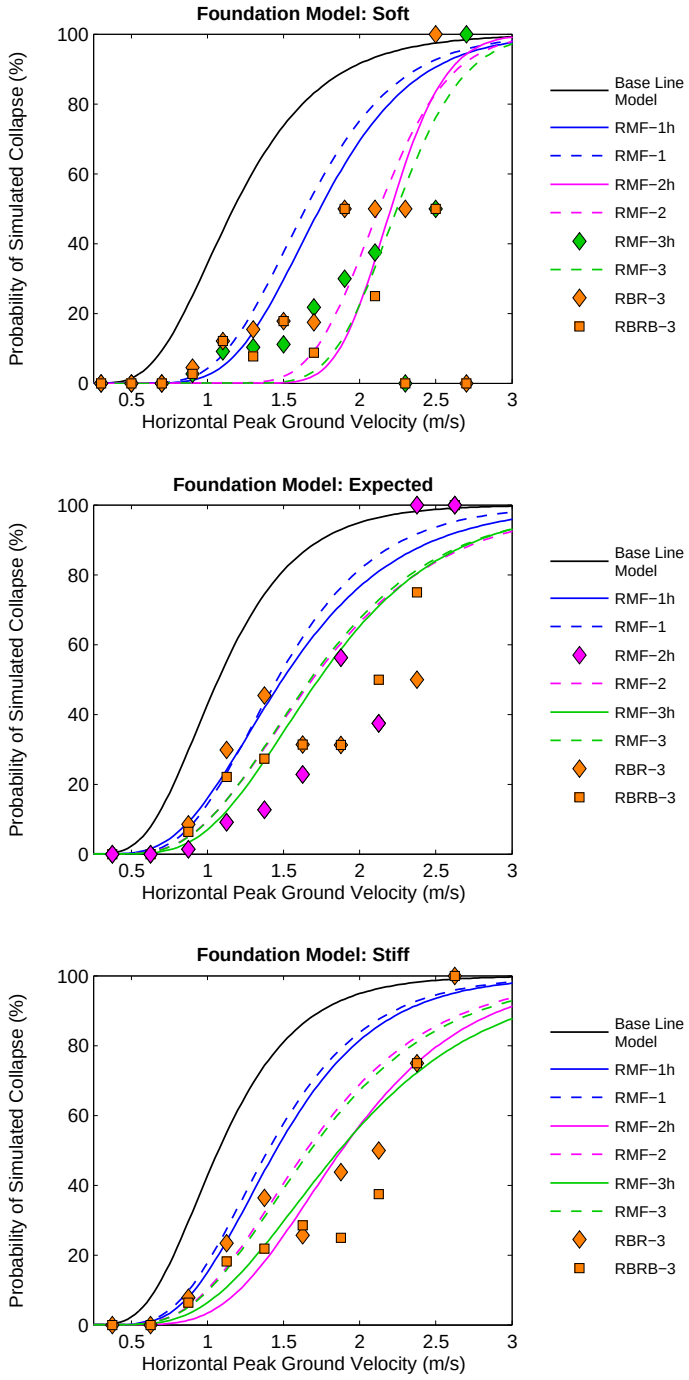

Figure 5.38: Fragility curves showing the probability of the building models realizing model collapse given horizontal peak ground velocity in the M_w 7.2 scenario earthquake on the Puente Hills fault system, assuming the "soft" (top figure), "expected" (middle figure), and "stiff" (bottom figure) foundation spring stiffnesses. Because almost none of the simulations resulted in model collapse of retrofit schemes RBR-1, RBR-2, RBRB-1, and RBRB-2, fragility curves are not constructed for those schemes. Furthermore, the data for some of the remaining retrofit schemes is not well represented by cumulative log-normal distribution functions, and the actual fractions of the simulations that resulted in simulated model collapse for each interval of 0.2 m/s horizontal peak ground velocity are plotted instead.

Table 5.4: Horizontal peak ground velocities in meters per second at which the building models realize a 20% chance of simulated "repairable" performance category or worse, "unrepairable" performance category or worse, and model collapse in the M_w 7.2 scenario earthquake on the Puente Hills fault system.

Building Performance:	"Repairable" or Worse			"Unrepairable" or Worse			Collapse		
Building Model: / **Foundation Model:**	"Soft"	"Expected"	"Stiff"	"Soft"	"Expected"	"Stiff"	"Soft"	"Expected"	"Stiff"
BLM[a]	0.28	0.30	0.30	0.60	0.58	0.55	0.85	0.78	0.78
RMF-1	0.28	0.30	0.30	0.78	0.68	0.75	1.38	1.07	1.07
RMF-1h	0.28	0.30	0.30	0.78	0.68	0.70	1.30	1.07	1.03
RMF-2h	0.30	0.35	0.33	0.80	0.83	0.85	1.97	-[b]	1.40
RMF-2	0.28	0.35	0.33	0.80	0.80	0.83	1.85	1.20	1.18
RMF-3h	0.30	0.35	0.33	0.73	0.80	0.75	-[b]	1.28	1.33
RMF-3	0.28	0.38	0.38	0.70	0.83	0.83	1.97	1.20	1.20
RBR-1	0.25	0.33	0.30	0.53	1.15	1.12	-[c]	-[c]	-[c]
RBR-2	0.23	0.33	0.30	0.55	1.20	1.25	-[c]	-[c]	-[c]
RBR-3	0.28	0.30	0.28	0.70	0.70	0.70	-[b]	-[b]	-[b]
RBRB-1	0.23	0.30	0.28	0.55	1.05	0.98	-[c]	-[c]	-[c]
RBRB-2	0.23	0.30	0.28	0.53	1.03	1.03	-[c]	-[c]	-[c]
RBRB-3	0.28	0.30	0.28	0.70	0.70	0.78	-[b]	-[b]	-[b]

[a] Base Line Model

[b] Fragility curve was not constructed because the data was not well represented by a cumulative log-normal distribution function.

[c] Fragility curve was not constructed because there were so few simulated collapses.

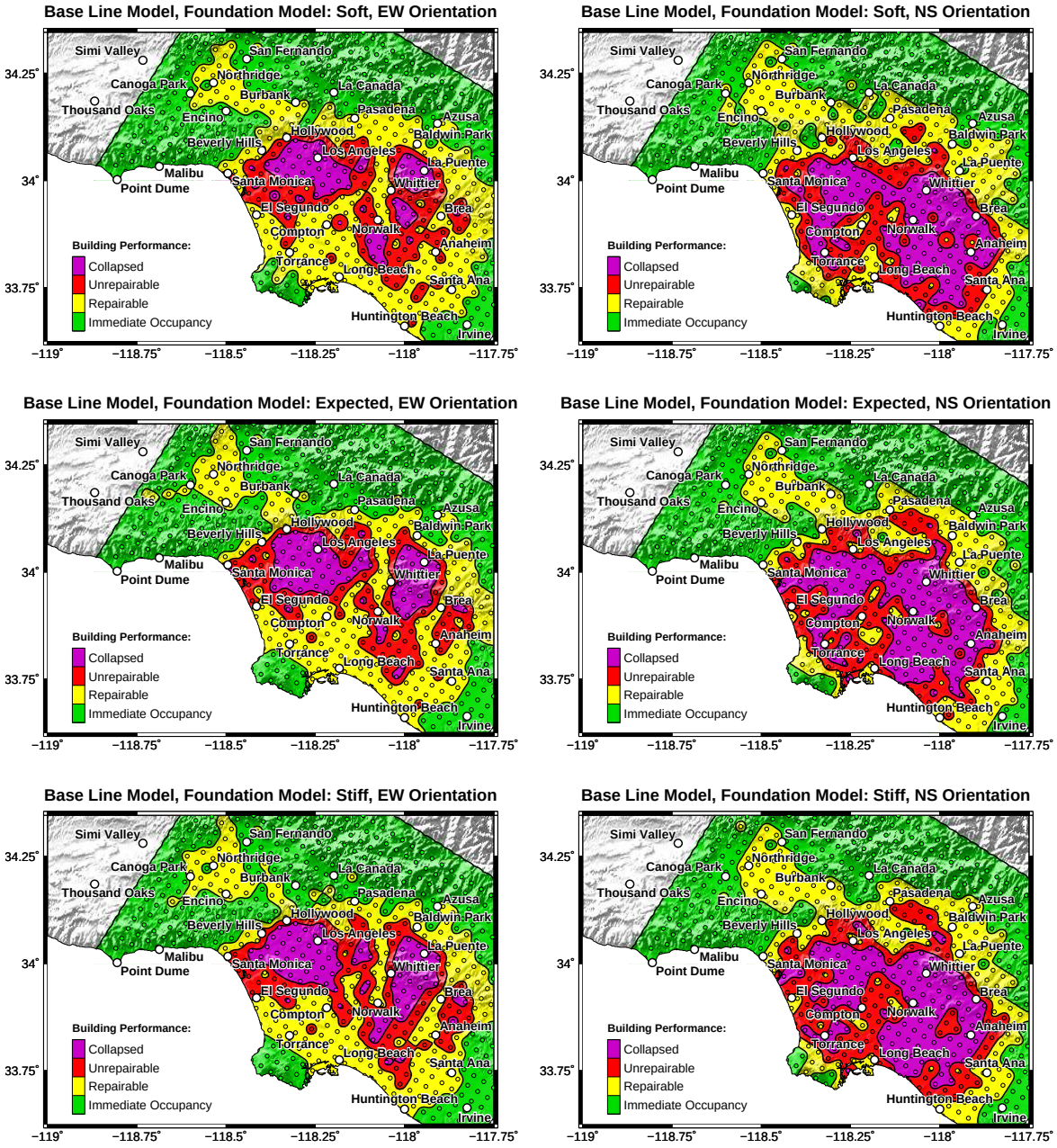

Figure 5.39: Maps of simulated building performance of the Base Line Model in the M_w 7.2 Puente Hills scenario earthquake oriented in east-west (EW) direction (left column) and north-south (NS) direction (right column). The maps in the top row show the model performance using the "soft" realization of the foundations, the maps in the center row show model performance using the "expected" realization of the foundations, and the maps in the bottom row show the model performance using the "stiff" realization of the foundations. The small circles show the simulated building performance at each site. A nearest neighbor method is used to interpolate the building performance between sites.

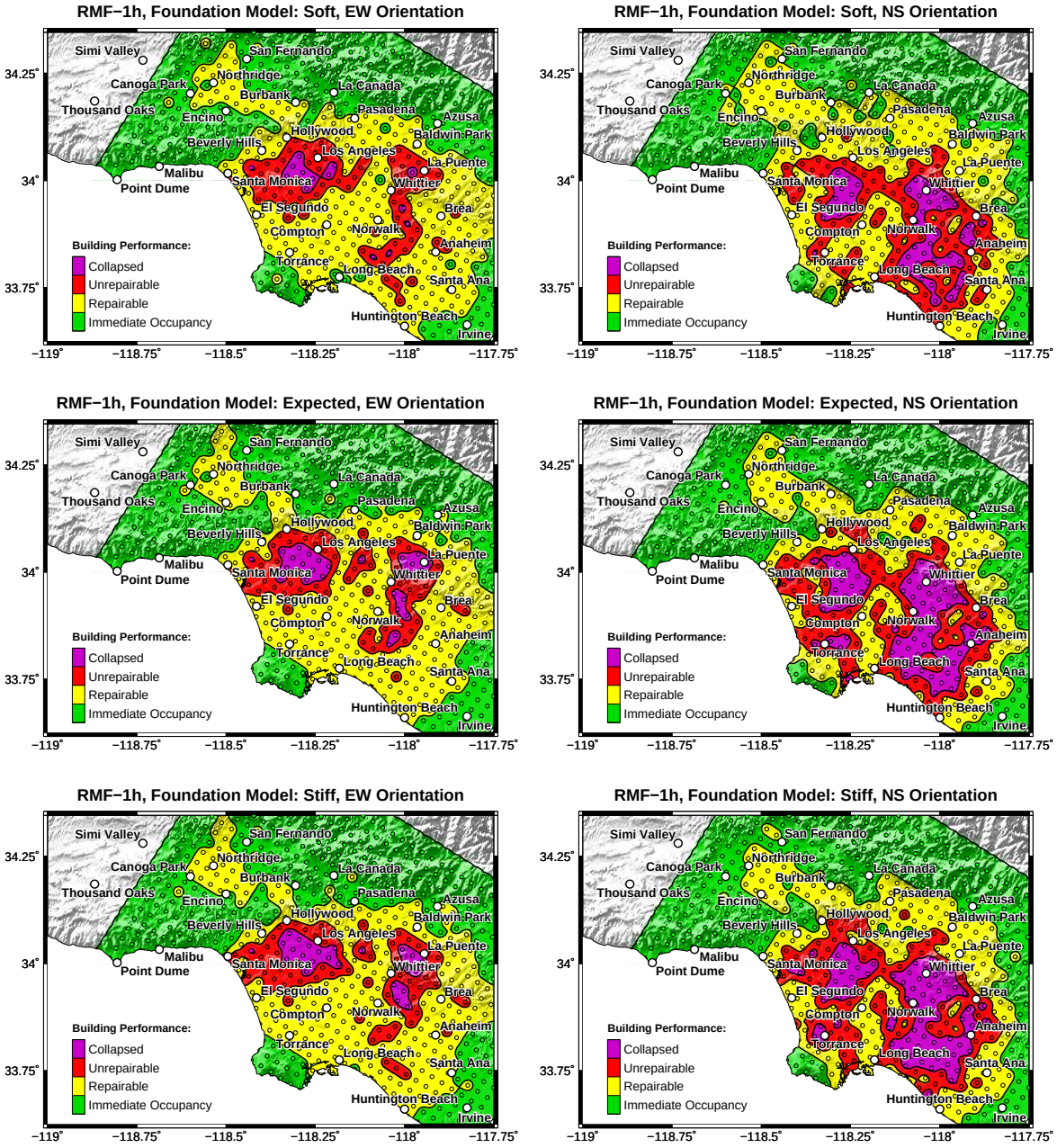

Figure 5.40: Maps of simulated building performance of retrofit scheme RMF-1h in the M_w 7.2 Puente Hills scenario earthquake oriented in east-west (EW) direction (left column) and north-south (NS) direction (right column). The maps in the top row show the model performance using the "soft" realization of the foundations, the maps in the center row show model performance using the "expected" realization of the foundations, and the maps in the bottom row show the model performance using the "stiff" realization of the foundations. The small circles show the simulated building performance at each site. A nearest neighbor method is used to interpolate the building performance between sites.

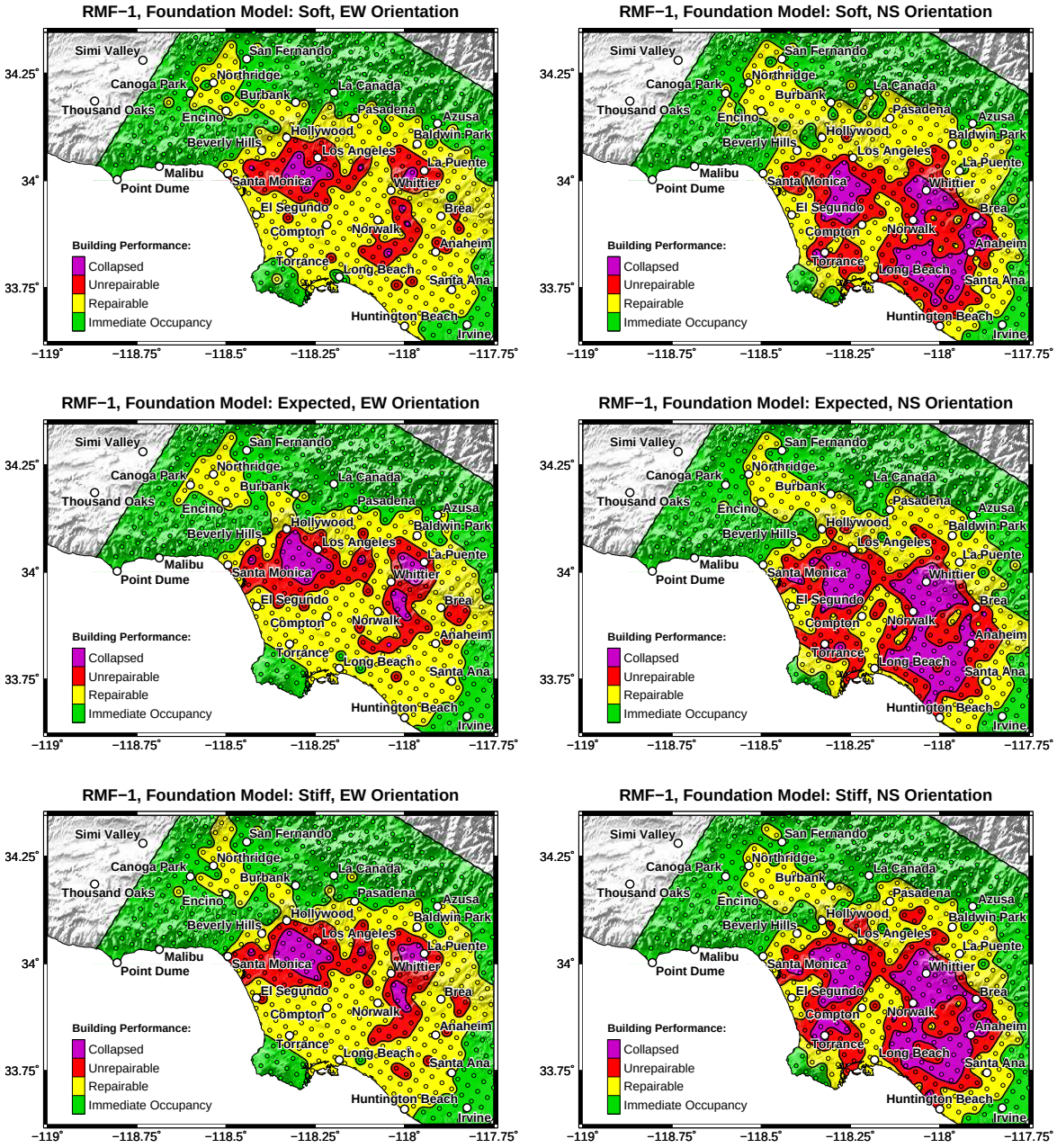

Figure 5.41: Maps of simulated building performance of retrofit scheme RMF-1 in the M_w 7.2 Puente Hills scenario earthquake oriented in east-west (EW) direction (left column) and north-south (NS) direction (right column). The maps in the top row show the model performance using the "soft" realization of the foundations, the maps in the center row show model performance using the "expected" realization of the foundations, and the maps in the bottom row show the model performance using the "stiff" realization of the foundations. The small circles show the simulated building performance at each site. A nearest neighbor method is used to interpolate the building performance between sites.

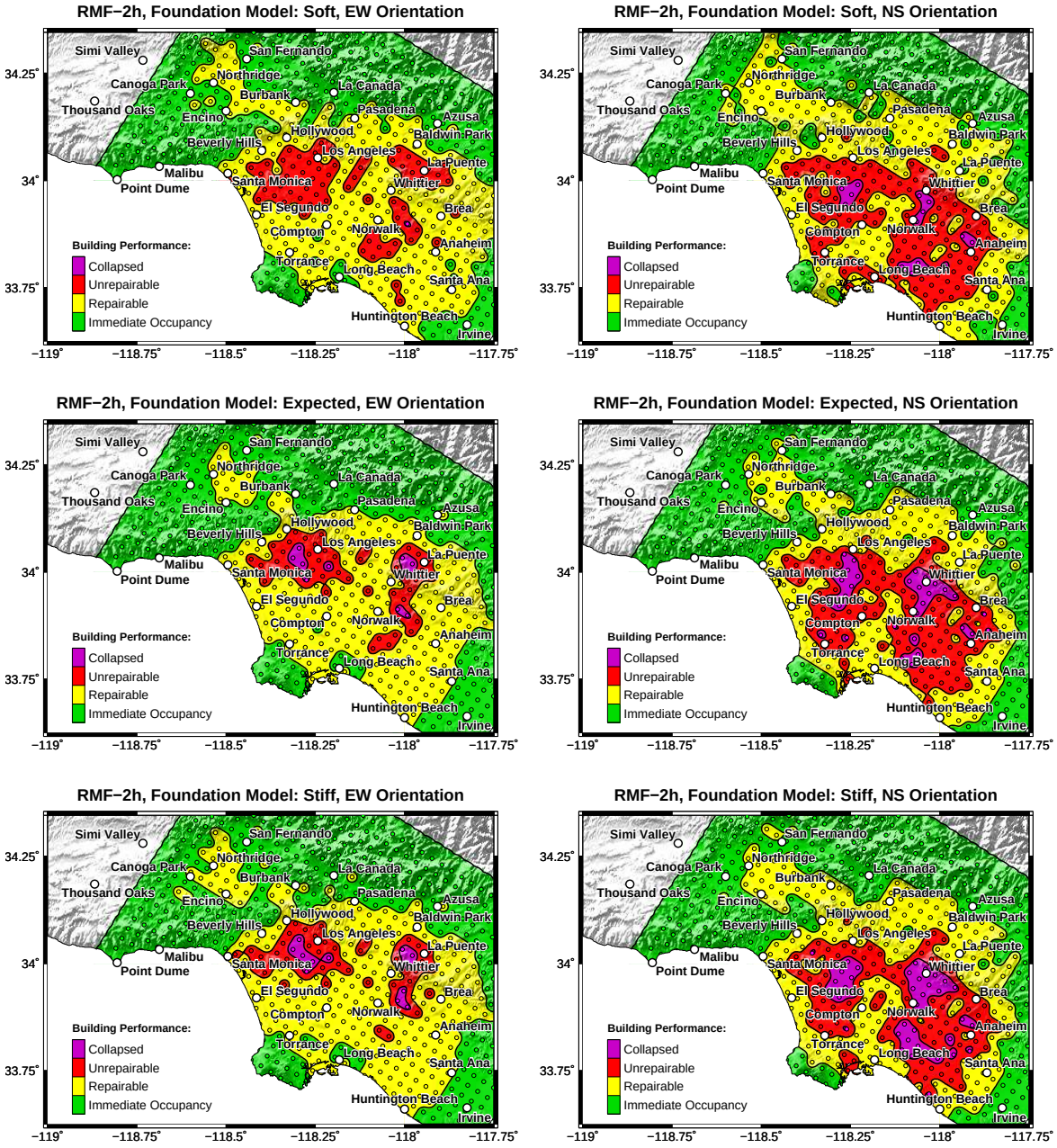

Figure 5.42: Maps of simulated building performance of retrofit scheme RMF-2h in the M_w 7.2 Puente Hills scenario earthquake oriented in east-west (EW) direction (left column) and north-south (NS) direction (right column). The maps in the top row show the model performance using the "soft" realization of the foundations, the maps in the center row show model performance using the "expected" realization of the foundations, and the maps in the bottom row show the model performance using the "stiff" realization of the foundations. The small circles show the simulated building performance at each site. A nearest neighbor method is used to interpolate the building performance between sites.

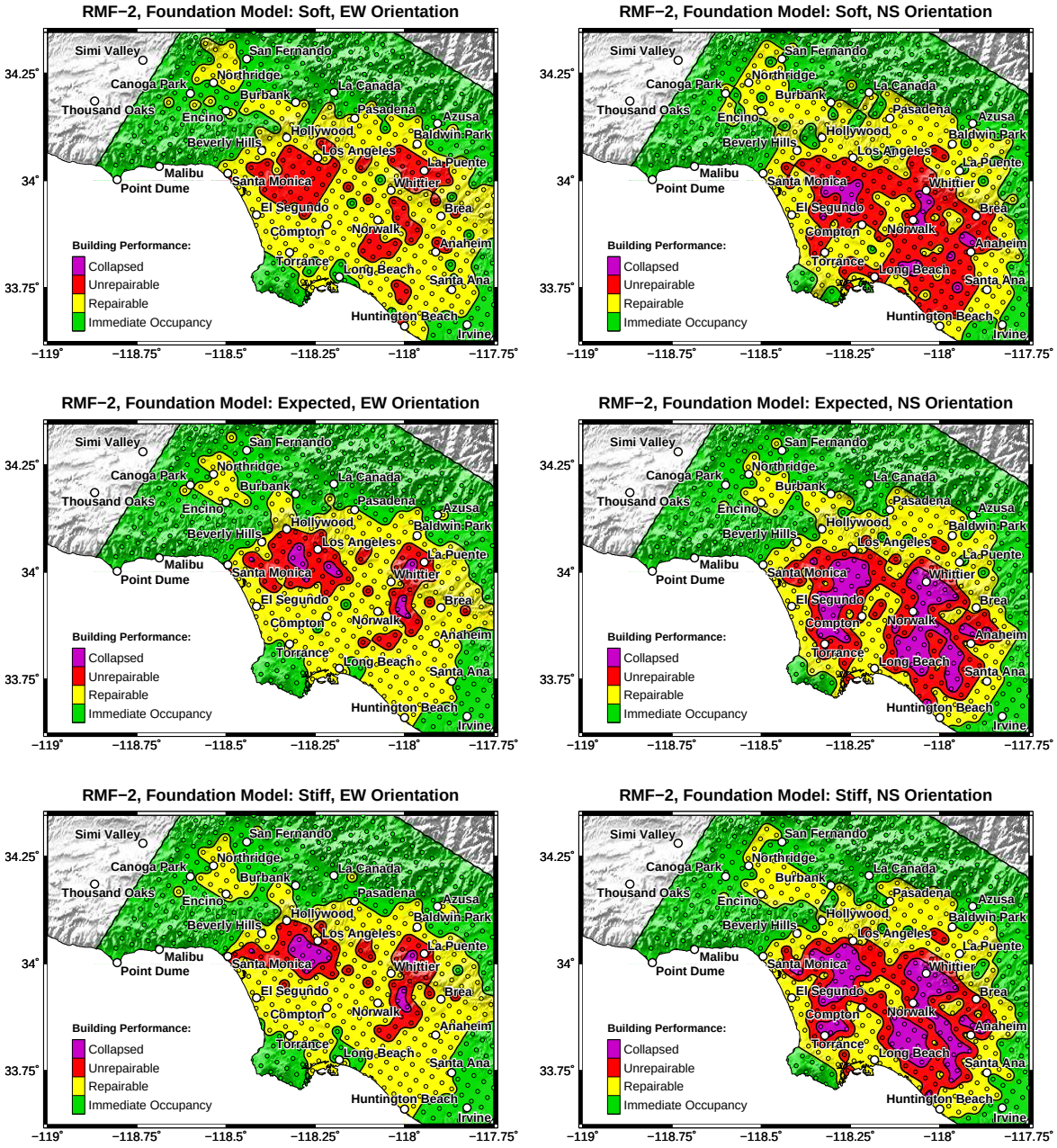

Figure 5.43: Maps of simulated building performance of retrofit scheme RMF-2 in the M_w 7.2 Puente Hills scenario earthquake oriented in east-west (EW) direction (left column) and north-south (NS) direction (right column). The maps in the top row show the model performance using the "soft" realization of the foundations, the maps in the center row show model performance using the "expected" realization of the foundations, and the maps in the bottom row show the model performance using the "stiff" realization of the foundations. The small circles show the simulated building performance at each site. A nearest neighbor method is used to interpolate the building performance between sites.

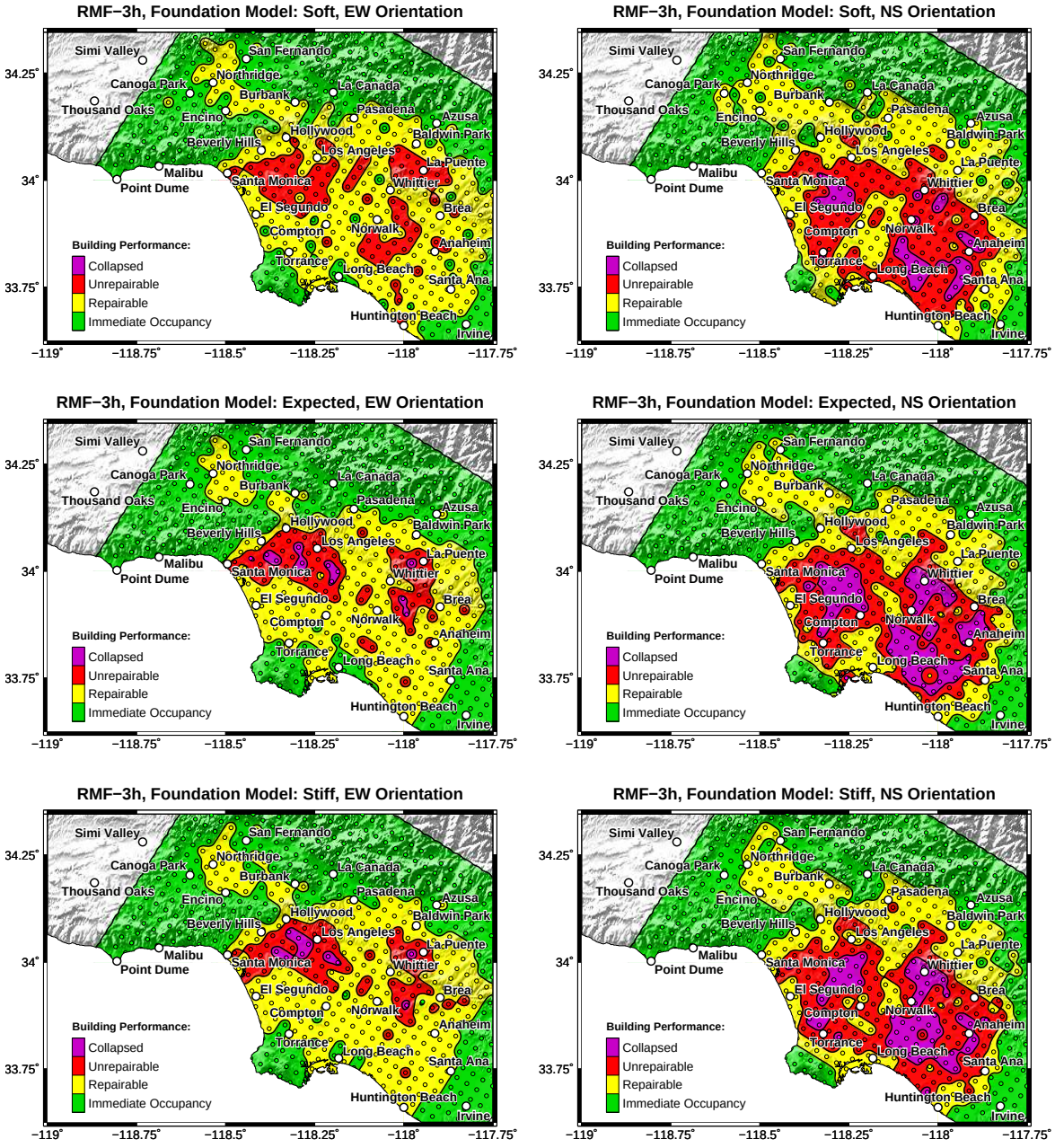

Figure 5.44: Maps of simulated building performance of retrofit scheme RMF-3h in the M_w 7.2 Puente Hills scenario earthquake oriented in east-west (EW) direction (left column) and north-south (NS) direction (right column). The maps in the top row show the model performance using the "soft" realization of the foundations, the maps in the center row show model performance using the "expected" realization of the foundations, and the maps in the bottom row show the model performance using the "stiff" realization of the foundations. The small circles show the simulated building performance at each site. A nearest neighbor method is used to interpolate the building performance between sites.

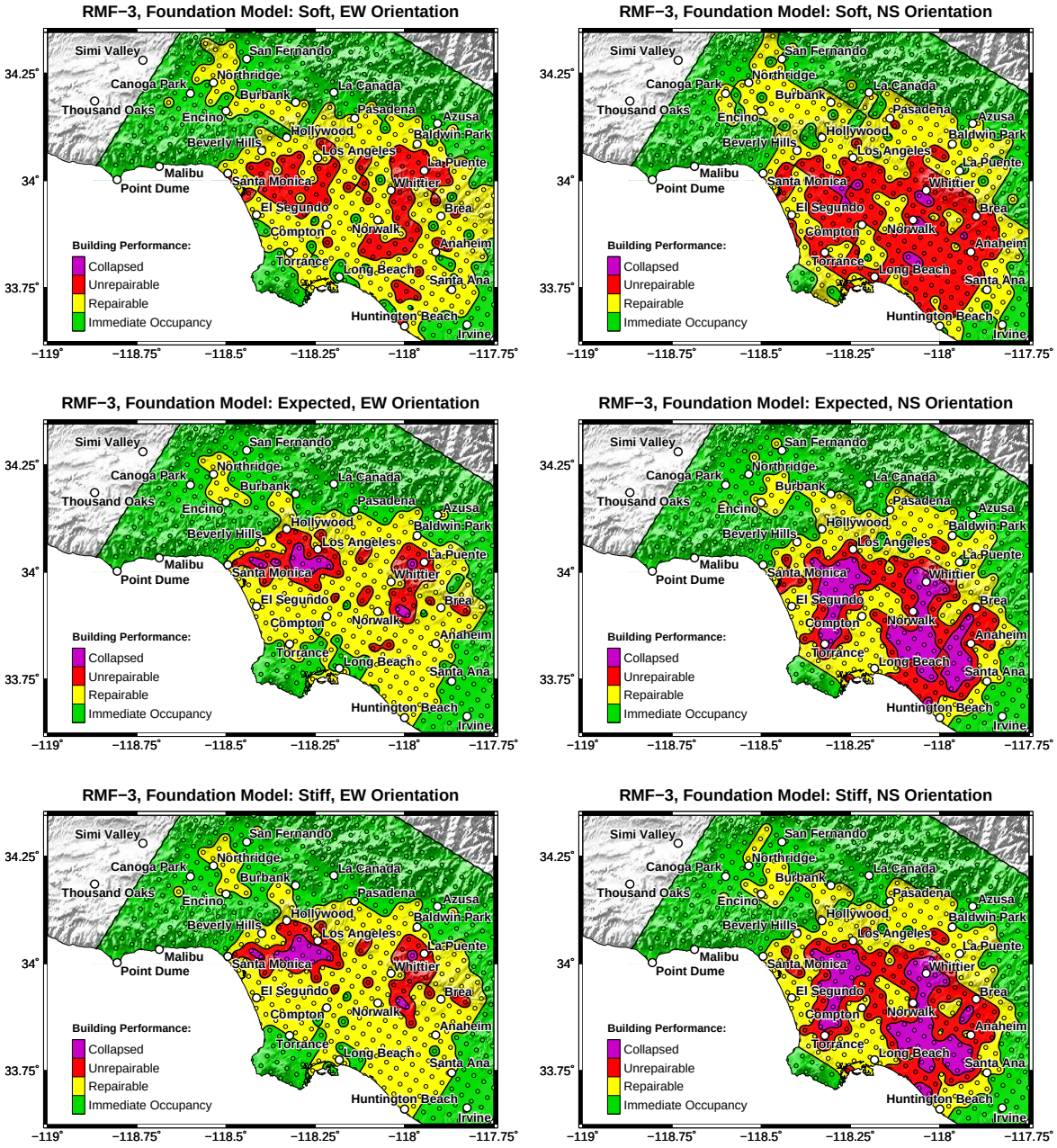

Figure 5.45: Maps of simulated building performance of retrofit scheme RMF-3 in the M_w 7.2 Puente Hills scenario earthquake oriented in east-west (EW) direction (left column) and north-south (NS) direction (right column). The maps in the top row show the model performance using the "soft" realization of the foundations, the maps in the center row show model performance using the "expected" realization of the foundations, and the maps in the bottom row show the model performance using the "stiff" realization of the foundations. The small circles show the simulated building performance at each site. A nearest neighbor method is used to interpolate the building performance between sites.

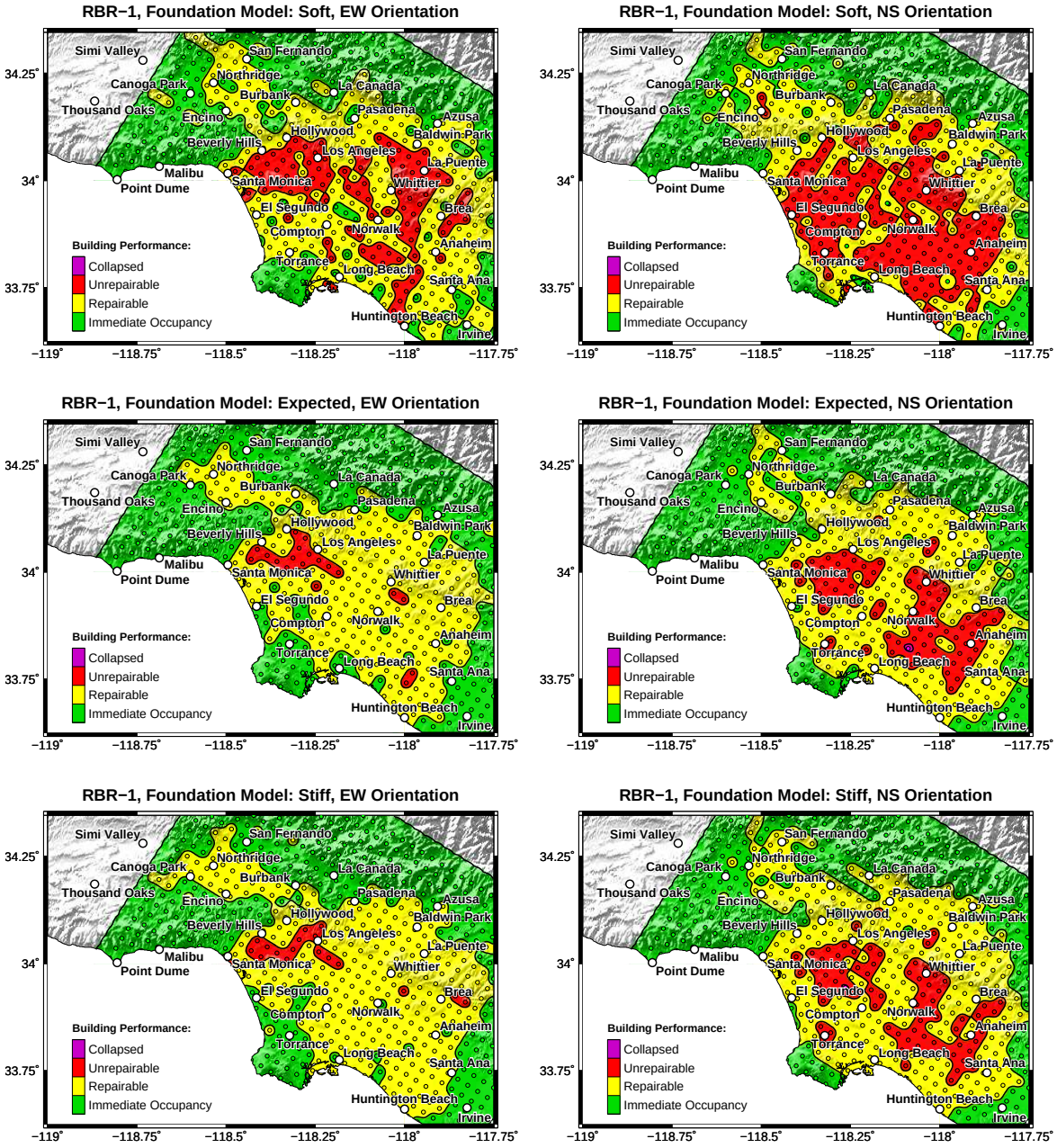

Figure 5.46: Maps of simulated building performance of retrofit scheme RBR-1 in the M_w 7.2 Puente Hills scenario earthquake oriented in east-west (EW) direction (left column) and north-south (NS) direction (right column). The maps in the top row show the model performance using the "soft" realization of the foundations, the maps in the center row show model performance using the "expected" realization of the foundations, and the maps in the bottom row show the model performance using the "stiff" realization of the foundations. The small circles show the simulated building performance at each site. A nearest neighbor method is used to interpolate the building performance between sites.

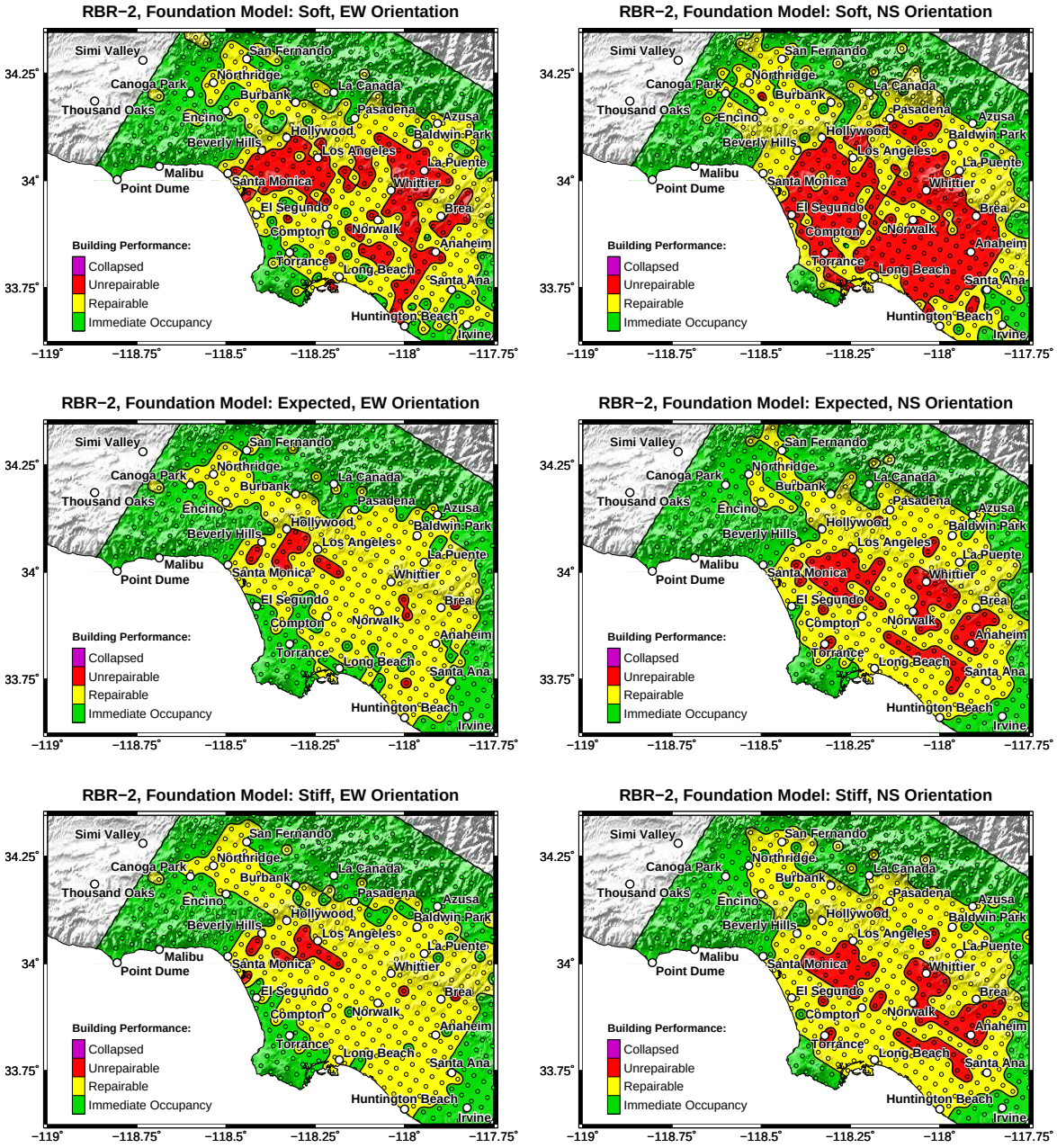

Figure 5.47: Maps of simulated building performance of retrofit scheme RBR-2 in the M_w 7.2 Puente Hills scenario earthquake oriented in east-west (EW) direction (left column) and north-south (NS) direction (right column). The maps in the top row show the model performance using the "soft" realization of the foundations, the maps in the center row show model performance using the "expected" realization of the foundations, and the maps in the bottom row show the model performance using the "stiff" realization of the foundations. The small circles show the simulated building performance at each site. A nearest neighbor method is used to interpolate the building performance between sites.

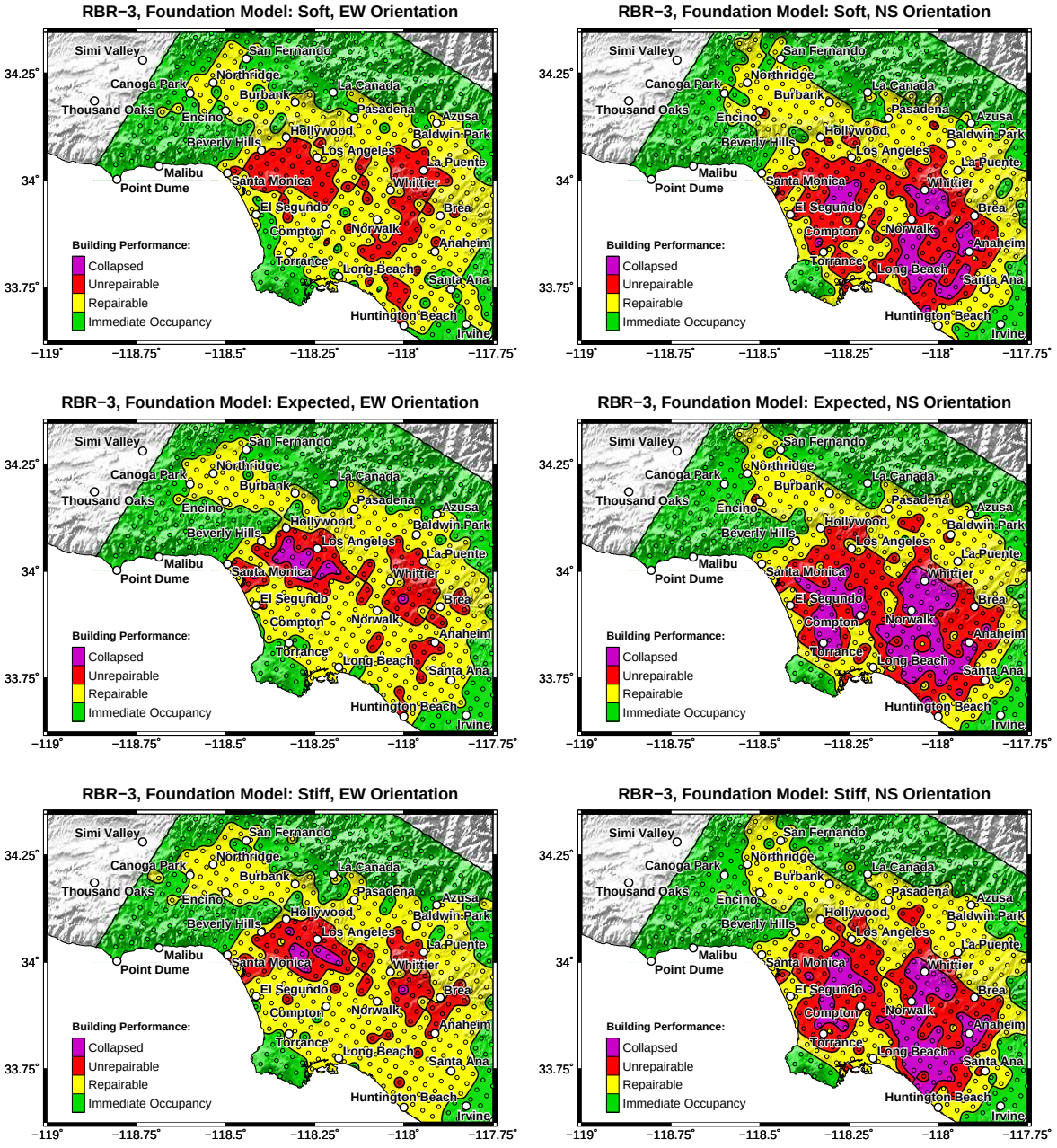

Figure 5.48: Maps of simulated building performance of retrofit scheme RBR-3 in the M_w 7.2 Puente Hills scenario earthquake oriented in east-west (EW) direction (left column) and north-south (NS) direction (right column). The maps in the top row show the model performance using the "soft" realization of the foundations, the maps in the center row show model performance using the "expected" realization of the foundations, and the maps in the bottom row show the model performance using the "stiff" realization of the foundations. The small circles show the simulated building performance at each site. A nearest neighbor method is used to interpolate the building performance between sites.

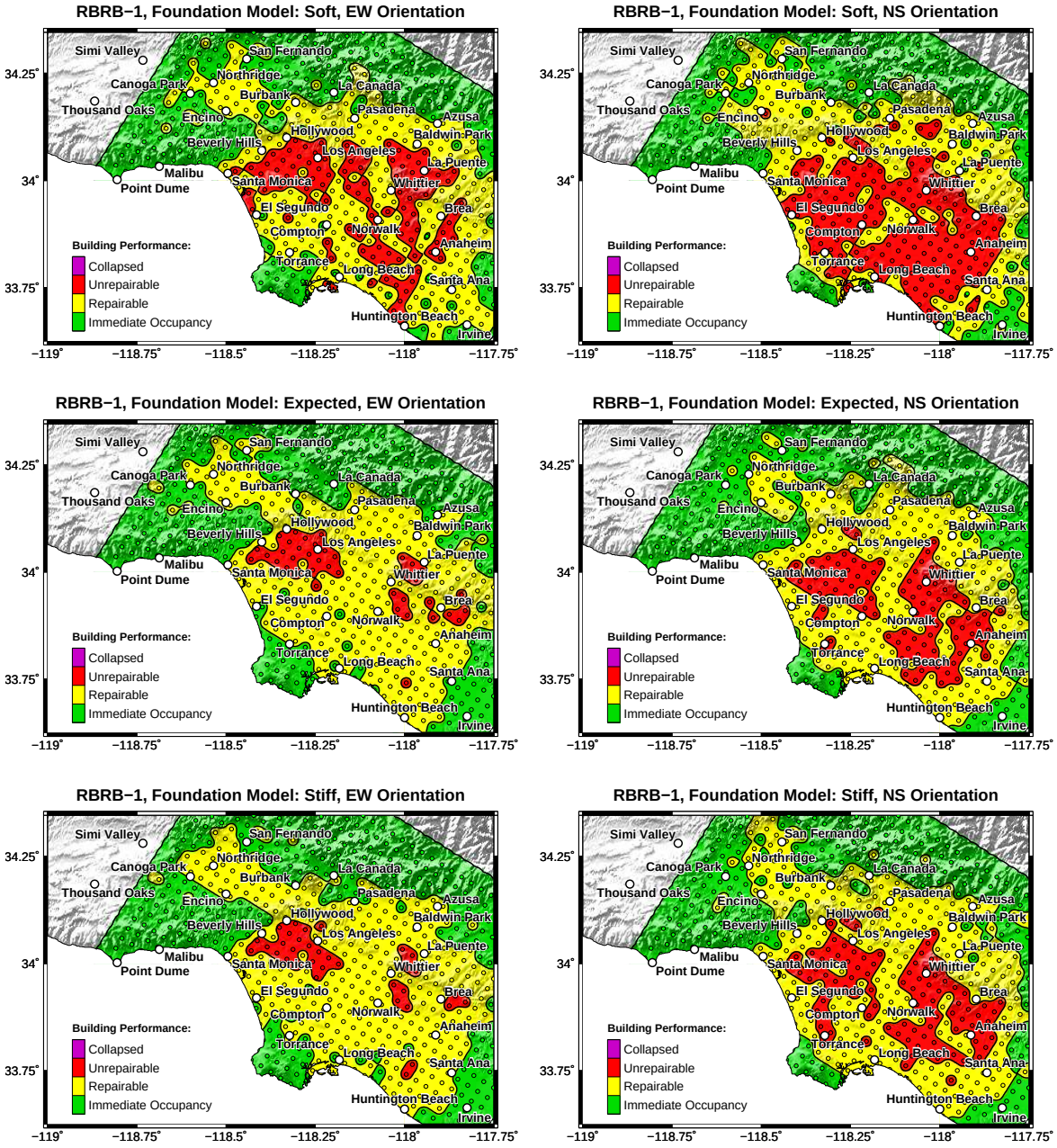

Figure 5.49: Maps of simulated building performance of retrofit scheme RBRB-1 in the M_w 7.2 Puente Hills scenario earthquake oriented in east-west (EW) direction (left column) and north-south (NS) direction (right column). The maps in the top row show the model performance using the "soft" realization of the foundations, the maps in the center row show model performance using the "expected" realization of the foundations, and the maps in the bottom row show the model performance using the "stiff" realization of the foundations. The small circles show the simulated building performance at each site. A nearest neighbor method is used to interpolate the building performance between sites.

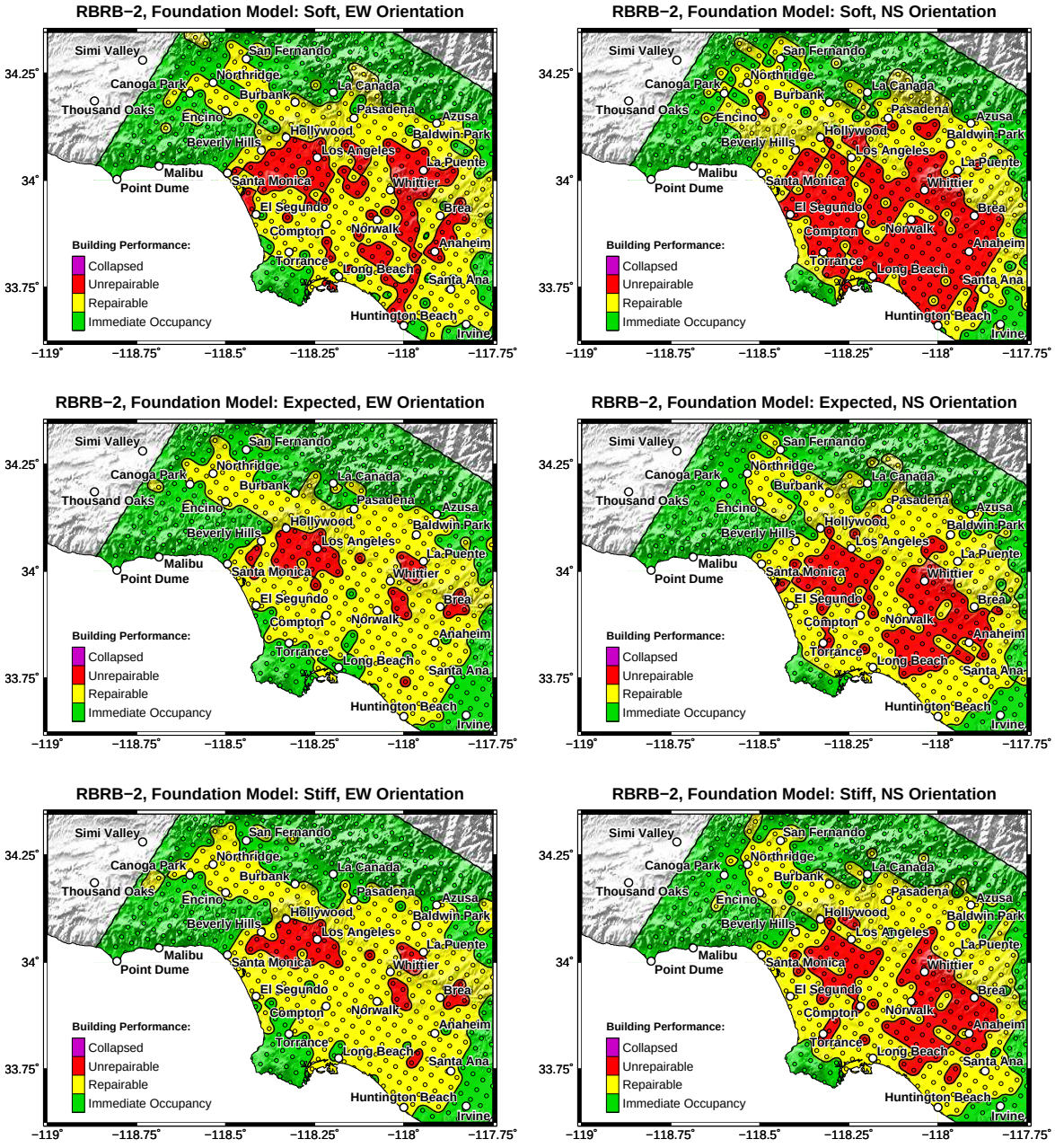

Figure 5.50: Maps of simulated building performance of retrofit scheme RBRB-2 in the M_w 7.2 Puente Hills scenario earthquake oriented in east-west (EW) direction (left column) and north-south (NS) direction (right column). The maps in the top row show the model performance using the "soft" realization of the foundations, the maps in the center row show model performance using the "expected" realization of the foundations, and the maps in the bottom row show the model performance using the "stiff" realization of the foundations. The small circles show the simulated building performance at each site. A nearest neighbor method is used to interpolate the building performance between sites.

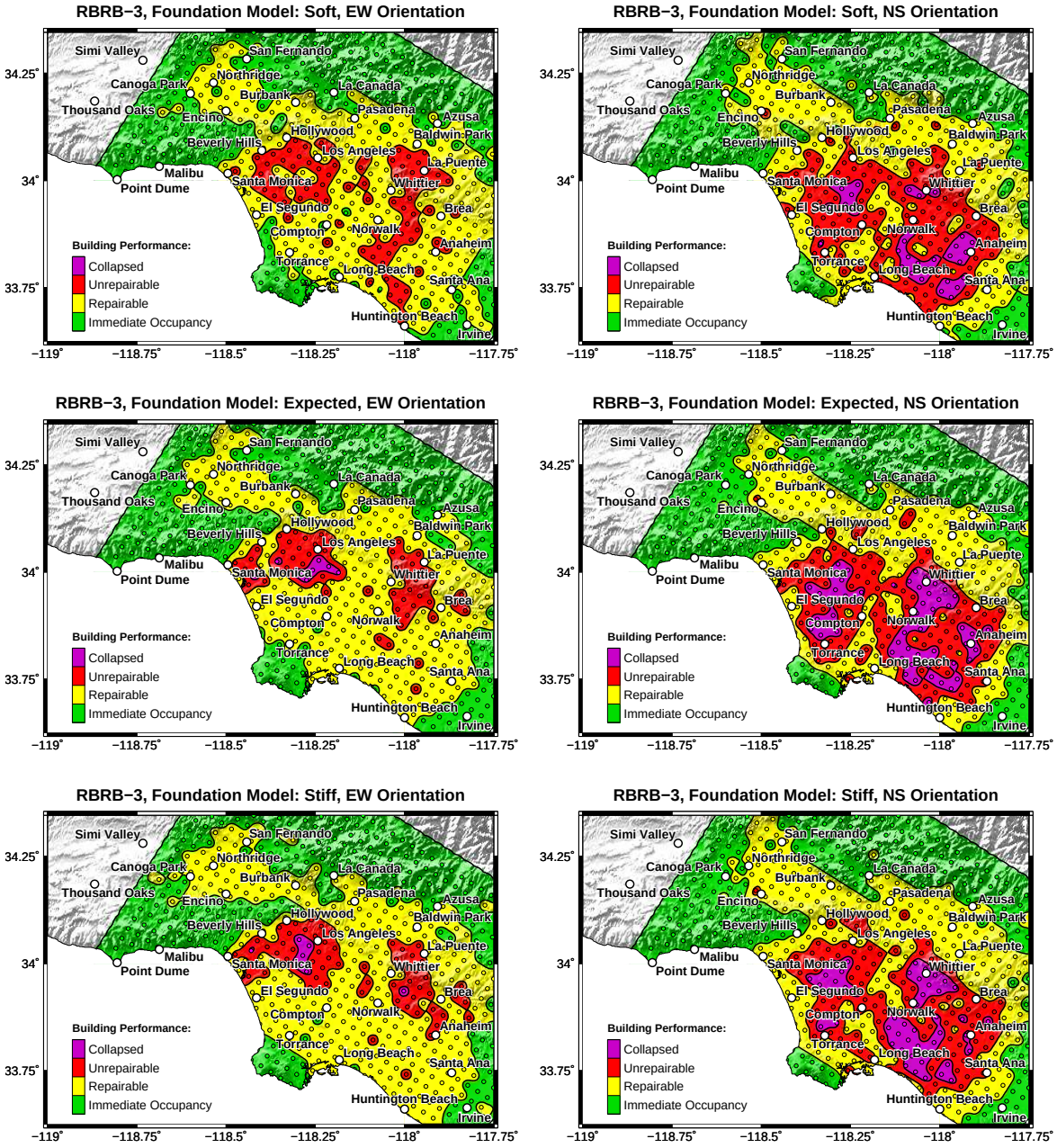

Figure 5.51: Maps of simulated building performance of retrofit scheme RBRB-3 in the M_w 7.2 Puente Hills scenario earthquake oriented in east-west (EW) direction (left column) and north-south (NS) direction (right column). The maps in the top row show the model performance using the "soft" realization of the foundations, the maps in the center row show model performance using the "expected" realization of the foundations, and the maps in the bottom row show the model performance using the "stiff" realization of the foundations. The small circles show the simulated building performance at each site. A nearest neighbor method is used to interpolate the building performance between sites.

5.4 Building Performance: Recorded Real Strong Ground Motions

In this section of the study, a collection of recorded ground motion time histories from actual earthquakes is scaled by scaling factors ranging from 0.6 to 2.0, in increments of 0.2, and the scaled ground motion records are applied to all thirteen building models. For each ground motion record and scaling factor, a performance category is assigned based on the average building responses in three simulations using different realizations of the strengths of beam-to-column moment resisting connections, column splices, and column base plates. Also, model collapse is assumed if it occurs in any of the three simulations. The results are presented in two types of graphics. The number of simulations that resulted in the "repairable", "unrepairable", and "collapse" performance categories are summarized for all building models in Figure 5.52. Then the simulated performance categories for each ground motion record and the range of scaling factors are presented for the building models as follows:

	Figure:		Figure:
Base Line Model	5.53	RBR-1	5.60
RMF-1h	5.54	RBR-2	5.61
RMF-1	5.55	RBR-3	5.62
RMF-2h	5.56	RBRB-1	5.63
RMF-2	5.57	RBRB-2	5.64
RMF-3h	5.58	RBRB-3	5.65
RMF-3	5.59		

The data in the incremental dynamic analyses using recorded ground motions from actual earthquakes is sparse, and showed a poor fit to cumulative log-normal distribution functions, and therefore fragility curves are not constructed.

The results show trends similar to what was observed in the simulated earthquakes. When employing the "expected" foundation model, the base line model is simulated to collapse in 74 cases (out of 160). At a scaling factor of unity, the building model is simulated to collapse in 6 out of all 20 ground motion records. It is even simulated to collapse when subjected to the TCU068 record from the Chi-Chi earthquake scaled down by a factor of 0.6. Furthermore, complete economic loss ("unrepairable" or "collapse" performance categories) of the base line model is simulated in 116 cases.

Retrofit schemes RBR-1, RBR-2, RBRB-1, and RBRB-2, all reduce the number of simulated collapses to only a few, but complete economic loss is simulated in 42 and 44 cases for RBR-1 and RBR-2, respectively, and in 59 and 58 cases for RBRB-1 and RBRB-2, respectively.

As was mentioned in the previous sections, it appears that braced-frames that employ buckling-restrained braces tend to have greater residual drifts. However, the buckling-restrained braces are likely to store significant residual forces, and the residual drifts may be recovered to some extent by replacing the deformed braces. Conventional brace elements are not expected to store residual forces to the same degree.

Out of the retrofit schemes that consider retrofitting the brittle beam-to-column moment resisting connections (RMF schemes), scheme RMF-3 performs best, with collapse being simulated in 32 cases, and complete economic loss simulated in 73 cases. Schemes RMF-2h, RMF-2, and RMF-3h are simulated to collapse in a similar number of cases, but complete economic losses are simulated in 81-86 cases. These results suggest that at a certain point, upgrading additional beam-to-column connections will result in minimal additional improvement in performance.

As before, the two retrofit schemes that implement brace elements in the lower half of the building model while leaving the upper half unaltered (schemes RBR-3 and RBRB-3) are somewhat successful in that the schemes are more effective in limiting deformations in the lower half of the building model, compared to the moment-frame half-height retrofit schemes (RMF-1h, RMF-2h, and RMF-3h), and thus reduce to a greater extent global P-delta overturning moments. However, as was mentioned in the previous sections, the resulting structures are stiffer than the moment-frame configurations and consequently attract larger seismic forces, which often results in excessive drifts in the upper half. A retrofit scheme that implements brace elements in the lower half of the building model in conjunction with upgrading beam-to-column moment connections in the upper half may present some additional improvement in building performance while keeping architectural impact low. Retrofit schemes RBR-3 and RBRB-3 are simulated to collapse in 48 and 35 cases, respectively, and complete economic loss is simulated in 83 cases for both schemes.

The “expected” and “stiff” foundation models resulted in very similar building performances. When employing the “stiff” foundation model, foundation reactions were in the elastic range for all building models. When employing the “expected” foundation model, foundation reactions were in the elastic range for all but four building models. Yielding of the foundation springs was ob-

served (in a few simulations) for retrofit schemes RBRB-1 and RBRB-2, but more noticeably for schemes RBR-1 and RBR-2, with residual foundation rotations up to around 1.5%. When employing the "soft" foundation model, the capacities of the foundation springs were frequently exceeded in all building models. As a result, all building models realized similar potential for exceeding the "immediate occupancy" foundation residual rotation limit, and only modest reduction in number of simulated complete economic losses of the building models is observed for the retrofit schemes. However, the foundations were never simulated to loose stability, although residual foundation rotations were observed to be as large as 9%, and the retrofit schemes achieve even more dramatic reduction in collapse potential, compared to when the "expected" and "stiff" foundation models are employed.

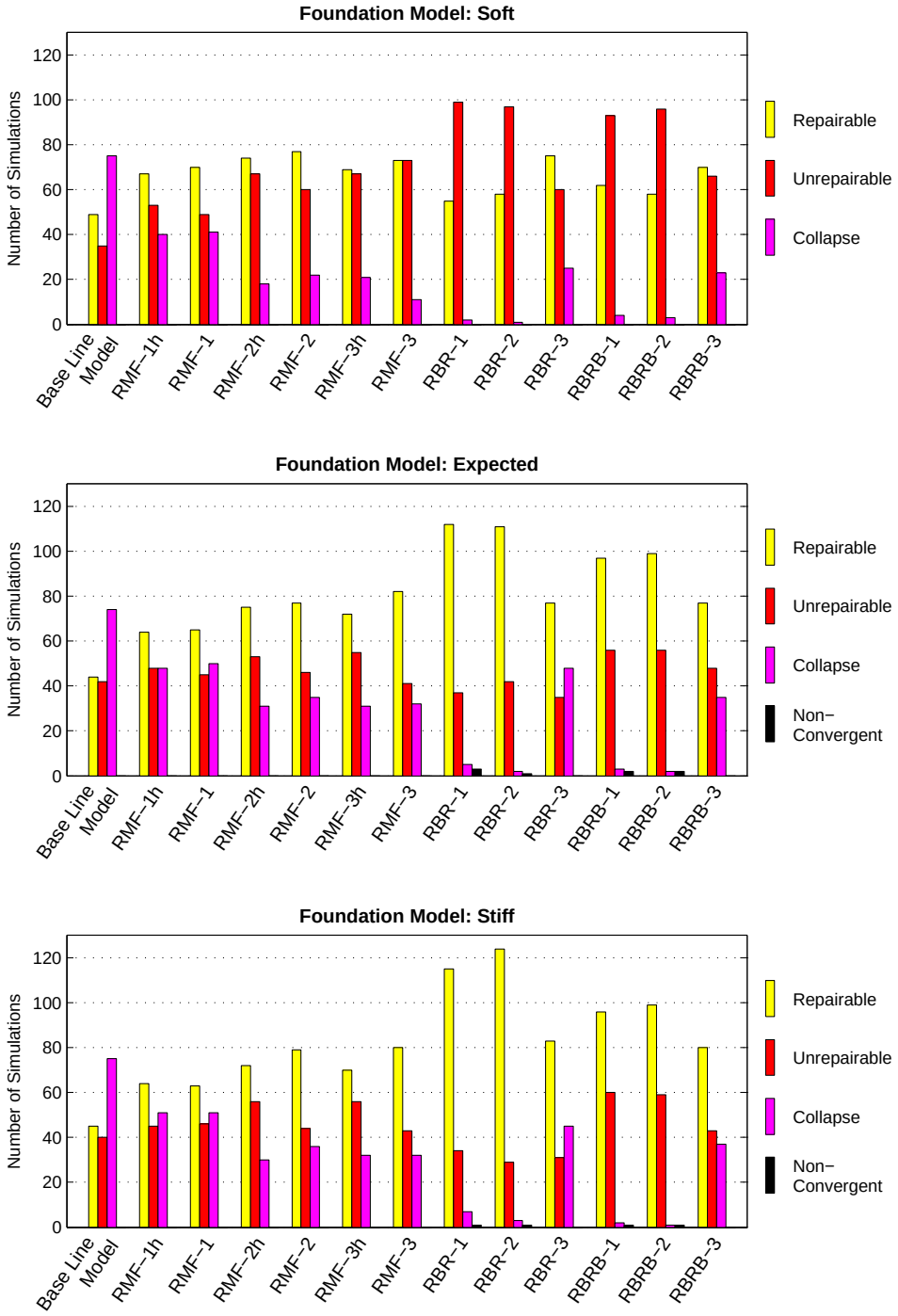

Figure 5.52: Summary of the number of simulations that resulted in the "repairable", "unrepairable", and "collapse" performance categories in the incremental dynamic analysis using recorded ground motions from actual earthquakes, for the "soft" (top figure), "expected" (middle figure), and "stiff" (bottom figure) realizations of the foundation springs. The total number of simulations carried out for each building model, for each realization of the foundation springs, is 160. A few simulations for retrofit schemes RBR-1, RBR-2, RBRB-1, and RBRB-2, for the "expected" and "stiff" foundation springs, failed to converge before showing a clear sign of model collapse. These simulations are labeled as "non-convergent".

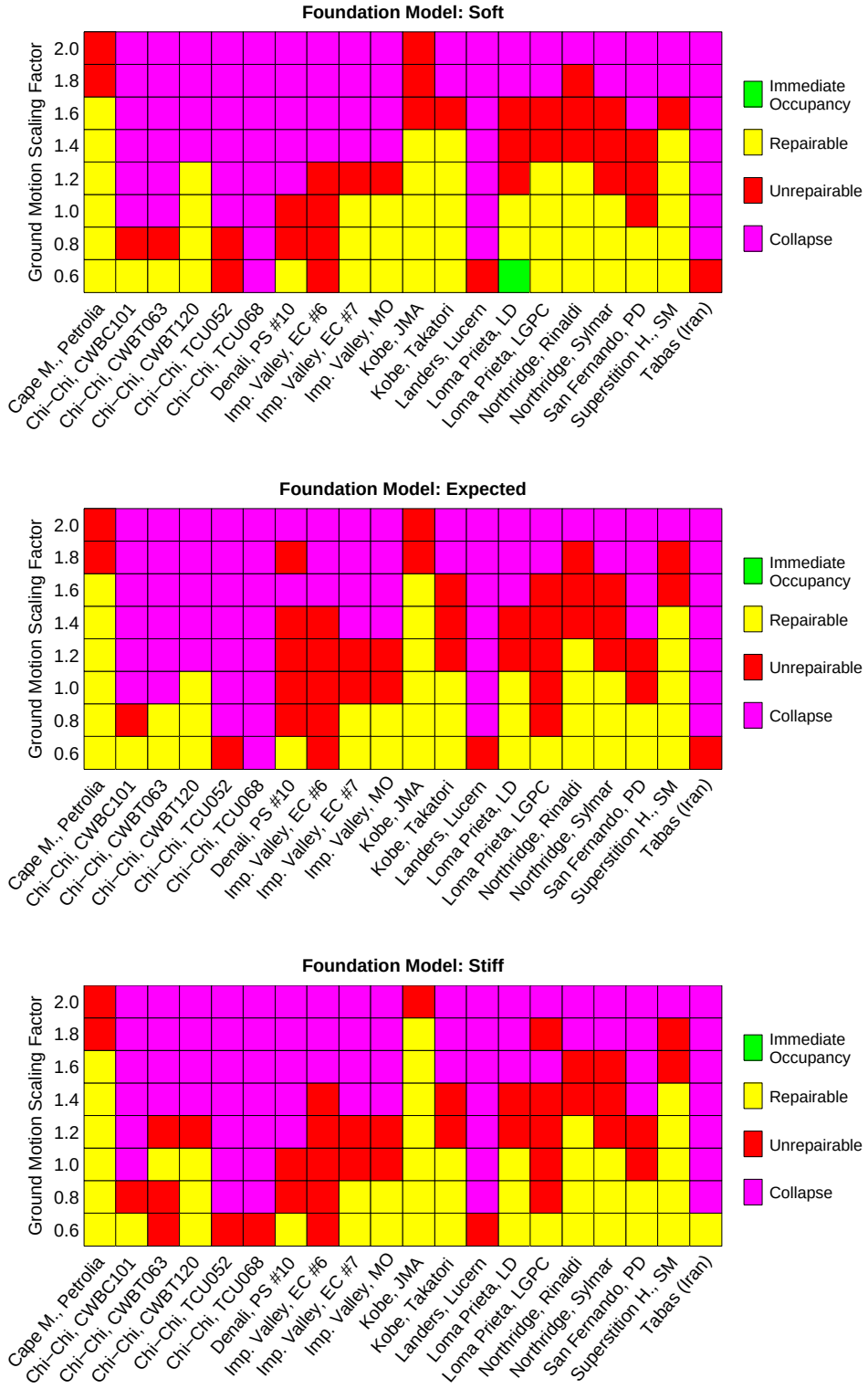

Figure 5.53: Simulated building performance categoreis for the Base Line Model in the incremental dynamic analyses using recorded ground motion time histories from actual earthquakes, assuming the "soft" (top figure), "expected" (middle figure), and "stiff" (bottom figure) realizations of the foundation springs.

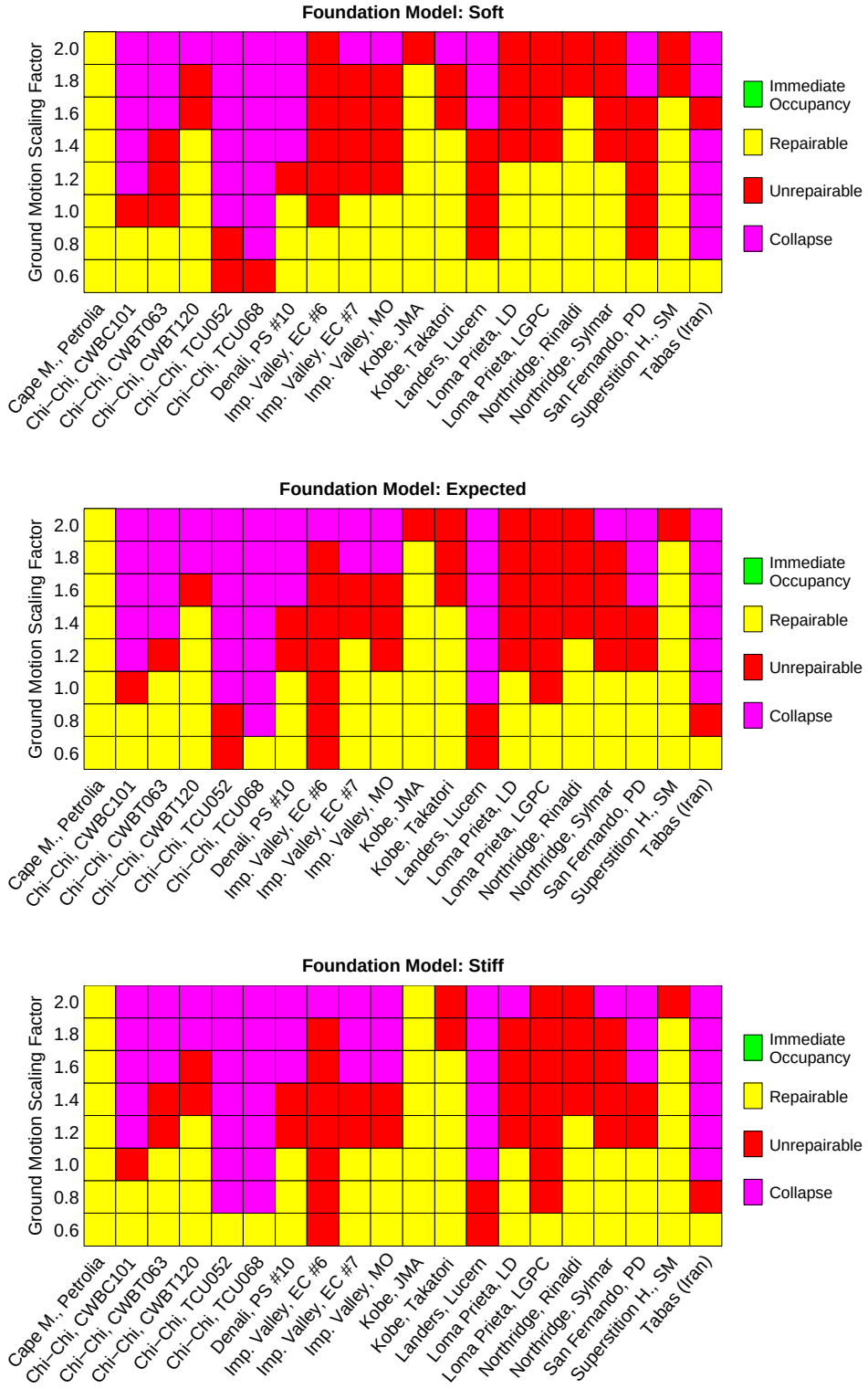

Figure 5.54: Simulated building performance categoreis for retrofit scheme RMF-1h in the incremental dynamic analyses using recorded ground motion time histories from actual earthquakes, assuming the "soft" (top figure), "expected" (middle figure), and "stiff" (bottom figure) realizations of the foundation springs.

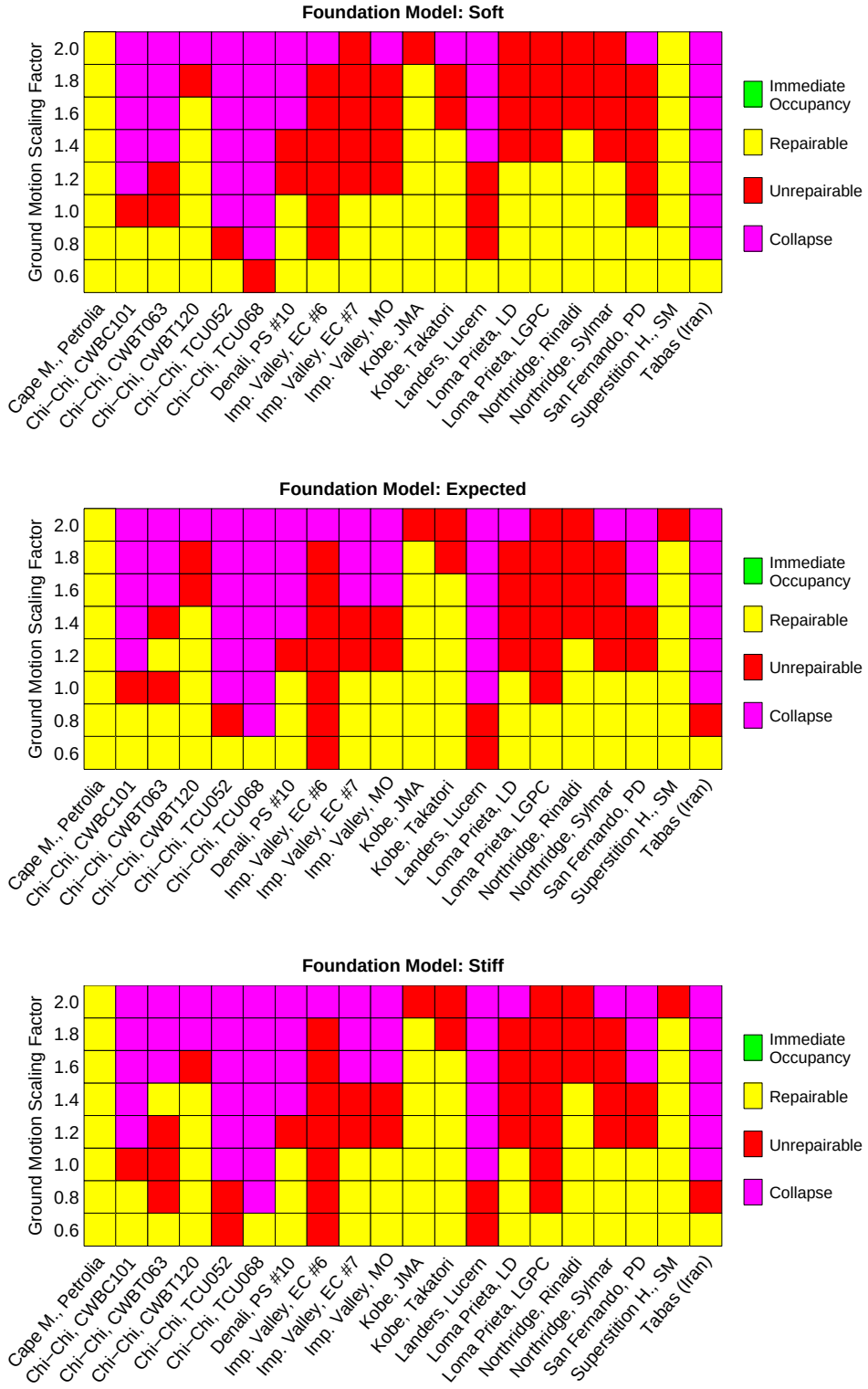

Figure 5.55: Simulated building performance categoreis for retrofit scheme RMF-1 in the incremental dynamic analyses using recorded ground motion time histories from actual earthquakes, assuming the "soft" (top figure), "expected" (middle figure), and "stiff" (bottom figure) realizations of the foundation springs.

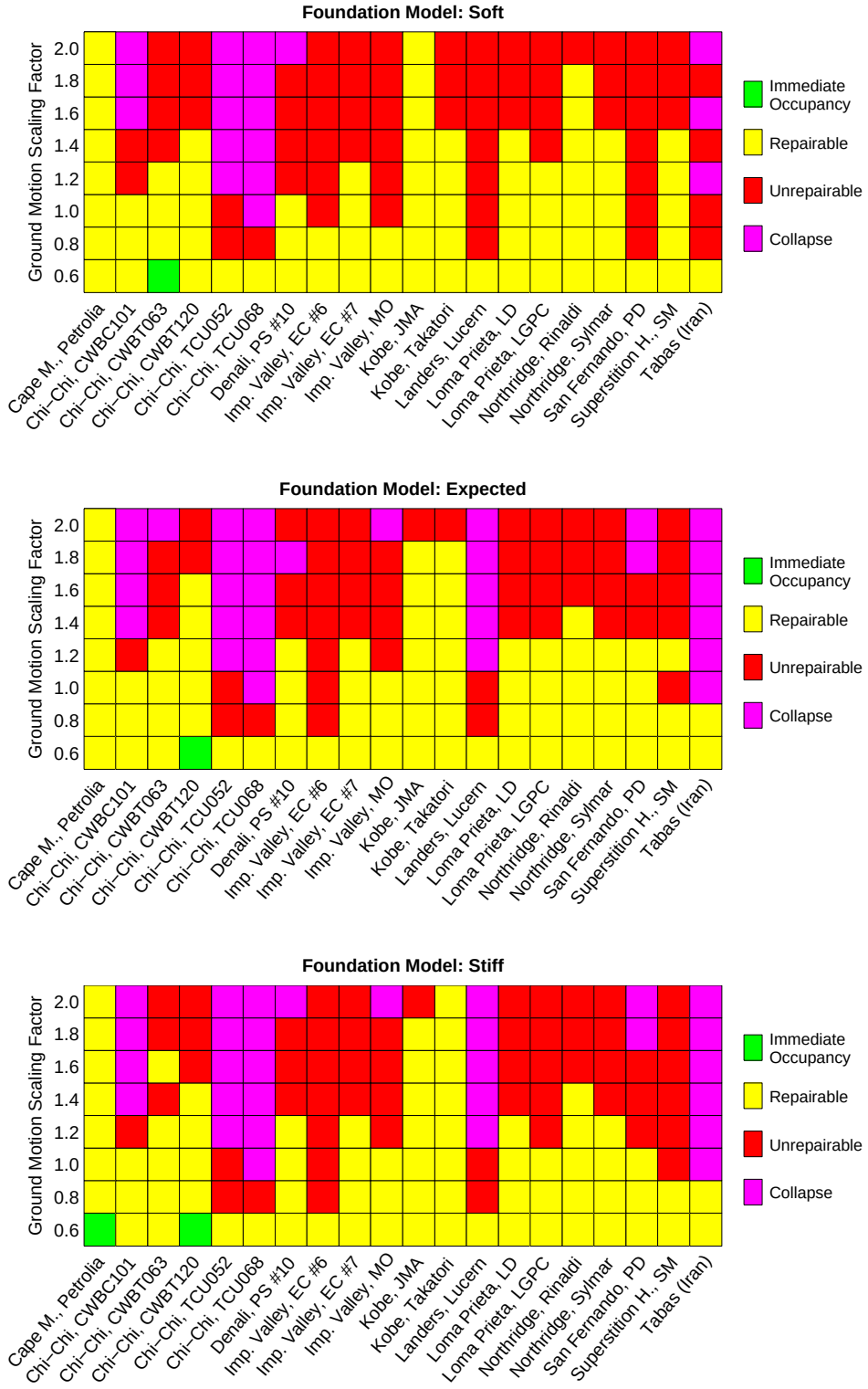

Figure 5.56: Simulated building performance categoreis for retrofit scheme RMF-2h in the incremental dynamic analyses using recorded ground motion time histories from actual earthquakes, assuming the "soft" (top figure), "expected" (middle figure), and "stiff" (bottom figure) realizations of the foundation springs.

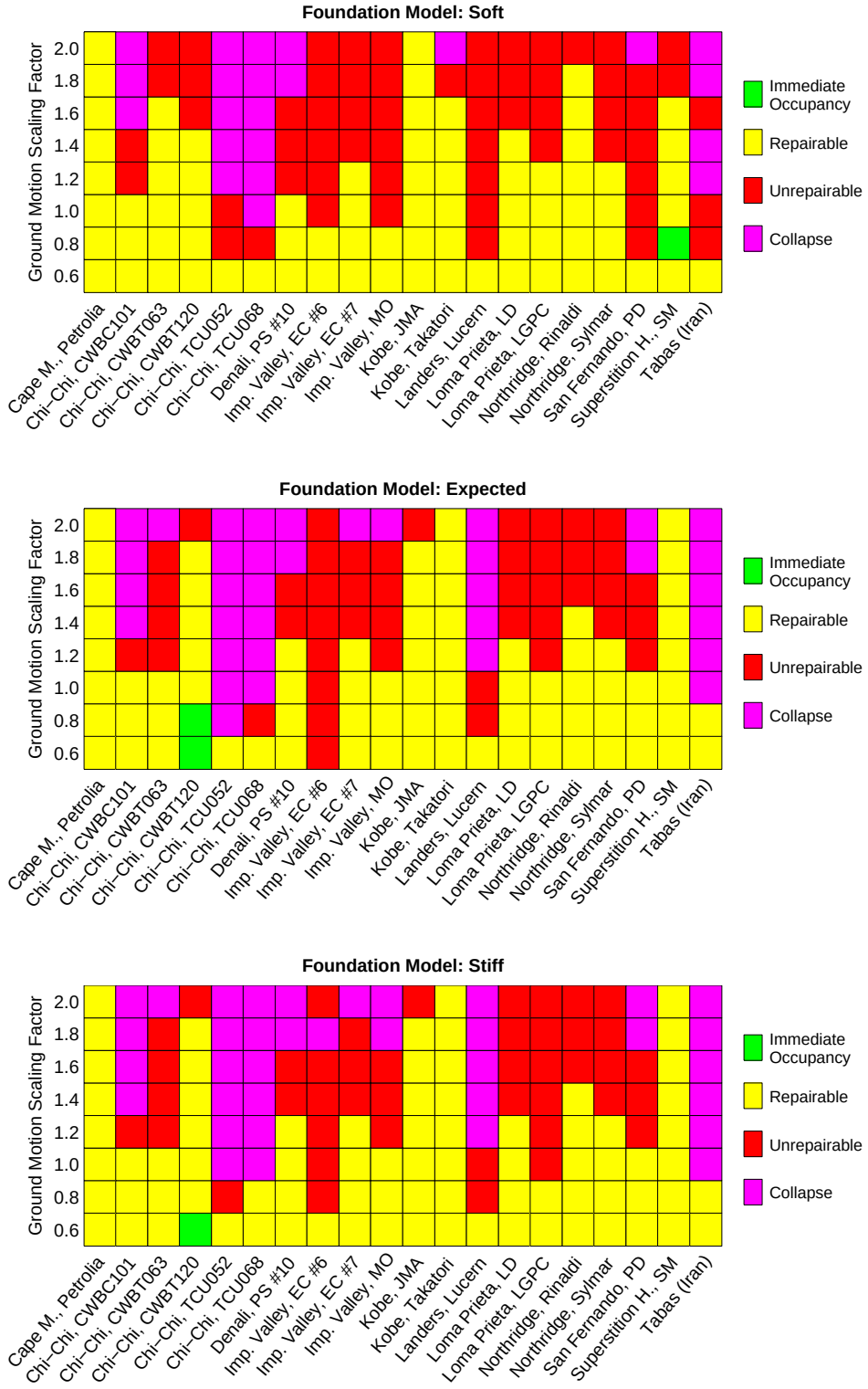

Figure 5.57: Simulated building performance categoreis for retrofit scheme RMF-2 in the incremental dynamic analyses using recorded ground motion time histories from actual earthquakes, assuming the "soft" (top figure), "expected" (middle figure), and "stiff" (bottom figure) realizations of the foundation springs.

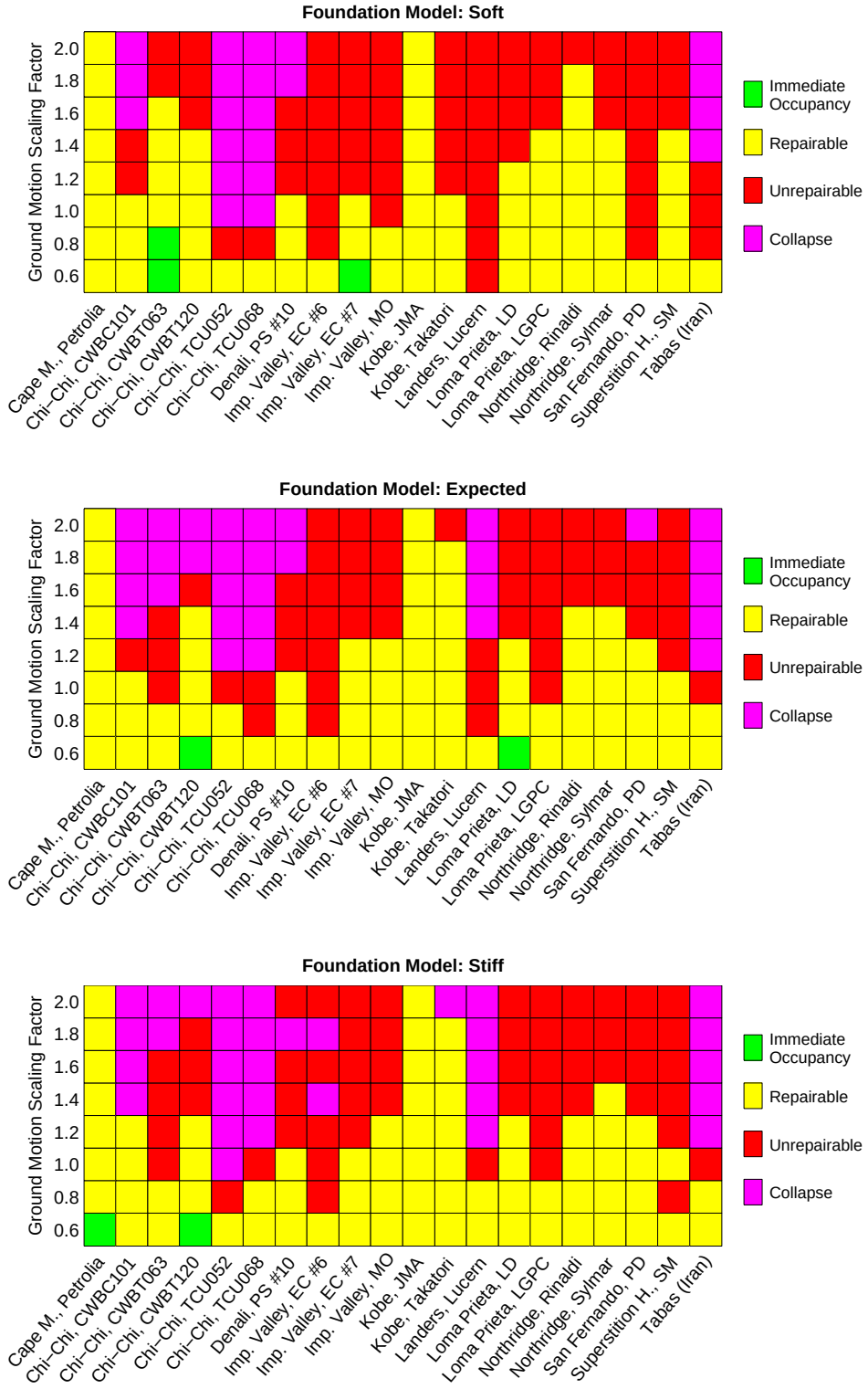

Figure 5.58: Simulated building performance categoreis for retrofit scheme RMF-3h in the incremental dynamic analyses using recorded ground motion time histories from actual earthquakes, assuming the "soft" (top figure), "expected" (middle figure), and "stiff" (bottom figure) realizations of the foundation springs.

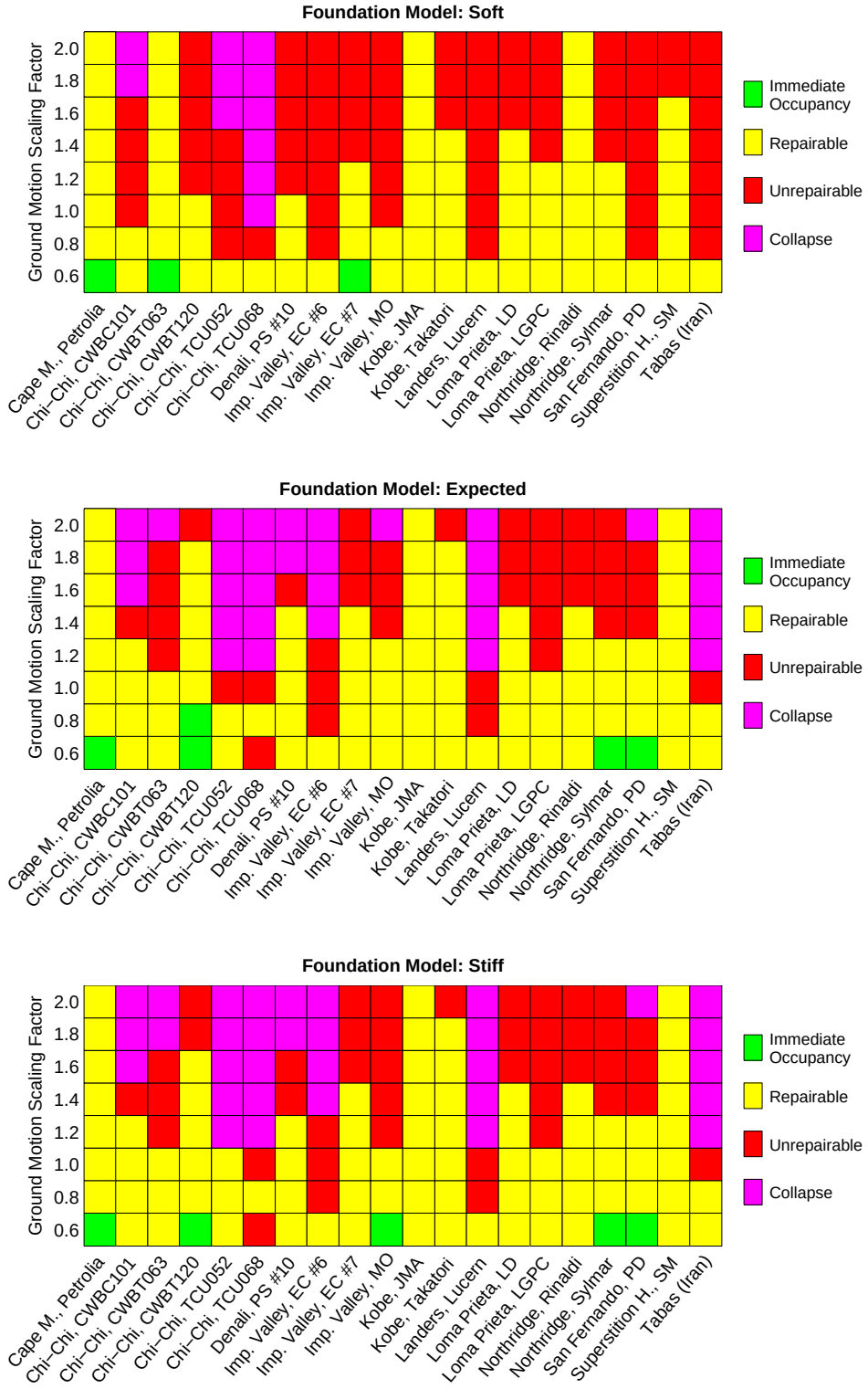

Figure 5.59: Simulated building performance categoreis for retrofit scheme RMF-3 in the incremental dynamic analyses using recorded ground motion time histories from actual earthquakes, assuming the "soft" (top figure), "expected" (middle figure), and "stiff" (bottom figure) realizations of the foundation springs.

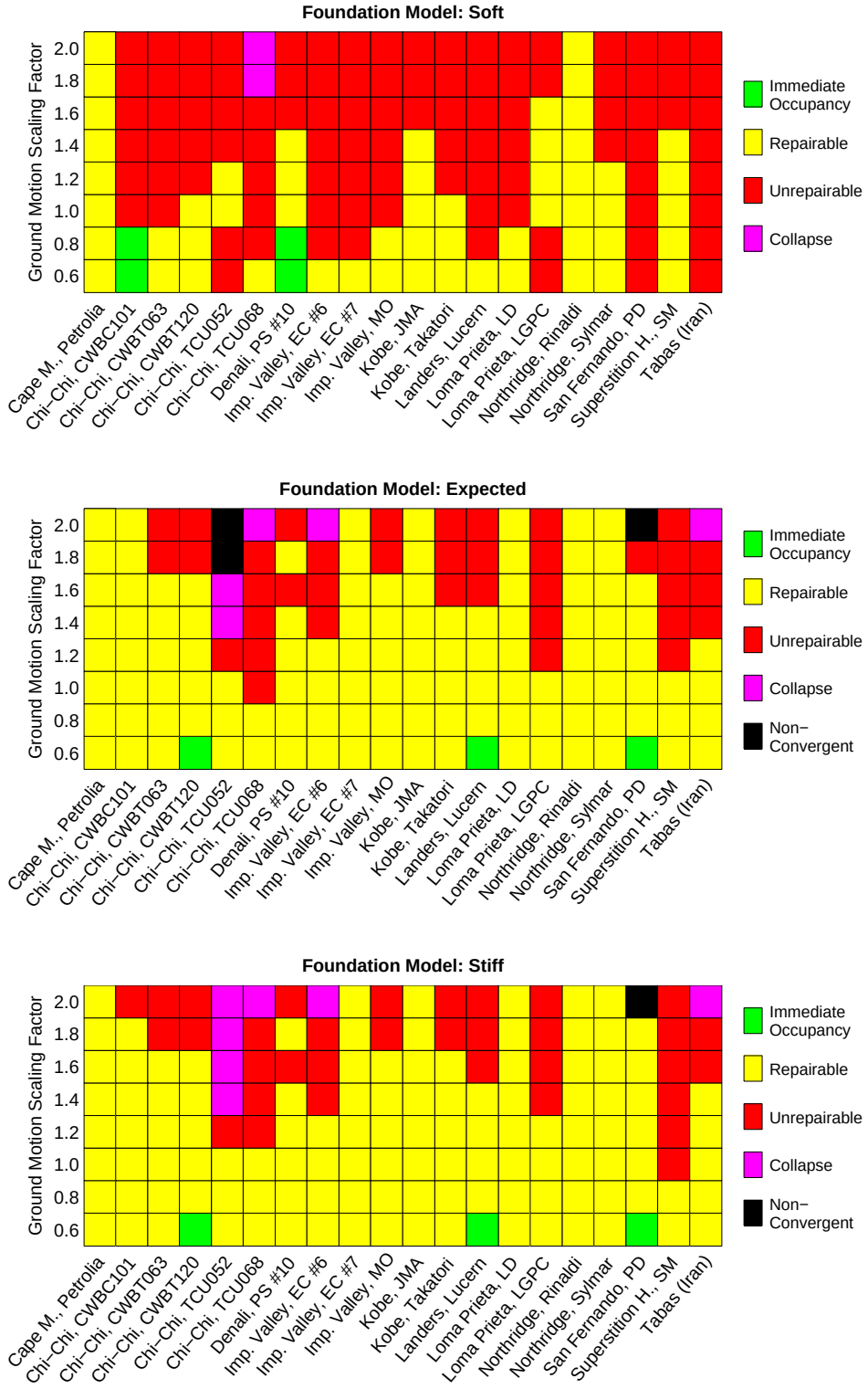

Figure 5.60: Simulated building performance categoreis for retrofit scheme RBR-1 in the incremental dynamic analyses using recorded ground motion time histories from actual earthquakes, assuming the "soft" (top figure), "expected" (middle figure), and "stiff" (bottom figure) realizations of the foundation springs.

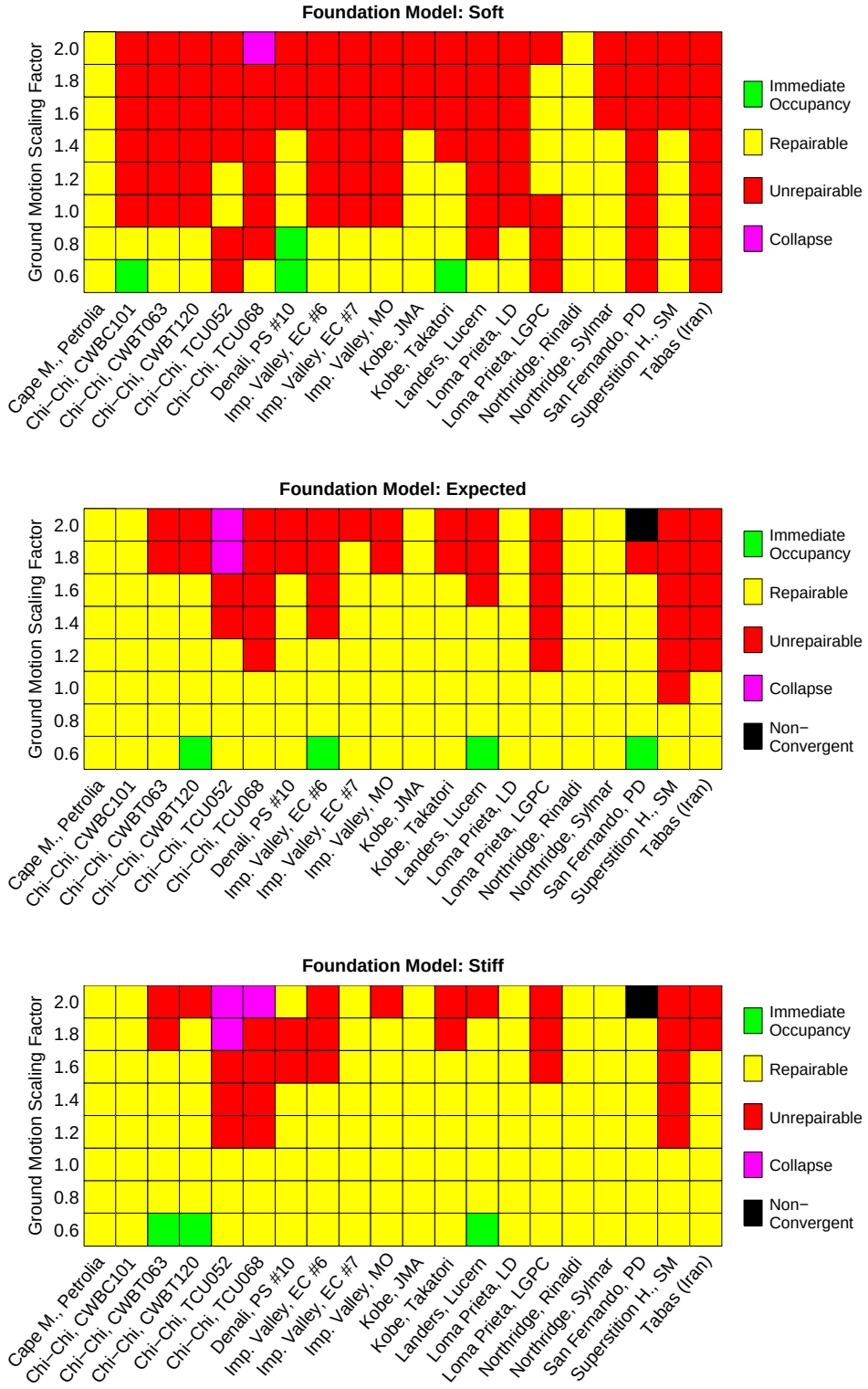

Figure 5.61: Simulated building performance categoreis for retrofit scheme RBR-2 in the incremental dynamic analyses using recorded ground motion time histories from actual earthquakes, assuming the "soft" (top figure), "expected" (middle figure), and "stiff" (bottom figure) realizations of the foundation springs.

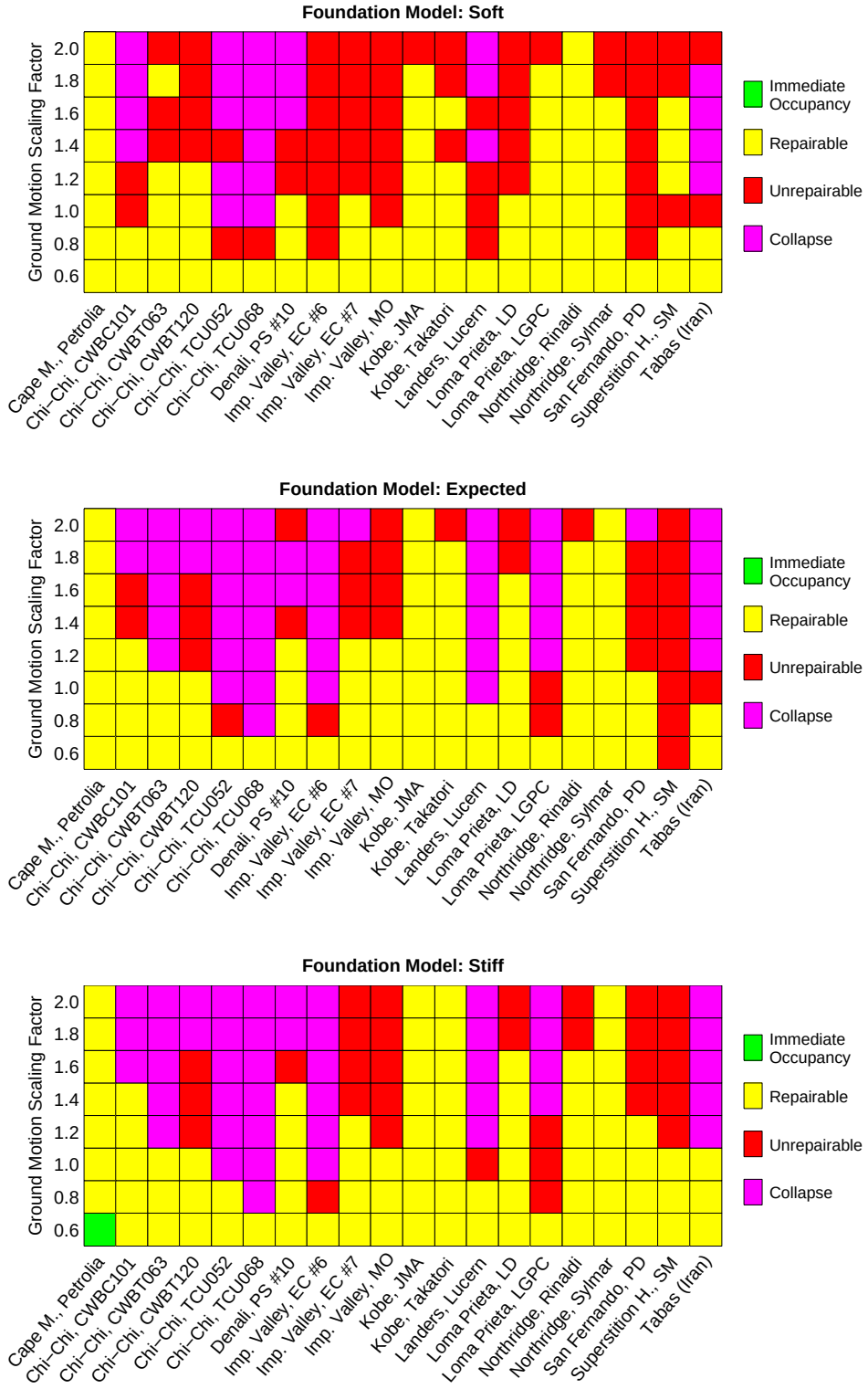

Figure 5.62: Simulated building performance categoreis for retrofit scheme RBR-3 in the incremental dynamic analyses using recorded ground motion time histories from actual earthquakes, assuming the "soft" (top figure), "expected" (middle figure), and "stiff" (bottom figure) realizations of the foundation springs.

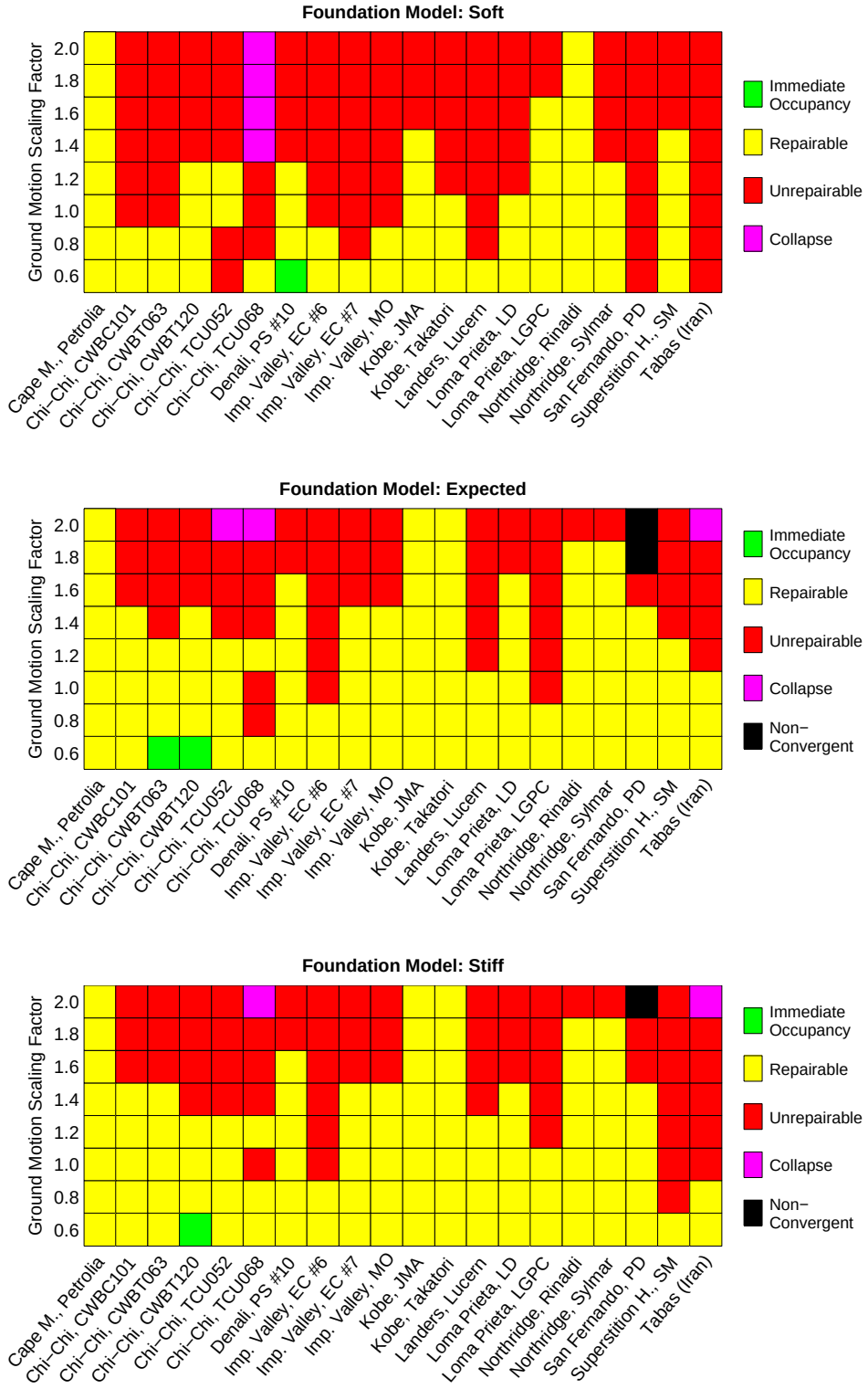

Figure 5.63: Simulated building performance categoreis for retrofit scheme RBRB-1 in the incremental dynamic analyses using recorded ground motion time histories from actual earthquakes, assuming the "soft" (top figure), "expected" (middle figure), and "stiff" (bottom figure) realizations of the foundation springs.

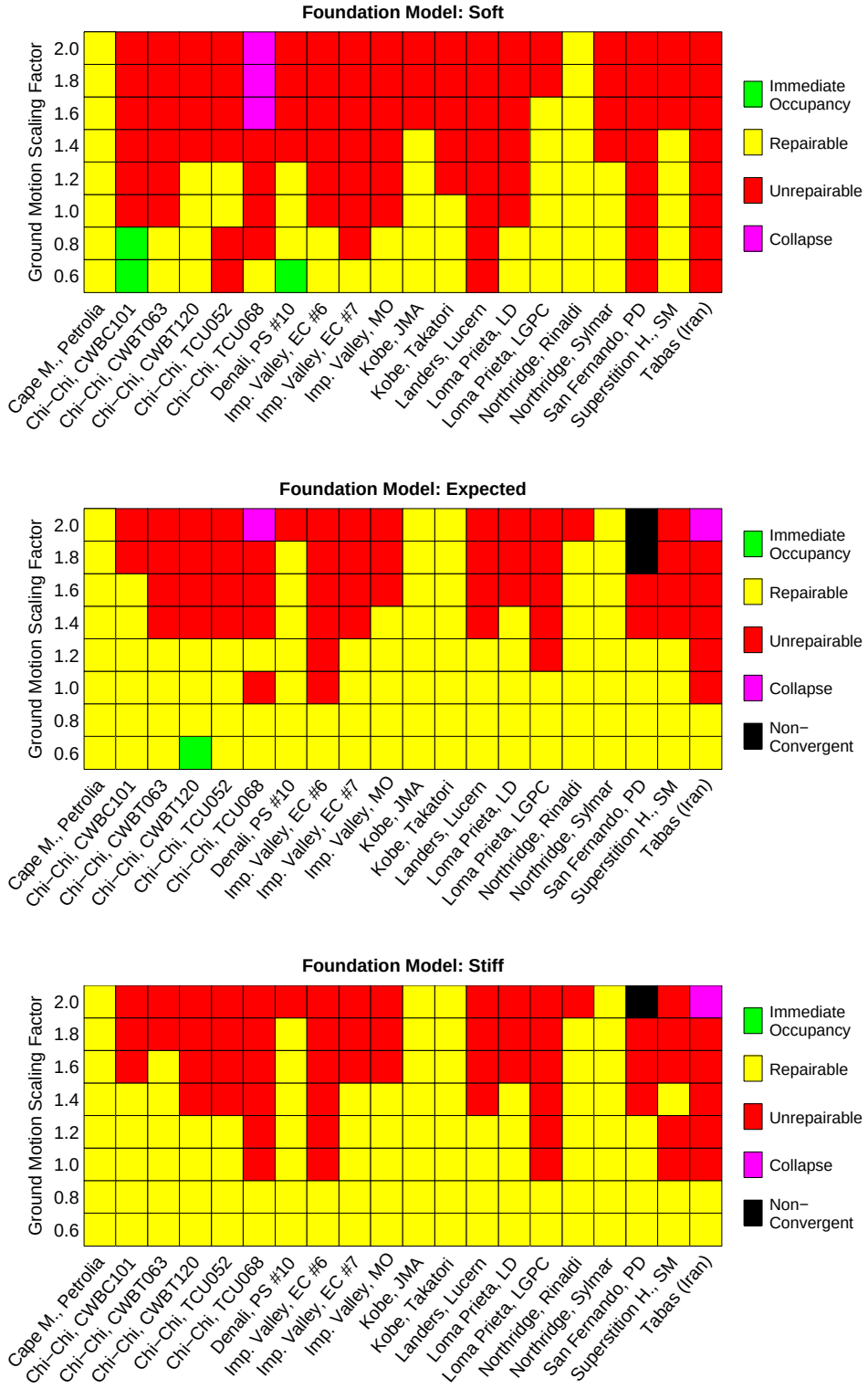

Figure 5.64: Simulated building performance categoreis for retrofit scheme RBRB-2 in the incremental dynamic analyses using recorded ground motion time histories from actual earthquakes, assuming the "soft" (top figure), "expected" (middle figure), and "stiff" (bottom figure) realizations of the foundation springs.

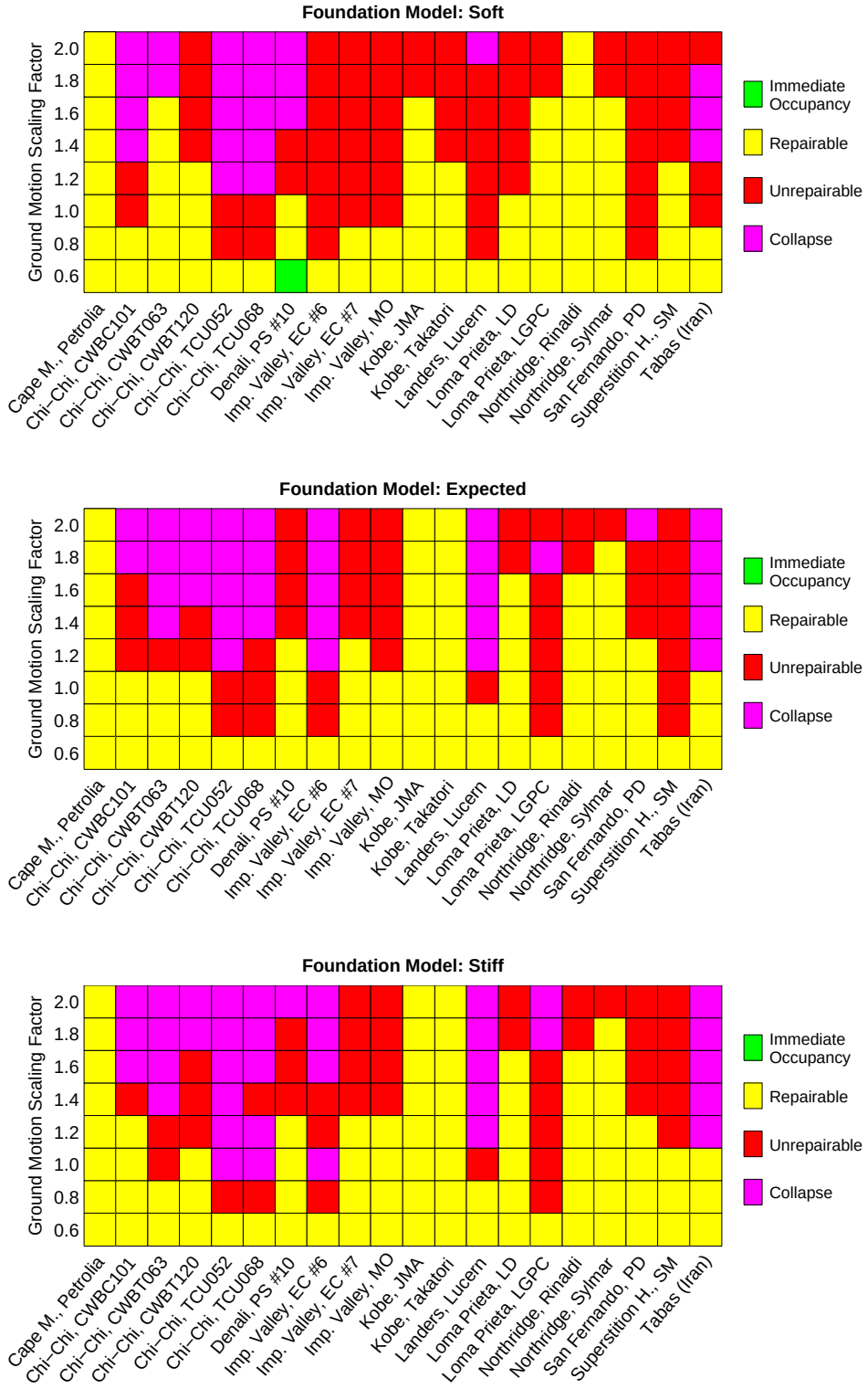

Figure 5.65: Simulated building performance categoreis for retrofit scheme RBRB-3 in the incremental dynamic analyses using recorded ground motion time histories from actual earthquakes, assuming the "soft" (top figure), "expected" (middle figure), and "stiff" (bottom figure) realizations of the foundation springs.

5.5 Building Performance: Overall

In this section, the results in the M_w 7.9 1857-like San Andreas fault earthquake scenario, the M_w 7.8 ShakeOut scenario earthquake on the San Andreas fault, the M_w 7.2 scenario earthquake on the Puente Hills fault system, and in the incremental dynamic analyses using recorded ground motions from actual earthquakes are gathered and summarized.

The number of simulations that resulted in the "repairable", "unrepairable", and "collapse" performance categories are summarized for all building models in Figure 5.66.

Also, fragility curves are constructed from the data from the M_w 7.9 1857-like San Andreas fault earthquake scenario, the M_w 7.8 ShakeOut scenario earthquake on the San Andreas fault, and the M_w 7.2 scenario earthquake on the Puente Hills fault system. The fragility curves show the probability of the building models realizing the "repairable" performance category or worse, the "unrepairable" performance category or worse, or model collapse, given horizontal peak ground velocity, and are presented in Figures 5.67, 5.68, and 5.69, respectively. The data from the incremental dynamic analyses using recorded ground motions from actual earthquakes is sparse, and showed a poor fit to cumulative log-normal distribution functions and was precluded when constructing the fragility curves.

When employing the "expected" foundation model, the base line model is simulated to collapse in 969 simulations (out of 4174), and complete economic loss ("unrepairable" or "collapse" performance categories) is simulated in 1447 simulations.

Retrofit schemes RBR-2, RBRB-1, and RBRB-2 achieve the greatest reduction in number of simulated collapses, or to 88, 81, and 78 simulations, respectively. Retrofit scheme RBR-1 is simulated to collapse in 125 simulations. Scheme RBR-1 is observed to localize deformations in a few stories just above the 8^{th} story, or where the bracing configuration is tapered. In contrast, schemes RBR-2, RBRB-1, and RBRB-2 deform more uniformly over the height, resulting in better performance.

As for complete economic losses, scheme RBR-2 performs best, with complete economic losses being simulated in 354 simulations. Complete economic losses of scheme RBR-1, RBRB-1, and RBRB-2 are simulated in 422, 485, and 468 simulations, respectively. As was mentioned in the previous sections, it appears that braced-frames that employ buckling-restrained braces tend to have greater residual drifts. However, the buckling-restrained braces are likely to store significant residual forces, and the residual drifts may be recovered to some extent by replacing the deformed braces.

Conventional brace elements are not expected to store residual forces to the same degree.

Out of the retrofit schemes that consider retrofitting the brittle beam-to-column moment resisting connections (RMF schemes), scheme RMF-3 is simulated to collapse in 450 simulations, and complete economic loss is simulated in 780 simulations. Interestingly, scheme RMF-2h is simulated to collapse in fewer simulations, or in 393 simulations. However, economic loss of scheme RMF-2h is simulated in 854 simulations. Retrofit schemes RMF-2 and RMF-3h are simulated to collapse in 464 and 509 simulations, respectively, and complete economic losses are simulated in 856 and 964 simulations, respectively.

Because of the complex nature of building responses under strong ground motions, it is difficult to give an argument that irrefutably justifies that repairing fewer beam-to-column connections will lead to lower collapse potential than if all the connections are upgraded. Also, in the simulated earthquakes the ground motion time histories from site-to-site have similar signatures, which characterize each simulated earthquake. In the ShakeOut scenario earthquake on the San Andreas fault and the earthquake scenario on the Puente Hills fault system, these commonalities in the ground motions happened to induce fewer simulated collapses for scheme RMF-2h compared to RMF-3. In the 1857-like San Andreas fault earthquake scenario and under the recorded ground motions from actual earthquake, scheme RMF-2h was not simulated to hold a lower collapse potential than scheme RMF-3. However, these results suggest that at a certain point, upgrading additional beam-to-column connections will result in minimal additional improvement in performance.

The two retrofit schemes that implement brace elements in the lower half of the building model while leaving the upper half unaltered (schemes RBR-3 and RBRB-3) are somewhat successful in that the schemes are more effective in limiting deformations in the lower half of the building model, compared to the moment-frame half-height retrofit schemes (RMF-1h, RMF-2h, and RMF-3h), and thus reduce to a greater extent global P-delta overturning moments. However, the resulting structures are stiffer than the moment-frame configurations and consequently attract larger seismic forces, which often results in excessive drifts in the upper half. A retrofit scheme that implements brace elements in the lower half of the building model in conjunction with upgrading beam-to-column moment connections in the upper half may present some additional improvement in building performance while keeping architectural impact low. Retrofit schemes RBR-3 and RBRB-3 are simulated to collapse in 571 and 491 simulations, respectively, and complete economic loss of the building models is simulated in 1049 and 981 simulations, respectively.

From the fragility curves constructed from the data, the simulated building performances can be related to horizontal peak ground velocities (PGV). For instance, the base line model realizes a 20% chance of simulated collapse at PGV of around 0.6 m/s. In comparison, a 20% chance of simulated collapse is realized at PGV around 1.8 m/s for retrofit schemes RBR-2, RBRB-1, and RBRB-2, at PGV of 1.6 m/s for scheme RBR-1, at PGV of 1 m/s for schemes RMF-2h, and at PGV of around 0.9 m/s for schemes RMF-2, RMF-3h, and RMF-3.

The horizontal peak ground velocities at which the building models realize a 20% chance of simulated "repairable" performance category or worse, "unrepairable" performance category or worse, and model collapse are summarized in Table 5.5.

The "expected" and "stiff" foundation models resulted in very similar building performances. When employing the "stiff" foundation model, foundation reactions were in the elastic range for all building models. When employing the "expected" foundation model, foundation reactions were in the elastic range for all but four building models. Yielding of the foundation springs was observed (in a few simulations) for retrofit schemes RBRB-1 and RBRB-2, but more noticeably for schemes RBR-1 and RBR-2, with residual foundation rotations up to around 1.5%. When employing the "soft" foundation model, unfortunately, some simulations for schemes RBR-1, RBR-2, and RBRB-2 failed to converge before showing a clear sign of collapse, which prevents a just comparison of the building models. The following observations can still be made. When employing the "soft" foundation model, the capacities of the foundation springs were frequently exceeded in all building models. As a result, all building models realized similar potential for exceeding the "immediate occupancy" foundation residual rotation limit, and only modest reduction in number of simulated complete economic losses of the building models is observed for the retrofit schemes. However, the foundations were never simulated to loose stability, although residual foundation rotations were observed to be as large as 10%, and the retrofit schemes achieve even more dramatic reduction in collapse potential, compared to when the "expected" and "stiff" foundation models are employed.

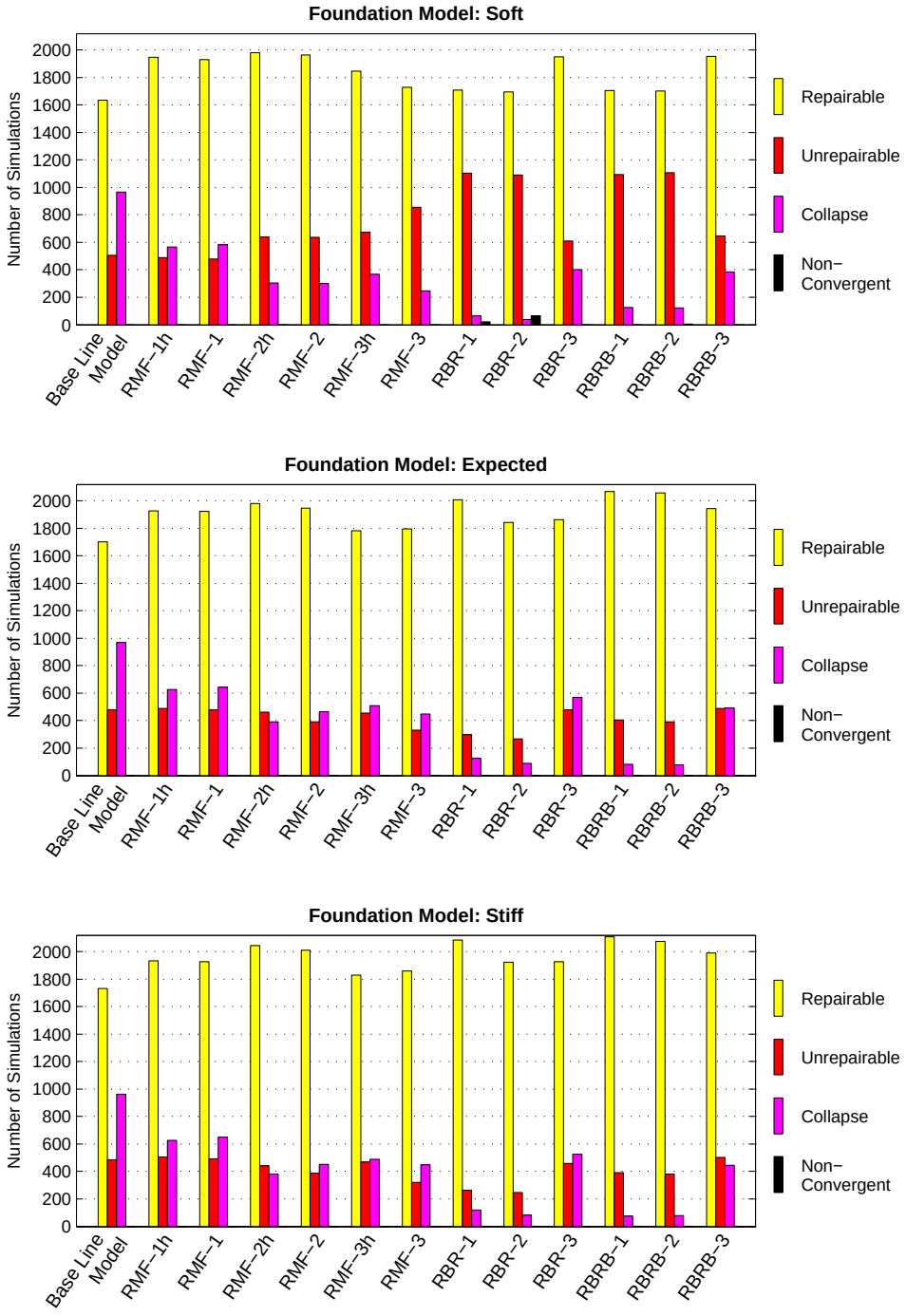

Figure 5.66: Summary of the number of simulations that resulted in the "repairable", "unrepairable", and "collapse" performance categories in all three simulated scenario earthquakes, and in the incremental dynamic analyses using recorded ground motions from actual earthquakes, assuming the "soft" (top figure), "expected" (middle figure), and "stiff" (bottom figure) foundation spring stiffnesses. The total number of simulations carried out for each building model, for each assumption on foundation spring stiffnesses, is 4154. Some simulations failed to converge before showing a clear sign of model collapse. These simulations are labeled as "non-convergent" and are removed from the data sets before constructing fragility curves.

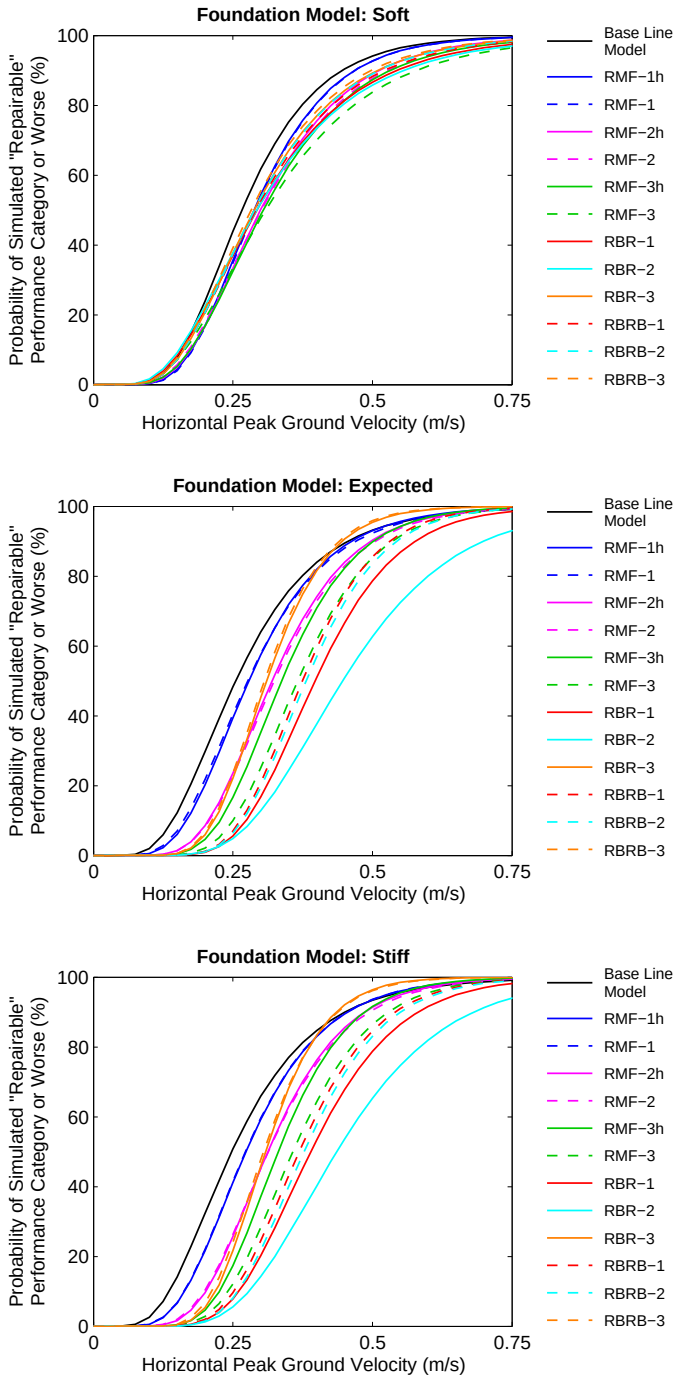

Figure 5.67: Fragility curves showing the probability of the building models realizing the "repairable" performance category or worse given horizontal peak ground velocity in the M_w 7.9 1857-like San Andreas fault earthquake scenario, the M_w 7.8 ShakeOut scenario earthquake on the San Andreas fault, and the M_w 7.2 scenario earthquake on the Puente Hills fault system, assuming the "soft" (top figure), "expected" (middle figure), and "stiff" (bottom figure) foundation spring stiffnesses.

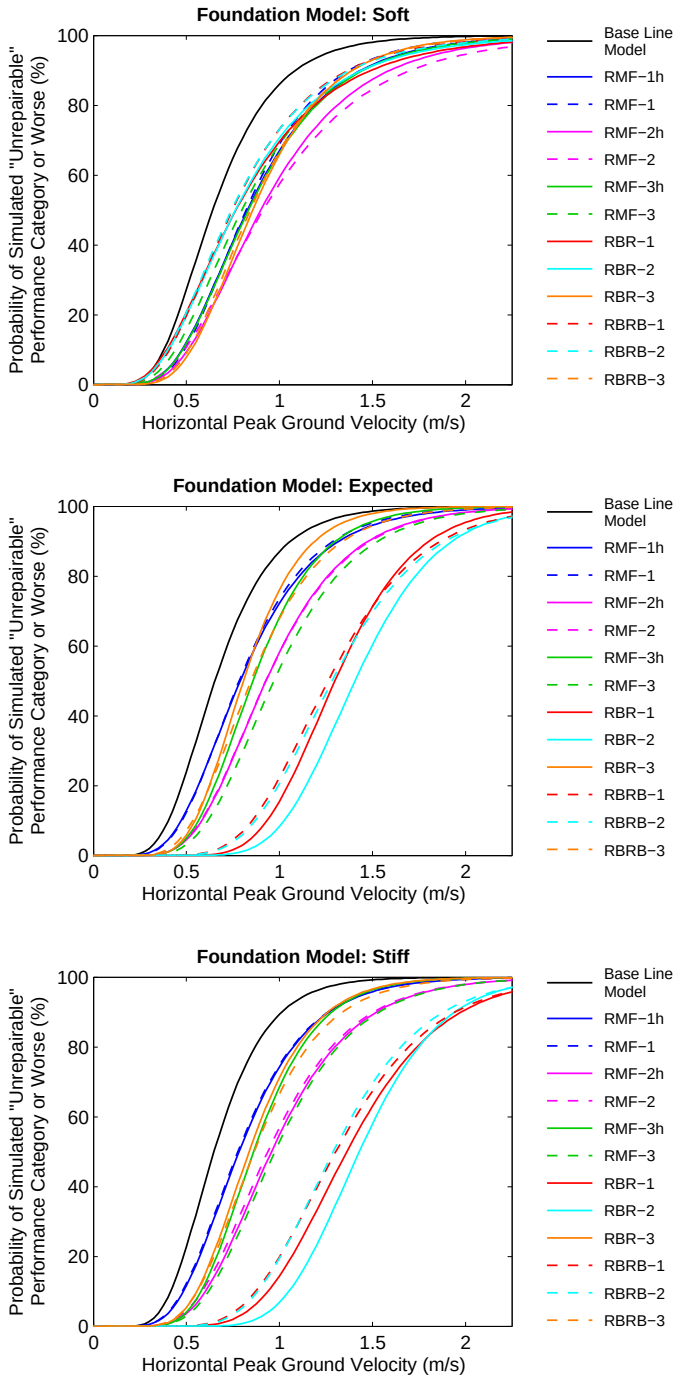

Figure 5.68: Fragility curves showing the probability of the building models realizing the "unrepairable" performance category or worse given horizontal peak ground velocity in the M_w 7.9 1857-like San Andreas fault earthquake scenario, the M_w 7.8 ShakeOut scenario earthquake on the San Andreas fault, and the M_w 7.2 scenario earthquake on the Puente Hills fault system, assuming the "soft" (top figure), "expected" (middle figure), and "stiff" (bottom figure) foundation spring stiffnesses.

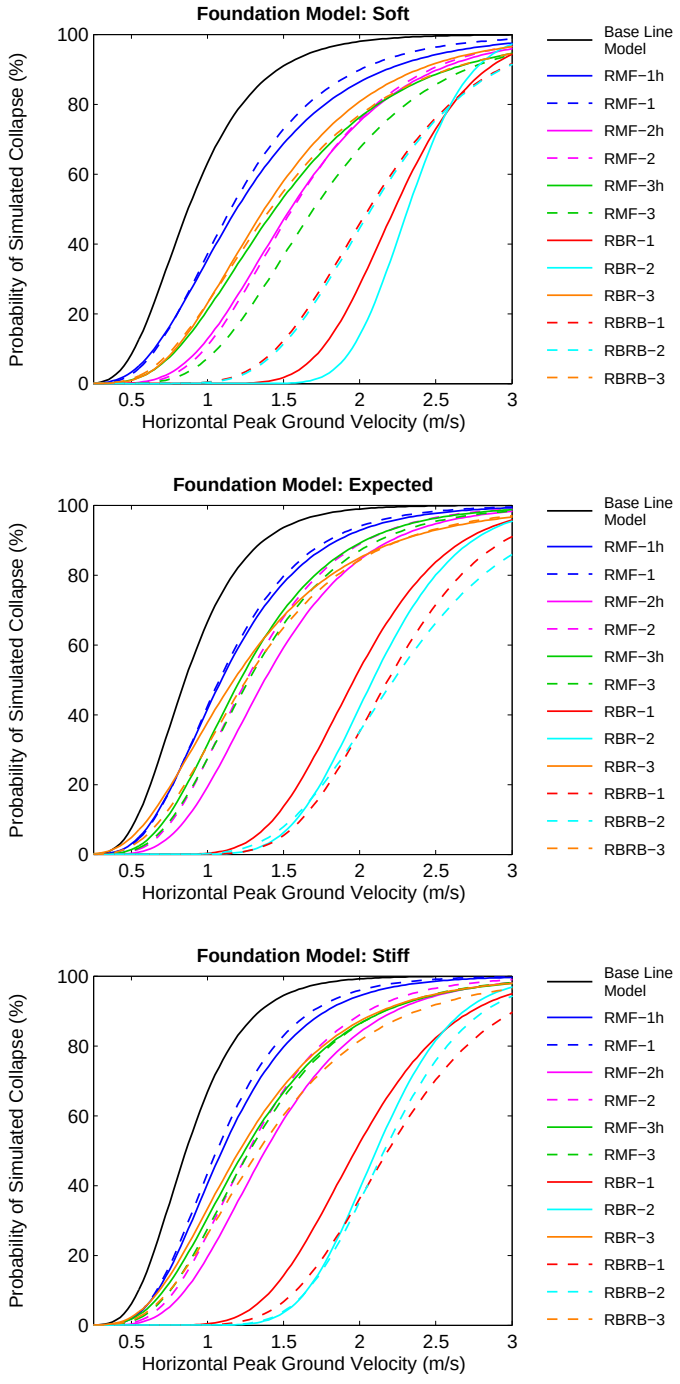

Figure 5.69: Fragility curves showing the probability of the building models realizing model collapse given horizontal peak ground velocity in the M_w 7.9 1857-like San Andreas fault earthquake scenario, the M_w 7.8 ShakeOut scenario earthquake on the San Andreas fault, and the M_w 7.2 scenario earthquake on the Puente Hills fault system, assuming the "soft" (top figure), "expected" (middle figure), and "stiff" (bottom figure) foundation spring stiffnesses.

Table 5.5: Horizontal peak ground velocities in meters per second at which the building models realize a 20% chance of simulated "repairable" performance category or worse, "unrepairable" performance category or worse, and model collapse in the M_w 7.9 1857-like San Andreas fault earthquake, the M_w 7.8 ShakeOut scenario earthquake on the San Andreas fault, and in the M_w 7.2 scenario earthquake on the Puente Hills fault system.

Building Performance:	"Repairable" or Worse			"Unrepairable" or Worse			Collapse		
Building Model: / **Foundation Model:**	"Soft"	"Expected"	"Stiff"	"Soft"	"Expected"	"Stiff"	"Soft"	"Expected"	"Stiff"
BLM[a]	0.20	0.18	0.18	0.45	0.48	0.48	0.62	0.62	0.65
RMF-1h	0.20	0.20	0.20	0.58	0.58	0.58	0.80	0.78	0.80
RMF-1	0.20	0.20	0.20	0.58	0.58	0.58	0.80	0.78	0.78
RMF-2h	0.20	0.25	0.23	0.62	0.68	0.70	1.12	1.00	1.00
RMF-2	0.20	0.25	0.23	0.60	0.68	0.68	1.15	0.90	0.93
RMF-3h	0.20	0.25	0.25	0.58	0.65	0.68	0.98	0.88	0.88
RMF-3	0.20	0.28	0.28	0.55	0.73	0.73	1.25	0.90	0.90
RBR-1	0.20[b]	0.30	0.30	0.50[b]	1.05	1.07	1.90[b]	1.60	1.60
RBR-2	0.20[b]	0.33	0.33	0.50[b]	1.15	1.18	2.08[b]	1.75	1.80
RBR-3	0.20	0.25	0.25	0.62	0.62	0.65	0.95	0.75	0.83
RBRB-1	0.20	0.30	0.28	0.50	0.98	1.00	1.62	1.80	1.78
RBRB-2	0.20[b]	0.30	0.30	0.50[b]	1.00	1.00	1.65[b]	1.75	1.83
RBRB-3	0.20	0.25	0.25	0.60	0.62	0.65	0.95	0.85	0.93

[a] Base Line Model

[b] Some simulations for retrofit schemes RBR-1, RBR-2, and RBRB-2 failed to converge before showing a clear sign of collapse, which may have an effect on these presented values.

5.6 Frequently Observed Collapse Mechanisms in the Building Models

To gain some understanding of how the building models behave towards their limit state, the collapse mechanisms most frequently observed for the building models are described in this section. Snapshots of the building models after detrimental collapse mechanisms have formed and at an instant before the building models are completely lost are presented in Figures 5.70 to 5.82 as follows:

	Figure:		Figure:
Base Line Model	5.70	RBR-1	5.77
RMF-1h	5.71	RBR-2	5.78
RMF-1	5.72	RBR-3	5.79
RMF-2h	5.73	RBRB-1	5.80
RMF-2	5.74	RBRB-2	5.81
RMF-3h	5.75	RBRB-3	5.82
RMF-3	5.76		

The figures show a view of frame A of the building models in their deformed state. The model deformations have been exaggerated by a factor of 3 for improved visualization. Beam and column elements are split into two, and each half is given a color depending on associated end plastic rotations. Brace elements are given a color depending on associated axial deformation. Plastic rotations in panel zones (if any) are shown as squares at the location of the joints and given a color depending on the degree of plastic deformation. The plastic deformations are normalized by yield deformations as follows:

$$\text{Beams and Column Elements:} \quad \theta_y = \frac{Z\sigma_y L}{6EI}$$
$$\text{Brace Elements:} \quad \delta_y = \frac{\sigma_y L}{E}$$
$$\text{Panel Zone Elements:} \quad \theta_y = \frac{\tau_y}{G}$$

Where Z is the cross-section plastic modulus, I is the cross-section moment of inertia, σ_y is material yield stress, τ_y is the material yield shear stress, E is the Young's modulus, G is the shear modulus, and L is the element length. For buckling-restrained elements, L is taken as the length of the yielding core L_{yc}.

Beam-to-column connections fractures are shown as black triangles, on top of corresponding beams if fractures occur in the top flange fibers, and on the bottom of beams if fractures occur in the

bottom flanges fibers. In a similar fashion, beam fiber ruptures near column faces are shown with red triangles. Column splice fractures and column baseplate fractures are also shown where they occur. If all fibers of a segment have ruptured or fractured, the element that contains that segment is removed from the building model.

Krishnan et al. described collapse mechanisms in steel moment-frame buildings as "quasi-shear bands", where plastic hinges form at the bottom of the columns of the lowest story of the shear quasi-shear band, and at the top of the columns of the highest story of the quasi-shear band, and all beams at intermediate levels exhibit excessive plastic hinging at both ends [50].

This description fits well to the collapse mechanisms observed for the moment-frame building models analyzed in the present study. However, hinging of the columns of the highest and lowest stories of the shear bands is often accommodated by fracturing of column splices, which are located approximately at one-third height of every second story.

The base line model is consistently observed to form such collapse mechanisms in the lower half of the building model, with wide spread fracturing of the brittle beam-to-column moment resisting connections in the lower half of the building model, while the upper half of the building model is virtually undamaged (Figure 5.70). From the perspective of dissipating energy through plastic deformation of structural elements, only half of the building model is being engaged in dissipating the seismic waves originating from the ground shaking.

In retrofit scheme RMF-1h, the lower half of the building model is strengthened to some degree, but it is proven not to be sufficient to spread the building damage over a greater portion of the building model. The building model is still observed to consistently form collapse mechanisms in the lower half of the building model, while the upper half remains virtually undamaged (Figure 5.71). It is therefore of little surprise that no additional improvement in structural performance is gained from retrofitting the remainder of the brittle beam-to-column moment resisting connections in that single moment-frame bay. Retrofit scheme RMF-1 is similarly observed to form collapse mechanisms in the lower half of the building model, while the upper half remains virtually undamaged (Figure 5.72).

As the brittle beam-to-column moment resisting connections are retrofitted in the second moment-frame bay only in the lower half of the building model (retrofit scheme RMF-2h), the strength of the lower half of the building model is now sufficient to transmit more of the seismic energy to the upper half of the building model. As a result, retrofit scheme RMF-2h is observed to form collapse

mechanisms in the form of shear bands in some instances in the upper half of the building model, and in other instances in the lower half of the building model (Figure 5.73).

In retrofit scheme RMF-2, all the brittle beam-to-column moment resisting connections in those two moment-frame bays are retrofitted, and collapse mechanisms are again observed to be confined to the lower half of the building model, but now some plastic deformations are observed in the upper half of the building model (Figure 5.74).

In retrofit scheme RMF-3h, the brittle beam-to-column moment resisting connections are retrofitted in all three moment-bays only in the lower half of the building model. The retrofit scheme is observed to form collapse mechanisms in the upper half of the building model, and less frequently in the lower half of the building model (Figure 5.75).

In retrofit scheme RMF-3, the remainder of the brittle beam-to-column moment resisting connections are retrofitted, and once again the building model is observed to consistently form collapse mechanisms in the lower half of the building models. In fact, the collapse mechanisms are frequently observed confined to the lowest quarter of the building model, but some plastic deformations are observed outside the detrimental shear band (Figure 5.76).

Retrofit schemes RMF-2h, RMF-2, RMF-3h, and RMF-3 realized comparable collapse potential in the analyses performed in this study, which suggests that at a certain point, upgrading additional beam-to-column connections will result in minimal additional improvement in performance.

The two retrofit schemes that consider implementing brace elements only in the lower half of the building model (schemes RBR-3 and RBRB-3) are successful in preventing formations of collapse mechanisms in the lower half of the building model, and the retrofit schemes are most frequently observed to form collapse mechanisms in the upper moment-frame portion of the building models (Figures 5.79 and 5.82). In a few instances, however, collapse mechanisms are observed to form in the lower braced portions of the building models.

The buckling-restrained version of this scheme realized a collapse potential comparable to schemes RMF-2h, RMF-2, RMF-3h, and RMF-3. The version that employed conventional brace elements did not perform as well. A retrofit scheme that implements brace elements in the lower half of the building in conjunction with upgrading beam-to-column moment connections in the upper half might present additional improvement in building performance while keeping architectural impact low.

The retrofit schemes that consider implementing conventional brace elements over the entire height of the building model (schemes RBR-1 and RBR-2) are also observed to form collapse mechanisms in localized bands of deformation. Under strong ground motions the brace elements buckle in compression, resulting in a dramatic drop in stiffness and strength. Furthermore, the brace elements do not necessarily buckle simultaneously over the entire height of the building. Hence, the braced-frame has a tendency to develop soft (and weak) stories in the most stressed portion of the building.

Another concern is that during buckling a brace element experiences strain concentrations in the plastic hinge that forms at mid-span. If the excessive strains do not already cause severing of the cross-section during the buckling phase, the strain hysteresis built into the cross-section dramatically limits the ductility of the element in consequent tension cycles. In the present study, conventional brace elements are observed to rupture through in tension at inter-story drift ratios in the range of 3-8%, depending on the previous cycles of deformation. If local buckling of the cross-sections was included in the modeling, complete element failure might be observed even sooner. So if the braced-frame survives a strong earthquake, it is questionable how much service the brace elements can provide in potential aftershocks. In addition, conventional braces are observed to experience large out-of-plane deformations during buckling, which could lead to hazards associated with falling debris.

Retrofit scheme RBR-1 is observed to localize most of the building deformation to a few stories just above the 8^{th} story, or where the bracing configuration is tapered. As a result, collapse mechanisms are observed to consistently form in those same stories (Figure 5.77). In the narrow band of deformation the brace elements that are in compression are in a severe mode of buckling and carry minimal compressive loads. The opposite brace elements have ruptured through in tension.

Retrofit scheme RBR-2 is observed to distribute deformations over a greater portion of the building model, resulting in better performance than scheme RBR-1. However, scheme RBR-2 is also observed to eventually form collapse mechanisms in narrow bands of deformation, but the collapse mechanisms do not always form in the same stories. Rather, the mechanisms are observed to form over four to seven stories somewhere in the middle portion of the building model (Figure 5.78)

The retrofit schemes that consider implementing buckling-restrained elements over the entire height of the building model (schemes RBRB-1 and RBRB-2) are not observed to form collapse

mechanisms in a narrow band of deformation. Rather, a large portion of the building models are deformed and collapse mechanisms form over the lower two-thirds of the building models (Figures 5.80 and 5.81). The two schemes are observed to collapse in a very similar fashion. Minimal differences were also shown in building performance between the two schemes.

Retrofit schemes RBR-2, RBRB-1, and RBRB-2 realized similar potential for collapse in the analyses performed in this study.

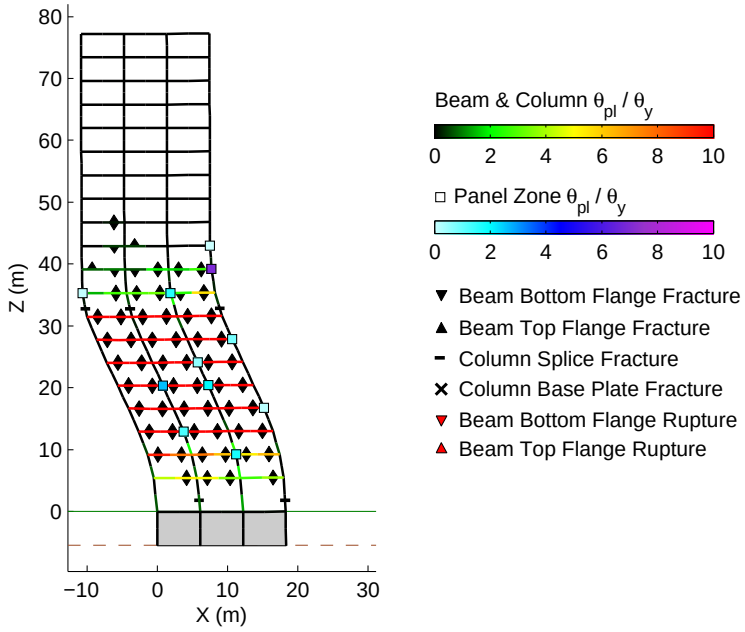

Figure 5.70: Frequently observed collapse mechanism in the base line model.

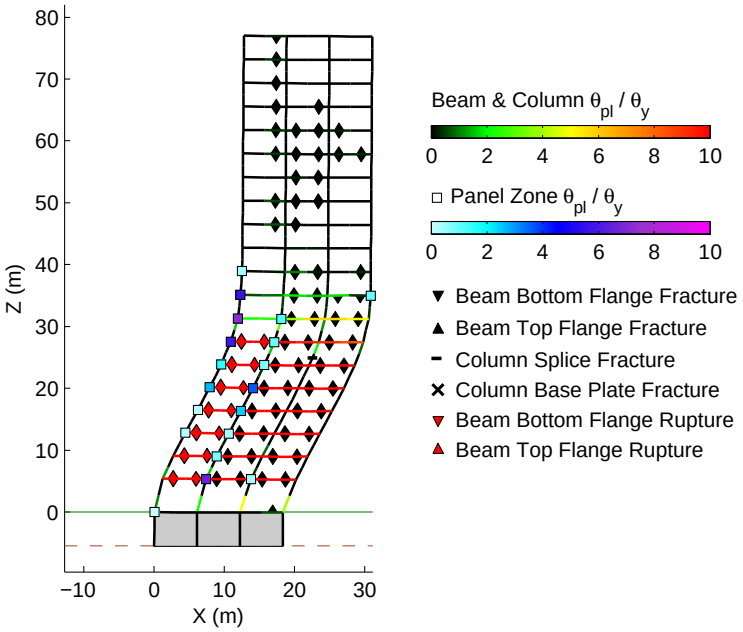

Figure 5.71: Frequently observed collapse mechanism in retrofit scheme RMF-1h.

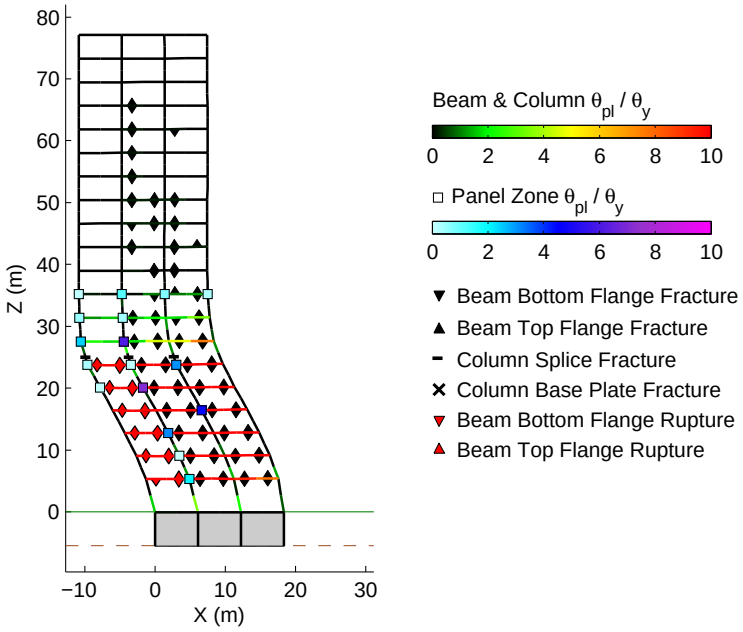

Figure 5.72: Frequently observed collapse mechanism in retrofit scheme RMF-1.

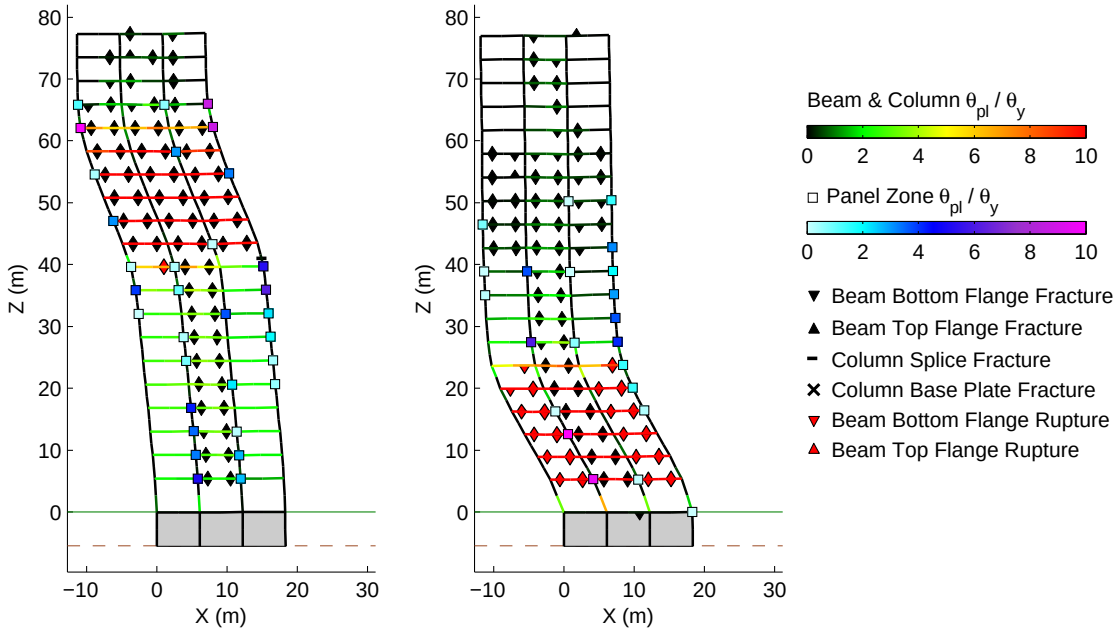

Figure 5.73: Frequently observed collapse mechanisms in retrofit scheme RMF-2h.

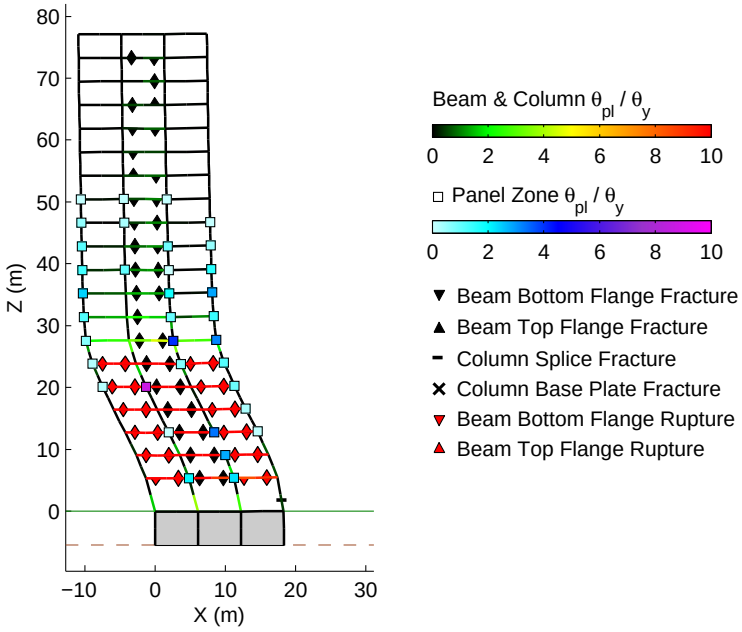

Figure 5.74: Frequently observed collapse mechanism in retrofit scheme RMF-2.

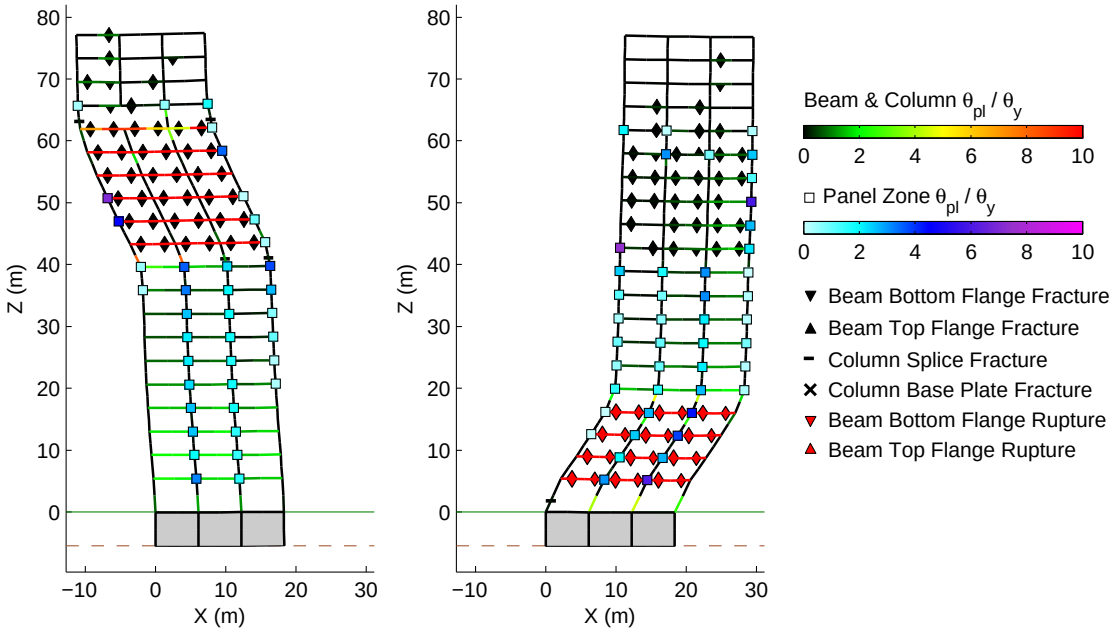

Figure 5.75: Frequently observed collapse mechanisms in retrofit scheme RMF-3h.

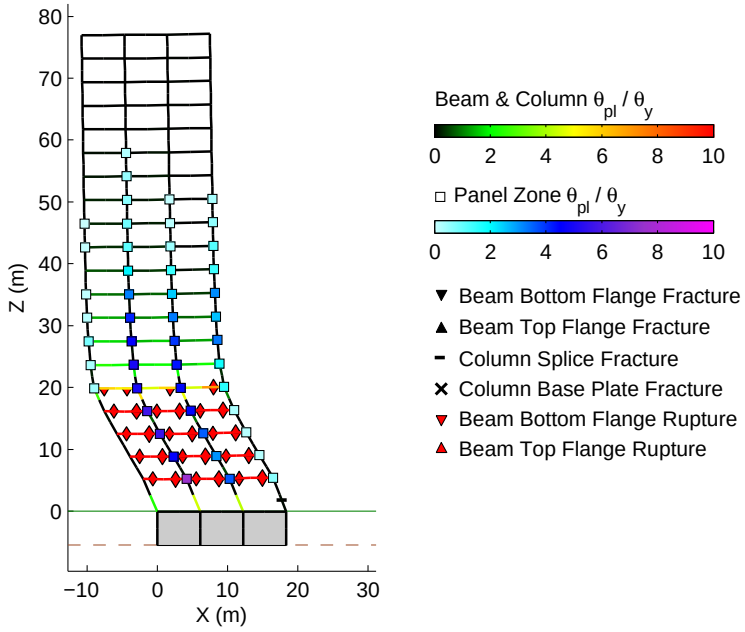

Figure 5.76: Frequently observed collapse mechanism in retrofit scheme RMF-3.

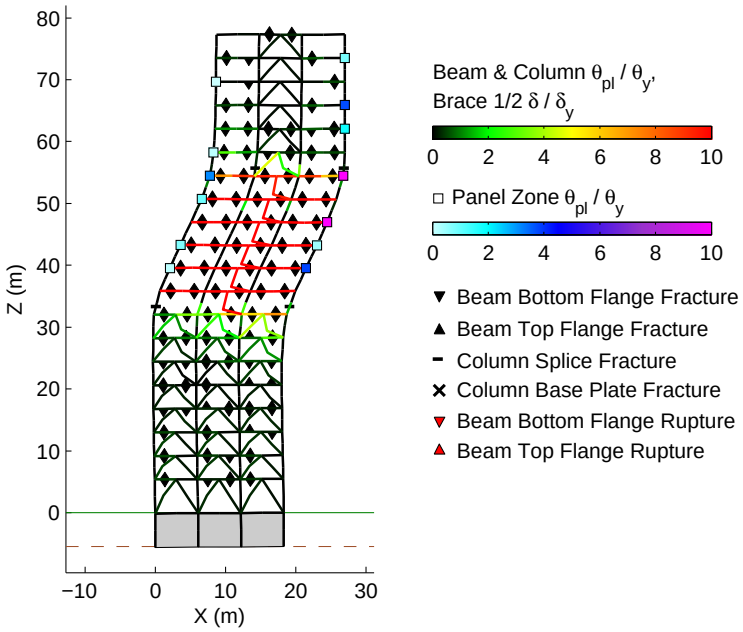

Figure 5.77: Frequently observed collapse mechanism in retrofit scheme RBR-1.

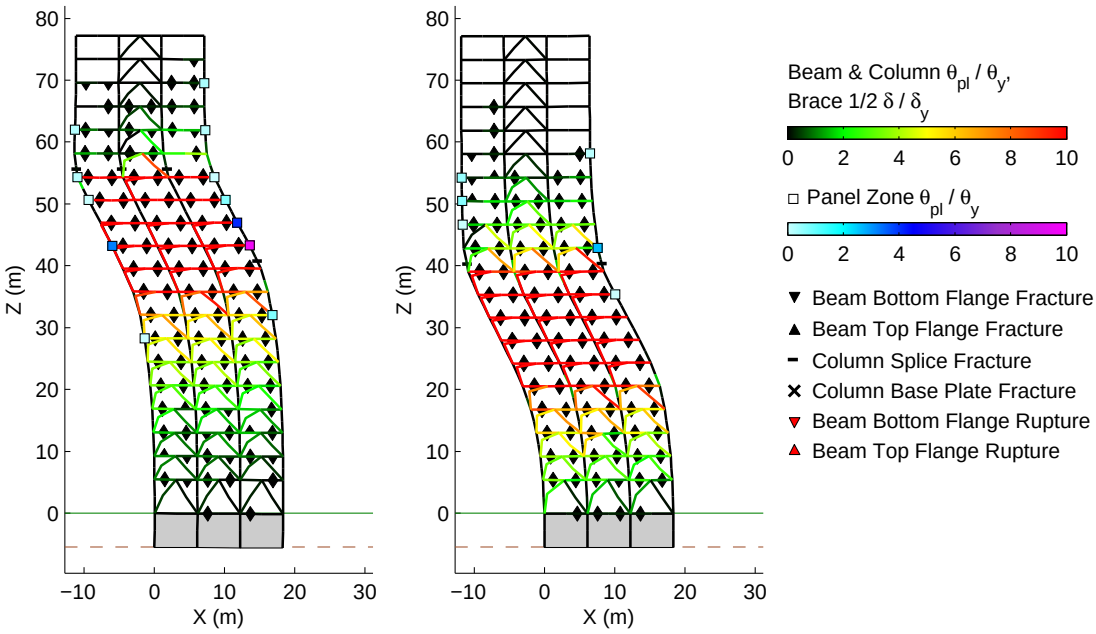

Figure 5.78: Frequently observed collapse mechanisms in retrofit scheme RBR-2.

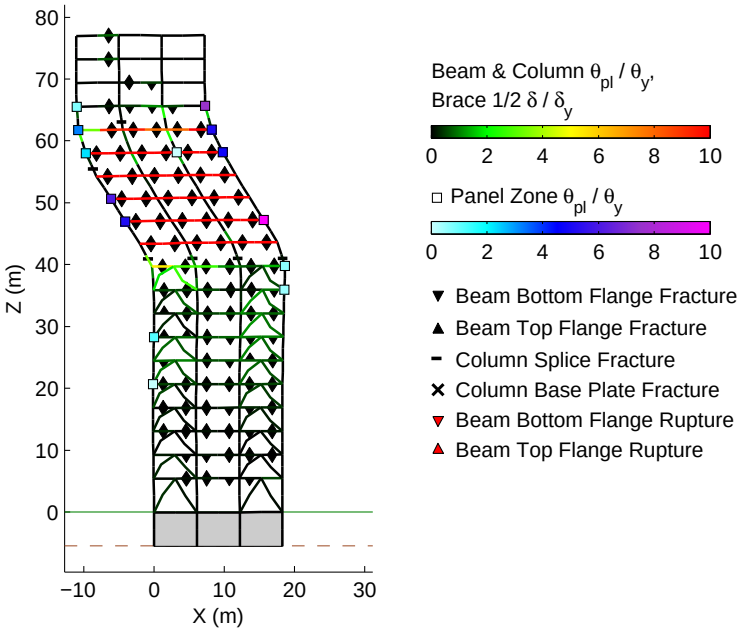

Figure 5.79: Frequently observed collapse mechanism in retrofit scheme RBR-3.

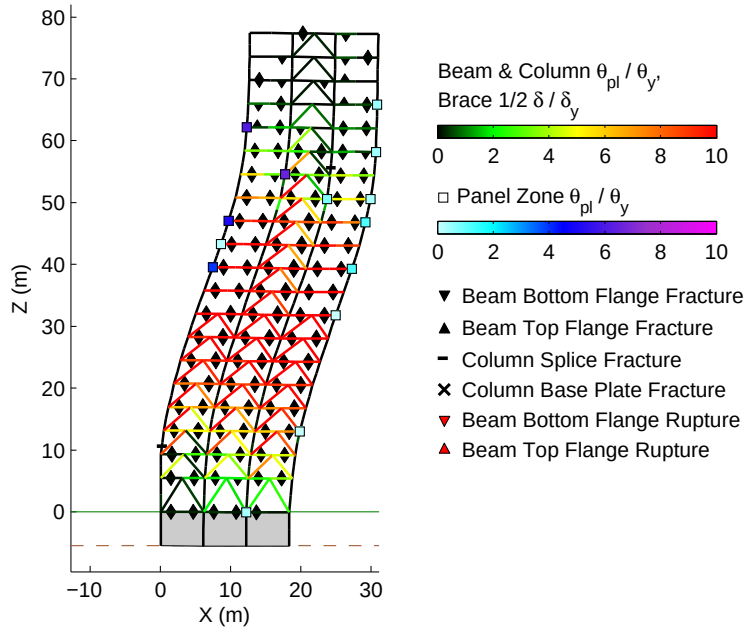

Figure 5.80: Frequently observed collapse mechanism in retrofit scheme RBRB-1.

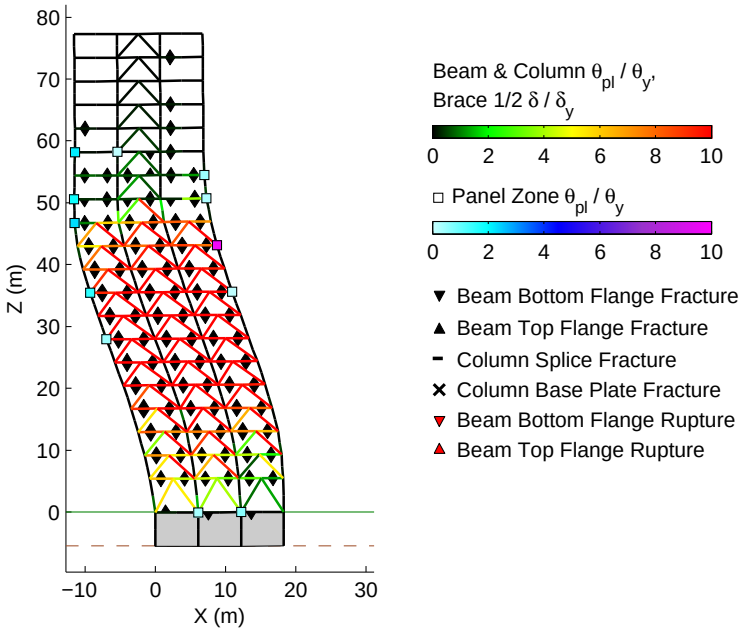

Figure 5.81: Frequently observed collapse mechanism in retrofit scheme RBRB-2.

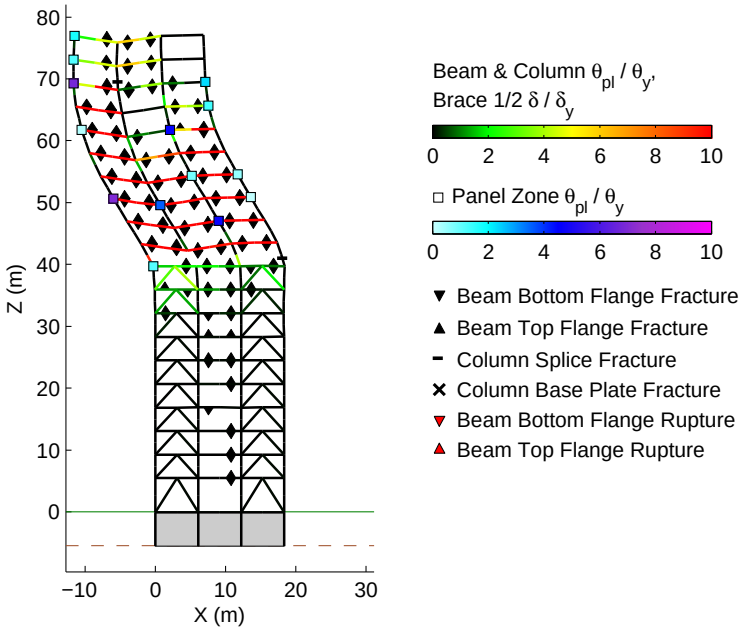

Figure 5.82: Frequently observed collapse mechanism in retrofit scheme RBRB-3.

Chapter 6

Summary, Conclusions, and Future Work

6.1 Summary of Research

This dissertation presents a case study of retrofitting a 20-story pre-Northridge steel moment-frame building. Twelve retrofit schemes were developed that present some range in degree of intervention. Three retrofitting techniques were considered: upgrading the brittle beam-to-column moment resisting connections, and implementing either conventional or buckling-restrained brace elements within the existing moment-frame bays. The retrofit schemes include some that are designed to the basic safety objective (BSO) of ASCE-41 Seismic Rehabilitation of Existing Buildings [4].

Detailed finite element models of the base line building and the retrofit schemes were constructed in STEEL, a nonlinear structural analyses program for steel frames developed at Caltech (also referred to as FRAME-2D). The building models include considerations of brittle beam-to-column moment resisting connection fractures, column splice fractures, column baseplate fractures, accidental contributions from "simple" non-moment resisting beam-to-column connections to the lateral force-resisting system, and composite actions of beams with the overlying concrete floor systems. Also, foundation interaction is included through nonlinear translational springs underneath basement columns. To address uncertainties associated with the modeling of the foundations "soft" (and weak), "stiff" (and strong), as well as expected foundation spring stiffnesses and capacities were applied.

A method for modeling buckling-restrained brace elements that accurately models the stiffness and ductility of the elements is presented, and the modeling of both conventional and buckling-restrained brace elements is validated against experimental data.

Then, the building models were analyzed under ground motions from three simulated earthquakes that produce intense ground shaking in the greater Los Angeles metropolitan area, and under recorded strong ground motions from actual earthquakes scaled with scaling factors ranging from 0.2 to 2.0 in increments of 0.2. These add up to a total of 4154 nonlinear dynamic analyses performed per building model, per assumption on foundation spring stiffnesses and capacity. Hence, the effectiveness of the retrofit schemes is robustly tested.

6.2 Summary of Results

From the analyses of the building models the following conclusions can be drawn:

- Pre-Northridge steel moment-frame buildings in the 20-story height can be expected to suffer severe damage and even building collapse in vast regions if a major earthquake strikes the greater Los Angeles metropolitan area. Similar observations were made by Hall et al. [38, 32, 33, 34], Olsen et al. [59], Krishnan et al. [45, 46, 47], and Muto and Krishnan [48, 57]. Although other building types, such as unreinforced concrete and masonry buildings, may be in even greater risk of suffering severe structural damage or collapse, the seismic risk of pre-Northridge steel moment-frame buildings should not be neglected.

- Retrofit schemes that convert existing moment-frames to braced-frames by implementing either conventional or buckling-restrained braces, and are designed to the basic safety objective (BSO) of ASCE 41 Seismic Rehabilitation of Existing Structures [4] using a nonlinear dynamic design procedure, are effective in reducing collapse potential and avoiding unrepairable building damage of pre-Northridge steel moment-frame buildings in the 20-story range.

- Relying on conventional brace elements to resist seismic lateral forces is not without complications. Under strong ground motions the brace elements buckle in compression, resulting in a dramatic drop in stiffness and strength. Furthermore, the brace elements do not necessarily buckle simultaneously over the entire height of the building. Hence, the braced-frame has a tendency to develop soft and weak stories in the most stressed portion of the building. Also, during buckling a brace element experiences strain concentrations in the plastic hinge that forms at mid-span. If the excessive strains do not already cause severing of the cross-section during the buckling phase, the strain hysteresis built into the cross-section dramatically limits the ductility of the element in

consequent tension cycles. In the present study conventional brace elements are observed to completely fail at inter-story drifts as low as 3%. If local buckling of the cross-sections was included in the modeling, complete element failure might be observed even sooner. So if the braced-frame survives a strong earthquake, it is questionable how much service the brace elements can provide in potential aftershocks. Also, conventional braces are observed to experience large out-of-plane deformations during buckling, which could lead to hazards associated with falling debris.

- In contrast, buckling-restrained braces have been developed to avoid the pitfalls associated with buckling in compression. Experiments have shown that the braces can reliably undergo multiple cycles of highly plastic deformations. Hence, the braces do not deteriorate in the same rapid fashion as conventional brace elements. Also, since the braces do not drop in strength during compression, structural behavior is better controlled. For instance, consider the bracing configuration that consisted of installing brace elements in all three moment-frame bays in the first eight stories, and then in a single bay in the remaining stories. When conventional brace elements were applied (scheme RBR-1), deformations were observed to localize in the region just above where the bracing configuration is tapered. This was not the case when buckling-restrained brace elements were applied.

- Although buckling-restrained brace elements have greater unit cost than conventional braces, the former type may actually be more economical. Adding brace elements to the existing structure renders it being much stiffer, which consequently leads to greater seismic forces. Hence, in addition to installing brace elements, columns (and foundations) may need to be strengthened. Because conventional braces experience a dramatic drop in strength during buckling, the braces need to be considerably over-sized in design. In contrast, buckling-restrained braces have almost symmetric properties in tension and compression, thus smaller cross sections are necessary. As a result, buckling-restrained braces induce lower seismic demands on columns and foundations, which may present savings in retrofit costs. Also, in the present study schemes RBR-2 and RBRB-1 (and RBRB-2) realized similar collapse potential. This suggests that fewer buckling-restrained brace elements may be needed to achieve a certain level of building performance, which presents further savings in retrofit costs over conventional braces and less impact on the architecture.

- Upgrading the brittle beam-to-column moment resisting connections results in some improved building performance. Also, the results in the analyses performed in this study suggest that at a

certain point, upgrading additional beam-to-column connections will result in minimal additional improvement in performance.

- The retrofit schemes that consider strengthening the lower half of the building by implementing brace elements while leaving the upper half unaltered (schemes RBR-3 and RBRB-3) are somewhat successful. The schemes are more effective in reducing deformations in the lower half of the building model than the moment-frame half-height retrofit schemes, and thus reduce to a greater extent global P-delta overturning moments. However, the resulting structures are stiffer than the moment-frame configurations and consequently attract larger seismic forces, which often proved to be too great for the upper portion. A retrofit scheme that implements brace elements in the lower half of the building in conjunction with upgrading beam-to-column moment connections in the upper half may present additional improvement in building performance while keeping architectural impact low.

- To address uncertainties associated with the modeling of foundation interaction, three realizations of the foundations were applied. The "expected" and "stiff" foundation models resulted in very similar building performances. When employing the "stiff" foundation model, foundation reactions were in the elastic range for all building models. When employing the "expected" foundation model, foundation reactions were in the elastic range for all but four building models. Yielding of the foundation springs was observed (in a few simulations) for retrofit schemes RBRB-1 and RBRB-2, but more noticeably for retrofit scheme RBR-1 and RBR-2, with residual foundation rotations up to around 1.5%. When employing the "soft" foundation model, the capacities of the foundation springs were frequently exceeded in all building models at only moderate levels of seismicity. As a result, all building models realized similar potential for exceeding the residual foundation rotation limits for the "immediate occupancy" and "repairable" performance categories. However, the foundations were never simulated to loose stability, although residual foundation rotations were observed to be as large as 10%. Also, the collapse potential of the building models when employing the "soft" foundation model were not too different from what was observed for the "expected" and "stiff" foundation models.

- In the present study, building responses were simulated under ground motions from three hypothetical large magnitude earthquakes that produce intense ground shaking in the greater Los Angeles metropolitan area: a M_w 7.9 1857-like San Andreas fault earthquake [46, 47, 44], the M_w 7.8 ShakeOut scenario earthquake on the San Andreas fault [27, 26], and a M_w 7.2 earthquake

on the Puente Hills fault system [25, 30]. In all three earthquake scenarios, the base line model is simulated to collapse in large regions in the greater Los Angeles metropolitan area. The two San Andreas fault earthquakes are simulated to produce longer duration of shaking, which proves to be a greater challenge for preventing collapse through retrofitting measures. The most destructive ground motion time histories are found in the 1857-like San Andreas fault earthquake. These time histories posses a combination of long duration and peak ground velocities in excess of 2.5 m/s. A few even have peak ground velocities in excess of 3.5 m/s. In contrast, the largest peak ground velocities observed in the ShakeOut scenario earthquake and the Puente Hills earthquake are around 2.5 m/s.

6.3 Future Work

In the present study it has been shown that the seismic performance of pre-Northridge steel moment-frame buildings in the 20-story range can be substantially improved by implementing conventional and buckling-restrained brace elements. Further directions that this research can be expanded to include the following:

- In order to communicate results better to decision makers, the costs associated with the retrofit schemes need to be evaluated. Such cost estimations should include retrofit take off costs, impact on leasing rates, impact on seismic insurance rates, and probabilistic seismic losses over the life-span of the building ($\sim$50 years). Given the poor performance observed for this class of buildings in this study and other studies [38, 32, 33, 34, 45, 46, 47, 48, 57], such analysis might even reveal a return on retrofit investments. At the very least, the reduced probabilistic seismic losses can serve as a counterweight against retrofit take off costs.

- Investigate the effectiveness of more retrofit devices, such as friction dampers, viscous dampers, viscoelastic solid dampers, and self-centering devices. A recent study showed that friction dampers were more optimal than buckling-restrained braces for retrofitting two three-story steel moment frames. In contrast, the study showed that buckling-restrained braces were more optimal than friction dampers for retrofitting a six-story steel moment-frame [3]. Hence, a retrofit study should consider multiple retrofit techniques.

- Developing algorithms that optimize utilization of the different types of retrofit devices. Such algorithms could also be helpful in the design of new structures. The optimization algorithms

should consider multiple performance levels such as the “repairable”, “unrepairable”, and “collapse” performance categories adopted in this study.

- Expand the research to include multiple index buildings. Such index buildings should be of varying heights and have varying footprints. By performing detailed retrofit analysis on a range of index buildings, individual owners of pre-Northridge steel moment-frame buildings, as well as a communities such as the greater Los Angeles metropolitan area, could be better enlightened to what retrofitting measures and associated costs are necessary to achieve acceptable seismic performance for this class of buildings.

Bibliography

[1] AISC. *Manual of Steel Construction, Load and Resistance Factor Design (Third Edition)*. American Institute of Steel Construction, Inc., USA, 2005.

[2] AISC. *Prequalified Connections for Special and Intermediate Steel Moment Frames for Seismic Applications Including Supplement No. 1*. American Institute of Steel Construction, Inc., USA, 2010.

[3] APOSTOLAKSI, G., AND DARGUSH, G. F. Optimal seismic design of moment-resisting frames with hysteretic passive devices. *Earthquake Engineering and Structural Dynamics 39*, 4 (2010), 355–376.

[4] ASCE. *Seismic Rehabilitation of Existing Buildings*. American Society of Civil Engineers, USA, 2007.

[5] BLACK, C., MAKRIS, N., AND AIKEN, I. Component testing, stability analysis and charecterization of buckling-restrained unbonded braces. Tech. Rep. PEER 2002/08, University of California, Berkeley, Berkeley, California, USA, 2003.

[6] BLACK, G. R., WENGER, W. A., AND POPOV, E. P. Inelastic buckling of steel struts under cyclic load reversals. Tech. Rep. UCB/EERC-80-40, Earthquake Engineering Research Center, University of California, Berkeley, California, 1980.

[7] CASAROTTI, E., STUPAZZINI, M., LEE, S., KOMATITSCH, D., PIERSANTI, A., AND TROMP, J. Cubit and seismic wave propagation based upon the spectral-element method: Advanced unstructured mesher for complex 3d geological media. *Proceedings of the 16th International Meshing Roundtable* (2008), 579–597.

[8] CHALLA, V. R. M. Nonlinear seismic behavior of steel planar moment-resisting frames. Tech. Rep. EERL 92-01, Earthquake Engineering Research Laboratory, California Institute of Technology, Pasadena, California, 1992.

[9] CHALLA, V. R. M., AND HALL, J. F. Earthquake collapse analysis of steel frames. *Earthquake Engineering and Structural Dynamics 23*, 11 (1994), 1199–1218.

[10] DAY, S., AND BRADLEY, C. Memory efficient simulation of anelastic wave propagation. *Bulletin of the Seismological Society of America 91* (2001), 520–531.

[11] DI SARNO, L., AND ELNASHAI, A. S. Bracing systems for seismic retrofitting of steel frames. *Journal of Constructional Steel Research 65* (2009), 452–465.

[12] DOLAN, J. F., CHRISTOFFERSON, S. A., AND SHAW, J. W. Recognition of paleoearthquakes on the puente hills thrust fault, california. *Science 300* (2003), 115–118.

[13] EBERHART-PHILLIPS, D., HAEUSSLER, P. J., FREYMUELLER, J. T., FRANKEL, A. D., RUBIN, C. M., CRAW, P., RATCHKOVSKI, N. A., ANDERSON, G., CARVER, G. A., CRONE, A. J., DAWSON, T. E., FLETCHER, H., HANSEN, R., HARP, E. L., HARRIS, R. A., HILL, D. P., HREINSDOTTIR, S., JIBSON, R. W., JONES, L. M., KAYEN, R., KEEFER, D. K., LARSEN, C. F., MORAN, S. C., PERSONIUS, S. F., PLAFKER, G., SHERROD, B., SIEH, K., SITAR, N., AND WALLACE, W. K. The 2002 Denali fault earthquake, Alaska: A large magnitude, slip-partitioned event. *Science 300* (2003), 1113–1118.

[14] EGUCHI, R. T., GOLTZ, J. D., TAYLOR, C. E., CHANG, S. E., FLORES, P. J., JOHNSON, L. A., SELIGSON, H. A., AND BLAIS, N. C. Direct economic losses in the Northridge earthquake: A three-year post-event perspective. *Earthquake Spectra 14*, 2 (1998), 245–264.

[15] FELL, B. V. Large-scale testing and simulation of earthquake-induced ultra low cycle fatigue in bracing members subjected to cyclic inelastic buckling. Tech. Rep. Ph.D. Dissertation, University of California, Davis, 2008.

[16] FELL, B. V., KANVINDE, A. M., DEIERLEIN, G. G., AND MYERS, A. T. Experimental investigation of inelastic cyclic buckling and fracture of steel braces. *Journal of Structural Engineering 135*, 1 (2009), 19–22.

[17] FEMA. *Prestandard and Commentary for the Seismic Rehabilitation of Buildings*. FEMA-356. Federal Emergency Management Agency, USA, 2000.

[18] FEMA. *Recommended Postearthquake Evaluation and Repair Criteria for Welded Steel Moment-Frame Buildings*. FEMA-352. Federal Emergency Management Agency, USA, 2000.

[19] FEMA. *Recommended Seismic Evaluation and Upgrade Criteria for Existing Welded Steel Moment Frame Buildings*. FEMA-351. Federal Emergency Management Agency, USA, 2000.

[20] FEMA. *State of the Art Report on Connection Performance*. FEMA-355D. Federal Emergency Management Agency, USA, 2000.

[21] FEMA. *NEHRP Recommended Provisions for Seismic Regulations for New Buildings and Other Structures*. FEMA-450 and FEMA-451. Federal Emergency Management Agency, USA, 2004.

[22] FEMA. *Techniques for the Seismic Rehabilitation of Existing Buildings*. FEMA-547. Federal Emergency Management Agency, 2006.

[23] FILIATRAULT, A., TREMBLAY, R., AND WANITKORKUL, A. Performance evaluation of passive damping systems for the seismic retrofit of steel moment-resisting frames subjected to near-field ground motions. *Earthquake Spectra 17*, 3 (2001), 427–456.

[24] GRAVES, R. W. Simulating seismic wave propagation in 3D elastic media using staggered grid finite difference. *Bulletin of the Seismological Society of America 85* (1996), 1091–1106.

[25] GRAVES, R. W. Broadband simulation for a Mw 6.7 earthquake on the Puente Hills fault. *Seismological Research Letters 76* (2005), 242.

[26] GRAVES, R. W., AAGAARD, B. T., AND HUDNUT, K. W. The ShakeOut earthquake source and ground motion simulations. *Earthquake Spectra 27*, 2 (2011).

[27] GRAVES, R. W., AAGAARD, B. T., HUDNUT, K. W., STAR, L. M., STEWART, J. P., AND JORDAN, T. H. Broadband simulations for M_w 7.8 southern San Andreas earthquakes: Ground motion sensitivity to rupture speed. *Geophysical Research Letters 35*, L22302, doi:10.1029/2008GL035750 (2008).

[28] GRAVES, R. W., AND PITARKA, A. Broadband time history simulations using a hybrid approachs. In *Proceedings of the 13th World Conference on Earthquake Engineering* (2004), p. Paper No. 1098.

[29] GRAVES, R. W., AND PITARKA, A. Broadband ground-motion simulation using a hybrid approach. *Bulletin of the Seismological Society of America 100*, 5A (2010), 2095–2123.

[30] GRAVES, R. W., AND SOMERVILLE, P. Broadband ground motion simulations for scenario ruptures of the Puente Hills fault. In *8^{th} National Conference on Earthquake Engineering, San Francisco, USA* (2006), Paper No. 1052.

[31] GUNEYISI, E. M. Seismic reliability of steel moment resisting framed buildings retrofitted with buckling restrained braces. *Earthquake Engineering and Structural Dynamics 41*, 5 (2012), 853–874.

[32] HALL, J. F. Parameter study of the response of moment-resisting steel frame buildings to near-source ground motions. Tech. Rep. EERL 95-08, Earthquake Engineering Research Laboratory, California Institute of Technology, Pasadena, California, 1995.

[33] HALL, J. F. Seismic response of steel frame buildings to near-source ground motions. Tech. Rep. EERL 97-05, Earthquake Engineering Research Laboratory, California Institute of Technology, Pasadena, California, 1997.

[34] HALL, J. F. Seismic response of steel frame buildings to near-source ground motions. *Earthquake Engineering and Structural Dynamics 27*, 12 (1998), 1445–1464.

[35] HALL, J. F. Problems encountered from the use (or misuse) of Rayleigh damping. *Earthquake Engineering and Structural Dynamics 35*, 5 (2006), 525–545.

[36] HALL, J. F., AND CHALLA, V. R. M. Beam-column modeling. *Journal of Engineering Mechanics 121*, 12 (1995), 1284–1291.

[37] HAMBURGER, R. O., KRAWINKLER, H., MALLEY, J. O., AND ADAN, S. M. Seismic design of steel special moment frames: A guide for practicing engineers. Tech. Rep. National Earthquake Hazards Reduction Program Seismic Design Technical Brief No. 2., National Institute of Standards and Technology, U.S. Department of Commerce, 2009.

[38] HEATON, T. H., HALL, J. F., WALD, D. J., AND HALLING, M. W. Response of high-rise and base-isolated buildings to a hypothetical m 7.0 blind thrust earthquake. *Science 267* (1995), 206–211.

[39] IWATA, Y., SUGIMOTO, H., AND KUWAMURA, H. Reparability limit of steel structural buildings based on the actual data of Hyogoken-Nanbu earthquake. *Technical Memorandum of Public Works Research Institute 4022* (2006), 86–95.

[40] JI, C., TAN, Y., HELMBERGER, D., AND TROMP, J. Modeling teleseismic P and SH static offsets for great strike-slip earthquakes. In *Proceedings of the American Geophysical Union Fall Meeting, USA* (2003).

[41] KOMATITSCH, D., LIU, Q., TROMP, J., SÜSS, P., STIDHAM, C., AND SHAW, J. H. Simulations of ground motion in the Los Angeles basin based upon the spectral element method. *Bulletin of the Seismological Society of America 94* (2004), 187–206.

[42] KOMATITSCH, D., AND TROMP, J. Introduction to the spectral element method for three-dimensional seismic wave propagation. *Geophys. J. Int. 139* (1999), 806–822.

[43] KRISHNAN, S. Three-dimensional nonlinear analysis of tall irregular steel buildings subject to strong ground motion. Tech. Rep. EERL 2003-01, Earthquake Engineering Research Laboratory, California Institute of Technology, Pasadena, California, USA, 2003.

[44] KRISHNAN, S., CASAROTTI, E., GOLTZ, J., JI, C., KOMATITSCH, D., MOURHATCH, R., MUTO, M., SHAW, J. H., TAPE, C., AND TROMP, J. Rapid estimation of damage to tall buildings using near real-time earthquake and archived structureal simulations. *Bulletin of the Seismological Society of America 102*, 6 (2012), 2646–2666.

[45] KRISHNAN, S., JI, C., KOMATITSCH, D., AND TROMP, J. Performance of 18-story steel moment frame buildings during a large San Andreas earthquake – a Southern California-wide end-to-end simulation. Tech. Rep. EERL 2005-01, http://caltecheerl.library.caltech.edu, Earthquake Engineering Research Laboratory, California Institute of Technology, Pasadena, California, USA, 2005.

[46] KRISHNAN, S., JI, C., KOMATITSCH, D., AND TROMP, J. Case studies of damage to tall steel moment frame buildings in southern California during large San Andreas earthquakes. *Bulletin of the Seismological Society of America 96*, 4 (2006), 1523–1537.

[47] KRISHNAN, S., JI, C., KOMATITSCH, D., AND TROMP, J. Performance of two 18-story steel moment frame buildings in southern California during two large simulated San Andreas earthquakes. *Earthquake Spectra 22*, 4 (2006), 1035–1061.

[48] KRISHNAN, S., AND MUTO, M. SHAKEOUT 2008: Tall steel moment frame building response. Tech. Rep. Technical report to the US Geological Survey, California Institute of Technology, Pasadena, California, USA, 2008.

[49] KRISHNAN, S., AND MUTO, M. Mechanism of collapse, sensitivity to ground motion features, and rapid estimation of the response of tall steel moment frame buildings to earthquake excitation. Tech. Rep. EERL 2011-02, Earthquake Engineering Research Laboratory, California Institute of Technology, Pasadena, California, USA, 2011.

[50] KRISHNAN, S., AND MUTO, M. Mechanism of collapse of tall steel moment frame buildings under earthquake excitation. *Journal of Structural Engineering 138*, 11 (2012), 1361–1387.

[51] LIGNOS, D. G., MORENO, D. M., AND BILLINGTON, S. L. Seismic retrofit of steel moment-resisting frames with high-performance fiber-reinforced concrete infill panels: Large-scale hybrid simulation experiments. *Journal of Structural Engineering 140*, 3 (2013).

[52] LIU, Q., POLET, J., KOMATITSCH, D., AND TROMP, J. Spectral-element moment tensor inversions for earthquakes in southern california. *Bulletin of the Seismological Society of America 94*, 5 (2004), 1748–1761.

[53] MCCORMICK, J., ABURANO, H., IKENAGA, M., AND NAKASHIMA, M. Permissible residual deformation levels for building structures considering both safety and human elements. In *Proceedings of the 14th World Conference on Earthquake Engineering* (2008), pp. Paper No. 05–06–0071.

[54] MERRIT, S., UANG, C., AND BENZONI, G. Subassemblage testing of CoreBrace buckling-restrained braces. Tech. Rep. TR-2003/01, University of California, San Diego, La Jolla, California, USA, 2003.

[55] MERRIT, S., UANG, C., AND BENZONI, G. Subassemblage testing of Star Seismic buckling-restrained braces. Tech. Rep. TR-2003/04, University of California, San Diego, La Jolla, California, USA, 2003.

[56] MOURHATCH, R., AND KRISHNAN, S. Simulation of broadband ground motion: Low-frequency spectral-element synthetics + high-frequency empirical greens function synthetics. *Bulletin of the Seismological Society of America* (2014), In submission.

[57] MUTO, M., AND KRISHNAN, S. Hope for the best, prepare for the worst: Response of tall steel buildings to the shakeout scenario earthquake. *Earthquake Spectra 27*, 2 (2011).

[58] NEWELL, J., UANG, C., AND BENZONI, G. Subassemblage testing of CoreBrace buckling-restrained braces (G-series). Tech. Rep. TR-2006/01, University of California, San Diego, La Jolla, California, USA, 2006.

[59] OLSEN, A., HEATON, T., AND HALL, J. Characterizing ground motions that collapse steel, moment-resisting frames or make them unrepairable. *Earthquake Spectra* (2013), in press.

[60] PETAK, W. J., AND ELAHI, S. The Northridge earthquake, USA, and its economic and social impact. In *EuroConference on Global Change and Catastrophe Risk Management, Earthquake Risks in Europe, IIASA, Laxenburg, Austria* (2000).

[61] PLESCH, A., TAPE, C., GRAVES, R., SHAW, J. H., SMALL, P., AND ELY, G. Updages for the cmv-h including new representation of the offshore santa maria and san bernadino basins and the new moho surface. In *SCEC 2011 Annual Meeting* (2011), Southern California Earthquake Center, pp. Poster B–128.

[62] REGENTS, U. C. Pacific Eearthquake Engineering Research ground motion database. http://peer.berkeley.edu/peer_ground_motion_database, 2010. [Online; accessed 1-June-2013].

[63] SABELLI, R., MAHIN, S., AND CHANG, C. Seismic demands on steel braced frame buildings with buckling-restrained braces. *Engineering Structures 25*, 5 (2003), 655–666.

[64] SANDIA NATIONAL LABORATORY, U. Cubit: Geometry and mesh generation toolkit. http://cubit.sandia.gov, 2011. [Online; accessed 15-Nov-2011].

[65] SHAW, J. H., PLESCH, A., DOLAN, J. F., PRATT, T. L., AND FIORE, P. Puente Hills blind-thrust system, Los Angeles, California. *Bulletin of the Seismological Society of America 92* (2002), 2946–2960.

[66] SHAW, J. H., AND SUPPE, J. Earthquake hazards of active blind-thrust faults under the central Los Angeles basin. *Journal of Geophysical Research 101*, B4 (1996), 8623–8642.

[67] SIEH, K. E. A study of late Holocene displacement history along the south-central reach of the San Andreas fault. Tech. Rep. Ph.D. Dissertation, Stanford University, California, USA, 1977.

[68] SIEH, K. E. Pre-historic large earthquakes produced by slip on the San Andreas fault at Pallett creek, California. *Journal of Geophysical Research 83* (1978), 3907–3939.

[69] SIEH, K. E. Slip along the San Andreas fault associated with the great 1857 earthquake. *Bulletin of the Seismological Society of America 68*, 5 (1978), 1421–1448.

[70] SYMANS, M. D., CHARNEY, F. A., WHITTAKER, A. S., CONSTANTINOU, M. C., KIRCHER, C. A., JOHNSON, M. W., AND MCNAMARA, R. Energy dissipation systems for seismic applications: current practice and recent developements. *Journal of Structural Engineering 134*, SPECIAL ISSUE: Design and Analysis of Structures with Seismic Damping Systems (2008), 3–21.

[71] TAFAKORI, E., BANAZADEH, M., JALALI, S. A., AND TEHRANIZADEH, M. Risk-based optimal retrofit of a tall steel building by using friction dampers. *The Structural Design of Tall and Special Buildings 22*, 9 (2013), 700–717.

[72] TROMP, J., KOMATITSCH, D., AND LIU, Q. Spectral-element adjoint methods in seismology. *Communications in Computational Physics 3*, 1 (2008), 1–32.

[73] URIZ, P., AND WHITTAKER, A. S. Retrofit of pre-Northridge steel moment-resisting frames using fluid viscous dampers. *The Structural Design of Tall and Special Buildings 10*, 5 (2001), 371–390.

[74] WILLS, C. J., AND CLAHAN, K. B. Developing a map of geologically defined site-condition categories for California. *Bulletin of the Seismological Society of America 96* (2006), 1483–1501.